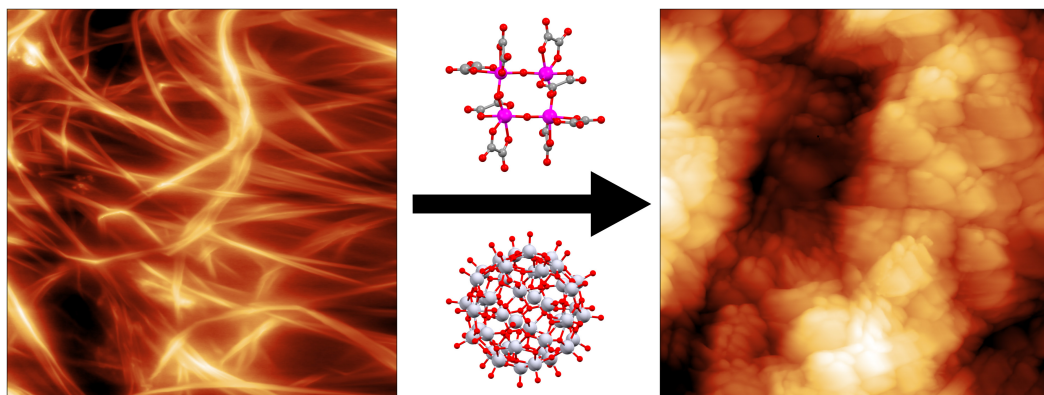




DOCTORAL THESIS No. 2025:53
FACULTY OF NATURAL RESOURCES AND AGRICULTURAL SCIENCES

Bio-based hybrid nanomaterials for theranostic and environmental applications

TROY C. BREIJAERT



Bio-based hybrid nanomaterials for theranostic and environmental applications

Troy C. Breijaert

Faculty of Natural Resources and Agricultural Sciences
Department of Molecular Sciences
Uppsala



SWEDISH UNIVERSITY
OF AGRICULTURAL
SCIENCES

DOCTORAL THESIS

Uppsala 2025

Acta Universitatis Agriculturae Sueciae
2025:53

Cover: Example of (bacterial) cellulose nanofibers being covered by metal oxides using either solution precursors or pre-formed nanoparticles

ISSN 1652-6880

ISBN (print version) 978-91-8046-562-5

ISBN (electronic version) 978-91-8046-567-0

<https://doi.org/10.54612/a.3vpjp8ffe7>

© 2025 Troy C. Breijaert, <https://orcid.org/0000-0003-0829-8553>

Swedish University of Agricultural Sciences, Department of Molecular Sciences, Uppsala, Sweden

The summary chapter is licensed under CC BY 4.0. To view a copy of this license, visit <https://creativecommons.org/licenses/by/4.0/>. Other licences or copyright may apply to illustrations and attached articles.

Print: SLU Grafisk service, Uppsala 2025

Bio-based hybrid nanomaterials for theranostic and environmental applications

Abstract

Bio-based nanomaterials are defined as materials of biological origin with one or more dimensions smaller than 100 nm. At this small scale, exciting properties start to emerge which leads to materials with a large variety in applications, including environmental remediation, metal waste recycling and theranostics (combined therapy and diagnostics). By modifying the surface of these bio-based nanomaterials it is possible to selectively change the affinity of biomaterials towards different metal ions and mineral oxide nanoparticles. This allows for the production of tailored bio-based hybrid materials. Present work is focussing on two key aspects, (1) metal selectivity and (2) theranostics. One of the aims was in modifying nanocellulose to produce a material suitable for the separation of late transition metals Nickel and Cobalt from Rare Earth elements and the mechanism behind this selectivity. Another track focussed on the introduction of mineral oxide nanoparticles onto cellulose-based nanomaterials derived from cotton or grown by microorganisms and their unique properties for their application as wound-dressing materials.

Keywords: Cellulose, Surface functionalization, Drug Delivery, Theranostics, Metal Sequestration.

Biobaserade hybridnanomaterial för teranostiska och miljötillämpningar

Sammanfattning

Biobaserade nanomaterial definieras som material av biologiskt ursprung med en eller flera dimensioner som är mindre än 100 nm. I denna lilla skala börjar spännande egenskaper att framträda, vilket leder till material med ett stort antal olika tillämpningar, bland annat miljösanering, återvinning av metallavfall och teranostik. Genom att modifiera ytan på dessa biobaserade nanomaterial är det möjligt att selektivt ändra biomaterialens affinitet mot olika metalljoner och mineraloxidnanopartiklar. Detta möjliggör produktion av skräddarsydda biobaserade hybridmaterial. Detta arbete fokuserar på två viktiga aspekter, (1) metallselektivitet och (2) teranostik. Ett av målen var att modifiera nanocellulosa för att producera ett material lämpligt för separation av sena övergångsmetaller nickel och kobolt från sällsynta jordartsmetaller och mekanismen bakom denna selektivitet. Medan resten fokuserar på ett annat spår som syftar till att införa mineraloxidnanopartiklar på cellulosabaserade nanomaterial som härrör från bomull eller odlas av mikroorganismer och deras unika egenskaper för tillämpningen som sårförbandsmaterial.

Nyckelord: Cellulosa, Ytmodifiering, Läkemedeltransport, Teranostik, Metallsekvestrering.

Biogebaseerde hybride nanomaterialen voor theranostische en milieutoepassingen

Samenvatting

Biogebaseerde nanomaterialen worden gedefinieerd als materialen van biologische oorsprong met één of meer dimensies kleiner dan 100 nm. Op deze kleine schaal beginnen spannende eigenschappen te ontstaan die leiden tot materialen met een grote verscheidenheid aan toepassingen, waaronder milieusanering, recycling van metaalafval en theranostica (gecombineerde therapie en diagnostiek). Door het oppervlak van deze biogebaseerde nanomaterialen te modificeren is het mogelijk om selectief de affiniteit van biomaterialen richting verschillende metaalionen en mineraaloxide nanodeeltjes te veranderen. Dit maakt de productie van op maat gemaakte biogebaseerde hybride materialen mogelijk. Het huidige werk richt zich op twee belangrijke aspecten, (1) metaalselectiviteit en (2) theranostiek. Een van de doelen was het modificeren van nanocellulose om een materiaal te produceren dat geschikt is voor de scheiding van de overgangsmetalen nikkel en kobalt van zeldzame aardmetalen en het mechanisme achter deze selectiviteit. Een ander deel richtte zich op de introductie van mineraaloxide nanodeeltjes op cellulose gebaseerde nanomaterialen afgeleid van katoen of gekweekt door micro-organismen en hun unieke eigenschappen voor hun toepassing als wondbedekkende materialen.

Trefwoorden: Cellulose, Oppervlakte functionalizatie, Geneesmiddelenafgifte, Theranostiek, Metaal sequestratie

Contents

List of publications.....	11
List of tables	15
List of figures.....	17
Abbreviations	25
1. Introduction.....	27
1.1 Cellulose.....	27
1.1.1 Cellulose, structure and sources	27
1.1.2 Cellulose nanomaterials	29
1.1.3 Chemical modification of cellulose.....	30
1.2 Metal Oxide Nanoparticles.....	33
1.2.1 Ferria	34
1.2.2 Titania	34
1.2.3 Ceria	35
1.3 Hybrid Materials.....	35
1.3.1 Cellulose hybrid materials.....	35
1.3.2 Increasing drug retention in hybrid materials via metal oxides	35
1.4 Characterization techniques	36
1.4.1 Atomic Force Microscopy	36
1.4.2 Fourier Transform Infrared Spectroscopy.....	37
1.4.3 Photoluminescence	38
1.4.4 Scanning Electron Microscopy	38
1.4.5 Transmission Electron Microscopy.....	40
1.4.6 Energy Dispersive X-ray Spectroscopy	41
1.4.7 Thermogravimetric Analysis	41
1.4.8 X-ray Diffraction.....	42
2. Materials and Methods.....	45
2.1 Synthesis of metal-amine complexes	45

2.2	Surface modification of cellulose materials.....	46
2.2.1	Synthesis of cellulose nanocrystals.....	46
2.2.2	Chlorination of cellulose nanocrystals	46
2.2.3	Amination of chlorinated cellulose nanocrystals.....	47
2.2.4	Phosphorylation of bacterial nanocellulose	47
2.2.5	Introduction of nano-ferria	48
2.2.6	Introduction of nano-titania	48
2.2.7	Introduction of photoluminescent cations & nano titania	48
2.3	Drug adsorption and release of pharmaceuticals	49
2.3.1	General drug adsorption	49
2.3.2	General drug desorption	49
2.3.3	Desorption media influence on surface structures.....	49
2.4	Chemical analysis and surface characterization.....	50
2.5	Wound healing cell studies	51
2.5.1	Cell viability / indirect cytotoxicity assay	51
2.5.2	Cell adhesion assay	52
2.5.3	Pseudo-wound closure	52
2.5.4	Immunofluorescence cell culturing	53
2.5.5	Fluorescence staining.....	53
2.5.6	Quantitative measurement of fluorescence Intensity.....	54
3.	Results and Discussion.....	55
3.1	Cellulose surface modification for sorption of metal (oxides).....	55
3.1.1	Chemical modification.....	55
3.1.2	Morphological change by chemical modification of cellulose	58
3.1.3	Metal sorption	63
3.1.4	Mechanistic explanation for metal sorption.....	66
3.2	Cellulose as a matrix for nanoparticles.....	68
3.2.1	Ceria / CeO ₂	70
3.2.2	Ferria / Fe _x O _x	73
3.2.3	Titania / TiO ₂	78
3.2.4	TiO ₂ surface structural changes	89
3.3	Controlled release of pharmaceuticals.....	94
3.3.1	Controlled release via daylight	95
3.3.2	Gel diffusion.....	96
3.3.3	Surface ligand competition and Lanthanide Influence	97
3.3.4	Photoluminescence	99

Conclusion and outlook	101
References.....	103
Popular science summary	113
Populärvetenskaplig sammanfattning	115
Acknowledgements	117

List of publications

This thesis is based on the work contained in the following papers, referred to by Roman numerals in the text:

- I. **Troy C. Breijaert**, Geoffrey Daniel, Daniel Hedlund, Peter Svedlindh, Vadim G. Kessler, Hjalmar Granberg, Karl Håkansson, Gulaim A. Seisenbaeva (2022). Self-assembly of ferria-nanocellulose composite fibres. *Carbohydrate polymers* **2022**, 291, 119560
- II. **Troy C. Breijaert**, Tetyana M. Budnyak, Vadim K. Kessler, Gulaim A. Seisenbaeva (2022). Tailoring a bio-based adsorbent for sequestration of late transition and rare earth elements. *Dalton Transactions* **2022**, 51 (47), pp. 17978-17986
- III. Servane Gaio, Fredric G. Svensson, **Troy C. Breijaert**, Gulaim A. Seisenbaeva, Vadim G. Kessler (2022). Nanoceria-nanocellulose hybrid materials for delayed release of antibiotic and anti-inflammatory medicines. *Materials Advances* **2022**, 3 (19), pp. 7228-7234
- IV. Marijana Lakić, **Troy C. Breijaert**, Geoffrey Daniel, Fredric G. Svensson, Vadim G. Kessler, Gulaim A. Seisenbaeva (2023). Uptake and separation of rare earth elements and late transition metal cations by nano-adsorbent grafted with diamino ligands. *Separation and Purification Technology* **2023**, 323, 124487
- V. **Troy C. Breijaert**, Marina Fontes, Paula de Abreu Fernandes, Hernane da Silva Barud, Sidney J.L. Ribeiro, Gulaim A.

Seisenbaeva (2025). Functionalization of bacterial nanocellulose-based wound dressing for increased drug retention. *Carbohydrate Polymer Technologies and Applications* **2025**, 10, 100756.

- VI. **Troy C. Breijaert**, Natalia Charczuk, Sidney J.L. Ribeiro, Gulaim A. Seisenbaeva. Photoluminescent Bacterial Nanocellulose-based Wound Dressing for Delayed Drug Release *Manuscript*.

Publications outside the scope of this thesis

- I. Inna V. Melnyk, Veronika Tomina, Halyna Yankovych, Hristo Kolev, Erika Dutkova, **Troy C. Breijaert**, Vadim G. Kessler, Gulaim A. Seisenbaeva. (2024). Insight into emulsion synthesis of self-assembled suprastructures formed by Janus silica particles with $-NH_2/-SH$ surface groups. *Nanoscale Advances* **2024**, 6, (12), pp.3146-3157
- II. Ye, Shabdan, **T.C. Breijaert**, G. Zh. Yeligbayeva, G.A. Seisenbaeva, U. Nakan, Preparation and antibacterial activity of hybrid Ag&TiO₂ Nanocellulose/polymer nanocomposite hydrogels. *In revision*

All published papers are reproduced with the permission of the publisher or published open access.

The contribution of Troy C. Breijjaert to the papers included in this thesis was as follows:

- I. Performed all synthetic work, adsorption and desorption of pharmaceuticals, wrote manuscript draft and editing.
- II. Performed all synthetic work, SEM/EDS, Cation adsorption and desorption experiments, PXRD, wrote major part of the manuscript.
- III. Performed some of the AFM measurements and analysis, SEM imaging, performed pH effect experiment.
- IV. Synthesis of $[\text{Co}(\text{H}_2\text{NC}_2\text{H}_4)_3\text{N}(\text{H}_2\text{O})(\text{NO}_3)](\text{NO}_3)_2$ complex, additional model fitting for adsorption isotherms, revision and editing of manuscript.
- V. Majority synthesis of BNC functionalized materials, performed XRD, FT-IR, SEM-EDS, AFM, conductometric titration experiments and analysis, performed drug desorption experiments, wrote manuscript draft and editing.
- VI. Synthesis of BNC functionalized materials, performed SEM-EDS, AFM measurements, FT-IR, drug sorption experiments, wrote manuscript draft and editing.

List of tables

Table 1. Example elemental composition table of cellulose chlorinated with thionyl chloride.....	56
Table 2. Example elemental composition table of chlorinated cellulose after treatment with TAEA.....	56
Table 3. Adsorption capacity and metal:ligand stoichiometry of tris(2-aminoethyl)amine modified cellulose	64
Table 4. Metal selectivity of tris(2-aminoethyl)amine modified cellulose as determined by EDS analysis of the adsorbent after equilibrating in equimolar aqueous metal mixtures.	65
Table 5. Metal-coordinate atom bond length table for hydrated Ni/Co-TAEA nitrate complexes. Where N(I) denoted the tertiary amine, N(II) denotes the back-left primary amine, increasing count in a clock-wise fashion.....	68
Table 6. Samples tested for cytotoxicity, pseudo-wound healing and cell adhesion assays.....	80

List of figures

Figure 1. Hierarchical structure of cellulose derived from plants. Reproduced from John Rojas et al. (2015)	27
Figure 2. Example morphologies of various cellulose sources with/without treatment.....	28
Figure 3. Schematic illustration of glycosidic bond hydrolysis in cellulose in the presence of sulfuric acid to form cellulose nanocrystals and sulfate half-esters (left) and cellulose microfibril disaggregation to form cellulose nanofibrils (right).....	30
Figure 4. Schematic representation of TEMPO oxidation of the glucose moiety within the cellulose-backbone and further conversion into carboxylic acid derivatives.....	31
Figure 5. Schematic representation of periodate oxidation of glucose within the cellulose backbone to form cellulose-dialdehyde and further conversion into aldehyde derivatives.....	31
Figure 6. Schematic representation of halogenation/tosylation of cellulose and further conversion via nucleophilic substitution.....	32
Figure 7. Schematic representation of etherification of cellulose with either halo-alkane or epoxide derivatives to form derivatives including sodium carboxymethyl cellulose, ethylcellulose, hydroxypropyl cellulose and click-sensitive azidohydroxypropyl cellulose.	33

Figure 8. Controlled acid hydrolysis of titanium alkoxides, capped with chargeable ligands leading to MTSAL formation. Produced with crystallographic data from Wright & Williams 1968; Schmid et al. 1991 and COD 7206075, partially adapted from Kessler et al. (2008).	34
Figure 9. Solution equilibrium between a TiBALDH-analogue, Titanium(IV) lactate and anatase TiO ₂ . Produced with crystallographic data from Fu et al. (2002); Seisenbaeva et al. (2013) and COD 7206075.	35
Figure 10. Schematic representation of an AFM measuring sample surface morphology (right) and Force curve information that is obtained via Bruker's <i>PeakForce Tapping</i> (left).	37
Figure 11. Schematic illustration of measuring photoluminescence and an example spectrum.	38
Figure 12. Schematic Illustration of a scanning electron microscope and the electron-sample interactions with different types of signals generated.	39
Figure 13. Schematic illustration of a transmission electron microscope. .	40
Figure 14. Principle of Energy Dispersive X-ray spectroscopy.	41
Figure 15. Bragg diffraction, constructive and deconstructive interference.	42
Figure 16. Diffraction patterns from a single crystal (top) and a nanocrystalline powder (bottom). With a single crystal, a diffraction pattern with discrete diffraction spots is obtained due to regular diffraction. For a nanocrystalline material the crystallites are randomly oriented resulting in a ring pattern.	43
Figure 17. Schematic illustration of the synthesis of chlorinated cellulose	46
Figure 18. Schematic illustration of cellulose-TAEA synthesis from chlorinated cellulose	47
Figure 19. Schematic illustration of the synthesis of phosphorylated cellulose	47

Figure 20. (left) phosphorylation degree estimated from conductometric titrations. (right) ATR-FTIR spectra of bacterial nanocellulose as the phosphorylation reaction progresses.	58
Figure 21. (left) AFM image of cellulose nanocrystals derived from acid hydrolysis of cotton. (right) SEM after chlorination and amination with TAEA.	59
Figure 22. Measured powder x-ray diffractograms (left, Mo Kα = 0.71073 Å) of cotton CNCs, chlorinated CNCs and cellulose-TAEA. (right) calculated idealized patterns for cellulose I α , II and III (Mo K α = 0.71073 Å, FWHM = 0.5) (French 2014).	60
Figure 23. AFM image of dried bacterial nanocellulose (5x5 μ m, left) and as prepared phosphorylated bacterial nanocellulose (3x3 μ m, right).	60
Figure 24. Dried bacterial nanocellulose stored in 0.1M HCl (A, B), miliQ (C, D) and 0.1M NaOH (E, F).	61
Figure 25. Phosphorylated bacterial nanocellulose stored in 0.1M HCl (A, B), miliQ (C, D) and 0.1M NaOH (E, F).	62
Figure 26. SEM image (5k magnification) of phosphorylated BNC stored in neutral (A) and acidic (B) conditions.	62
Figure 27. X-ray diffractograms of bacterial nanocellulose stored under acidic, neutral or basic conditions. (left) BNC, (right) phosphorylated BNC.	63
Figure 28. Langmuir isotherms of late transition metals (A) Ni ²⁺ , (B) Co ²⁺ and rare earth elements (C) Nd ³⁺ , (D) Sm ³⁺	64
Figure 29. Adsorption kinetics of (A) Ni ²⁺ , (B) Co ²⁺ , (C) Nd ³⁺ , (D) Sm ³⁺ by tris(2-aminoethyl)amine modified cellulose in a 24h period.	65
Figure 30. pH-Dependent desorption of (A) Ni ²⁺ , (B) Co ²⁺ , (C) Nd ³⁺ and (D) Sm ³⁺ from TAEA-modified cellulose.	66

Figure 31. Single crystal structure of $[\text{Ni(II)}(\text{TAEA})(\text{H}_2\text{O})(\text{NO}_3)]\text{NO}_3$ (left), $[\text{Co(III)}(\text{TAEA})(\text{H}_2\text{O})(\text{NO}_3)](\text{NO}_3)_2$ (middle) and $[\text{N}(\text{C}_2\text{H}_4\text{NH}_3)_3](\text{NO}_3)_3$ (right, reproduced from Bazzicalupi et al. 2009)..... 67

Figure 32. AFM images (not published) of various cellulose morphologies depending on source and treatment. (A) whatman filter paper (64 wt% H_2SO_4 , 45°C, 45 min), (B) Cotton regenerated from cupramonium (64 wt% H_2SO_4 , 45°C, 45 min), (C) Cotton (64 wt% H_2SO_4 , 45°C, 45 min), (D) Filter paper regenerated from cupramonium (20% H_2SO_4 , 70°C, 60 min), (E) Air-dried bacterial nanocellulose, (F) Supercritically dried bacterial nanocellulose..... 69

Figure 33. PXRD diffractograms of ceria produced at 80°C (a) and ceria produced in situ in a CNC suspension. The asterisk indicates the characteristic diffraction planes of cerianite-ceria (JCPDS 00-034-0394). Reproduced from Gaio et al. 2022. 70

Figure 34. (A) SEM image of CNC/PEG_CeO₂ with 50wt% ceria, (B) AFM image of ceria produced at 80°C in the presence of CNCs. 71

Figure 35. SEM images of CNC/PEG/CeO₂ drug composites containing ampicillin (a, 500x / b 5000x), triclosan (c, 500x / d 5000x) and diclofenac (e, 500x / f, 5000x)..... 71

Figure 36. Photocatalytic degradation of methylene blue under a 15W lamp (a) methylene blue, (c) CeO₂_80C, (e) CeO₂_600C and under a 300W simulated daylight lamp (b) methylene blue, (d) CeO₂_80C, (f) CeO₂_600C. Reproduced from Gaio et al. 2022. 73

Figure 37. X-ray diffractograms of a synthesized iron oxide – carboxymethylated CNF composite and synthesized iron oxide nanoparticles, measured using a Mo $\text{K}\alpha$ source. JCPDS reference patterns for magnetite (00-019-0629) and maghemite (00-039-1346) overlaid. 73

Figure 38. (A) Magnetization vs magnetic field for C-CNF:FeOx in powder and liquid form. (B) C-CNF:FeOx as paper flakes and (C) C-CNF:FeOx compressed and dried. 74

Figure 39. AFM images of an iron oxide – carboxymethylated nanofibril composite. Top-down view at (A) 1x1 μm , (B) 500x500 nm, (C) 200x200 nm. 3D view at (D) 1x1 μm and (F) 200x200 nm.	75
Figure 40. TEM images of iron-oxide carboxymethylated cellulose nanofibril composite without staining and at varying magnification.	76
Figure 41. Unstained TEM image of an iron oxide – C-CNF composite. Arrows indicate small iron oxide particles associated with cellulose fibrils and their respective dimensions.	77
Figure 42. TEM images of a cross-sectioned, resin-embedded iron oxide C-CNF composite. Large aggregates are visible on the surface, while smaller particles appear aligned with the individual fibrils. Inset show particle size distribution in nm.	77
Figure 43. AFM images of phosphorylated bacterial nanocellulose (A, 3x3 μm , B, 1x1 μm), covered by TiBALDH (C, 3x3 μm , D, 1x1 μm) and TATT (E, 3x3 μm , F, 1x1 μm).	79
Figure 44. X-ray diffractograms of BNC, phosphorylated-BNC, TATT-covered p-BNC and TiBALDH covered p-BNC (left) and TiO_2 composites after sintering at 500°C (right).	79
Figure 45. Cell viability of L929 murine fibroblasts and SaOS-2 osteoblast-like cells upon contact with eluates from functionalized BNC samples.....	81
Figure 46. Effect of functionalized BNC composites on migration of L929 murine fibroblasts and SaOS-2 osteoblast like cells by evaluating the pseudo-wound closure at 0, 6, 24 and 48 hours.	82
Figure 47. Murine fibroblast L929 cells adhered on various BNC composites after 72h of incubation.	85
Figure 48. Osteoblast-like SaOS-2 cells adhered on various BNC composites after 72h of incubation.	86
Figure 49. Confocal imaging of murine L929 fibroblasts and SaOS-2 osteoblasts: F-actin (green) was labelled with phalloidin-iFluor 488 (green),	

and the nuclei (blue) counterstained with DAPI. Fluorescence staining of the actin cytoskeleton was registered on fibroblasts and osteoblasts cultured for 7 days with different eluates from BNC-PO₄, BNC-PO₄-TATT and BNC-PO₄-TiBALDH. Control cells was maintained with only conventional media. 87

Figure 50. Confocal imaging of murine L929 fibroblasts and SaOS-2 osteoblasts: Type I-Collagen (red) was labelled with Rabbit Recombinant Monoclonal anti-Collagen I conjugated to Alexa Fluor® 594 and nuclei counterstained with DAPI (blue). Fluorescence staining of collagen Type I was registered on fibroblasts and osteoblasts cultured for 7 days with different eluates from BNC-PO₄, BNC-PO₄-TATT and BNC-PO₄-TiBALDH. Control cells were maintained with only conventional media. 87

Figure 51. Confocal imaging of murine L929 fibroblasts and SaOS-2 osteoblasts: fibronectin (red) was labelled with Rabbit Recombinant Monoclonal anti-Fibronectin conjugated to Alexa Fluor® 555 and nuclei counterstaining, with DAPI (blue). Fluorescence staining of fibronectin was registered on fibroblasts and osteoblasts cultured for 7 days with different eluates from BNC-PO₄, BNC-PO₄-TATT and BNC-PO₄-TiBALDH. Control cells were maintained with only conventional media. 88

Figure 52. Measurement of fluorescence intensity of F-actin, type-I collagen and fibronectin on L929 fibroblasts and SaOS-2 osteoblasts cultured for 7 days with different eluates from BC-PO₄, BC-PO₄-TATT and BC-PO₄-TiBALDH. Control cells were maintained with only conventional media.... 88

Figure 53. AFM images of BNC-PO₄ (A: 3x3 µm, B, 1x1 µm, C: 300x300 nm) , BNC-PO₄-Eu (D: 3x3 µm, E: 1x1 µm, F: 300x300 nm) , BNC-PO₄-TATT (G: 3x3 µm, H: 1x1 µm, I: 300x300 nm) and BNC-PO₄-Eu-TATT (J: 3x3 µm, K: 1x1 µm, L: 300x300 nm). 90

Figure 54. AFM images of BNC-PO₄-Eu-TATT covered by ciprofloxacin (A: 5x5 µm, B: 3x3 µm, C: 1x1 µm) and tetracycline (D: 5x5 µm, E: 3x3 µm, F: 1x1 µm). 91

Figure 55. Likely surface coordination species formed by ciprofloxacin and tetracycline 91

Figure 56. AFM images of citrate-desorbed BNC-PO ₄ -Eu-TATT covered by ciprofloxacin (A: 5x5 μm, B: 3x3 μm, C: 1x1 μm) and tetracycline (D: 5x5 μm, E: 3x3 μm, F: 1x1 μm) and citrate-desorbed BNC-PO ₄ -Eu-TATT (G: 5x5 μm, H: 3x3 μm, I: 1x1 μm).	92
Figure 57. AFM images of BC-PO ₄ -Eu-TATT after storing for 24 hours in simulated body fluid (A: 3x3 μm, B: 1x1 μm, C: 1x1 μm) or simulated human sweat (D: 3x3 μm, E: 1x1 μm, F: 1x1 μm).	93
Figure 58. Cross-section of an 18-chain CNF model.	94
Figure 59. Adsorption of tetracycline at room temperature (left) and light-controlled desorption of tetracycline at room temperature (right).	95
Figure 60. Average inhibitory effect of the different materials (left) and structure of tested antibiotics (right). CNC/PEG/BTCA/CeO ₂ , CNC/PEG/BTCA/triclosan, CNC/PEG/BTCA/CeO ₂ /triclosan, CNC/PEG/BTCA/ampicillin and CNC/PEG/BTCA/CeO ₂ /ampicillin have been abbreviated in the figure as CNC/BTCA/CeO ₂ , CNC/triclosan, CNC/CeO ₂ /triclosan, CNC/ampicillin and CNC/CeO ₂ /ampicillin.	97
Figure 61. Desorption of the broad-spectrum antibiotic Tetracycline from phosphorylated bacterial nanocellulose sheets covered by TiO ₂ derived from TiBALDH (left , black) and colloidal triethanolamine terminated TiO ₂ (right , red).	98
Figure 62. Desorption kinetics of the antibiotics Ciprofloxacin (left) and Tetracycline (right) from TATT-modified bacterial cellulose with (black) and without (red) Europium(III) doping.	98
Figure 63. (left) The emission spectra of Eu(III)-doped BNC-PO ₄ -TATT / drug composites after excitation at 393 nm and (right) decay curves recorded at 393 nm.	99
Figure 64. Photoluminescence under UV-irradiation of Eu(III)-doped phosphorylated BNC-Titania composites with tetracycline (left) and ciprofloxacin (right).	100

Abbreviations

ADP	Ammonium dihydrogen phosphate
AFM	Atomic force microscopy
AGU	Anhydroglucose unit
ATR	Attenuated total reflection
BET	Brunauer-Emmett-Teller
BNC	Bacterial nanocellulose
BTCA	1,2,3,4-Butanetetracarboxylic acid
C-CNF	Carboxymethylated cellulose nanofibrils
CNC	Cellulose nanocrystals
CNF	Cellulose nanofibrils
DLS	Dynamic Light Scattering
DMAc	<i>N,N</i> -dimethylacetamide
DMEM	Dulbecco's Modified eagle Medium
DMF	<i>N,N</i> -dimethylformamide
EDS	Energy dispersive x-ray spectroscopy
FBS	Fetal Bovine Serum
FT-IR	Fourier transform infrared spectroscopy
LTM	Late transition metal
MTSAL	Micelles templated by self-assembly of ligands

MTT	3-(4,5-dimethylthiazol-2-yl)-2,5-diphenyltetrazolium bromide
MWCO	Molecular Weight Cut-off
NP	Nanoparticle
PBS	Phosphate-buffered saline
PEG	Polyethylene glycol
PL	Photoluminescence
PXRD	Powder X-ray diffraction
QNM	Quantitative nanomechanical mapping
REE	Rare earth element
SBF	Simulated Body Fluid
SCXRD	Single-crystal X-ray diffraction
SEM	Scanning electron microscopy
TAEA	Tris (2-aminoethyl)amine
TATT	Triethanolamine terminated titania
TEM	Transmission electron microscopy
TGA	Thermogravimetric analysis
TiBALDH	Titanium bis(ammonium lactate) dihydroxide

1. Introduction

1.1 Cellulose

1.1.1 Cellulose, structure and sources

Cellulose is the most abundant polymer on earth, representing about 1.5×10^{12} tons of total annual biomass production.(Klemm et al. 2005). It is a polymer consisting of β -1,4-linked glucose and it is found in the plant cell wall as a structural polymer (fig. 1). It is commonly found with other matrix components such as lignin, hemicelluloses, pectin and other components in varying quantities and can be isolated from this matrix through a series of treatments.

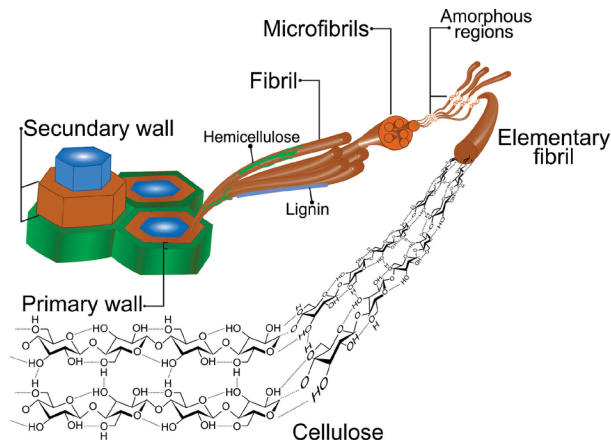


Figure 1. Hierarchical structure of cellulose derived from plants. Reproduced from John Rojas et al. (2015)

Originally described by the French chemist Anselme Payen as a resistant fibrous solid that remained after treatment of plant tissues with acids, he determined the molecular formula to be $C_6H_{10}O_5$ via elemental analysis (Payen 1838). In 1883 E. Flechsig claimed that cellulose could be converted entirely into glucose, however this claim was based on the reducing power of a complex mixture (Flechsig 1883). Irvine and Soutar more conclusively demonstrated in 1920 that cellulose consists of poly-glucose anhydride via acetolysis of cellulose, conversion to α -methyl glucoside and finally to glucose in a 85% yield (later increasing to 95% yield)(Irvine & Soutar 1920; Irvine & Hirst 1922). Monier-Williams managed to obtain glucose in a 91% yield via direct hydrolysis of cellulose with sulfuric acid (Monier-Williams 1921). The methylation of cellulose contributed greatly to the cellulose \rightarrow glucose question, with Irvine and Hirst demonstrating that the glucose moiety only has free hydroxyl groups on the 2,3,6-positions (Irvine & Hirst 1923).

Besides structural information based on chemical modification, the use of x-rays has been valuable in the study of cellulose. One of the earliest mentions of x-ray scattering by cellulose was by Herzog and Jancke, later Freudenberg & Braun presented proof that cellulose consists of long linear chains of repeating cellobiose units with β -1,4 connected glucose units (Freudenberg & Braun 1928). Since then many polymorphs of cellulose and derivatives have been discovered of which cellulose I is found in nature, with varying ratios of cellulose I α and I β (Atalla & VanderHart 1984).

Beyond polymorphism and chemical identity, cellulose is a fascinating material due to the wide variety of morphologies that may be obtained depending on the cellulose source and treatment and its bio-renewable nature (fig. 2).

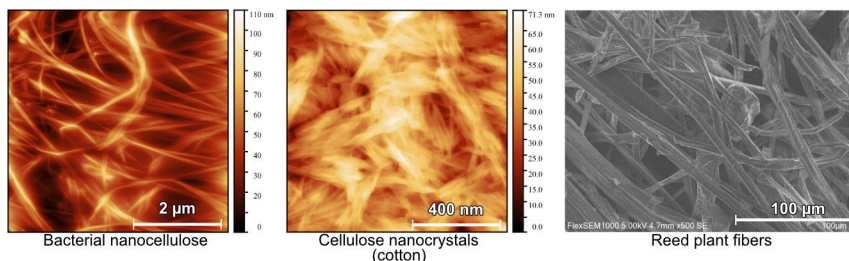


Figure 2. Example morphologies of various cellulose sources with/without treatment

1.1.2 Cellulose nanomaterials

Cellulose nanomaterials are highly versatile, and researchers continue to explore numerous ways of incorporating cellulose into materials for environmental remediation, biomedical applications and other interdisciplinary fields. Natural cellulose consists of large fibres which can be observed with the naked eye. These larger cellulose fibres can easily be converted into cellulose nanomaterials using a variety of methods, resulting in cellulose nanofibers (CNFs), cellulose nanocrystals (CNCs) or bacterial nanocellulose (BNC). The distinction between the three is made based on their nature, dimensions and extraction methods, as the characteristics of these materials is highly dependent on their source and the processing conditions. Chemical characteristics between CNFs, CNCs and BNC are very similar, being homopolymers of glucose. However, their physical characteristics are remarkably different. CNCs are typically produced via controlled acid hydrolysis of cellulose fibres, while CNFs are typically obtained via mechanical processing (fig. 3). Controlled hydrolysis used to produce CNCs leads to the formation of narrow, high aspect ratio, rod-like, crystalline particles due to the hydrolysis of the amorphous domains that exists around and between crystalline cellulose domains that are more susceptible to acid hydrolysis. When using sulfuric acid, the hydroxyl groups present on the surface of CNCs are partially sulfated during hydrolysis, forming negatively charged particles with increased colloidal stability. In terms of physical properties, CNCs are crystalline particles with high-specific strength and modulus, though suffer from relatively poor thermal stability due to the presence of sulfate groups on the surface. CNFs by contrast are typically produced via mechanical processes such as homogenization, grinding and ultrasonic treatment, usually with some form of pre-treatment. The general idea is to remove undesirable components such as lignin and hemicelluloses, followed by disaggregating the larger microfibers to obtain nanofibers of cellulose with very high aspect ratios. These large nanofibers are prone to form relatively stable hydrogels at lower concentrations than CNCs.

Bacterial nanocellulose materials are unique, being derived not from plant materials, but instead grown by bacteria via fermentation in the form of a hydrogel. BNC has a high native purity, consisting of cellulose, microbial cells, nutrients and secondary metabolites that can be easily washed out. It has outstanding physical and mechanical properties due to its

unique 3D structure. BNC is characterized by narrow 70-150 nm microfibrils with lengths commonly exceeding 1 μm (Klemm et al. 2005). These fibres are interwoven with one another to form mechanically stable fibrous mats with high surface area, elasticity and mechanical flexibility.

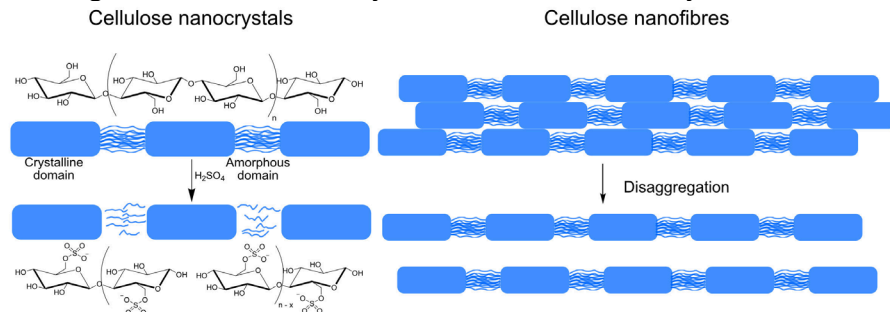


Figure 3. Schematic illustration of glycosidic bond hydrolysis in cellulose in the presence of sulfuric acid to form cellulose nanocrystals and sulfate half-esters (**left**) and cellulose microfibril disaggregation to form cellulose nanofibrils (**right**).

1.1.3 Chemical modification of cellulose

Cellulose has a very rich and diverse chemistry owing to the presence of nucleophilic hydroxyl-groups. Chemical modifications of cellulose can broadly be divided into three categories, namely: modification of reducing end-groups, homogeneous modification and heterogeneous (surface) modification (Cumpstey 2013; Heise et al. 2021).

Modification of the reducing end-group of cellulose is limited to the reducing end of the cellulose chain, which can still undergo ring opening/closing reactions (mutarotation). Its chemistry is aldehyde specific and for conventional natural cellulose sources its usefulness is somewhat limited by the number of reducing end-groups per unit weight/area. With nanocellulose, this type of end-group modification can encourage assembly relying on the asymmetric nature of the particles involved (Heise et al. 2021).

Homogeneous modification of cellulose requires dissolution of a cellulose starting material and modification of the cellulose chain occurs across the entire cellobiose backbone. Dissolution of cellulose may be achieved via the use of special solvent systems such as Schweizer's reagent (metal ammine complex), DMAc/LiCl, DMSO/TBAF, NMMO, NaOH/Urea/Water or ILs (Chanzy et al. 1980; McCormick 1981; Burchard et al. 1994; Zhou & Zhang 2000; Zhu et al. 2006; Köhler & Heinze 2007). Alternatively, dissolution may be achieved via reactive dissolution, whereby

the modification reaction is carried out under set conditions and as the reaction progresses the solubility of cellulose in the chosen solvent system increases until fully dissolved.

Another approach is heterogeneous (surface) modification. Due to the difficulty of dissolving cellulose, it is common for reactions carried out to be at least partially heterogeneous in nature. Heterogeneous synthesis can be a great benefit as it allows for surface modification without the risk of altering the existing cellulose structure.

The reactive hydroxyl-groups allow for quite diverse chemistry. For example, TEMPO oxidation of the surface accessible C6-hydroxyl-groups leads to the formation of a carboxylic acid (fig. 4), (da Silva Perez et al. 2003) which itself may be converted into esters, amides, reactive acyl chlorides and carboxylate salts.

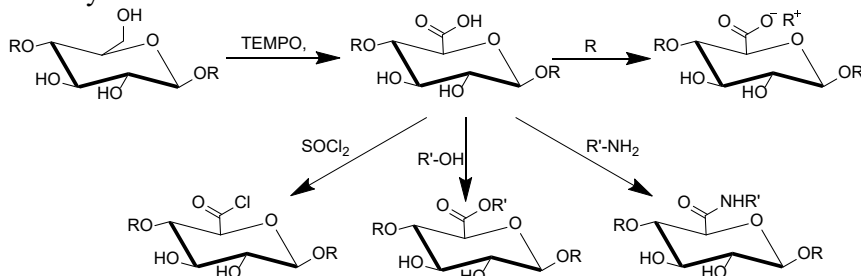


Figure 4. Schematic representation of TEMPO oxidation of the glucose moiety within the cellulose-backbone and further conversion into carboxylic acid derivatives.

Periodate oxidation of the C2-C3 carbon-carbon bonds (fig. 5) leads to the formation of dialdehydes within the cellulose chain, which then allows for the modification of the resulting aldehyde into imines, alcohols, amines, carboxylic acids, oximes etc (Kim et al. 2000).

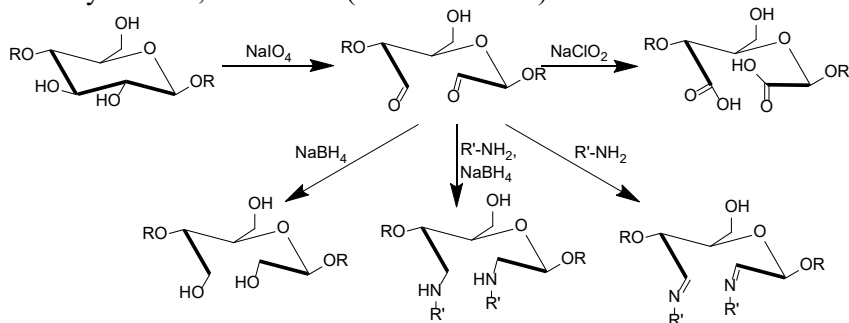


Figure 5. Schematic representation of periodate oxidation of glucose within the cellulose backbone to form cellulose-dialdehyde and further conversion into aldehyde derivatives.

Chlorination or tosylation leads to conversion of a hydroxyl-group into one that is liable to nucleophilic substitution to form cellulose ethers, amines, thioethers, azides etc (fig. 6). This is not without its downsides however as cellulose may start dissolving as the reaction progresses. These reactions are commonly carried out in aprotic amphiphilic solvents such as DMF or DMAc, and with the reduction in inter- and intramolecular hydrogen bonding as the reaction progresses, the probability of reactive dissolution increases (Labafzadeh et al. 2015).

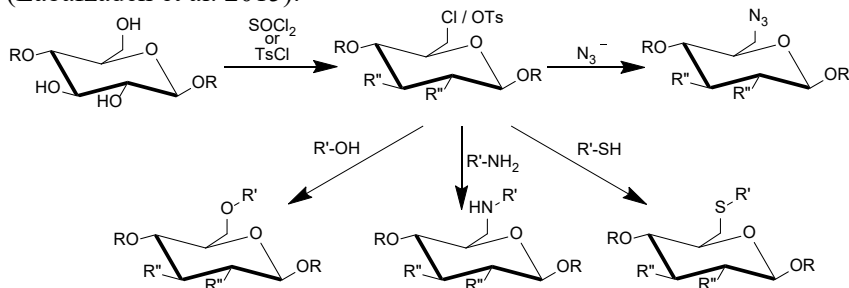


Figure 6. Schematic representation of halogenation/tosylation of cellulose and further conversion via nucleophilic substitution.

The last type of reaction briefly discussed is etherification of cellulose. Cellulose ethers form an important class of cellulose products with large scale industrial use. Common forms include: carboxymethyl cellulose, ethyl cellulose, hydroxypropyl cellulose and many more. They are commonly produced via Williamson-ether synthesis or Ring-opening reactions with substituted epoxides (fig. 7). Because of the mild conditions, the use of substituted epoxides is particularly interesting to introduce “click”-chemistry suitable functional groups (Liang et al. 2023).

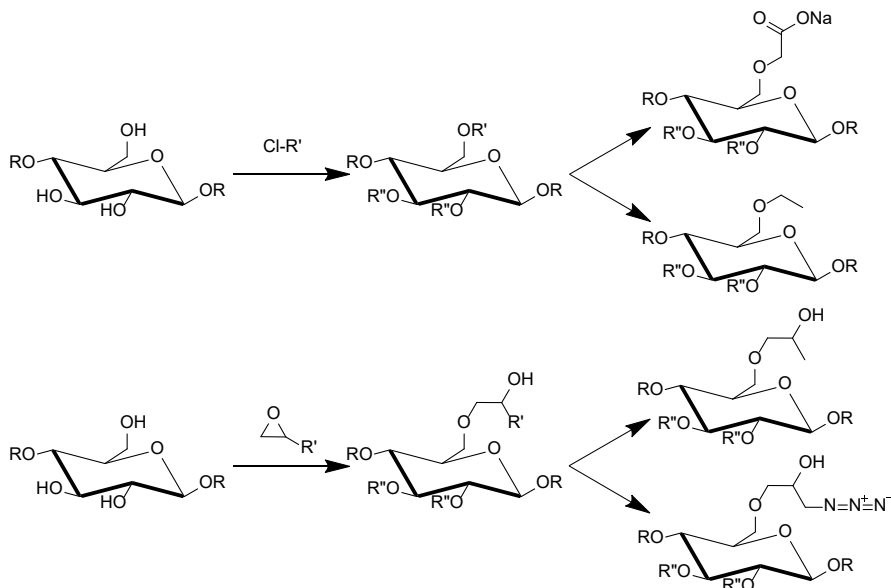


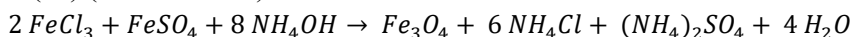
Figure 7. Schematic representation of etherification of cellulose with either halo-alkane or epoxide derivatives to form derivatives including sodium carboxymethyl cellulose, ethylcellulose, hydroxypropyl cellulose and click-sensitive azidohydroxypropyl cellulose.

1.2 Metal Oxide Nanoparticles

Metal oxide nanoparticles are small (1-100 nm) particles containing main group or transition metals. Many of these particles are ubiquitous in nature and one could strongly argue that life has evolved in the presence of mineral oxide nanoparticles. Oxide nanoparticles can form naturally via weathering of minerals or synthetically in a lab. Synthetic oxide nanoparticles can be specifically doped (adding elements other than the main constituents) to enhance physical or chemical properties (e.g. for catalysis). These particles, due to their small size have a massive total surface area per unit mass (i.e. specific surface area), which makes them ideal for many applications (e.g. catalysis, physi-/chemisorption) as the chemical and physical properties of nanoparticles are dependent on how the surface interacts with its surroundings.

1.2.1 Ferria

Some of the most common natural nanoparticles are derived from iron-containing minerals such as akaganeite, lepidocrocite, goethite, ferrihydrite (iron(III) oxide-hydroxides), hematite, maghemite (iron(III) oxides) and magnetite (mixed valence oxide of Fe(II) / Fe(III)). The latter two (maghemite and magnetite), displaying Fe(II)-deficient and inverse spinel structure respectively, are particularly interesting as they are attracted to magnets and can be magnetized to become permanent magnets themselves (e.g. natural lodestone). Synthetically, magnetite is also relatively simple to produce, for example via co-precipitation from a source of iron(II) and iron(III) (Massart 1981):



1.2.2 Titania

Another kind of commonly encountered mineral nanoparticle is titanium(IV) oxide (TiO_2). Titania finds common industrial use as a pigment (Pigment White 6), photocatalyst and is generally considered affordable with low toxicity. This low toxicity is a particularly useful trait for medical applications as oxides form naturally on the surface of most metal implants, including titanium. Synthetically, titanium dioxide can be accessed via several processes, however for more specialized applications it is common to use sol-gel routes that often rely on the controlled hydrolysis of titanium alkoxides such as $\text{Ti}(\text{OEt})_4$. For example, the controlled micro-hydrolysis of titanium ethoxide with a capping ligand leads to the formation of well-defined oligonuclear oxo-alkoxide species, which upon further hydrolysis form a uniform sol of well-defined colloidal nanoparticles (fig. 8, Kessler et al. 2006).

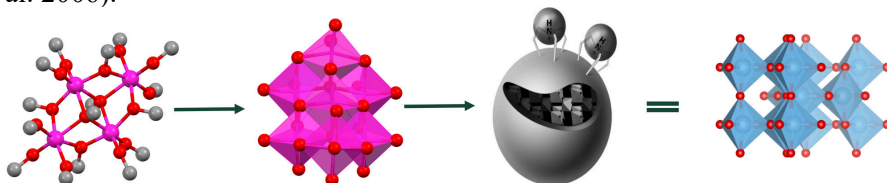


Figure 8. Controlled acid hydrolysis of titanium alkoxides, capped with chargeable ligands leading to MTSAL formation. Produced with crystallographic data from Wright & Williams 1968; Schmid et al. 1991 and COD 7206075, partially adapted from Kessler et al. (2008).

A quite fascinating way to produce well-defined nanoparticles of titania that does not rely on the controlled hydrolysis of titanium alkoxide species is via an equilibrium shift of an otherwise water-soluble, stable precursor such as ammonium oxo-lactato titanate, otherwise known as TiBALDH (fig. 9). This leads to the formation of small, crystalline nanoparticles capped with lactate ligands (Seisenbaeva et al. 2013).

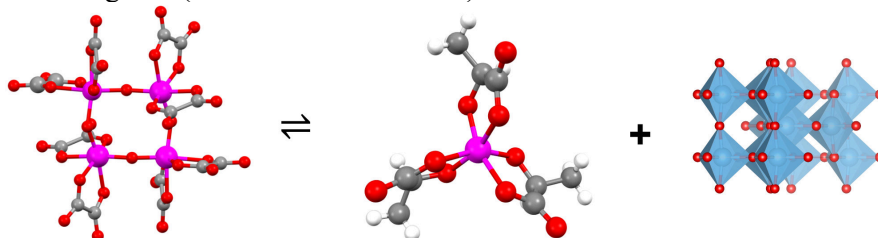


Figure 9. Solution equilibrium between a TiBALDH-analogue, Titanium(IV) lactate and anatase TiO_2 . Produced with crystallographic data from Fu et al. (2002); Seisenbaeva et al. (2013) and COD 7206075.

1.2.3 Ceria

A less common metal oxide, derived from the rare-earth element cerium is cerium(IV) oxide. Like titania it is generally considered bio-compatible with low toxicity and has interesting redox properties due to its non-stoichiometric compositions and the ease with which cerium can switch between the Ce^{3+} and Ce^{4+} oxidation states (Popov et al. 2016).

1.3 Hybrid Materials

1.3.1 Cellulose hybrid materials

Hybrid materials specifically refer here to materials based on cellulose in combination with a metal (oxide). The material itself being neither entirely organic, nor inorganic and the smallest dimension being a few nanometres to tens of nanometres.

1.3.2 Increasing drug retention in hybrid materials via metal oxides

Cellulose itself has a relatively poor affinity for various pharmaceuticals; primarily derived from hydrogen-bonding and van der Waals interactions. When placed in an environment with competing interactions, many

pharmaceuticals will quickly desorb from the surface of cellulose. Metal oxide derived nanoparticles exhibit a more nuanced behaviour as many pharmaceuticals form relatively strong inner-/outer sphere complexes with metal oxide particles. This increases the affinity for pharmaceuticals which can be exploited to produce materials suitable for controlled drug delivery applications, by combining cellulose with metal oxide particles. To be desorbed from the particle surface, a strongly competing ligand will need to be introduced. Hence desorption will occur in a more controlled manner (Galkina et al. 2015).

1.4 Characterization techniques

1.4.1 Atomic Force Microscopy

Atomic Force Microscopy (AFM) is a high-resolution, non-optical imaging technique based on the interactions between a sample surface and a probe tip. Unlike optical- or electron-based imaging techniques (i.e. optical microscopy or electron microscopy), which rely on interactions of light or electrons with a sample surface, AFM relies on close-range physical, electrostatic or magnetic interactions to characterize a sample surface (fig. 10). A relatively simplistic way to describe AFM is that it collects surface information by feeling the surface with a mechanical probe, which consists of an extremely thin tip on a cantilever, supported on a chip. The probe is brought into close proximity to the sample surface and the probe and sample are moved relative to each other in a rasterized pattern. During this, a quantity is measured in discrete locations (pixels) via the displacement of the free end of the cantilever by reflecting a laser off the cantilever into a segmented photodetector. From this, a pseudo-colour image is created where the measured quantity is represented via a colour-gradient. Commonly this measured quantity is height and thus information can be obtained about a sample's physical dimensions.

AFM imaging can broadly be divided into *contact* or *non-contact modes* (ignoring more specialized techniques such as magnetic force microscopy). During *contact mode* the cantilever is brought towards the surface until the tip contacts the surface, after which the probe is moved laterally in a rasterized pattern. Any change in height will cause the cantilever and by extension the laser to be deflected and by measuring the cantilever deflection

the sample topography can be plotted as a function of xy . *Contact mode* suffers from a major drawback in that the lateral force exerted on the sample is high, resulting in sample damage or the movement of loosely attached objects. As such, it has largely been superseded by *non-contact mode* AFM whereby the tip is only intermittently brought into contact with the sample surface, thereby greatly reducing lateral forces. A form of non-contact mode AFM is *PeakForce Tapping™* (proprietary) which relies on non-resonant oscillations to intermittently bring the tip into contact with the sample surface and the position of the Z-piezo is modulated by peak force (related to the cantilever deflection) applied to the cantilever tip.

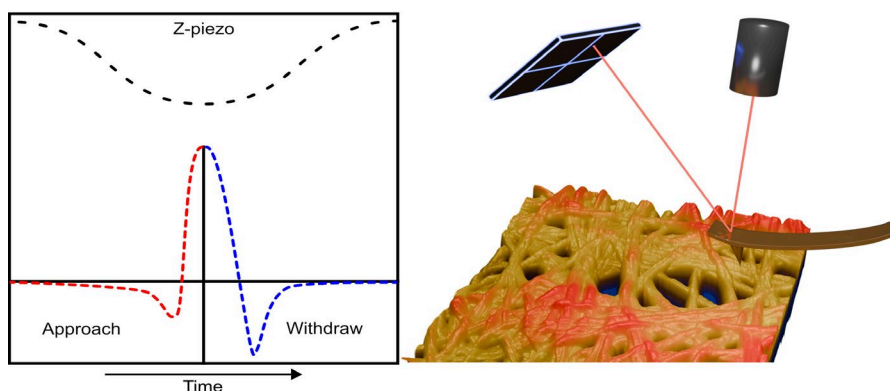


Figure 10. Schematic representation of an AFM measuring sample surface morphology (**right**) and Force curve information that is obtained via Bruker's *PeakForce Tapping* (**left**).

1.4.2 Fourier Transform Infrared Spectroscopy

Light interacts with matter, particularly in the vibrational infrared region (2.5-25 μm). When a molecule absorbs IR light that matches the natural vibrational frequency for a particular vibration, it is excited to a higher energy state, increasing vibrational amplitude. However, only bonds with a changing dipole moment over time can absorb IR light; symmetric bonds like H_2 and Cl_2 cannot. Different functional groups absorb IR light within specific ranges, typically between 1500-4000 cm^{-1} range. The 400-1500 cm^{-1} region, known as the fingerprint region, contains unique molecule-specific vibrations, though many inorganic vibrations also occur between 400-1000 cm^{-1} . IR spectroscopy thus provides structural information and a unique spectral fingerprint for each molecule.

1.4.3 Photoluminescence

Photoluminescence is a photon-induced process where light is emitted from matter after the absorption of photons. Absorption of a photon excites one of the electrons of a molecule to a higher electronic excited state, after which it returns to a lower energy state upon emission of a photon (luminescence). This luminescence can give information on the nature of the emitting excited state and exploited for qualitative or quantitative analysis. The emission spectra provides information about the nature and energy of the emitting excited state and is characteristic for the emitting species. Here a fixed wavelength is used to excite the sample, and the intensity of emitted radiation is monitored as a function of wavelength. While in an excitation spectrum, the emission is monitored at a fixed wavelength and the excitation wavelength is varied (fig. 11).

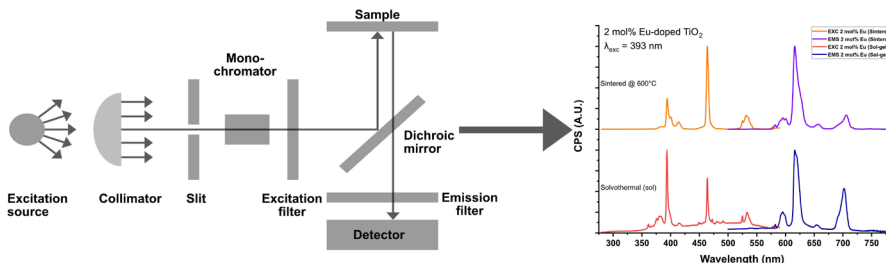


Figure 11. Schematic illustration of measuring photoluminescence and an example spectrum.

1.4.4 Scanning Electron Microscopy

For many years optical microscopy has been the gold standard for observing the microscopic. However, the size of objects we can observe is limited by the diffraction limit of light. For visible light in the range of 400-750 nm, with a numerical aperture of 1.4 ($d = \frac{\lambda}{2n \sin \theta} = \frac{\lambda}{2NA}$), this limit lies between 143-268 nm. Which is large compared to many fundamental objects of natural or synthetic origin. To go beyond the optical diffraction limits, electrons can be used to indirectly observe objects. Electrons can be seen as behaving as both a particle and a wave. It has a wavelength dependant on its kinetic energy according to the de Broglie relation (taking relativity into account for high voltages):

$$\lambda = \frac{h}{\sqrt{2m_0E(1 + \frac{E}{2m_0c^2})}}$$

Where λ is the electron wavelength, m_0 is the rest mass of an electron, c is the speed of light, h is Planck's constant and E is the acceleration voltage. From the de Broglie relation we can gather that an increase in acceleration voltage will lead to a decrease in wavelength.

Scanning electron microscopy (SEM) creates rasterized images of a sample surface by scanning the surface with a focussed electron beam and detecting emitted electrons (fig. 12). Tungsten filament systems typically operate at 5-15 keV acceleration voltage, with the beam focussed by condenser coils and guided by deflection coils across the surface. Electrons with deviating paths are filtered out by apertures. The interaction between beam and surface generates various signals depending on the acceleration voltage and sample composition. Lower acceleration voltage reduce electron penetration depth, providing more surface-accurate imaging

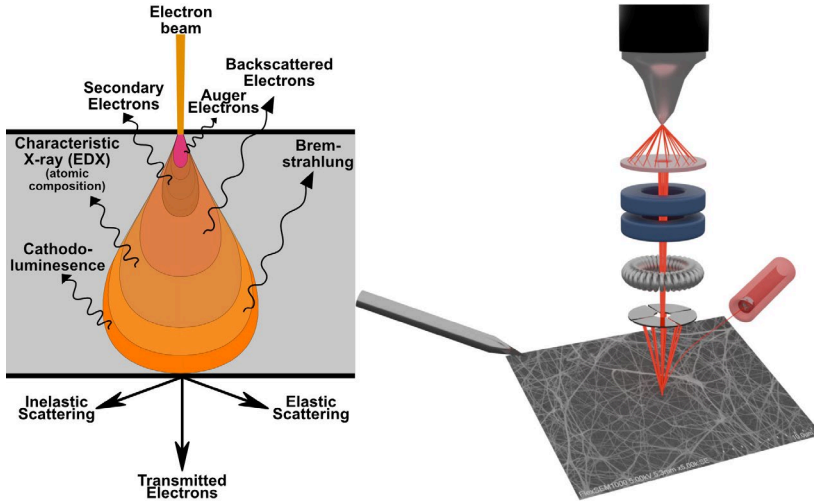


Figure 12. Schematic Illustration of a scanning electron microscope and the electron-sample interactions with different types of signals generated.

1.4.5 Transmission Electron Microscopy

Transmission Electron Microscopy (TEM) uses an electron beam to image samples at the nanometer or sub-nanometer scale. Unlike SEM, which scans the surface in a rasterized pattern, TEM transmits electrons through the sample and captures the image via a fluorescent screen, CDD camera or direct electron detectors (fig. 13). Electron interaction with the sample depends on the acceleration voltage, typically 100-300 KeV, which allows for reliable transmission and shorter wavelengths. Sample contrast depends on the atomic number, heavier elements like tungsten scatter more electrons and appear darker, while lighter elements scatter very weakly and often require staining with heavy metals such as osmium tetroxide, phosphotungstic acid or uranyl acetate. High-resolution TEM enables the visualization of atomic structures and crystalline order, aiding in phase identification and electron crystallography. TEM also supports techniques like EDS to analyse chemical composition, making it essential for nanoscale characterization.

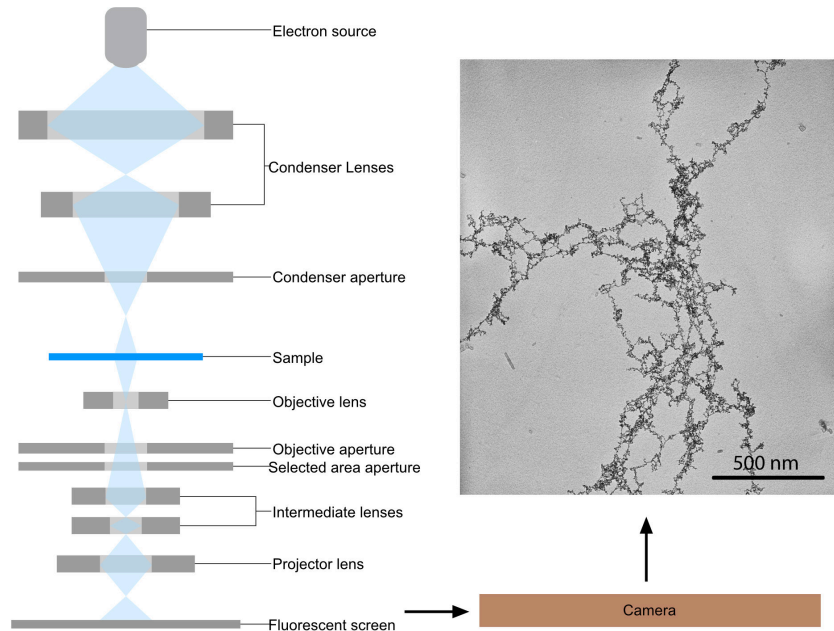


Figure 13. Schematic illustration of a transmission electron microscope.

1.4.6 Energy Dispersive X-ray Spectroscopy

Energy dispersive x-ray spectroscopy (EDS) is a technique used to obtain information on the chemical composition of a material. In principle, it relies on the interaction of some source of X-ray excitation, such as electrons in SEM-EDS, with a sample (fig. 14). In EDS, the high kinetic energy of the electron beam collides with one of the inner shell electrons of an atom, ejecting it. This results in an electron vacancy in one of the inner electron shells, which is then filled by an electron from a higher-energy shell and the energy difference between these shells is emitted as X-ray light. The energy of the emitted X-rays from a specimen is element specific and thus provides valuable information on qualitative and quantitative chemical composition of the sample being measured.

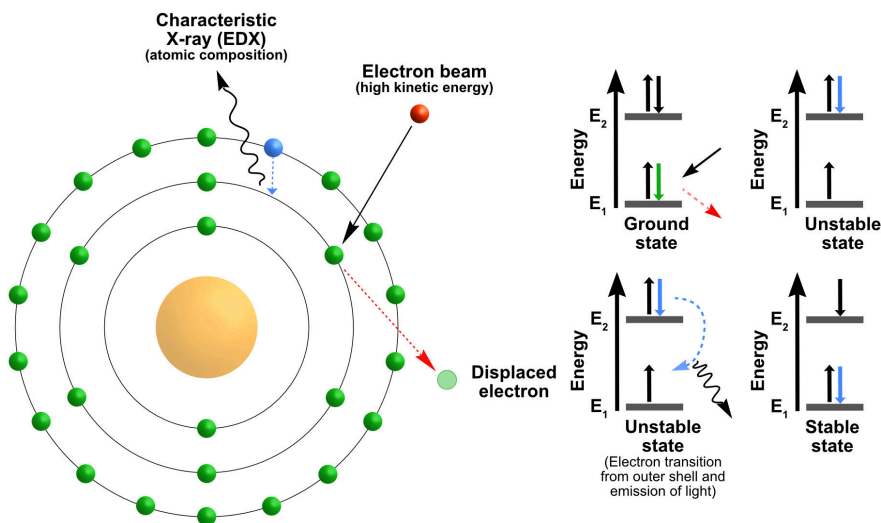


Figure 14. Principle of Energy Dispersive X-ray spectroscopy.

1.4.7 Thermogravimetric Analysis

Thermogravimetric analysis is a method of thermal analysis whereby the mass of a sample is measured over time. During this measurement the temperature may be held constant (isothermal analysis) or the temperature is changed over time in a linear manner (dynamic). This provides information not only on the thermal stability of a material but also on oxidative mass loss and combustion temperature. Oxidative mass loss is useful for determining the mass of an inorganic (oxide) substance within an organic matrix.

1.4.8 X-ray Diffraction

Light interacts with matter through vibrational excitation, electronic excitation or light diffraction. X-rays, with wavelengths under 10 nm ($<10^{-8}$ m), undergo elastic scattering by a material's electrons, resulting in diffraction. Generally, atoms with higher atomic numbers diffract more X-ray light because they have more electrons to scatter it; hence, heavy elements like tungsten and rhenium diffract more light than ones like hydrogen. Elastic scattering can be visualized like ocean waves hitting a lighthouse, generating secondary circular waves. Similarly, when X-rays hit electrons, they produce secondary spherical waves. In a regular array of atoms, these waves mostly interfere destructively and cancel out, but in certain directions they interfere constructively (fig. 15). Bragg's model describes diffraction as mirror-like reflections from evenly spaced planes within a crystal.

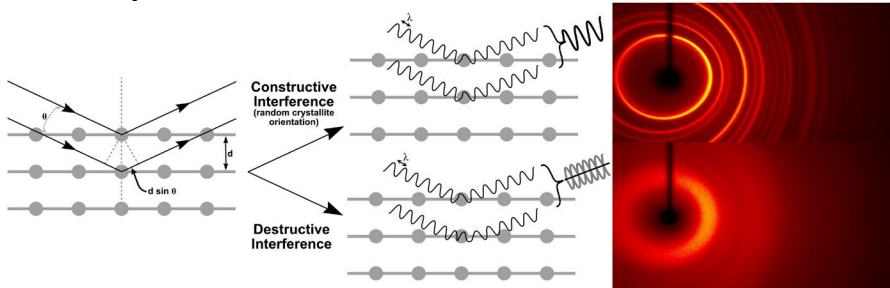


Figure 15. Bragg diffraction, constructive and deconstructive interference.

Crystal planes, spaced by a distance d , produce constructive interference when the x-ray incidence angle θ creates a path difference equal to an integer multiple n of the wavelength λ , described by Bragg's law: $n\lambda = 2d \sin \theta$. These planes are oriented in space according to Miller indices (h, k, l). Once the wavelength and scattering angle (2θ) are known, the space group and unit cell dimensions can be determined.

In single-crystal X-ray diffraction, molybdenum $K\alpha$ radiation ($\lambda = 0.7107$ Å), comparable to interatomic distances, is commonly used. A single crystal is precisely oriented relative to the X-ray beam and detector, producing sharp, well-defined diffraction peaks (fig. 16). The angles and intensities of these reflections reveal atomic positions within the lattice. By rotating the crystal, various diffraction planes are accessed, allowing the molecular structure to be solved computationally. In powder X-ray diffraction, the sample consists of randomly oriented microcrystals, producing a ring pattern

in the diffractogram. This makes structural determination more challenging without a reference, though models can be refined using Rietveld refinement. Copper $K\alpha$ radiation ($\lambda = 1.5406 \text{ \AA}$) is commonly used for powder diffraction, providing better angular (2θ) resolution due to its longer wavelength.

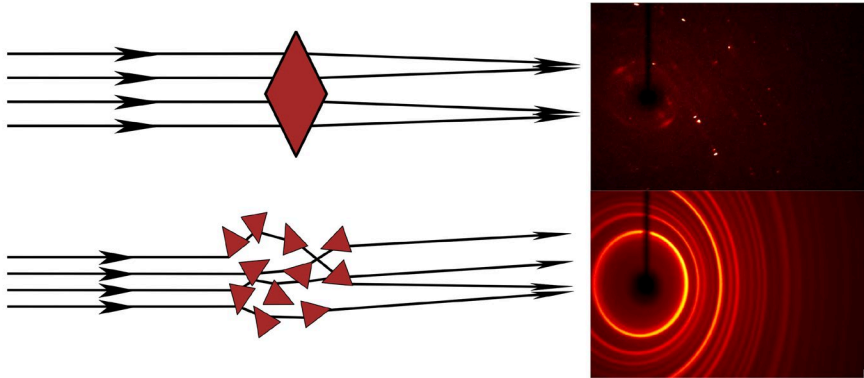


Figure 16. Diffraction patterns from a single crystal (**top**) and a nanocrystalline powder (**bottom**). With a single crystal, a diffraction pattern with discrete diffraction spots is obtained due to regular diffraction. For a nanocrystalline material the crystallites are randomly oriented resulting in a ring pattern.

2. Materials and Methods

2.1 Synthesis of metal-amine complexes

[Ni(II)(TAEA)(H₂O)(NO₃)]NO₃ (1). Ni(II)(NO₃)₂·6H₂O (279.8 mg, 1 mmol) was dissolved in 4 mL of miliQ, followed by the addition of 1 mol equivalent (143 µl) of tris(2-aminoethyl)amine (TAEA) and the solution was allowed to slowly evaporate at room temperature, yielding violet block-shaped (prismatic) crystals.

[Co(III)(TAEA)(H₂O)(NO₃)](NO₃)₂ (2). Co(II)(NO₃)₂·6H₂O (290 mg, ~1mmol) was dissolved in 4 ml of MiliQ, followed by the addition 1 mol equivalent (143 µl) of tris(2-aminoethyl)amine (TAEA) dissolved in 1ml miliQ, that has previously been acidified to pH 3 using 1M nitric acid. The solution was allowed to slowly evaporate at room temperature until a glassy product had formed. Final red plate-shaped crystals were obtained by low temperature crystallization at -20°C.

[N(C₂H₄NH₃)₃](NO₃)₃ (3). 1 mmol of REE(III)(NO₃)₂·6H₂O (REE = Sm, Dy) was dissolved in 4 mL of miliQ, followed by the addition of 1 mol equivalent (143 µl) of tris(2-aminoethyl)amine (TAEA), and the solution was allowed to slowly evaporate at room temperature, yielding colourless plate-shaped crystals in a gel-like matrix.

2.2 Surface modification of cellulose materials

2.2.1 Synthesis of cellulose nanocrystals

Cellulose nanocrystals derived from cotton were synthesized via the common sulfuric acid hydrolysis method (Reid et al. 2017). Briefly, 16 grams of raw surgical cotton was suspended in 280 ml of 64wt% sulfuric acid at 45°C for 45 minutes. Afterwards the CNC suspension was decanted into 10-fold excess of water and allowed to settle. The supernatant was decanted, and the remaining CNC suspension dialysed (MWCO = 12 kDa) against miliQ until the conductivity remained unchanged. The resulting CNC suspension was stored as is at 4°C until used.

2.2.2 Chlorination of cellulose nanocrystals

A CNC suspension corresponding to 3.0 grams of CNC (18.3 mmol) by dry weight was lyophilized and suspended in 60 ml sieve-dried DMF, forming a 5 wt% CNC suspension in a round-bottom flask. The flask was fitted with a reflux condenser and drierite-packed drying tube. The suspension was heated to 80°C and 10.5 ml (145 mmol, 7-8 mol eq.) thionyl chloride was added dropwise. The suspension was allowed to stir for 4 hours, after which it was poured into water and neutralized with 3% ammonia until the pH became neutral. The resulting suspension was homogenized using a high-shear mixed (13500 min⁻¹, 10 minutes) and collected via centrifugation (10k rpm, 10 minutes). Particles were washed several times with water and either lyophilized or stored in aqueous media. The approach is summarized in figure 17.

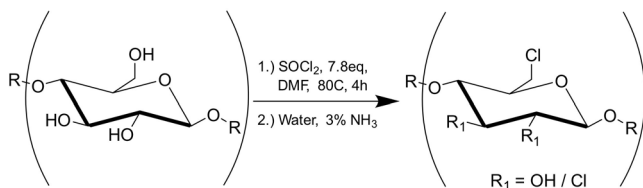


Figure 17. Schematic illustration of the synthesis of chlorinated cellulose

2.2.3 Amination of chlorinated cellulose nanocrystals

An aqueous suspension of chlorinated cellulose (1.5 gram cellulose) was collected via centrifugation, water decanted and replaced with 1,4-dioxane. The suspension was washed with 1,4-dioxane 4 times, after which the suspension was transferred to a round-bottom flask followed by the addition of 1.4 ml TAEA (9.3 mmol, 2.2 equivalent based on chlorine). The flask was fitted with a reflux condenser and refluxed overnight. The product was collected via centrifugation and washed with water until the conductivity remained unchanged and lyophilized. Amine content was determined via conductometric titration. The approach is summarized in figure 18.

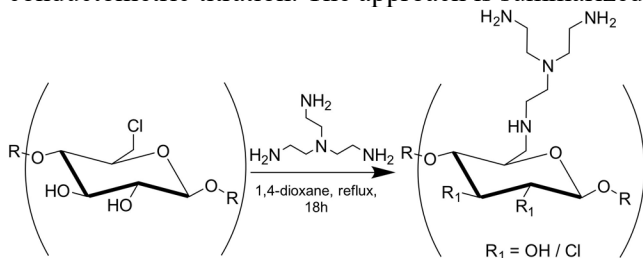


Figure 18. Schematic illustration of cellulose-TAEA synthesis from chlorinated cellulose

2.2.4 Phosphorylation of bacterial nanocellulose

Bacterial nanocellulose was phosphorylated according to a modified literature procedure (Ait Benhamou et al. 2021). Briefly, a solution of 450 mg NH₄H₂PO₄, 1.2 gram urea and 10 ml ultrapure was prepared and poured into a petri dish containing an approximately 10x10 cm dry BCN sheet and allowed to soak overnight. After soaking the sheet was transferred to a ceramic plate and placed in pre-heated 160°C oven for 20 minutes. The approach is summarized in figure 19.

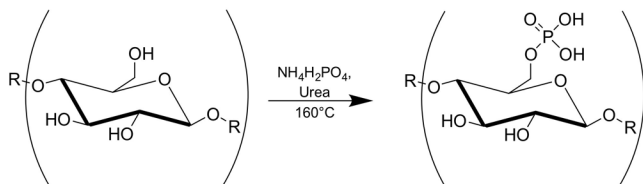


Figure 19. Schematic illustration of the synthesis of phosphorylated cellulose.

2.2.5 Introduction of nano-ferria

22 grams of 2.26 wt% carboxymethylated cellulose nanofibrils (500 mg, C-CNF) was transferred to a 250 ml round-bottom flask and diluted with 200 ml nitrogen purged ultrapure water and vigorously stirred for 30 minutes under continuous nitrogen flow. Then 324 mg (2 mmol) of anhydrous FeCl_3 and 334 (1.2 mmol) $\text{Fe(II)SO}_4 \cdot 7\text{H}_2\text{O}$ was added forming a 1.7:1 $\text{Fe}^{3+}/\text{Fe}^{2+}$ stoichiometry. The pH was adjusted to pH 5 and stirred for 30 minutes before dropwise addition of 1.5 M NH_4OH until pH 9. The product was allowed to settle, washed and collected via centrifugation.

2.2.6 Introduction of nano-titania

For functionalization of a bacterial nanocellulose sheet with nano-titania, an approximately 5x5 cm sheet of bacterial nanocellulose was suspended in 5 ml ultrapure water, followed by the addition of 10 mmol of TiBALDH 50wt% solution per gram of phosphorylated bacterial nanocellulose. The sheets were allowed to soak overnight under continuous agitation and thoroughly washed with ultrapure water prior to analysis. For the preparation of TATT-coated cellulose sheets the same molar ratio of TATT to phosphate was used, however the sheets were allowed to soak over several days. TATT was obtained according to Kessler et al. (2008).

2.2.7 Introduction of photoluminescent cations & nano titania

To obtain an Eu(III) doped bacterial nanocellulose sheet covered with TiO_2 grafted onto the surface, 10 ml of solution containing of 10 mol% (based on P) $\text{Eu(NO}_3)_3 \cdot 5\text{H}_2\text{O}$ was prepared. The europium solution was added to a petri dish containing a sheet of phosphorylated BCN and equilibrated on an orbital shaker overnight. The sheet was washed at least 3 times, re-suspended in 10 ml water followed by the addition of 3 mol equivalent TATT (120 mg/ml, 1.5M) and allowed to equilibrate on an orbital shaker for one week.

2.3 Drug adsorption and release of pharmaceuticals

2.3.1 General drug adsorption

To prepare pharmaceutical loaded composites generally 70 mg/L pharmaceutical of solutions and 0.4-0.8 mg/ml composites were used. The pharmaceutical solutions were acidified with 0.8-1 mol equivalent of hydrochloric acid to aid in solubilisation before use. The composite / drug mixture was heated to 50-55°C overnight and the drug adsorption determined via UV-VIS at 357 nm for tetracycline and 316 nm for ciprofloxacin.

2.3.2 General drug desorption

An appropriate amount of drug-cellulose composites were placed in a Duran[®] bottle together with 0.02M citrate buffer (pH 6.0) to reach a final maximum concentration of 44 mg/L desorbed pharmaceutical. Aliquots were taken in intervals and measured. Samples were prepared and measured in triplicate.

2.3.3 Desorption media influence on surface structures

To examine the influence of desorption media composition on cellulose-TiO₂ hybrid material, sheets of TATT-covered phosphorylated bacterial nanocellulose were stored for 24 hours in 0.02M citrate media, updated simulated body fluid with 2 mM lactic acid (Marques et al. 2011) or simulated human sweat (custom recipe). SBF was chosen as it has an ion concentration close to human blood plasma, lactic acid was added as human plasma contains lactic acid (Adeva-Andany et al. 2014) and titania is known to interact with lactic acid. Simulated human sweat was prepared using a custom recipe based on concentration values found for urea (22.2 mM, Huang et al. 2002), lactic acid (25 mM, Kumar et al. 2023), ammonia (7 mM, Sato 1977), potassium (7 mM, Sato 1977), magnesium (0.55 mM, Montain et al. 2007), calcium (1 mM, Sato 1977), sodium (120 mM, Sato 1977) chloride (130 mM, Sato 1977) sulfate (0.084 mM, Cole & Landry 1985) and phosphate (0.20 mM, Talbert et al. 1933).

2.4 Chemical analysis and surface characterization

Samples were characterized using a Bruker Dimension FastScan Atomic Force Microscope (AFM) with a Nanoscope V controller in ScanAsyst mode using a Fastscan-B AFM probe (Silicon tip, f_0 :400kHz, k :4 N/m, Tip radius: 5 nm nominally) and a scan rate of 1-3Hz. Data was processed using Gwyddion 2.56 with align rows-median to remove skipping lines.

Scanning Electron Microscopy (SEM) observations of cellulose materials were performed using a Hitachi FlexSEM 1000 at an acceleration voltage of 3-7 keV, spot size 20, and 5-mm working distance. For Energy Dispersive X-ray Spectroscopy (EDS) an acceleration voltage of 15 keV, spot size 50 and 10-mm working distance were used. For Cell Adhesion Assays a JEOL JSM-IT500HR SEM was used, using a working distance of 8 mm and an acceleration voltage of 5 keV. Samples were prepared on carbon tape without any special treatment.

Transmission Electron Microscopy (TEM) samples were deposited on holey carbon grids and observed using a Philips CM/12 microscope fitted with LaB6 and operated at 80 or 100 keV. For sectioning samples were embedded in LR White resin, dehydrated in ethanol and sectioned using a Reichert Ultracut E ultramicrotome and collected on copper grids. Sections were observed unstained or stained with 2% w/v aq. uranyl acetate.

Fourier Transform Infrared (FTIR) analysis was performed on a Perkin Elmer Spectrum 100 FT-IR Spectrometer using an ATR module or transmission window.

Titration was performed using a Metrohm Titrando 888 (2.888.0310), fitted with an 856 conductivity module (2.856.0010), 800 Dosino (2.800.0010), 5-ring conductivity measuring cell ($c = 0.7$, 6.0915.100), using TIAMO Light 2.5 as automation software. Titres were determined using tris(hydroxymethyl)aminomethane (HCl) and potassium hydrogen phthalate (NaOH). Amine / phosphate content was determined via conductometric titration by titration of protonated amine / phosphate.

Powder X-ray Diffraction (PXRD) data was obtained on a Bruker APEX-II diffractometer equipped with an AXS Smart APEX CCD Area Detector and graphite-monochromated Mo-K α ($\lambda = 0.71073$ Å) radiation source or a Bruker D8 QUEST ECO diffractometer equipped with a Photon III Area Detector and graphite-monochromated Mo-K α radiation source. Data was processed with the EVA-12 software package.

Single-crystal X-ray diffraction data for crystals 1 and 3 were collected on a Bruker SMART Apex-II diffractometer equipped with a graphite monochromated sealed-tube Mo-K α ($\lambda = 0.71073$ Å) radiation source using omega-scans to obtain full hemisphere data. For crystal 2 the data was collected using a Bruker D8 Quest ECO diffractometer at room temperature using a Mo-K α (0.71073 Å) radiation source. The structures were solved using direct methods.

The specific surface area and pore volume/area were determined from nitrogen adsorption/desorption isotherms on freeze-dried samples at -196 °C (Micromeritics ASAP 2020 Surface Area and Porosity Analyser, Norcross, GA, USA). The samples were degassed at 120 °C for 3 h before the measurements.

Magnetic measurements were performed using a Lake Shore Cryotronics Series 7400 vibrating sample magnetometer (VSM). Measurements were performed at 300 K ($26,85$ °C) in the magnetic field range ± 10 kOe with the magnetic moments normalized using the weight of iron oxide solid phase.

2.5 Wound healing cell studies

2.5.1 Cell viability / indirect cytotoxicity assay

Cytotoxicity assays on functionalized BNC films were performed according to the ISO 10993-5/10993-12 norm, using the extract dilution method MTT assay. Human osteoblast-like SaOS-2 cells and L929 murine fibroblasts cells were obtained from the American Type Culture Collection (ATCC, VA, USA). Cells were seeded in 96-well plates at 10^4 cells per well in 100 μ L of DMEM supplemented with 10% FBS and 1% of chlorhexidine. The cells were incubated at 37 °C in 5% CO $_2$ atmosphere for 24 h. Simultaneously, the extract media from functionalized BNC films were prepared using 3 cm 2 of each film into 3 mL of DMEM culture that was stirred at 37 °C for 24 h. 100 μ L of each extract medium was added to each well. Two different controls were included: culture media only, i.e., no cells and cells incubated in culture medium alone (survival control). After 24 h of incubation, the extract media was removed, and the wells were washed with 0.01 M phosphate-buffered saline (PBS). Thereafter, 100 μ L of MTT (1 mg/mL) was added into each well, and the cells were further incubated for 4 h. Finally, the supernatant was removed and 50 μ L isopropanol was added

into each well. The absorbances were measured at a wavelength of 570 nm and then converted into percentages of cell viability (Mosmann 1983). All samples were performed in triplicate.

2.5.2 Cell adhesion assay

Cell adhesion studies were performed using the same SaOS-2 / L929 cell lines. Cells (5×10^4 cells/well) were seeded on functionalized BNC films (1 cm^2) inserted into a 24-well well-plate and incubated for 72h at 37°C at 5% CO_2 . After incubation, the media was removed and cells washed with sterile filtered 0.01M PBS (pH 7.4). Cells were fixated with 3% glutaraldehyde in 0.01M PBS for 30 minutes and washed with 0.01M PBS. Samples were progressively dehydrated through ascending ethanol washing (30%, 50%, 70%, 95%, 100% (x2), 3 minutes each). Dry samples were sputter coated with carbon to produce a 10 nm-carbon layer and observed via SEM.

2.5.3 Pseudo-wound closure

To evaluate pseudo-wound closure, L929 fibroblast and SaOS-2 osteoblast-like cells were cultured with a density of 1×10^5 cells/well in a 24-well plate and incubated at 37°C in 5% CO_2 atmosphere. Extraction media was prepared from functionalized BNC films were prepared using 3 cm^2 of each film into 3 mL of DMEM culture that was stirred at 37°C for 24 h. The wells were washed twice with PBS and a straight line scratched through the cell-layer using a ruler and a 200 μl pipette tip. The resulting gap was imaged at 0, 6, 24 and 48 hours using an inverted optical microscope with 10x objective until the pseudo-wound had fully closed (Cappiello et al. 2018; Morais et al. 2023). Samples were measured in triplicate and the size of the pseudo-wound was measured at all time points using imageJ2 (Rueden et al. 2017). The pseudo-wound closure (%) was calculated according to the following equation, where x corresponds to time of recording:

$$\% \text{ pseudo - wound closure} = \frac{\text{Area } t(0) - \text{Area } t(x)}{\text{Area } t(0)} \times 100\%$$

2.5.4 Immunofluorescence cell culturing

Murine L929 fibroblasts were cultured in Dulbecco's Modified Eagle Medium (DMEM, Gibco®) with 10% fetal bovine serum (FBS, Gibco®) and 1% ciprofloxacin (Sigma, St. Louis, MO, USA) at 37 °C in a humidified condition with 5% CO₂ and 95% air. SAOS-2 osteoblasts were cultured in McCoy (ThermoFisher™) with 10% FBS and 1% ciprofloxacin at the same parameters described above. The cells were used after two consecutive passages.

2.5.5 Fluorescence staining

Cells were seeded onto the 24-well polystyrene cell culture plate, at a density of 3000-5000 cells/well in a humidified environment with 5% CO₂ and 95% air for 48 h. Simultaneously, the eluates from different samples were prepared using 1 cm²/mL and maintained in agitation for 24 h in DMEM and McCoy with 5% FBS and 1% ciprofloxacin, respectively. Then, the conventional media was replaced with 500 µL/well of each eluate from phosphorylated BNC, phosphorylated BNC+TATT, phosphorylated BNC+TiBALDH and control (cells maintained only with conventional media) for 48 h at the same temperature and CO₂ level described above. Afterward, the eluates were removed, and the wells were washed with phosphate saline buffer (PBS, 1X), and cells were fixed with 3% glutaraldehyde for 30 min at 4°C. The cells were washed again with PBS (three times) and treated with 0.1% Triton X-100 for 5 min at room temperature. After incubation, the wells were washed with PBS, and the cells were incubated with phalloidin-iFluor 488 in 1% BSA/PBS (1 µg/mL) for 1 h at 37 °C. Concomitantly, the wells were incubated overnight with Rabbit Recombinant Monoclonal Anti-Collagen I conjugated to Alexa Fluor® 594 (1:200) and Rabbit Recombinant Monoclonal Anti-Fibronectin conjugated to Alexa Fluor® 555 (1:200) at 4 °C. The cell markers were visualized using a Zeiss LSM800 confocal microscope equipped with a 40x/1.4 NA objective. Excitation wavelengths used were: 488 nm for phalloidin-iFluor 488®, 594 nm for Alexa Fluor 594® (Collagen I) and 555 nm for Alexa Fluor 555® (Fibronectin). Emission wavelengths: 505-550 nm for phalloidin-iFluor 488®, 610-650 nm for Alexa fluor 594® and 570-620 nm for Alexa Fluor 555®. Image resolution: 1024 x 1024 pixels with 8-bit depth.

2.5.6 Quantitative measurement of fluorescence Intensity

Fibroblast and osteoblast cells were initially seeded in 96-well plates at a density of 5,000 cells per well. The cells were cultured in conventional medium and incubated at 37°C in a humidified atmosphere with 5% CO₂. After 24 hours, the conventional medium was replaced with eluates from phosphorylated bacterial cellulose (BNC), phosphorylated BNC+TATT, and phosphorylated BNC+TiBALDH. The culture medium was replaced with the corresponding eluates every two days for a total culture duration of 7 days. After 7 days, the eluates were carefully removed, and the cells were washed three times with phosphate-buffered saline (PBS) to remove any residual media or eluates. The cells were then fixed by incubating with 3% glutaraldehyde for 30 min at 4°C. Following fixation, cells were permeabilized using 0.1% Triton X-100 in PBS for 5 minutes. Subsequently, the cells were incubated with the fluorescence markers following the protocol described above. The fluorescence intensity was quantified using the FLUOstar Omega Microplate Reader. Each well was scanned for fluorescence at the specific excitation and emission wavelengths corresponding to the fluorophores used. This assay was performed in two independent experiments.

3. Results and Discussion

3.1 Cellulose surface modification for sorption of metal (oxides)

For cellulose to have strong interactions with transition or lanthanide metals, its chemical structure must be modified in some manner as simple alcohols only weakly coordinate to these elements. There are various ways of modifying the glucose backbone of cellulose to increase the affinity between biopolymer and metal cation. By introducing a coordinating ligand with high affinity for a particular cation according to HSAB theory (Pearson 1963), this affinity can be tuned.

3.1.1 Chemical modification

There are many ways of modifying the chemical nature of cellulose towards strong interactions with metal cations or particles, two ways that were explored more deeply in this work is the introduction of a tripodal amine and a Lewis basic phosphate group.

Chlorination

To introduce a tripodal amine to the cellulose backbone, cellulose was chlorinated using thionyl chloride in DMF (illustrated in fig. 17). The chlorination should occur either via direct interaction of the hydroxyl-group with thionyl chloride or via a Vilsmeier-Haack type intermediate formed from the interaction between DMF and thionyl chloride. Via this method (table 1) a relatively high amount of chlorine (9.99 wt%) can be installed onto cellulose. An approximate 2.81 ± 0.04 mmol g⁻¹ chlorine can be measured throughout the sample. Sulfur in this sample has several possible

sources, such as the formation of sulfate-half esters (RO-SO_3^-) during the production of cellulose nanocrystals using sulfuric acid (Reid et al. 2017). Another possible source of sulfur is from thionyl chloride. During chlorination with thionyl chloride a chlorosulfite intermediate is formed which can hydrolyse to form a sulfite-ester (RO-SO_2^- , McCormack & Lawes 2000).

Table 1. Example elemental composition table of cellulose chlorinated with thionyl chloride

Element	Line Series	Weight %	Weight % σ	Atomic %
C	K Series	46.11	0.69	55.88
O	K Series	43.93	0.63	39.96
Cl	K Series	8.46	0.17	3.47
S	K Series	1.50	0.08	0.68
Total		100.00		100.00

Amination

Chlorination of cellulose leads to the (partial) replacement of hydroxyl groups across cellulose with chloride, which easily undergoes nucleophilic substitution to form interesting cellulose-based derivatives. For example, by reacting with the tripodal amine tris(2-aminoethyl)amine (illustrated in fig. 18). Tris(2-aminoethyl)amine was chosen as it is a tripodal multidentate ligand which in principle should have high affinity for intermediate Lewis acidic late transition metal such as Co^{2+} , Ni^{2+} , Fe^{3+} . The purpose of the modified cellulose material was separation of Co^{2+} / Ni^{2+} from REE. Via EDS (table 2) it was observed that the chlorine content was reduced to approximately $1.76 \pm 0.06 \text{ mmol g}^{-1}$ after treatment with TAEA. Nitrogen could be estimated at 1.17 mmol g^{-1} .

Table 2. Example elemental composition table of chlorinated cellulose after treatment with TAEA.

Element	Line Series	Weight %	Weight % σ	Atomic %
C	K Series	53.48	1.21	61.57
O	K Series	35.93	0.89	31.05
Cl	K Series	4.78	0.14	1.86
S	K Series	0.39	0.005	0.17
N	K Series	5.42	1.91	5.35
Total		100.00		100.00

Nitrogen is unfortunately difficult to accurately measure via EDS as it partially overlaps with carbon and oxygen. The amine content was additionally evaluated via conductometric titration by conversion to its protonated form and back-titrating with base, yielding an amine content of 0.84 mmol g⁻¹. The difference may be explained by not all amines being solvent accessible in water.

Phosphorylation

The other functional group that was explored in this work was phosphate. Phosphorous(V) oxyanions are quite useful as they have a high affinity for many (particularly hard Lewis acidic) elements, binding via electrostatic interactions. In this work, phosphate was used to strongly bind to lanthanides and TiO₂. Organophosphates are relatively straightforward to synthesize. They may be synthesized via alcoholysis of phosphorus oxychloride, oxidation of organophosphites or via esterification of phosphoric acid. Here cellulose was phosphorylated via thermal treatment of cellulose with ammonium dihydrogen phosphate to form cellulose phosphate esters.

The reaction can be followed by EDS, ATR-FTIR or via conductometric titration of the protonated phosphate against standardized NaOH (fig. 20). As the reaction progresses the at% of P increases to around 3.3% in EDS, while for ATR the introduction of phosphate leads to the appearance to several unique vibrations around 1232 cm⁻¹, 925 cm⁻¹, 838 cm⁻¹, 495 cm⁻¹. These were attributed to P=O, P-O(R), P-O(C) and P-O-P/P=O deformation respectively (Thomas & Chittenden 1964a; b). As the reaction progresses a final phosphorous content of 2.7 mmol g⁻¹ could be reached after 60 minutes. However, it was noted that the films became increasingly brittle as the reaction progressed.

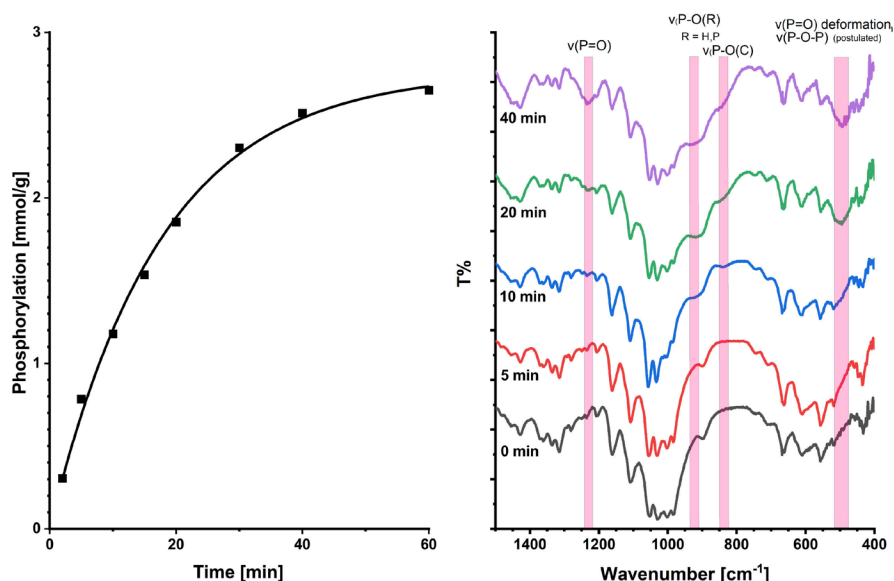


Figure 20. **(left)** phosphorylation degree estimated from conductometric titrations. **(right)** ATR-FTIR spectra of bacterial nanocellulose as the phosphorylation reaction progresses.

3.1.2 Morphological change by chemical modification of cellulose

As the cellulose backbone is modified, it is important to note that morphological changes may occur depending on the reaction conditions. This was clearly illustrated with the synthesis of tris(2-aminoethyl)amine modified cellulose. Here the starting product were cellulose nanocrystals derived from cotton via acid hydrolysis. The original CNCs were approximately 40 x 150 nm, rod shaped crystals of cellulose, while after chlorination and amination the morphology has changed to become globular with dimensions between 90 - 500 nm (fig. 21).

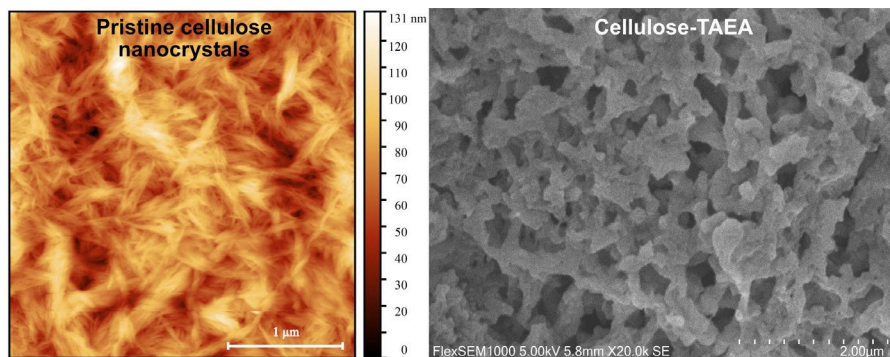


Figure 21. **(left)** AFM image of cellulose nanocrystals derived from acid hydrolysis of cotton. **(right)** SEM after chlorination and amination with TAEA.

This may appear odd, after all cellulose is recalcitrant to dissolution in most solvent systems. Taking a closer look at the synthesis conditions provides a possible explanation as to why the morphology has changed. The solvent used for chlorination was *N,N*-dimethylformamide, a polar aprotic solvent closely related to *N,N*-dimethylacetamide, which is used to dissolve cellulose in combination with lithium chloride to disrupt hydrogen-bonding (Striegel 1997). Cellulose itself is amphiphilic and relies on intra- / intermolecular hydrogen bonding and van der Waals interactions to keep the polymer chains together (Lindman et al. 2010). During the initial chlorination reaction some of the intra-/intermolecular hydrogen bonds are broken as the hydroxyl-groups are replaced by chlorine and as the reaction progresses the polymer is increasing solvated, leading to (partial) reactive dissolution of cellulose. Evidence for this can be observed not only from AFM/SEM but also from XRD (fig. 22) where a clear change in diffraction pattern (i.e. packing) can be observed between pristine cotton CNCs and the chlorinated / aminated products.

Change in morphology is not solely the domain of solvents and reactive dissolution; surface modification and pH play a remarkable role. Taking as an example dried bacterial nanocellulose and comparing it to phosphorylated bacterial nanocellulose, morphological differences between the two may be observed (fig. 23). The main difference being the spacing between fibres. Their overall shape remains unchanged, though a minor increase in fibre thickness from 64.9 ± 13.0 nm (BNC) to 65.7 ± 12.8 nm (pBNC) was observed.

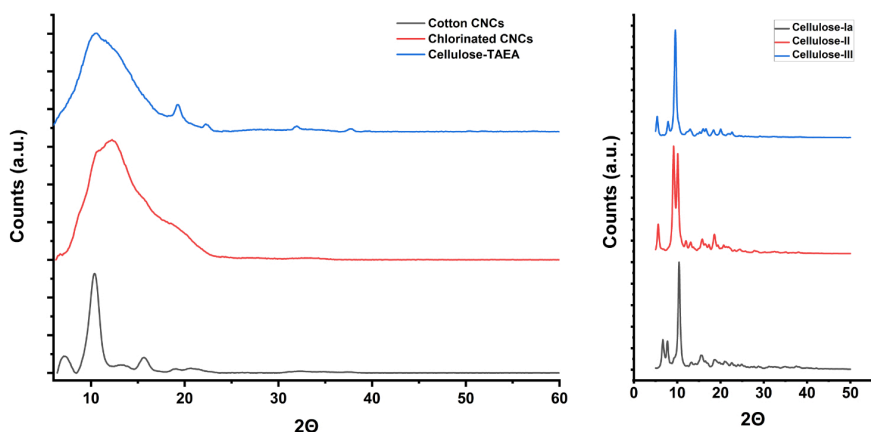


Figure 22. Measured powder x-ray diffractograms (**left**, Mo K α = 0.71073 Å) of cotton CNCs, chlorinated CNCs and cellulose-TAEA. (**right**) calculated idealized patterns for cellulose Ia, II and III (Mo K α = 0.71073 Å, FWHM = 0.5) (French 2014).

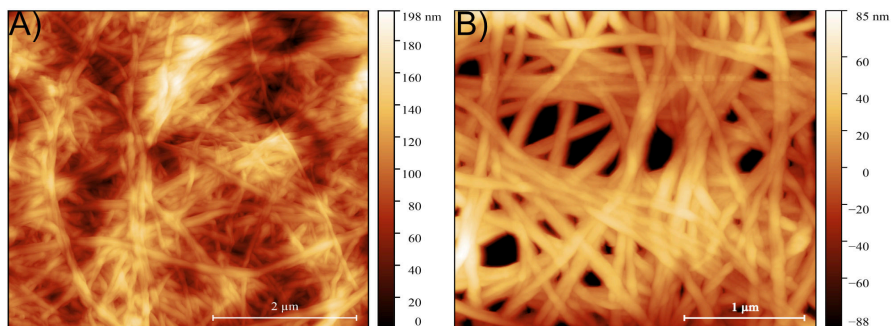


Figure 23. AFM image of dried bacterial nanocellulose (5x5 μm , **left**) and as prepared phosphorylated bacterial nanocellulose (3x3 μm , **right**).

These two celluloses behave differently depending on the solution pH. Storing dried BNC under neutral aqueous conditions (fig. 23 A & 24 C, D) led to a minor swelling of the fibres to 70.9 ± 12.4 nm, together with an increase in the spacing between fibres. For phosphorylated BNC stored under similar conditions the distance between fibres appeared much greater and the fibres looked ribbon-like (fig. 25 C, D).

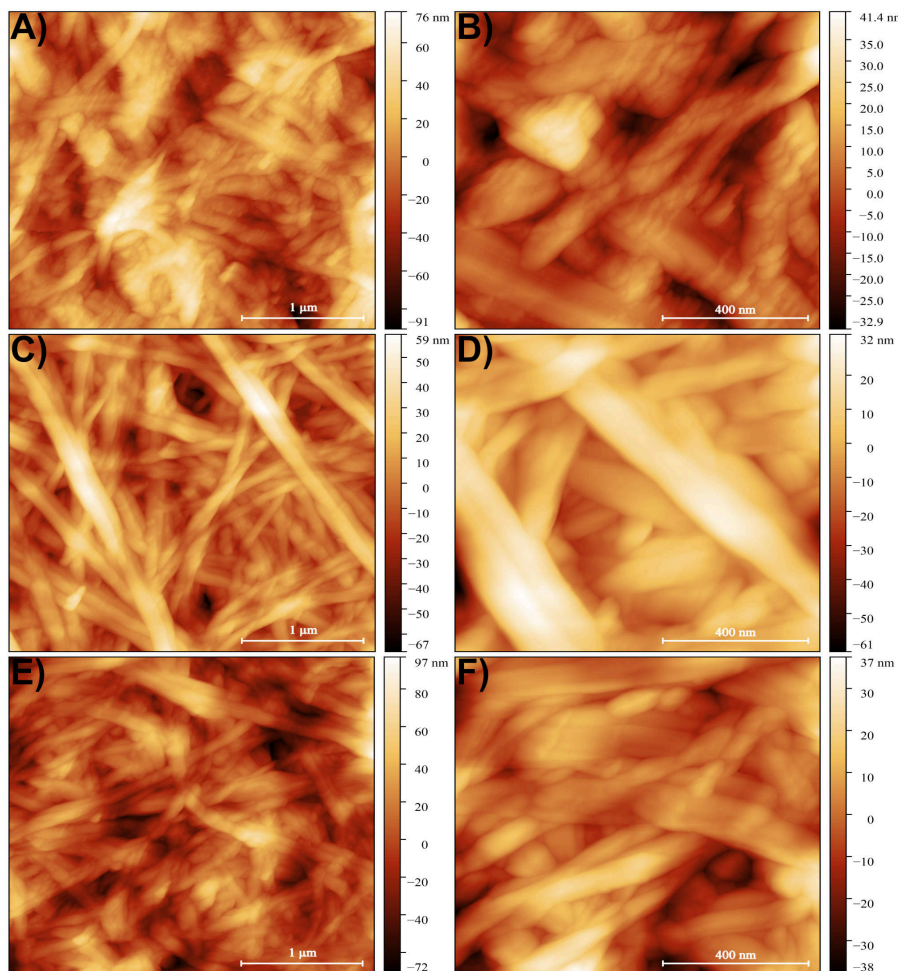


Figure 24. Dried bacterial nanocellulose stored in 0.1M HCl (A, B), miliQ (C, D) and 0.1M NaOH (E, F).

Storing dried BNC under acidic conditions had the effect of removing some of the amorphous domains on fibre surface (fig. 24 A, B), thereby exposing crystalline domains (22.3 ± 5.3 nm) on the surface. The fibres retained the overall shape, shrinking a little (50.9 ± 13.9 nm). For the phosphorylated BNC stored under similar conditions, the difference is significant. No crystalline domains could be observed on the surface of the fibre and the overall shape was sharply ribbon-like with increased spacing between fibres (fig. 25 A, B). AFM did not do the increase in fibre spacing justice; this was better observed via SEM (fig. 26).

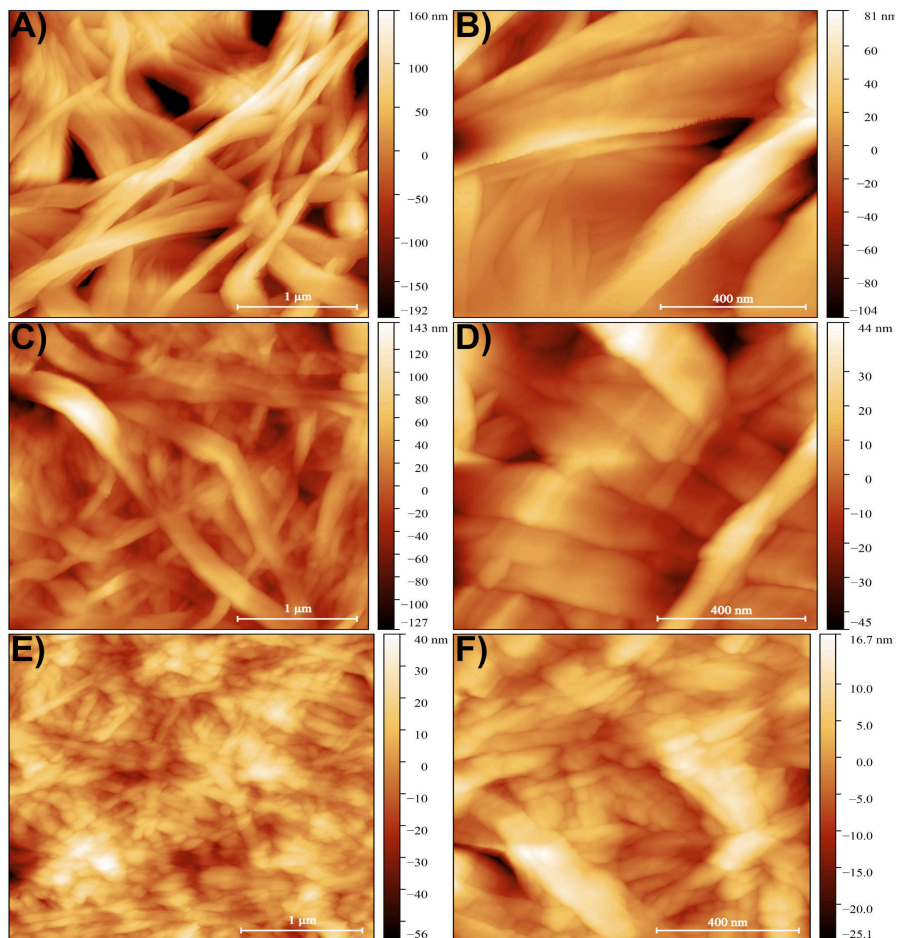


Figure 25. Phosphorylated bacterial nanocellulose stored in 0.1M HCl (A, B), miliQ (C, D) and 0.1M NaOH (E, F).

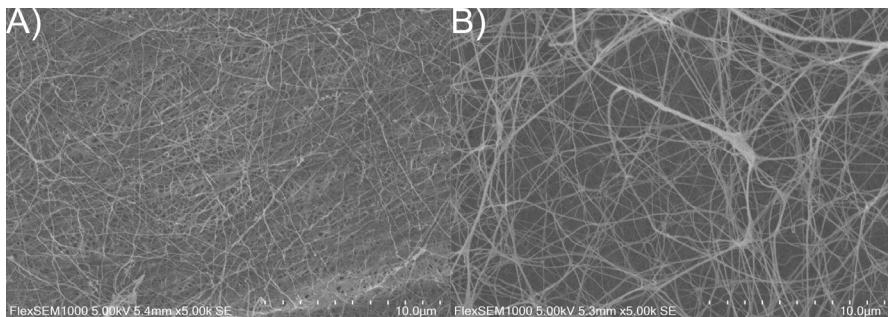


Figure 26. SEM image (5k magnification) of phosphorylated BNC stored in neutral (A) and acidic (B) conditions.

Treatment with aqueous base caused some minor globular structures to appear together with the emergence of ribbon-like fibres and a decrease in overall fibre thickness to 60 ± 12.4 nm (fig. 24 E, F). Similar but noticeably more pronounced, domains (44.8 ± 9.1 nm) were observed for phosphorylated BNC (fig. 25 E, F) when stored under basic conditions. These changes not only affected the overall morphology but also impacted the molecular packing as well as observed in the obtained X-ray diffractograms (fig. 27). It should be noted that the X-ray source used here was a Mo-source ($\lambda = 0.71073$ nm) instead of the more conventional Cu-source ($\lambda = 1.54056$ nm), leading to a loss in angular resolution and making it difficult to determine how the packing had changed. Overall, it was observed that upon swelling in neutral conditions the crystallite size (determined via Scherrer-equation) increased in both cases. For BNC this was from 6.3 nm to 12.6 nm, while for phosphorylated BNC this was from 12 nm to 17 nm.

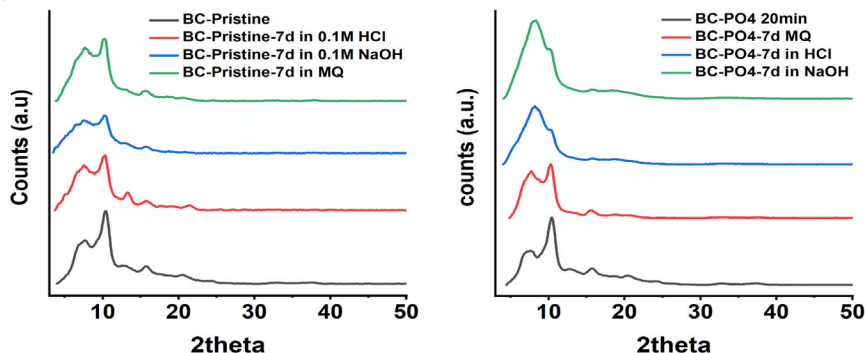


Figure 27. X-ray diffractograms of bacterial nanocellulose stored under acidic, neutral or basic conditions. **(left)** BNC, **(right)** phosphorylated BNC.

3.1.3 Metal sorption

One of the potential applications of cellulose nanomaterials is as an adsorbent material for the hydrometallurgical separation of metals, such as those found in the recycling of rare-earth based permanent magnets. Thus, the TAEA-modified cellulose material (0.84 mmol g^{-1} ligand) was evaluated for the sorption of Co^{2+} , Ni^{2+} , Nd^{3+} and Sm^{3+} . Langmuir absorption isotherms (saturation of surface binding sites, fig. 28), indicated that the TAEA-modified material had a good affinity for late transition metals cobalt and nickel even at low concentrations. While the material could adsorb REEs, its adsorption capacity at lower concentration was lower. Overall, the material

still exhibited high adsorption of REEs. The obtained adsorption capacity for each metal and the corresponding metal to ligand stoichiometry is presented in table 3. For each metal, the calculated adsorption capacity was close to the ligand content indicating that adsorption occurred in a near 1:1 ratio, with surface adsorption limited by the ligand content.

The produced TAEA-modified material showed very high kinetic selectivity (fig. 29) for Co^{2+} , reaching 53% saturation within one hour and 83% in 6 hours. Followed by Nd^{3+} (40% in 6 hours) and Ni^{2+} (34% in 6 hours). As Co^{2+} is rapidly adsorbed compared to other tested metals, it may provide some kinetic selectivity between separation of cobalt from metal mixtures.

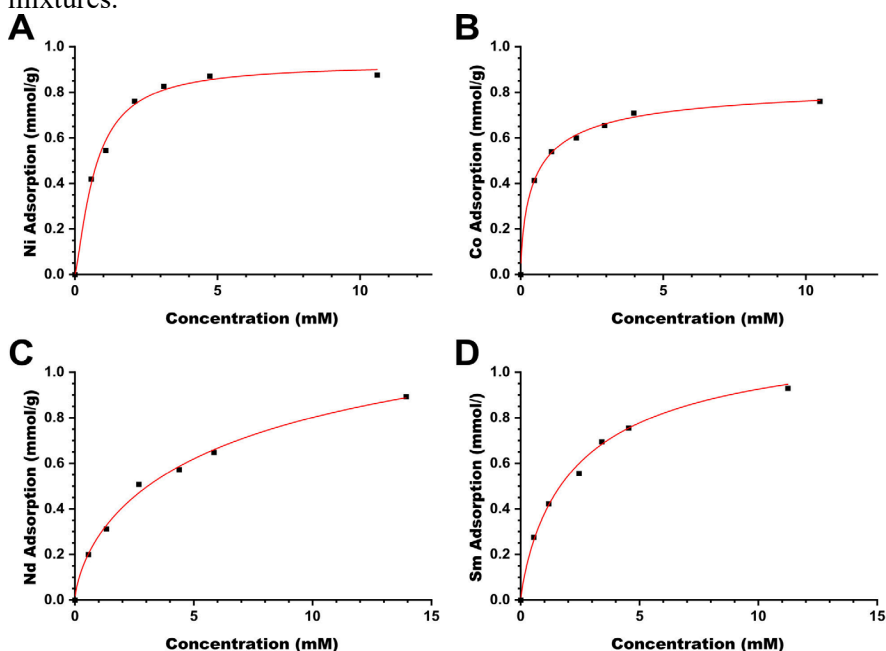


Figure 28. Langmuir isotherms of late transition metals (A) Ni^{2+} , (B) Co^{2+} and rare earth elements (C) Nd^{3+} , (D) Sm^{3+} .

Table 3. Adsorption capacity and metal:ligand stoichiometry of tris(2-aminoethyl)amine modified cellulose

Metal	Adsorption capacity [mmol g^{-1}]	Metal/ligand stoichiometry
Co^{2+}	0.76	0.90
Ni^{2+}	0.88	1.04
Nd^{3+}	0.79	0.94
Sm^{3+}	0.82	0.97

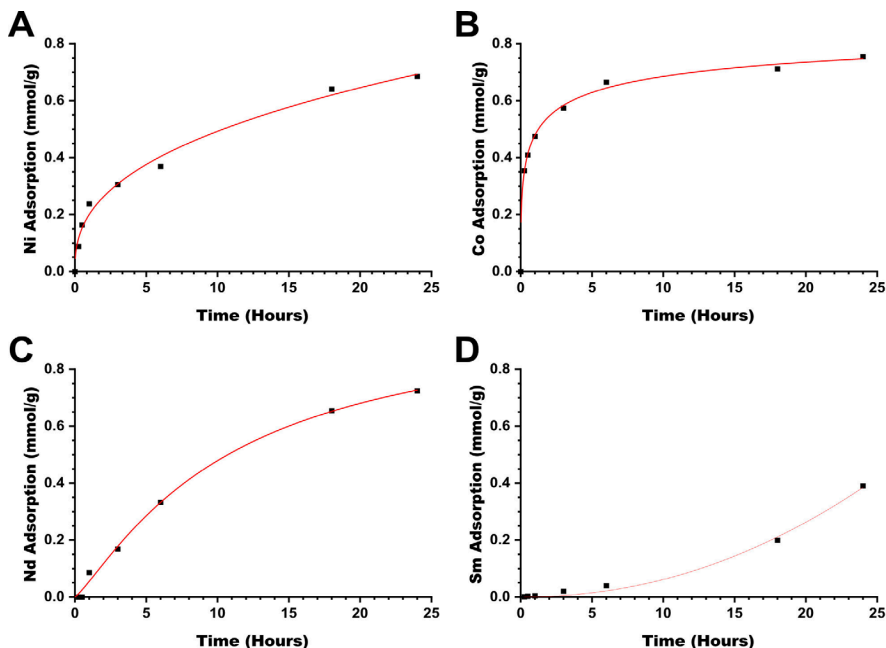


Figure 29. Adsorption kinetics of (A) Ni^{2+} , (B) Co^{2+} , (C) Nd^{3+} , (D) Sm^{3+} by tris(2-aminoethyl)amine modified cellulose in a 24h period.

Table 4. Metal selectivity of tris(2-aminoethyl)amine modified cellulose as determined by EDS analysis of the adsorbent after equilibrating in equimolar aqueous metal mixtures.

Metal Mixture	Metal ratio
Ni:Co	1 : 1.1
Nd:Ni	1 : 5.1
Sm:Co	1 : 5.7
Sm:Nd	1 : 1.2

When the material was placed in equimolar mixtures of metals (table 4) and allowed to equilibrate for 48 hours, the material demonstrated a 5:1 selectivity towards LTMs $\text{Ni}^{2+}/\text{Co}^{2+}$, suitable for separation of LTMs and REEs. pH dependant desorption experiments (fig. 30) indicated that for most metals at least 50% recovery was possible, except for cobalt. Cobalt appeared to be more resilient to acid treatment for recycling of the material.

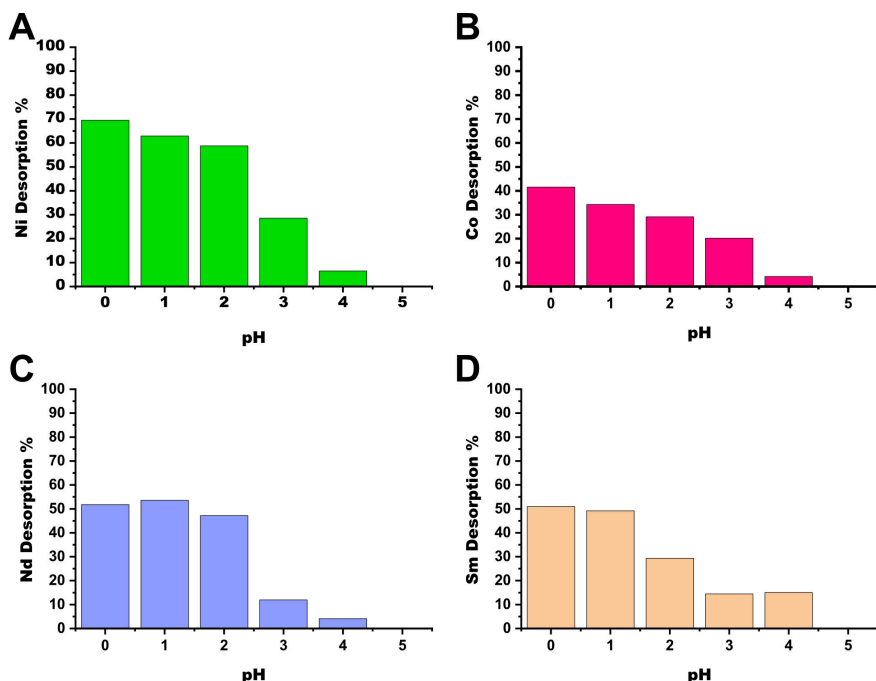


Figure 30. pH-Dependent desorption of (A) Ni²⁺, (B) Co²⁺, (C) Nd³⁺ and (D) Sm³⁺ from TAEA-modified cellulose.

3.1.4 Mechanistic explanation for metal sorption

To better understand the metal adsorption mechanism and potential surface complexes on TAEA-modified cellulose, X-ray quality crystals were grown, yielding the structures shown in figure 31. Single crystal X-ray analysis revealed octahedrally coordinated Co(III) and Ni(II) centers, each coordinated by four nitrogen atoms from TAEA, one water molecule, and one inner-sphere nitrate ion. Interestingly, while nickel remained in the +2 oxidation state, cobalt had oxidized to +3, likely stabilized by the coordinated amines (Greenwood & Earnshaw 1997). This is supported by shorter bond lengths in the cobalt complex (table 5). For example, the water molecule bound to nickel has a bond length of 2.201(5) Å, considerably longer than in the cobalt complex (1.970(9) Å), which is comparable to the longest primary amine-cobalt bond.

In both complexes, two primary amines form tight bonds (Table 5, M-N III/IV), while the third is weaker (Table 5, M-N II). The tertiary amine atom in the cobalt complex is tightly bound (1.918(6) Å), more so than any

primary amines, whereas in the nickel complex it is more weakly bound (2.094(6) Å). The nitrate is more strongly bound than the primary amines in the cobalt complex, but weaker in the nickel complex. Complexation of cobalt to TAEA caused a visible colour change from pink to dark red, indicating increased crystal field splitting and a low-spin 3d⁶ configuration. This suggests strong metal–ligand bonding and a high activation energy for ligand exchange, potentially limiting cobalt desorption at low pH.

Attempts to crystallize the ligand together with lanthanide metal nitrate (Sm³⁺, Dy³⁺) lead solely to the crystallization of N(C₂H₄NH₃)₃](NO₃)₃. The obtained structure of which was identical to the structure previously reported (Bazzicalupi et al. 2009). These structures show that the sorption mechanism between late transition metals Co/Ni is principally different from that of lanthanides. The exact mechanism for lanthanide adsorption onto TAEA-modified cellulose is unknown. However, an argument can be made that the uptake may involve retention of either the hydrated cations or hydroxide forms. An additional argument for this was provided in the work of Bhunia et al. (2013), where the structures of several mixed-ligand complexes of Ni(II) and REE(III) with TAEA and Schiff base carboxylates were reported. In a competition between carboxylate and amino ligands the Ni(II) cations were binding exclusively to nitrogen atoms in TAEA and REE cations to the carboxylate oxygen atoms, in line with Pearson’s hard and soft acid-base theory (Pearson 1963).

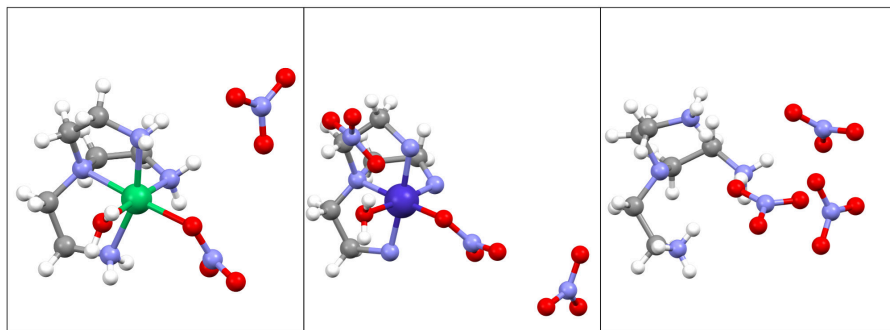
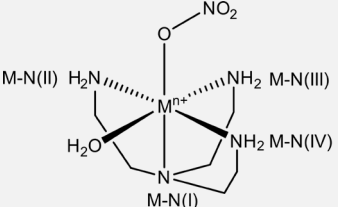


Figure 31. Single crystal structure of [Ni(II)(TAEA)(H₂O)(NO₃)]NO₃ (left), [Co(III)(TAEA)(H₂O)(NO₃)](NO₃)₂ (middle) and [N(C₂H₄NH₃)₃](NO₃)₃ (right, reproduced from Bazzicalupi et al. 2009).

Table 5. Metal-coordinate atom bond length table for hydrated Ni/Co-TAEA nitrate complexes. Where N(I) denoted the tertiary amine, N(II) denotes the back-left primary amine, increasing count in a clock-wise fashion.

	Co	Ni	
M-N(I, tertiary)	1.919(6)	2.095(6)	
M-N(II, primary)	1.966(9)	2.109(6)	
M-N(III, primary)	1.938(10)	2.072(6)	
M-N(IV, primary)	1.930(12)	2.085(6)	
M(I)-O(NO₃)	1.924(5)	2.101(5)	
M(I)-O(H₂O)	1.970(10)	2.201(5)	

3.2 Cellulose as a matrix for nanoparticles

Celluloses come in many different shapes and size, depending on their source and treatment (fig. 32). Each have their own unique physical properties. Cellulose may be chemically modified for tailored applications such as metal adsorption or to increase affinity for various nanoparticles. This allows for many variations of composites to be prepared with tailored chemical and physical properties. Herein three examples based on biocompatible metal oxide nanoparticles will be discussed.

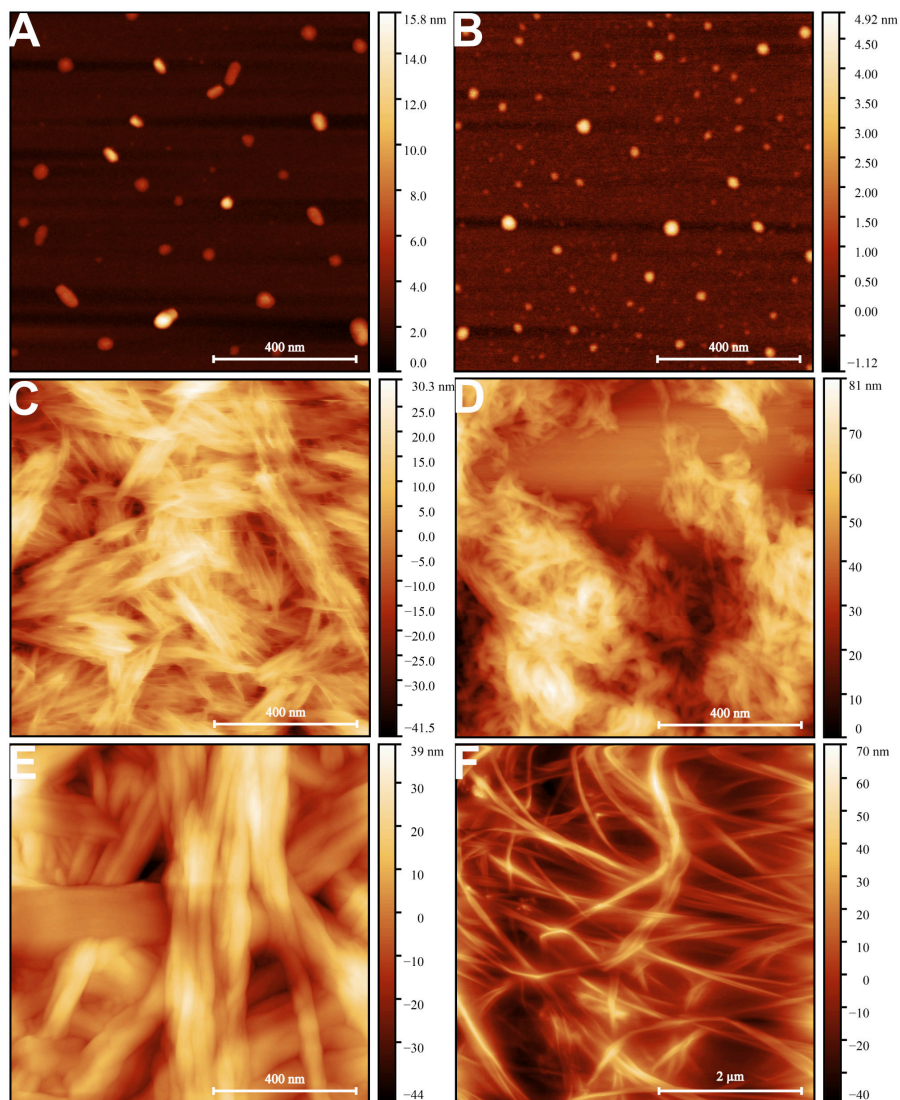


Figure 32. AFM images (not published) of various cellulose morphologies depending on source and treatment. (A) whatman filter paper (64 wt% H_2SO_4 , 45°C, 45 min), (B) Cotton regenerated from cupramonium (64 wt% H_2SO_4 , 45°C, 45 min), (C) Cotton (64 wt% H_2SO_4 , 45°C, 45 min), (D) Filter paper regenerated from cupramonium (20% H_2SO_4 , 70°C, 60 min), (E) Air-dried bacterial nanocellulose, (F) Supercritically dried bacterial nanocellulose.

3.2.1 Ceria / CeO₂

Many nanoparticles are capable of producing reactive oxygen species (*e.g.* TiO₂, Fe₃O₄, Ag) proposed to contribute to their cytotoxicity (Marano et al. 2011). Ceria or cerium(IV) oxide is generally considered to be a biocompatible material with low toxicity (Roberta et al. 2021). It has been widely used in redox catalysis due to the ability of cerium ions to switch between Ce³⁺ and Ce⁴⁺ oxidation states, forming tuneable nonstoichiometric oxides (Montini et al. 2016). Ceria reacts with biologically relevant reducing agents and has the ability to quench reactive oxygen species, protecting against oxidative stress (Karakoti et al. 2010), which make it an interesting oxide for biological applications.

Ceria nanoparticles were produced via the precipitation from a cerium(IV) salt in basic media at 80°C, leading to the formation of the cerianite-ceria with a fluorite crystal structure (fig. 33). Incorporation of CNC modified with 1,2,3,4-butanetetracarboxylic acid (BTCA) into the reaction media did not affect the resulting phase of ceria oxide produced. It did however influence the morphology of the final product. When incorporating pre-formed, dry ceria particles into a BTCA modified CNC suspension the product was formed with large ceria aggregates unevenly distributed over the surface. In-situ formation of ceria nanoparticles, on the contrary, led to a more even distribution of nanoparticles with a small particle size of around 30 nm in diameter (fig. 34).

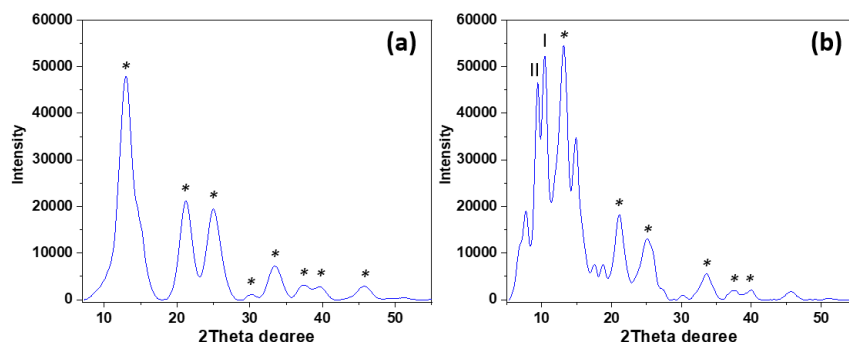


Figure 33. PXRD diffractograms of ceria produced at 80°C (a) and ceria produced in situ in a CNC suspension. The asterisk indicates the characteristic diffraction planes of cerianite-ceria (JCPDS 00-034-0394). Reproduced from Gaio et al. 2022.

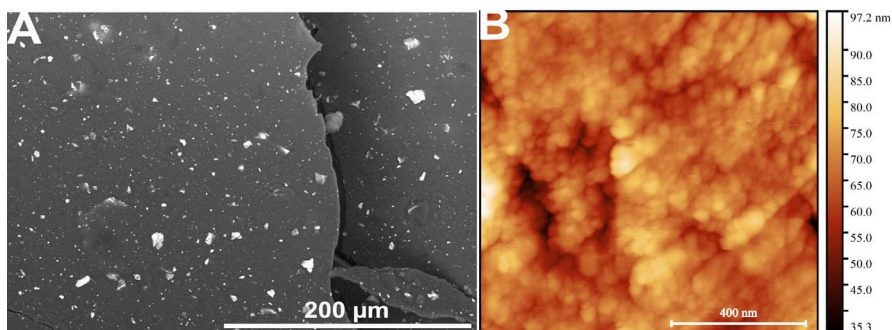


Figure 34. (A) SEM image of CNC/PEG-CeO₂ with 50wt% ceria, (B) AFM image of ceria produced at 80°C in the presence of CNCs.

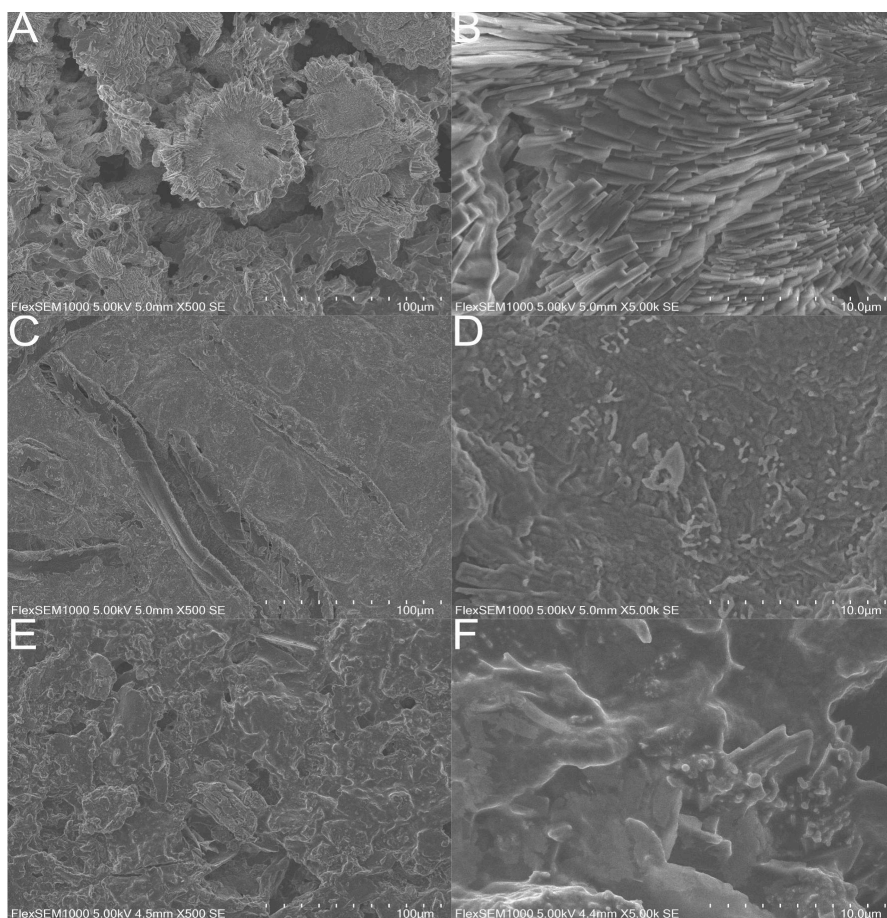


Figure 35. SEM images of CNC/PEG/CeO₂ drug composites containing ampicillin (a, 500x / b 5000x), triclosan (c, 500x / d 5000x) and diclofenac (e, 500x / f, 5000x).

Interestingly, the morphology and surface roughness of the final product was affected by the included pharmaceutical (fig. 35). For two of the pharmaceutical loaded composites (triclosan / diclofenac), the roughness of the surface had increased compared to a film produced with pristine CNCs and CeO₂ nanoparticles (fig 35, C-F). This was attributed to the surface modification of the CNCs by BTCA and the presence of pharmaceuticals affecting the formation of ceria nanoparticles inside the material. More interestingly, some pharmaceuticals like ampicillin (fig. 35, A, B) had a structure directing effect, effectively modulating the growth of ceria, forming plate-like microstructures within the composite material.

Many oxide nanoparticles are capable of forming reactive oxygen species which has been proposed to contribute to their cytotoxicity (Marano et al. 2011). Ceria however can also reduce ROS (Grulke et al. 2014). As the generation of reactive oxygen species by a wound dressing material is undesirable, the photocatalytic activity of CeO₂ produced in the presence of CNC-BTCA at 80°C and a sample sintered at 600°C were investigated by following the decomposition of methylene blue under two different light sources (fig. 36). Low temperature ceria displayed greater methylene blue degradation compared to the sample sintered at 600°C, which was attributed to a larger total surface area for the low temperature sample. Typically, during annealing extensive particle aggregation and crystallite growth occurs, leading to a reduction of active surface area. The overall methylene blue degradation was low with close to 90% of the initial methylene blue remaining after irradiation under a 300W simulated daylight lamp, indicating limited production of ROS.

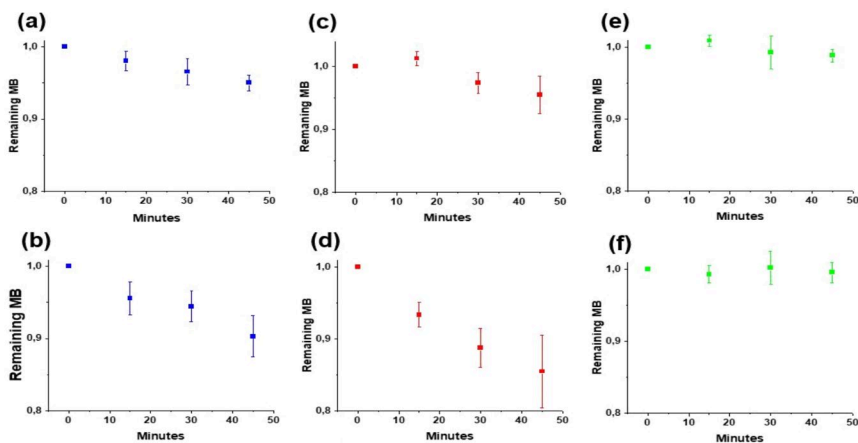


Figure 36. Photocatalytic degradation of methylene blue under a 15W lamp (a) methylene blue, (c) CeO_2 _80C, (e) CeO_2 _600C and under a 300W simulated daylight lamp (b) methylene blue, (d) CeO_2 _80C, (f) CeO_2 _600C. Reproduced from Gaio et al. 2022.

3.2.2 Ferria / Fe_xO_x

Iron oxides are another category of biocompatible metal oxides. They are common in nature due to the abundance of iron in natural environments.

Magnetite is easily formed by the co-precipitation of a 2:1 mol ratio of Fe(III) and Fe(II) by increasing the pH to 9-10, with or without the presence of a cellulose source, such as carboxymethylated cellulose nanofibrils (fig. 37). Initially it is forming a black dispersion, which slowly turns brown with time due to partial oxidation.

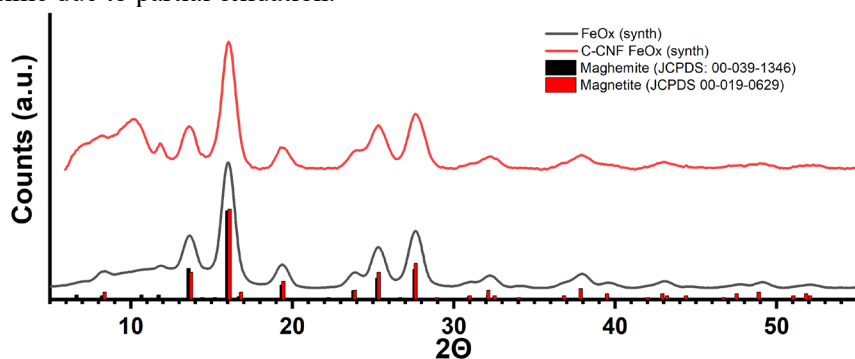


Figure 37. X-ray diffractograms of a synthesized iron oxide – carboxymethylated CNF composite and synthesized iron oxide nanoparticles, measured using a $\text{Mo } k\alpha$ source. JCPDS reference patterns for magnetite (00-019-0629) and maghemite (00-039-1346) overlaid.

The initial X-ray pattern corresponded well to the formation of magnetite/maghemite which are virtually indistinguishable using a Mo-source. One relatively intense reflection at $11.8\ 2\theta$ remained unaccounted for. It did not belong to cellulose Ia, Ib or II, as it was also present in the prepared synthetic magnetite sample (fig. 37). It may belong to the [211] miller index of maghemite, or more probable to ferrihydrite / hydrous ferric oxyhydroxide, a product of iron(III) precipitation.

The magnetization vs magnetic field for the ferria – C-CNF composite (fig. 38, A) showed the measured magnetization at an applied field of 10 KOe to be 63 emu/g and 53 emu/g for the samples in powder and liquid form respectively after 10 months in storage. Both samples exhibited superparamagnetic behaviour at 300K, with zero remanence and coercivity. Both measured magnetization values were smaller than expected for magnetite and maghemite which might be due to partial oxidation that occurred with time. The samples were stored for 10 months before measurements and thus revealed remarkable oxidation stability. The material itself may be processed into magnetic papers, powders or even compressed to form a material reminiscent of pencil rubber (fig. 38, B,C)

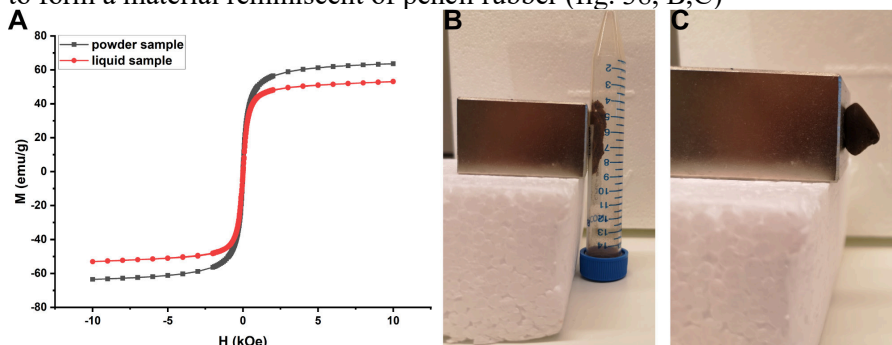


Figure 38. (A) Magnetization vs magnetic field for C-CNF:FeOx in powder and liquid form. (B) C-CNF:FeOx as paper flakes and (C) C-CNF:FeOx compressed and dried.

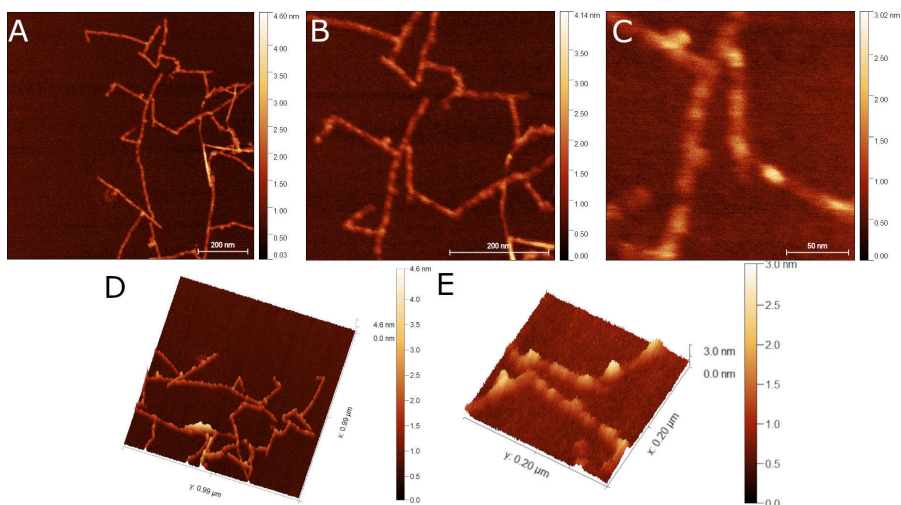


Figure 39. AFM images of an iron oxide – carboxymethylated nanofibril composite. Top-down view at (A) 1x1 μm , (B) 500x500 nm, (C) 200x200 nm. 3D view at (D) 1x1 μm and (E) 200x200 nm.

Examining the nanoscale structures formed when iron oxides were precipitated in the presence of C-CNFs by AFM (fig. 39) and TEM (fig. 40), revealed that the reaction could produce long fibre-like structures with iron oxides decorated along the axis of these fibres. The observed structures had an average width of 18.55 ± 1.66 nm with the length of the fibres ranging from 70 nm to nearly a micrometer. Examination of the composite by TEM without negative staining (fig. 40 & 41) showed the iron oxide – C-CNF network was composed of single fibrils with a cross-section of 3-4.5 nm or double fibrils of 5.5-8 nm as well as strongly scattering elements of 5.5-8 nm distributed along the lateral dimensions of the network. Due to the iron oxide nanoparticles bound to individual carboxymethyl cellulose fibrils, the sample did not require staining with heavy metals to be visible by TEM, as is commonly required.

SEM confirmed that the product was not completely homogeneous; showing some aggregates with iron oxide distributed across the aggregates according to EDS. Embedding these aggregates in resin, cross-sectioning and examination by TEM (fig. 42) suggested a relatively homogeneous structure with some larger iron oxide aggregates precipitated on the surface of the larger fibre aggregates. Broadly speaking, the iron oxides forms could be divided into three categories. Self-assembled fibril structures containing surface-bound iron oxide particles, large iron oxide particles formed on the

surface of C-CNF aggregates and larger C-CNF iron oxide aggregates internally containing very small particles. While the surface adsorbed iron oxide nanoparticles grew into larger size due to Ostwald ripening (5.5-8 nm), the iron oxide nanoparticles encapsulated within remained in the order of 1.5-2.5 nm. Indicating that carboxymethylated cellulose nanofibrils not only allow for the formation of C-CNF-iron oxide network clusters, but it is also effective in retaining iron oxide particle size ranges to a few nanometres.

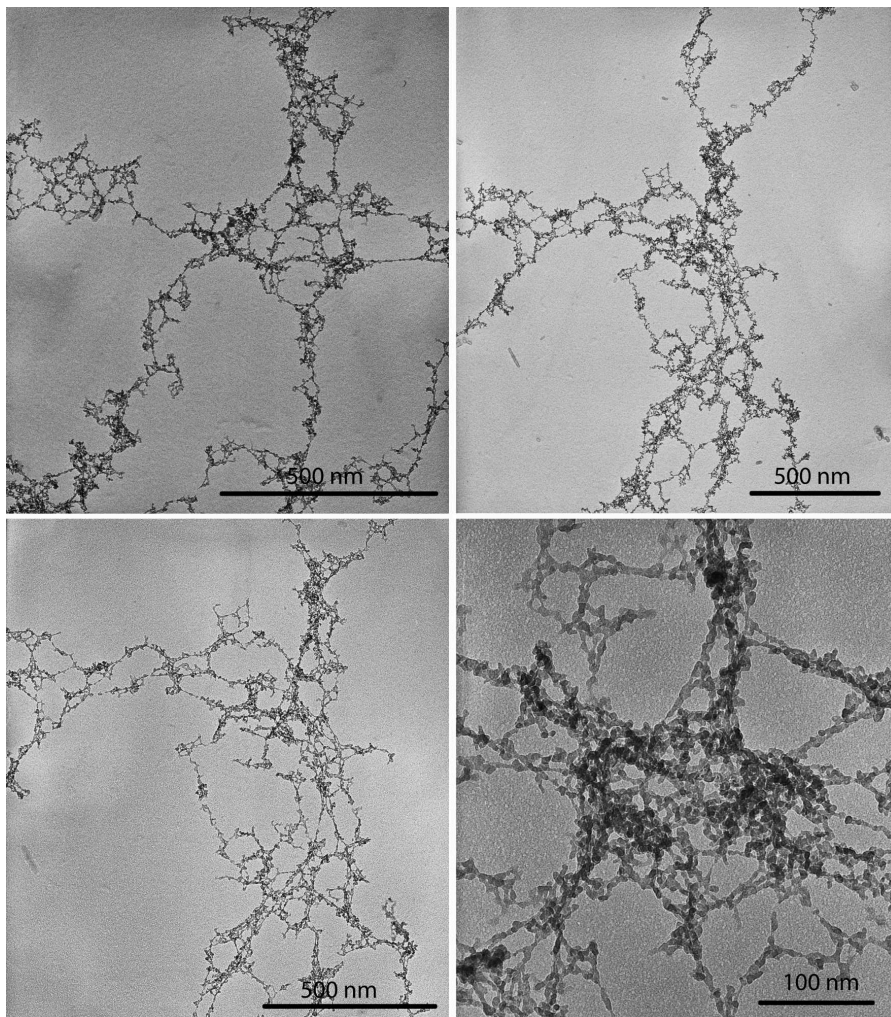


Figure 40. TEM images of iron-oxide carboxymethylated cellulose nanofibril composite without staining and at varying magnification.

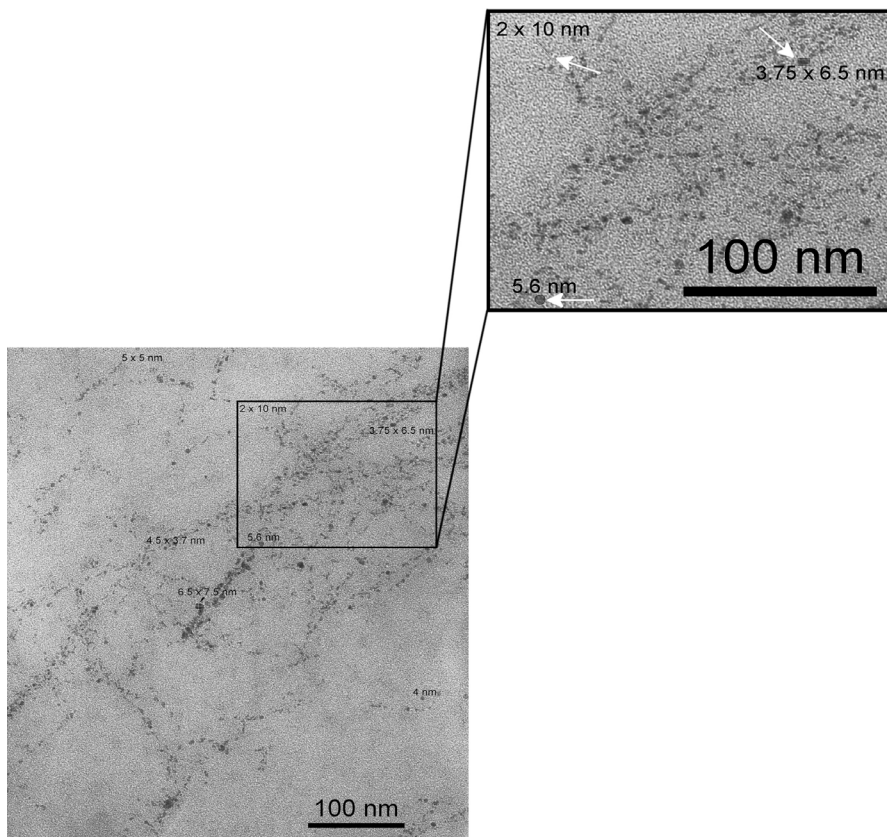


Figure 41. Unstained TEM image of an iron oxide – C-CNF composite. Arrows indicate small iron oxide particles associated with cellulose fibrils and their respective dimensions.

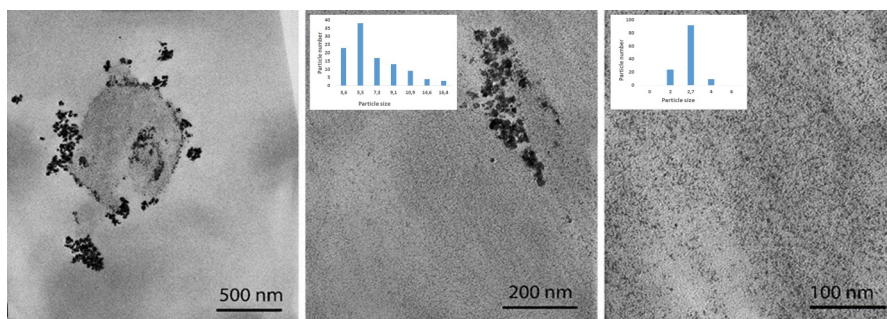


Figure 42. TEM images of a cross-sectioned, resin-embedded iron oxide C-CNF composite. Large aggregates are visible on the surface, while smaller particles appear aligned with the individual fibrils. Inset show particle size distribution in nm.

3.2.3 Titania / TiO_2

The third category of biocompatible metal oxide particles applied was titanium oxide (TiO_2), specifically the anatase phase of titania. The particles in this work were primarily derived from the controlled hydrolysis of a metal alkoxide precursor capped with an easily charged ligand (fig. 8, section 1.2.2, referred to as TATT). Other particles were derived from an equilibrium shift in a water-soluble titania precursor (fig. 9, section 1.2.2, referred to as TiBALDH). These particles were principally different. TATT particles had been shown to induce very strong blood coagulation, (Svensson et al. 2021) which then promotes wound-healing by initiating an immune response (Seisenbaeva et al. 2017). However, there was no coagulation when TiBALDH derived particles were used. The proposed reason for this difference in physiological response related to particle surface capping. In TATT, an easily desorb-able ligand was used which was leaving in aqueous media, producing essentially a “bare” surface of hydrated TiO_2 . TiBALDH-derived particles, however, were capped by lactate. Introducing these particles onto a suitable substrate, such as phosphorylated bacterial nanocellulose (fig. 43), two distinct composites were obtained, with different surface morphologies.

Directly after phosphorylation, the original bacterial nanocellulose fibres were around 65.7 ± 12.8 nm. Introduction of TATT, which were preformed particles around 3-4 nm in size, onto the phosphorylated BNC led to relatively uniform coverage of the cellulose fibres and an increase in fibre thickness to 71.6 ± 6.6 nm (fig. 43 E, F). This was expected, as the added colloid consisted of well-defined pre-formed hydrated TiO_2 nanoparticles, that coordinated to the surface via the introduced phosphate groups. These particles might then also aggregate / gelate to form a product with uniform coverage, without readily distinguishable nanoparticles, though particle aggregates are present. TiBALDH is a water soluble TiO_2 precursor which exists in equilibrium between a tetrameric titanium-oxo species capped by lactate (fig. 9, section 1.2.2) and anatase TiO_2 nanoparticles (Seisenbaeva et al. 2013). This equilibrium can be shifted with the addition of less-polar solvents or charge-compensating ligands. Adding diluted TiBALDH to phosphorylated BNC led to the formation of titania crystallites across the surface (fig. 43 C, D). The surface titania structures were circa 5-10 nm in height in the smaller range and up to 25 nm in the larger range. Length wise the structures were variable, ranging between 30-160 nm.

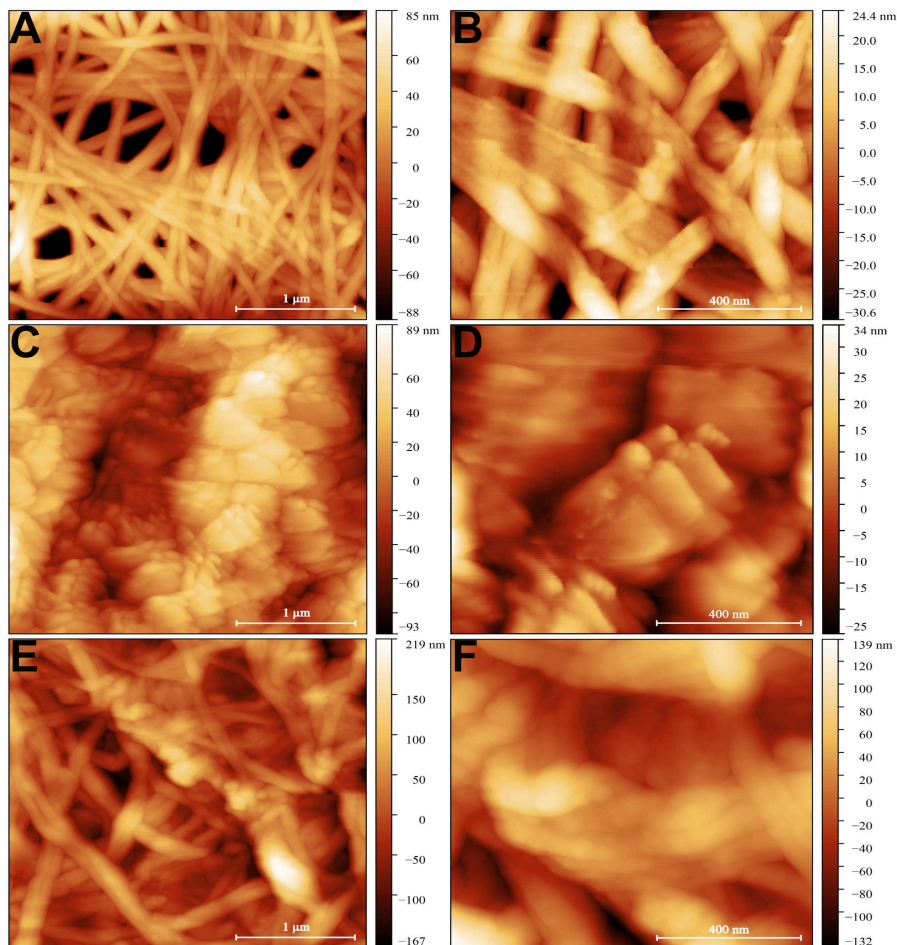


Figure 43. AFM images of phosphorylated bacterial nanocellulose (A, 3x3 μm, B, 1x1 μm), covered by TiBALDH (C, 3x3 μm, D, 1x1 μm) and TATT (E, 3x3 μm, F, 1x1 μm).

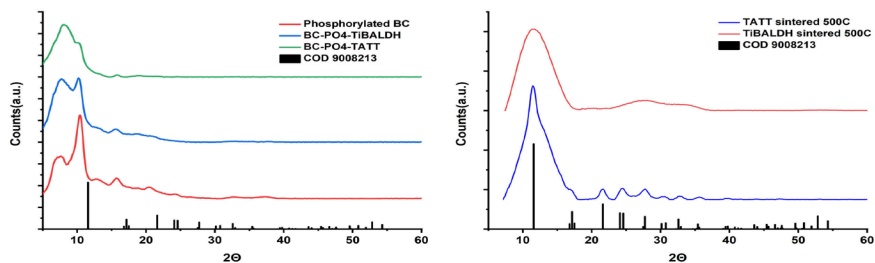


Figure 44. X-ray diffractograms of BNC, phosphorylated-BNC, TATT-covered p-BNC and TiBALDH covered p-BNC (**left**) and TiO₂ composites after sintering at 500°C (**right**).

Initial XRD analysis of the films could not detect the presence of titania, presumably due to the small size of crystalline domains and low titania content. However, after sintering the samples at 500°C, anatase TiO₂ could be detected in both samples (7.5 wt% TiBALDH, 14.5 wt% TATT, fig. 44).

Dried bacterial nanocellulose sheets were produced under static growing conditions and required no processing other than washing, drying and sterilization to provide films suitable as wound dressing materials. The dressings were quite suitable for irregularly shaped wounds as it had high mechanical strength, enabled efficient management of wound exudates as well as allowing for visual wound inspection due to its translucency (Wahid et al. 2021). By modifying the surface of bacterial nanocellulose and introducing titania, composites could be obtained with excellent wound-healing and delayed drug release properties.

The obtained composites (table 6) were tested for cytotoxicity, pseudo-wound healing and cell adhesion. The materials were further examined using fluorescence staining to examine the development of the actin cytoskeleton, which plays a central role during cell migration (Le Clainche & Carlier 2008; Gardel et al. 2010). The development type-I collagen and fibronectin, which are two critical extracellular matrix (ECM) components that contribute to wound healing and tissue regeneration, had been examined (Kanta 2015).

Table 6. Samples tested for cytotoxicity, pseudo-wound healing and cell adhesion assays.

Sample	Nomenclature
1	BNC-PO ₄ ~2.7-4 wt%
2	BNC-PO ₄ ~0.5-1.5 wt%
10	BNC-PO ₄ - TiBALDH
11	BNC-PO ₄ - TATT
30	BNC-PO ₄ - TiBALDH + tetracycline
31	BNC-PO ₄ - TATT + tetracycline
32	dry BNC-PO ₄ - TATT + tetracycline after desorption in citrate buffer
33	dry BNC-PO ₄ - TiBALDH + tetracycline after desorption in citrate buffer
34	BNC wet membrane + 10 mol % 2:1 TiBALDH: AgNO ₃
35	Cotton cellulose nanocrystals + 10 mol% 2:1 TiBALDH:AgNO ₃

The functionalized BNC films showed no toxicity towards both L929 murine fibroblasts and SaOS-2 osteoblast-like cells, maintaining high cell viability above 85% (fig. 45). Phosphorylated BNC showed no decrease in cell viability for L929 Murine Fibroblasts, regardless of phosphate content. However, high phosphate content (2.7-4 wt%) did contribute to a slight decrease in cell viability for osteoblast-like SaOS-2 cells. Covering the phosphorylated BNC with TiO₂ (either TATT or TiBALDH) maintained cell viability close to 100%. This indicated that both these base composites were non-cytotoxic.

Covering TiO₂ derived from TATT with the broad-spectrum antibiotic tetracycline led to a decrease in cell viability. Interestingly, the TiBALDH derived product displayed no such behaviour despite similar drug loading (41.4 ± 4.8 mg TATT / 46.5 ± 2.2 mg/g TiBALDH). After desorption in citrate media however, the cell viability for the TiBALDH derived composite loaded with tetracycline did decrease slightly, while for the TATT derived composite it remained the same.

Previously it was reported that BNC/TiO₂ composites accelerated wound closure in an *in-vivo* model, while pure BNC did not exhibit this behaviour (Khalid et al. 2017). This was clearly demonstrating that the introduction of TiO₂ (and presumably other similar oxides) into these types of composites could have beneficial effects towards wound healing. To evaluate the produced composites for their wound-healing capabilities, samples were prepared and the pseudo-wounds produced. The principle of this method was based on the creation of a 500 μ m gap (i.e. pseudo-wound) on a confluent cell monolayer, after which the cells at the edge of the artificial wound start migrating into the cell-free area, forcing cell-cell contacts.

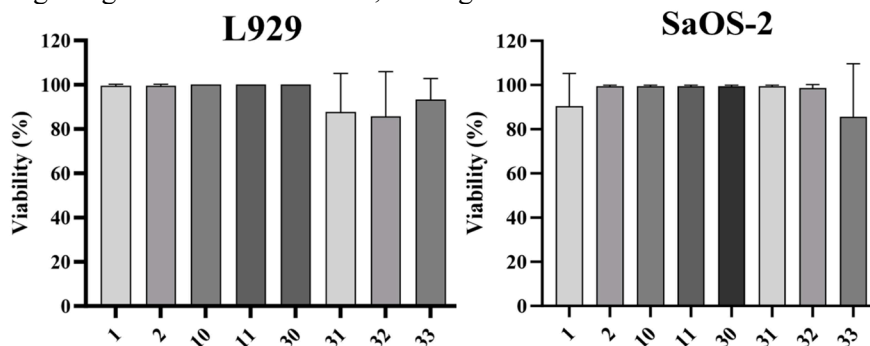


Figure 45. Cell viability of L929 murine fibroblasts and SaOS-2 osteoblast-like cells upon contact with eluates from functionalized BNC samples.

The cell area coverage was determined at different time and compared to a positive control of simple media (fig. 46). Of the samples tested, the low phosphate (0.5-1.5 wt% P), TATT-covered, TiBALDH-covered and TiBALDH-tetracycline covered BNC samples had a positive effect on L929 cell migration. Enabling 100% pseudo-wound closure within 24 hours. Contrary to this, the TATT-tetracycline sample had a negative effect on cell migration for L929 murine fibroblasts, which can be associated to its increased toxicity towards these cells. Similarly, after desorption in citrate media the TiBALDH-tetracycline covered sample (table 6, #33) displayed a negative effect on pseudo-wound closure for L929 murine fibroblasts, which can be associated to the decrease in cell-viability. For SaOS-2 osteoblast like cells only the TATT (table 6, #10) and TiBALDH-tetracycline (table 6, #33) promoted wound-closure within 24-hours.

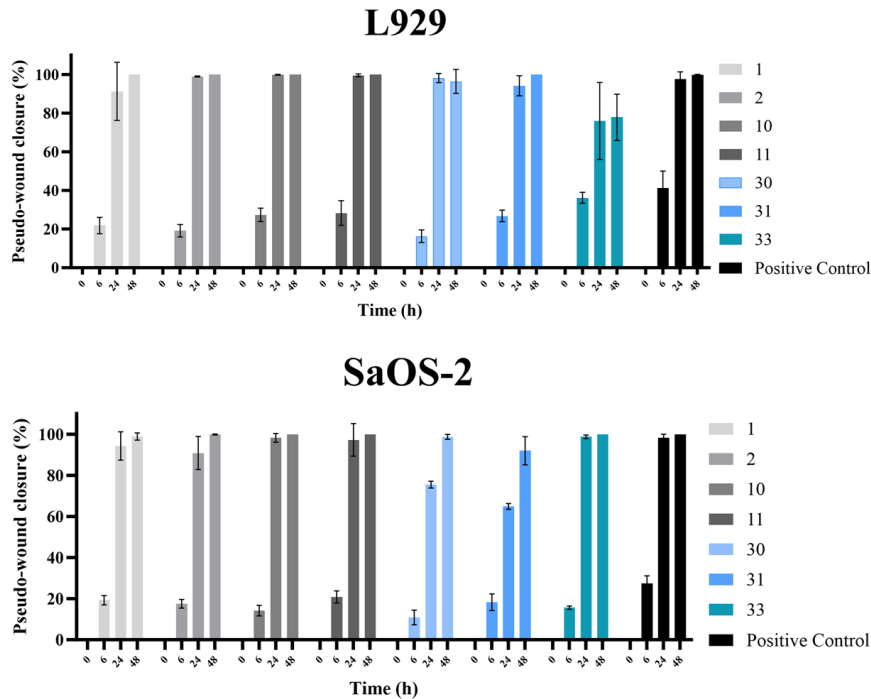


Figure 46. Effect of functionalized BNC composites on migration of L929 murine fibroblasts and SaOS-2 osteoblast like cells by evaluating the pseudo-wound closure at 0, 6, 24 and 48 hours.

This is quite interesting as covering p-BNC with either TiBALDH (table 6, #10) or TATT (table 6, #11) had a positive effect on L929 cell migration, indicating that the material is quite beneficial for wound-healing applications involving these types of cells. For osteoblast-like SaOS-2 cells however, only the TiBALDH covered sample (table 6, #10) had any beneficial effect. Covering BNC-TATT with tetracycline (table 6, #31) negatively influenced pseudo-wound healing, which can be tied to its increase in cell toxicity. Covering BNC-TiBALDH with tetracycline (table 6, #30) had a positive effect towards fibroblasts but lost its positive effect towards osteoblasts. Curiously, allowing the BNC-TiBALDH-Tetracycline sample to desorb in citrate media (table 6, #33) causes it to exhibit a negative effect on wound healing for fibroblasts, while simultaneously displaying a positive effect for osteoblasts once more. The reason for this behaviour is yet unknown and requires further investigation.

Adhesion is the first response of a cell when it encounters a (bio-) material. It plays an essential role in the regulation of the subsequent biological behaviour of the cell. During the cell adhesion process, cells initially sediment to the surface with their spherical bodies. Then, cells flatten mostly via nonspecific interaction and if the surface is suitable, cells spread with focal adhesion maturation and the creation of stable contacts via actin cytoskeleton reorganization.

In the case of the phosphorylated bacterial nanocellulose (table 6, #1, 2) and the titania covered nanocelluloses (table 6, #10, 11), SEM imaging for L929 murine fibroblasts (fig. 47) and SaOS-2 osteoblast-like cells (fig. 48) suggested good attachment, adhesion and proliferation for these cells. High cell spreading and fully developed actin cytoskeletons were also visible.

During cell migration, protrusions are extended from the cell, which establishes adhesion points. The actin cytoskeleton was previously observed to play a central role in this process (Le Clainche & Carlier 2008; Gardel et al. 2010). In addition to actin, type-I collagen and fibronectin, two extracellular matrix components, contribute significantly to wound healing and tissue regeneration (Kanta 2015). Fibronectin is an extracellular matrix component which plays a pivotal role in controlling cell adhesion, spreading, migration, proliferation and differentiation (Parisi et al. 2020). Type-I collagen is the most abundant extracellular matrix component, which provides a scaffold for protein and proteoglycan binding, facilitating cell interactions. To investigate the expression of F-actin, collagen type-I and

fibronectin biomarkers in fibroblast and osteoblast cells, samples were analysed via confocal immunofluorescence. The biomarkers in question were observed (fig. 49, 50 & 51) in both cell lines for phosphorylated BNC (table 6, #2), BNC-TiBALDH (table 6, #10) and BNC-TATT (table 6, #11).

Quantitative fluorescence measurements (fig. 52) demonstrated that phosphorylated BNC significantly increased F-actin expression in both L929 fibroblast and SaOS-2 osteoblast-like cells. Fibronectin and collagen type-I expression however were similar between samples. Though it should be clearly stated that the control sample received 10% Fetal Bovine Serum (FBS) while the examined samples (table 6, #2, #10, #11) received 5%, suggesting that TiO₂ particles derived from TATT or TiBALDH on phosphorylated BCN, as well as pure phosphorylated BNC positively influenced the expression of F-Actin, collagen type-I and fibronectin. Further molecular quantification assays and in-vivo studies would be beneficial to explore the mechanism by which these composites enhance the expression of protein and cytoskeletal markers as well as thoroughly establishing their contribution to tissue regeneration.

L929

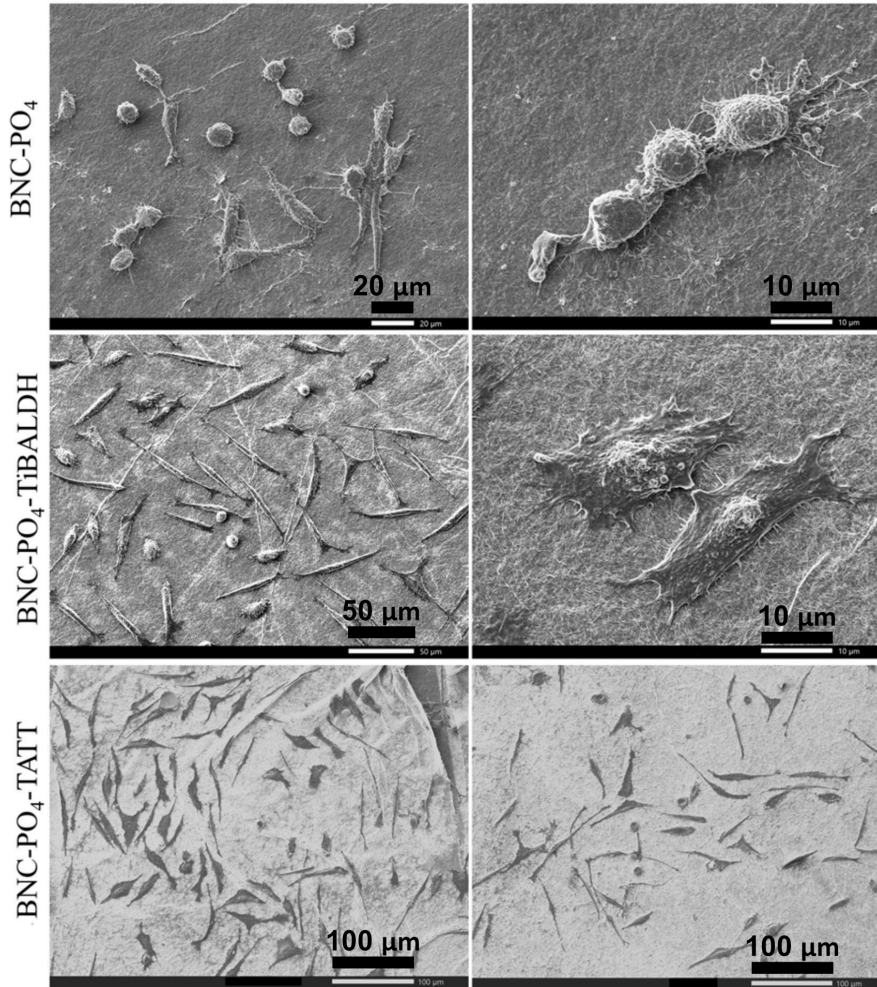


Figure 47. Murine fibroblast L929 cells adhered on various BNC composites after 72h of incubation.

SaOS-2

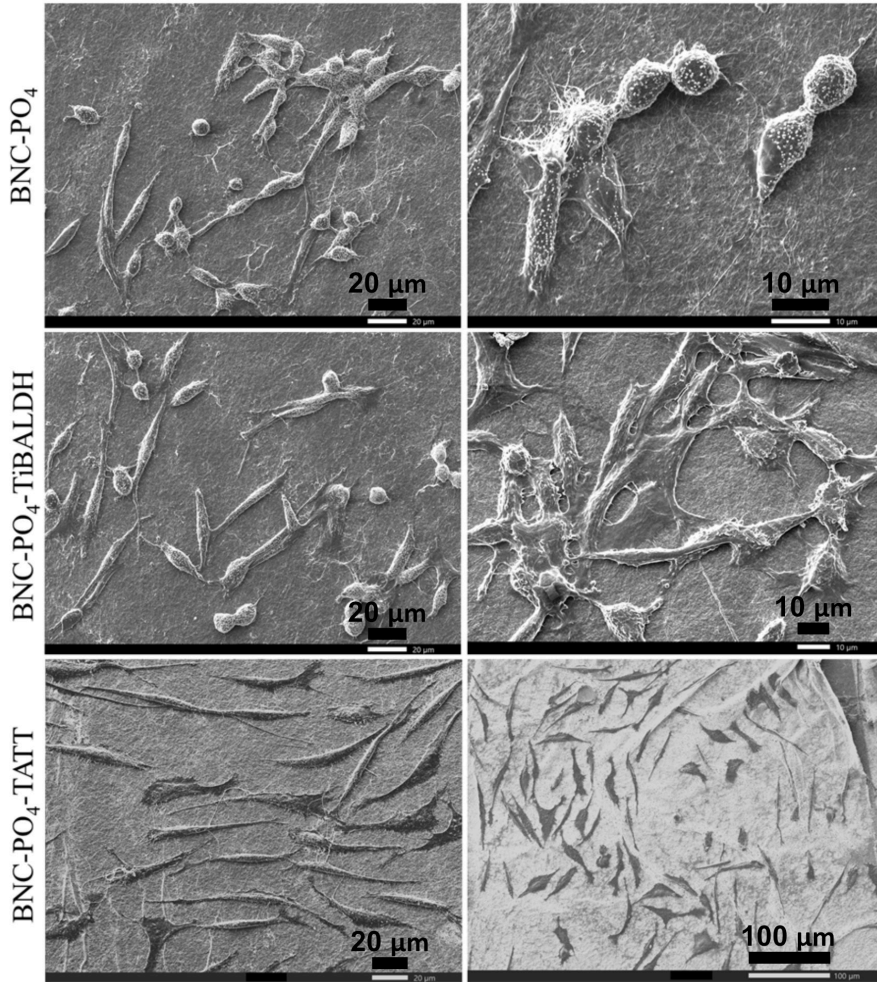


Figure 48. Osteoblast-like SaOS-2 cells adhered on various BNC composites after 72h of incubation.

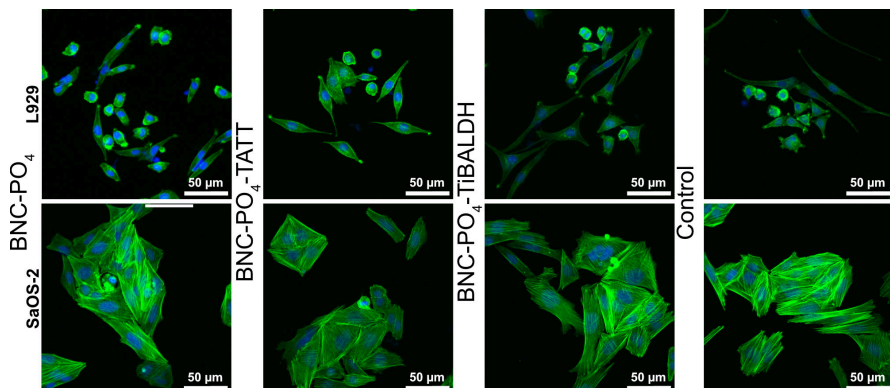


Figure 49. Confocal imaging of murine L929 fibroblasts and SaOS-2 osteoblasts: F-actin (green) was labelled with phalloidin-iFluor 488 (green), and the nuclei (blue) counterstained with DAPI. Fluorescence staining of the actin cytoskeleton was registered on fibroblasts and osteoblasts cultured for 7 days with different eluates from BNC-PO₄, BNC-PO₄-TATT and BNC-PO₄-TiBALDH. Control cells was maintained with only conventional media.

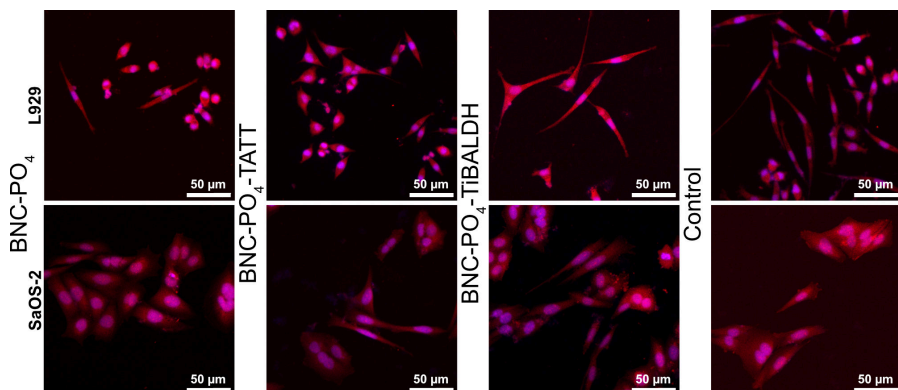


Figure 50. Confocal imaging of murine L929 fibroblasts and SaOS-2 osteoblasts: Type I-Collagen (red) was labelled with Rabbit Recombinant Monoclonal anti-Collagen I conjugated to Alexa Fluor® 594 and nuclei counterstained with DAPI (blue). Fluorescence staining of collagen Type I was registered on fibroblasts and osteoblasts cultured for 7 days with different eluates from BNC-PO₄, BNC-PO₄-TATT and BNC-PO₄-TiBALDH. Control cells were maintained with only conventional media.

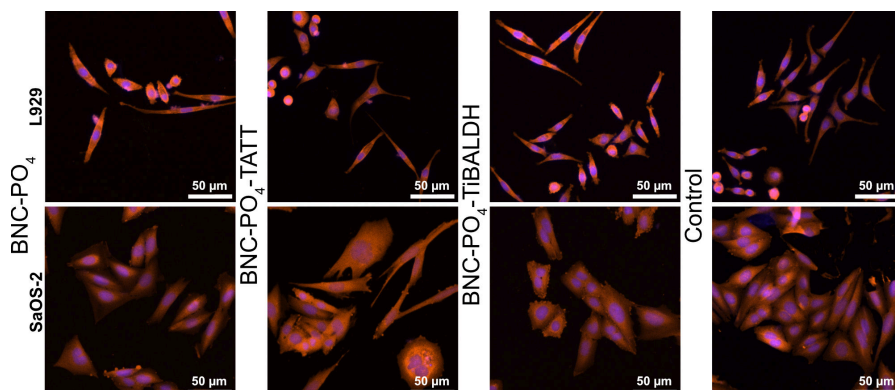


Figure 51. Confocal imaging of murine L929 fibroblasts and SaOS-2 osteoblasts: fibronectin (red) was labelled with Rabbit Recombinant Monoclonal anti-Fibronectin conjugated to Alexa Fluor® 555 and nuclei counterstaining, with DAPI (blue). Fluorescence staining of fibronectin was registered on fibroblasts and osteoblasts cultured for 7 days with different eluates from BNC-PO₄, BNC-PO₄-TATT and BNC-PO₄-TiBALDH. Control cells were maintained with only conventional media.

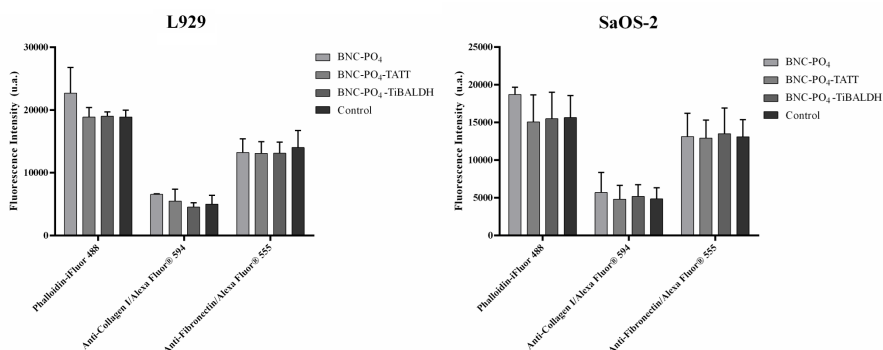


Figure 52. Measurement of fluorescence intensity of F-actin, type-I collagen and fibronectin on L929 fibroblasts and SaOS-2 osteoblasts cultured for 7 days with different eluates from BC-PO₄, BC-PO₄-TATT and BC-PO₄-TiBALDH. Control cells were maintained with only conventional media.

3.2.4 TiO₂ surface structural changes

In the preceding section two sources of titania were explored to uniformly cover the surface of bacterial cellulose for biomedical applications. Here we observed that depending on the source of titania, different surface structures can be obtained. To steer the functionality of the material from drug delivery / wound healing to increasingly theranostic (therapeutic and diagnostic) applications, a photoluminescent Europium(III)-doped composite of phosphorylated BNC covered by TATT was prepared.

To examine the surface changes brought upon the composite by the inclusion of Eu³⁺-cations, it was examined via AFM at various stages (fig. 53). Here it could be seen, as expected, that the inclusion of Eu³⁺ (10 mol% based on P) has no noticeable influence on the morphology of the phosphorylated fibres (fig. 53 D-F). There was however a noticeable difference between phosphorylated BNC fibres covered by TATT and those doped with Eu³⁺ before covering with TATT. Solely covering with TATT led to the uniform covering of the fibres as demonstrated in the preceding section and visible in figure 53 G-I. When covering Eu³⁺-doped phosphorylated BNC with TATT there was a noticeable change in surface morphology (fig. 53 J-L). The inclusion of Eu³⁺ led to the appearance of 16.6±5.0 nm (n=28) TiO₂ agglomerates on the surface of the fibres, while retaining an otherwise similar microscale surface structure.

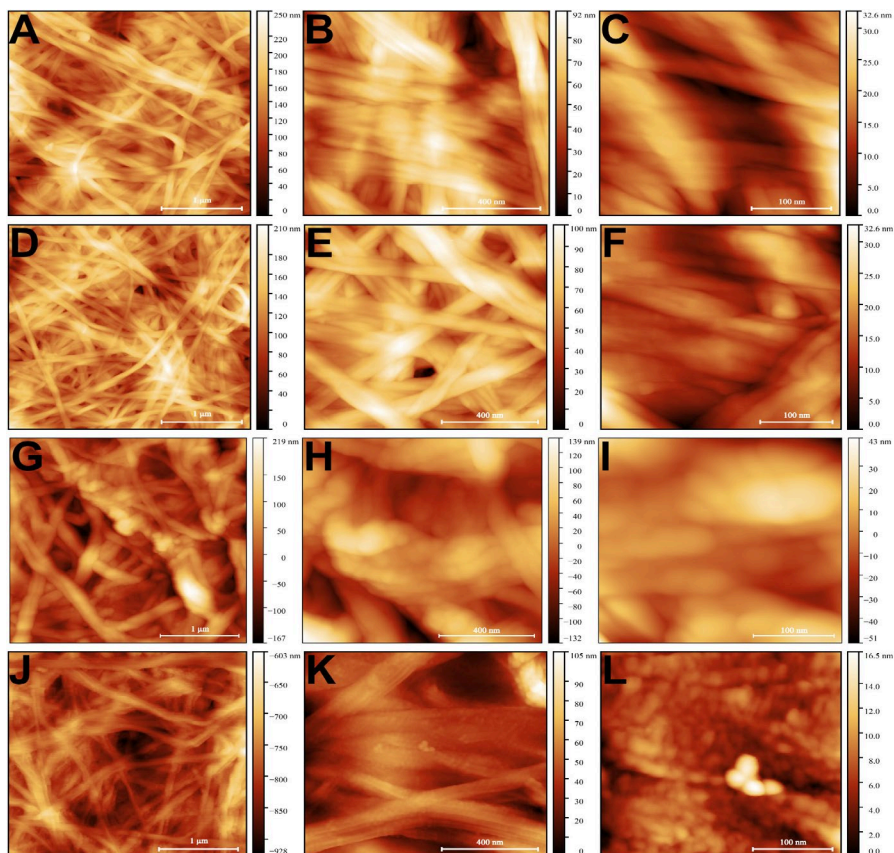


Figure 53. AFM images of BNC-PO₄ (A: 3x3 μ m, B: 1x1 μ m, C: 300x300 nm), BNC-PO₄-Eu (D: 3x3 μ m, E: 1x1 μ m, F: 300x300 nm), BNC-PO₄-TATT (G: 3x3 μ m, H: 1x1 μ m, I: 300x300 nm) and BNC-PO₄-Eu-TATT (J: 3x3 μ m, K: 1x1 μ m, L: 300x300 nm).

Exposing the titania surface to pharmaceuticals had an interesting effect on the observed surface morphology, which was dependent on the pharmaceutical used. With the hydrothermal adsorption of ciprofloxacin, a broad-spectrum antibiotic, the microscale morphology of the fibres remained largely preserved, though at the nanoscale the previously observed aggregates were no longer as clearly defined (fig. 54 A-C). The visible aggregate's size had increased to 25.2 ± 12.7 nm ($n=18$), with the fibre width increased to 86.8 ± 27.8 nm ($n=27$). This indicated that ciprofloxacin had largely spread uniformly across the surface, though likely forming local precipitates along the length of the fibre. A possible mechanism for the initial coordination to the titania surface involved coordination of the ring carbonyl

and a carboxylic oxygen to the metal centre (fig. 55), which was a motif commonly observed in many quinolone-metal complexes, including for Eu(III) (Turel 2002; Čurman et al. 2008). On a metal oxide surface it might instead involve both oxygen atoms in the carboxylic group and a metal-OH₂-site hydrogen-bonding with the adjacent carbonyl (Paul et al. 2012; Gu et al. 2015). After initial coordination it might then further precipitate via π - π or H-bonding interactions. Comparing this then with tetracycline-covered fibres, it appeared that tetracycline largely precipitated directly on the surface and obscured the original fibre morphology (fig. 54 D-F). Coordination to the oxide surface in tetracycline was more complicated, for divalent metal ions, coordination via the kenolate (C11-C12) could be observed (Palm et al. 2008) but additional coordination modes are probable, via O₁-O_{amide}, O₁-O₁₂ for example (Marcial et al. 2011). On titania, the coordination usually proceeds via phenoxide oxygen atoms connected to C10 and C12, potentially also C11 (Galkina et al. 2015).

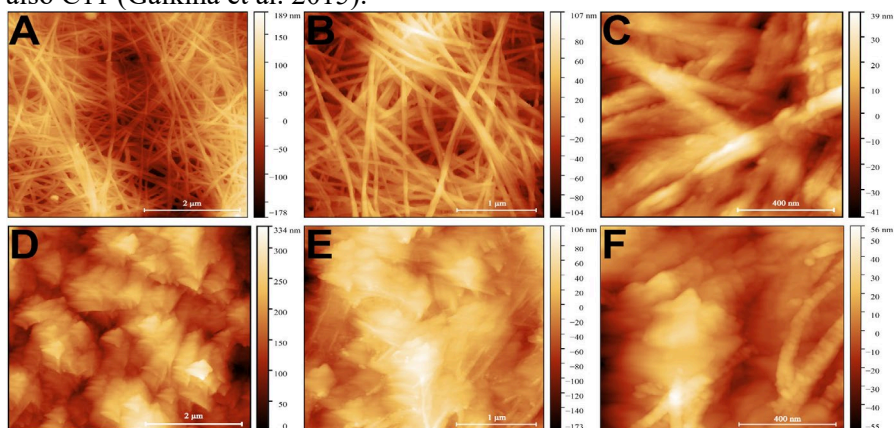


Figure 54. AFM images of BNC-PO₄-Eu-TATT covered by ciprofloxacin (A: 5x5 μ m, B: 3x3 μ m, C: 1x1 μ m) and tetracycline (D: 5x5 μ m, E: 3x3 μ m, F: 1x1 μ m).

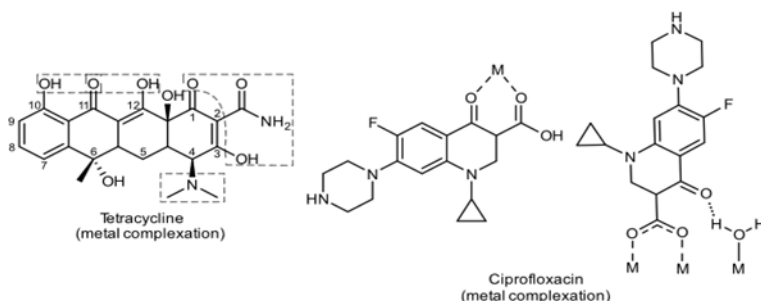


Figure 55. Likely surface coordination species formed by ciprofloxacin and tetracycline

Equilibrating the TATT/drug-covered samples in citrate media at pH 6 had a remarkable, but predictable effect on the surface morphology. As Titanium (IV) was known to form water soluble complexes with citrate and lactate which were quite biocompatible (Groenke et al. 2012; Engelberg et al. 2020). This was important to realise as in both blood (1-2 mM) and sweat (5-40 mM) lactic acid is a constituent that cannot be ignored (Decker & Rosenbaum 1942; Baker 2019), nor can citric acid in blood be completely ignored (50-120 μ M) (Nielsen & Sørensen 1981). Observed in figure 56, equilibration in citrate media removed part of the titania coating, leading to the desorption of pharmaceuticals. A similar effect was observed when using lactic acid. With tetracycline some aggregates remained visible.

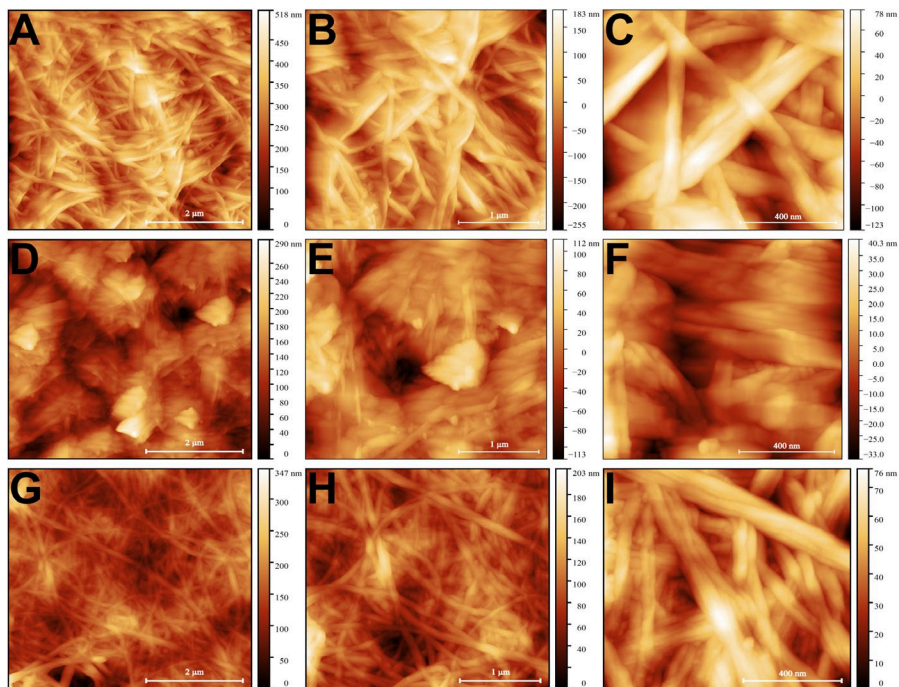


Figure 56. AFM images of citrate-desorbed BNC-PO₄-Eu-TATT covered by ciprofloxacin (A: 5x5 μ m, B: 3x3 μ m, C: 1x1 μ m) and tetracycline (D: 5x5 μ m, E: 3x3 μ m, F: 1x1 μ m) and citrate-desorbed BNC-PO₄-Eu-TATT (G: 5x5 μ m, H: 3x3 μ m, I: 1x1 μ m).

Under physiological conditions, other ions and coordinating ligands are present. In an attempt to simulate such conditions a BNC-Eu-TATT composite was stored in simulated body fluid, a complex mixture of salts, with an ion concentration similar to human blood plasma (Marques et al. 2011). SBF was originally developed to mimic surface structural changes that occurred *in vivo* in (bio)glass ceramics by formation of a hydroxyapatite film on the ceramics (Kokubo et al. 1990). Under these conditions, the fibres were covered by a glassy precipitate, which was likely hydroxyapatite, which obscured much of the fibre morphology (fig 57 A-C).

As the material was designed as a dermal dressing, a solution was prepared to mimic human sweat, containing a high amount of lactic acid (25 mM) as well as 1 mM calcium and 0.2 mM phosphate. Under these conditions, a precipitate will still form on the surface, though much of the original fibre morphology is maintained, likely due to the presence of lactic acid (fig 57 D-F).

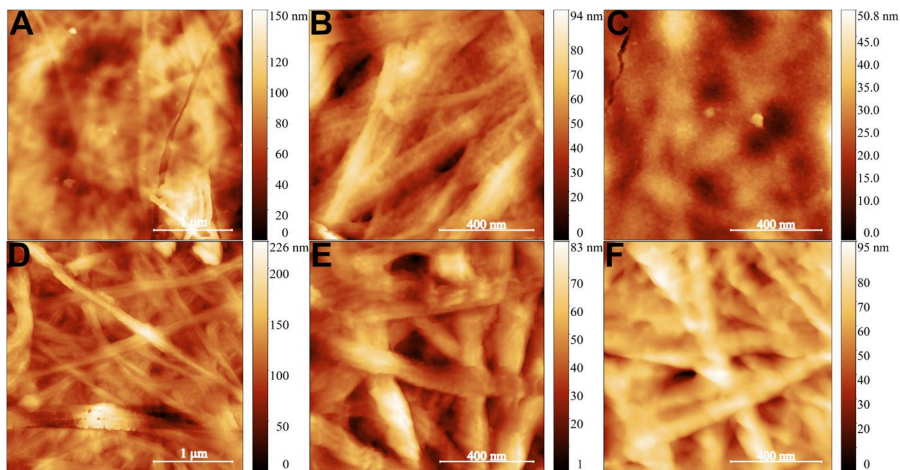


Figure 57. AFM images of BC-PO₄-Eu-TATT after storing for 24 hours in simulated body fluid (A: 3x3 μm, B: 1x1 μm, C: 1x1 μm) or simulated human sweat (D: 3x3 μm, E: 1x1 μm, F: 1x1 μm).

3.3 Controlled release of pharmaceuticals

A purpose in creating cellulose-metal oxide hybrid materials was for the delayed release of pharmaceuticals, such as antibiotics, in dermal wound-dressing materials. Nominally, when a source of cellulose, like CNFs, are mixed with pharmaceuticals there is some expected adsorption onto the accessible surface area, particularly along the flat face (fig. 58) of a microfibril for hydrophobic pharmaceuticals. This may find some use when using essentially elementary fibrils (3.5 nm / ~18 chain) (Lombardo et al. 2018). Using thicker cellulose sources such as BNC (10-50 nm) however quickly limits the accessible surface area.

Another downside of using pure cellulose is the rapid release of pharmaceuticals when exposed to a desorption medium due to the poor affinity of many pharmaceuticals towards cellulose (Löbmann & Svagan 2017). Here, there is a rapid release of pharmaceutical agent into the wound environment, which may have localized cytotoxic effects as well as limiting the effect duration. A potential way of reducing drug release rate is via complexation with metals/metal oxides to form hydrolytically stable complexes, as shown in the following sections.

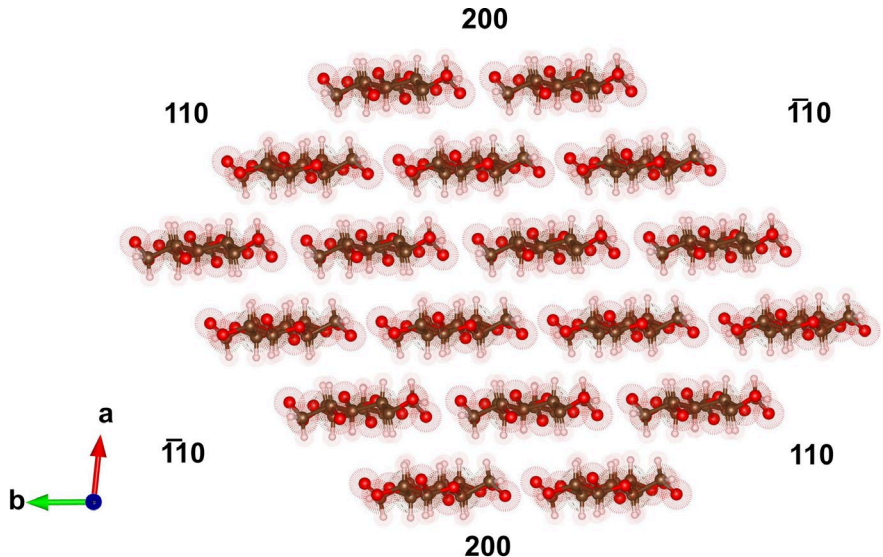


Figure 58. Cross-section of an 18-chain CNF model.

3.3.1 Controlled release via daylight

Magnetite / maghemite nanoparticles were not only of interest due to their magnetic properties, but also due to their optical properties. They are known to display photo-thermal conversion (i.e. light to heat conversion) which can be exploited for therapeutic and drug delivery purposes (Sadat et al. 2014; Wang et al. 2014; Estelrich & Busquets 2018; Johnson et al. 2018).

To examine the suitability of the iron-containing CNF composite (discussed in section 3.2.2) for drug delivery, it was initially allowed to equilibrate with the broad-spectrum antibiotic tetracycline (fig 59, left). The adsorption after 72h at room temperature reaching 62 mg/g (139.5 $\mu\text{mol/g}$), with up to 27 mg/g (60.8 $\mu\text{mol/g}$) within the first 4 hours, indicating that tetracycline had affinity towards the iron-containing composite. As the photo-thermal properties of the composites were of interest to control drug release, samples were prepared with tetracycline pre-adsorbed and allowed to desorb in citrate media either in darkness or under the effect of a daylight lamp. It was apparent that samples under daylight displayed significantly increased drug desorption rates compared to the composites remaining in the dark (fig. 59, right). This indicated that the desorption rate of pharmaceuticals could be directly influenced by light. In this example, leading to $\sim 2\times$ (21.6 mg/g vs 42.6 mg/g) the amount of drug released in a 20 hour window.

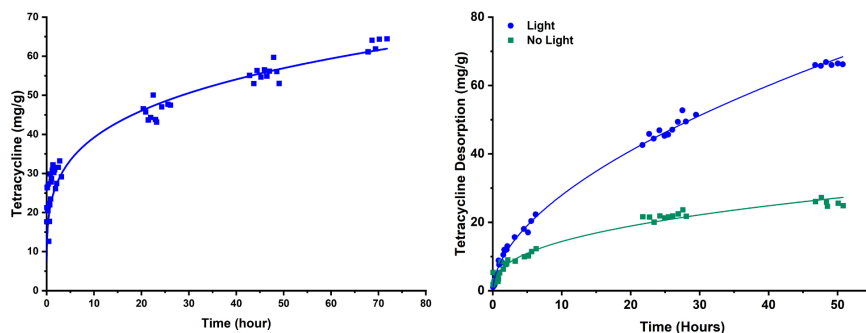


Figure 59. Adsorption of tetracycline at room temperature (**left**) and light-controlled desorption of tetracycline at room temperature (**right**).

3.3.2 Gel Diffusion

In the preceding section, sorption of pharmaceuticals was measured under constant stirring in a low viscosity aqueous system, which principally should have led to rapid release of pharmaceuticals compared to relying on diffusion alone. This would be especially true when there were no strong interactions between composite and adsorbed pharmaceuticals.

From SEM imaging (section 3.2.1 Ceria, fig. 34) it was observed that ampicillin had a structure directing effect for the formation of ceria particles, indicating that there was a reasonably strong interaction between ampicillin and ceria. However, when this composite was placed in isotonic sodium chloride and constantly stirred, ampicillin desorbed rapidly, reaching 85-100% desorption in 15 minutes. This highly dynamic system, with constant stirring led to mechanical washing of the product and weakening of hydrogen bonding in aqueous media.

In gel diffusion experiments, reduced diffusion of pharmaceuticals was measured as effectively the diffusion gradient from the point of contact to the outer edges through a viscous, obstructive media, resembling a skin patch. To examine the antibacterial properties of the ceria containing composites, the inhibitory effect of different materials on the growth of *E. coli* was measured via disc diffusion experiments (fig. 60, left). CNCs when mixed with PEG had a negligible antibacterial activity as expected. The addition of 1,2,3,4-butanetetracarboxylic acid (BTCA) resulted in increased antibacterial activity due to unbound/hydrolysed BTCA (Gaio et al. 2022). In-situ growth of CeO_2 into the preceding product led to a composite with a substantially lower inhibitory effect, likely due to the adsorption of BTCA on ceria via its carboxylic acid groups.

Interestingly, there was a significant difference in inhibitory effect between composites containing the antibacterial agents triclosan and ampicillin, which could be traced to the antibiotic's structure. With triclosan there was a non-significant difference in inhibitory zone, regardless of whether ceria was present. This was likely due to the limited affinity of the phenolic group to the ceria surface. In contrast, there was a significant difference when using ampicillin. Ampicillin appeared tightly bound near the composite, likely due to the carboxylic acid group having better affinity for the surface of ceria compared to phenolic-hydroxyl in triclosan.

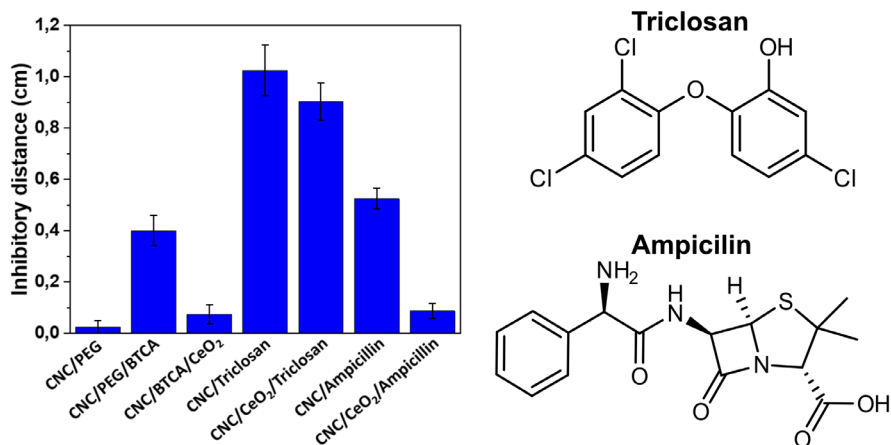


Figure 60. Average inhibitory effect of the different materials (**left**) and structure of tested antibiotics (**right**). CNC/PEG/BTCA/CeO₂, CNC/PEG/BTCA/triclosan, CNC/PEG/BTCA/CeO₂/triclosan, CNC/PEG/BTCA/ampicillin and CNC/PEG/BTCA/CeO₂/ampicillin have been abbreviated in the figure as CNC/BTCA/CeO₂, CNC/triclosan, CNC/CeO₂/triclosan, CNC/ampicillin and CNC/CeO₂/ampicillin.

3.3.3 Surface Ligand competition and Lanthanide Influence

In section 3.2.3 two titania-containing composites derived from TATT and TiBALDH respectively, based on phosphorylated bacterial cellulose were presented. In the view of their different surface capping, any pharmaceutical that adsorbs onto the surface of titania should adsorb easily on TATT and be in competition with lactate on TiBALDH-derived titania.

There were, however, only minor differences in terms of drug adsorption when using the broad-spectrum antibiotic tetracycline. The TATT-derived composite had 46.5 ± 2.2 mg/g (104.6 ± 4.9 μ mol/g) tetracycline adsorbed while the TiBALDH-derived composite had 41.4 ± 4.8 mg/g (93.1 ± 10.8 μ mol/g) adsorbed. Placing the materials into 20 mM citrate buffer led to the desorption of tetracycline, which was followed by UV-VIS spectroscopy (fig. 61). In the case of the TATT, $39.4 \pm 0.2\%$ tetracycline was released within 5 hours, reaching up to $61.4 \pm 1.7\%$ release after 120 hours. For TiBALDH a release of $30.8 \pm 2.9\%$ was measured after 5 hours, reaching $53.3 \pm 2.9\%$ after 120 hours.

Comparing then the previously mentioned tetracycline with ciprofloxacin, another broad-spectrum antibiotic, showed an expected difference in desorption behaviour (fig. 62). Ciprofloxacin desorbed more rapidly than tetracycline and interestingly, the desorption rate in both cases was influenced by the presence of Europium(III) coordinated to phosphorylated bacterial nanocellulose.

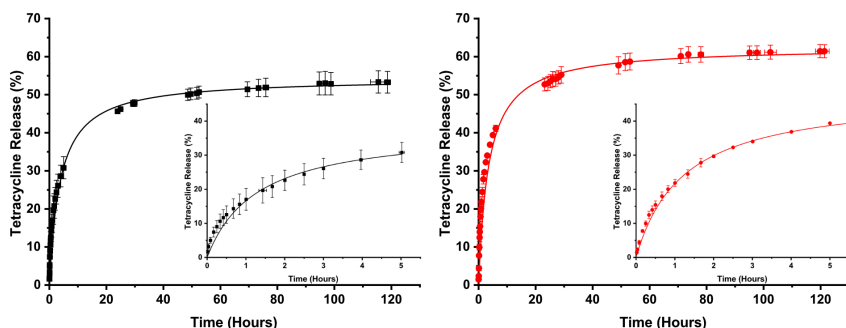


Figure 61. Desorption of the broad-spectrum antibiotic Tetracycline from phosphorylated bacterial nanocellulose sheets covered by TiO_2 derived from TiBALDH (**left**, black) and colloidal triethanolamine terminated TiO_2 (**right**, red).

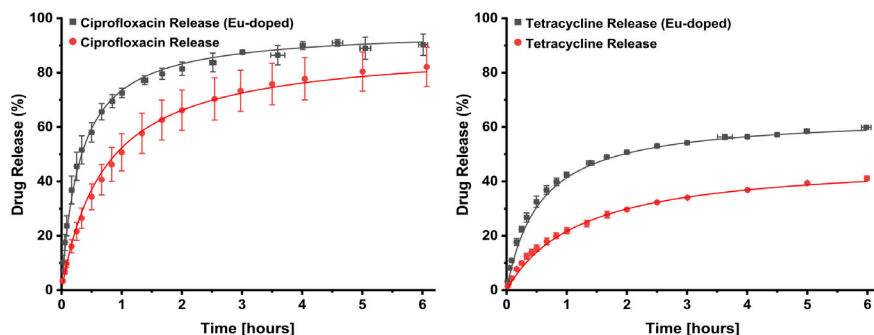


Figure 62. Desorption kinetics of the antibiotics Ciprofloxacin (**left**) and Tetracycline (**right**) from TATT-modified bacterial cellulose with (**black**) and without (**red**) Europium(III) doping.

3.3.4 Photoluminescence

Lanthanides, such as Europium(III) not only affected the desorption behaviour of pharmaceuticals from mineral metal oxide coated composites as shown in figure 62, they were also useful for as photoluminescent trackers. They they emit light after being illuminated. Europium(III) displayed characteristic red emission after stimulation with 393 nm light due to the $^5D_0 \rightarrow ^7F_{2,4}$ transition, which was sensitive to the chemical environment and loading (see fig. 63). Covering with TATT led to a reduction in intensity

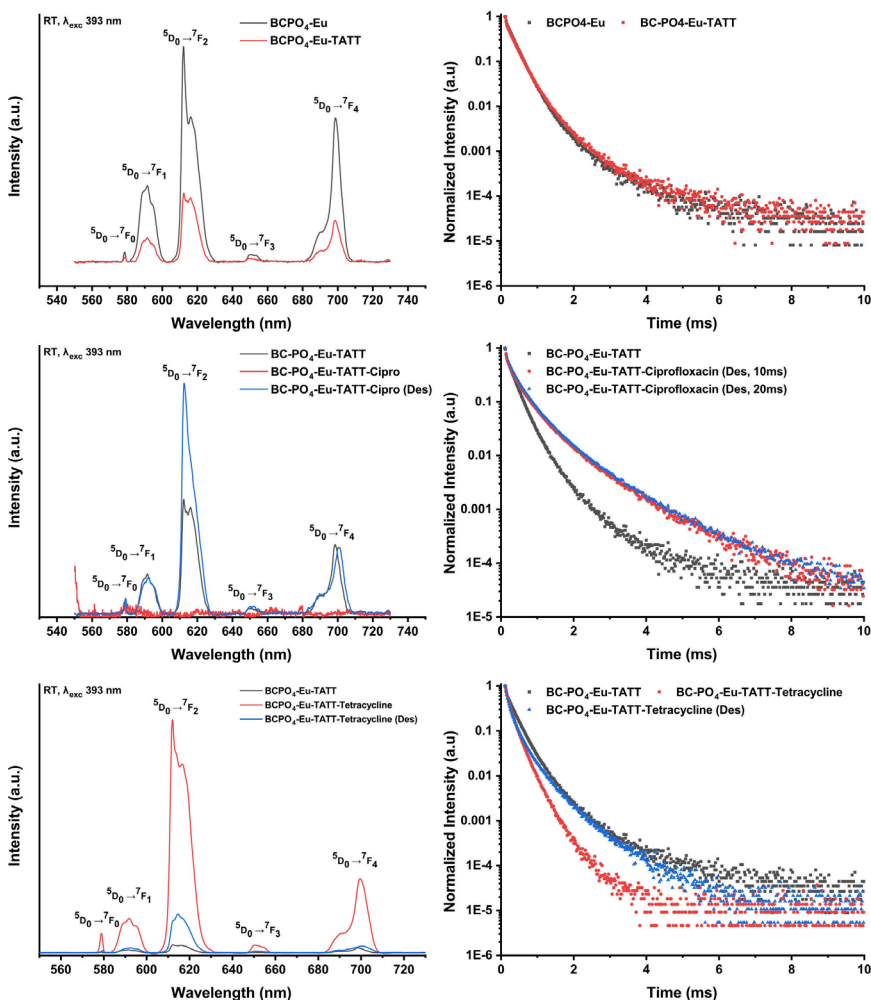


Figure 63. (left) The emission spectra of Eu(III)-doped BNC-PO₄-TATT / drug composites after excitation at 393 nm and (right) decay curves recorded at 393 nm.

without affecting the photo-decay. Adsorption of ciprofloxacin led to complete quenching of photoluminescence, while desorption in citrate buffer led to the re-emergence of photoluminescence. Adsorption of tetracycline led to very intense luminescence compared to TATT covered BNC, which upon desorption was significantly reduced.

As the photoluminescence was so sensitive, its emission could be used as a sensor for pharmaceutical release. In more practical terms this emission could even be observed with the naked eye upon stimulation with common UV-light sources. (fig. 64)

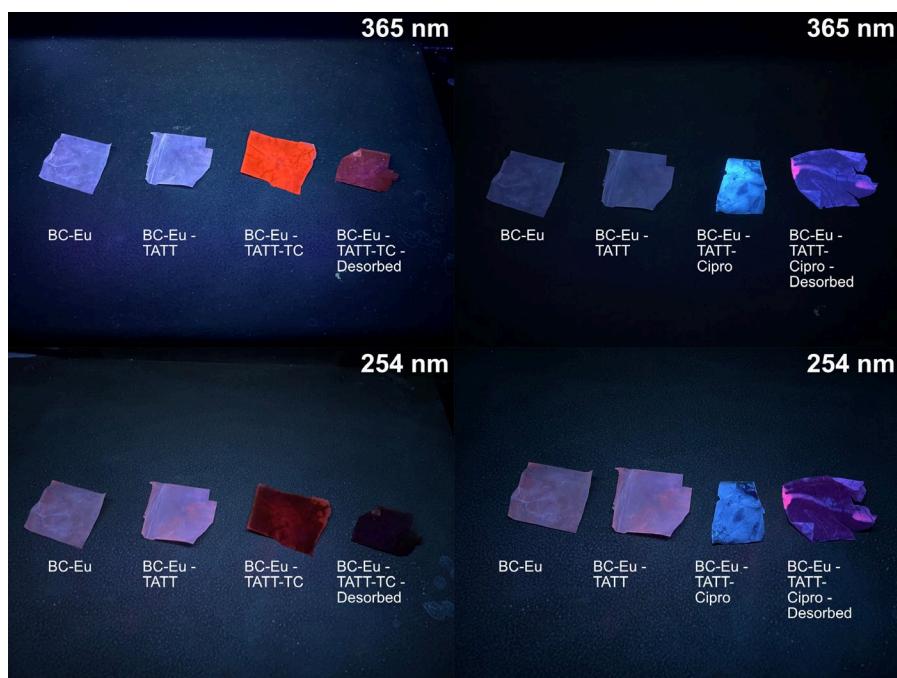


Figure 64. Photoluminescence under UV-irradiation of Eu(III)-doped phosphorylated BNC-Titania composites with tetracycline (**left**) and ciprofloxacin (**right**).

Conclusion and outlook

The work within this thesis was dedicated to the development of new cellulose-based hybrid materials for environmental and theranostic applications. For environmental applications cellulose is an attractive starting material due to its bio-renewable and compatible nature. Herein it's application towards the selective separation of rare earth elements from late transition metals has been demonstrated. Cellulose-metal oxide hybrid materials were investigated for drug delivery applications, revealing fascinating properties depending on substrate and metal oxide used. For magnetite/maghemite, the rate of drug release could be controlled by using daylight, while the inclusion of the photoluminescent cation Europium(III) allowed drug release to be followed visually. This can be useful in clinical settings. Non-cytotoxic metal oxides were demonstrated to enhance cell migration, adhesion, proliferation and the expression of markers related to wound-healing. Demonstrating their potential for promoting tissue regeneration.

I would like to propose several directions for the continuation of this research. (1) Further studies on the sequestration and separation of metals for hydrometallurgical and environmental applications. (2) Combining metal ion-selective cellulose materials with catalysts for environmental remediation via the combined removal of heavy metal ions and persistent organic pollutants. (3) Studies on the environmental, ecological and toxicological impact of the production, use and disposal of cellulose-based hybrid materials should be considered (4) Further in vivo studies on the biocompatibility and wound-healing properties of metal-oxide-nanocellulose based hybrids to assess their long-term safety and performance. (5) Further investigation into the use of photoluminescent particles / cations for tracking drug release and studies on biocompatibility.

The promising potential nanomaterials have for biomedical and environmental applications relate to their high reactivity, surface structure and interference with systems at a molecular level. Combining bottom-up synthesis using well-defined molecular precursors or in-situ formation of nanostructures with natural biopolymers lead to many new and attractive material with interesting properties.

References

- Adeva-Andany, M., López-Ojén, M., Funcasta-Calderón, R., Ameneiros-Rodríguez, E., Donapetry-García, C., Vila-Altesor, M. & Rodríguez-Seijas, J. (2014). Comprehensive review on lactate metabolism in human health. *Mitochondrion*, 17, 76–100. <https://doi.org/10.1016/j.mito.2014.05.007>
- Ait Benhamou, A., Kassab, Z., Nadifiyine, M., Salim, M.H., Sehaqui, H., Moubarik, A. & El Achaby, M. (2021). Extraction, characterization and chemical functionalization of phosphorylated cellulose derivatives from Giant Reed Plant. *Cellulose*, 28 (8), 4625–4642. <https://doi.org/10.1007/s10570-021-03842-6>
- Atalla, R.H. & VanderHart, D.L. (1984). Native Cellulose: A Composite of Two Distinct Crystalline Forms. *Science*, 223 (4633), 283–285. <https://doi.org/10.1126/science.223.4633.283>
- Baker, L.B. (2019). Physiology of sweat gland function: The roles of sweating and sweat composition in human health. *Temperature: Multidisciplinary Biomedical Journal*, 6 (3), 211–259. <https://doi.org/10.1080/23328940.2019.1632145>
- Bazzicalupi, C., Bencini, A., Bianchi, A., Danesi, A., Giorgi, C. & Valtancoli, B. (2009). Anion Binding by Protonated Forms of the Tripodal Ligand Tren. *Inorganic Chemistry*, 48 (6), 2391–2398. <https://doi.org/10.1021/ic8013128>
- Bhunja, A., Yadav, M., Lan, Y., Powell, A.K., Menges, F., Riehn, C., Niedner-Schatteburg, G., Jana, P.P., Riedel, R., Harms, K., Dehnen, S. & Roesky, P.W. (2013). Trinuclear nickel–lanthanide compounds. *Dalton Transactions*, 42 (7), 2445–2450. <https://doi.org/10.1039/C2DT31023F>
- Burchard, W., Habermann, N., Klüfers, P., Seger, B. & Wilhelm, U. (1994). Cellulose in Schweizer's Reagent: A Stable, Polymeric Metal Complex with High Chain Stiffness. *Angewandte Chemie International Edition in English*, 33 (8), 884–887. <https://doi.org/10.1002/anie.199408841>
- Cappiello, F., Casciaro, B. & Mangoni, M.L. (2018). A Novel In Vitro Wound Healing Assay to Evaluate Cell Migration. *Journal of Visualized Experiments*, (133), 56825. <https://doi.org/10.3791/56825>

- Chanzy, H., Peguy, A., Chaunis, S. & Monzie, P. (1980). Oriented cellulose films and fibers from a mesophase system. *Journal of Polymer Science: Polymer Physics Edition*, 18 (5), 1137–1144. <https://doi.org/10.1002/pol.1980.180180517>
- Cole, D.E.C. & Landry, D.A. (1985). Determination of inorganic sulfate in human saliva and sweat by controlled-flow anion chromatography: Normal values in adult humans. *Journal of Chromatography B: Biomedical Sciences and Applications*, 337, 267–278. [https://doi.org/10.1016/0378-4347\(85\)80040-2](https://doi.org/10.1016/0378-4347(85)80040-2)
- Cumpstey, I. (2013). Chemical Modification of Polysaccharides. *ISRN Organic Chemistry*, 2013, 1–27. <https://doi.org/10.1155/2013/417672>
- Čurman, D., Živec, P., Leban, I., Turel, I., Polishchuk, A., Klika, K.D., Karaseva, E. & Karasev, V. (2008). Spectral properties of Eu(III) compound with antibacterial agent ciprofloxacin (cfqH). Crystal structure of [Eu(cfqH)(cfq)(H₂O)₄]Cl₂·4.55H₂O. *Polyhedron*, 27 (5), 1489–1496. <https://doi.org/10.1016/j.poly.2008.01.014>
- Decker, D.G. & Rosenbaum, J.D. (1942). THE DISTRIBUTION OF LACTIC ACID IN HUMAN BLOOD. *American Journal of Physiology-Legacy Content*, 138 (1), 7–11. <https://doi.org/10.1152/ajplegacy.1942.138.1.7>
- Engelberg, N., Bino, A. & Tshuva, E.Y. (2020). Preparation, structural characterization and cytotoxicity of hydrolytically stable Ti(IV) citrate complexes. *Inorganica Chimica Acta*, 503, 119429. <https://doi.org/10.1016/j.ica.2020.119429>
- Estelrich, J. & Busquets, M.A. (2018). Iron Oxide Nanoparticles in Photothermal Therapy. *Molecules*, 23 (7), 1567. <https://doi.org/10.3390/molecules23071567>
- Flechsigg, E. (1883). Ueber Darstellung und chemische Natur des Cellulosezuckers. 7 (6), 523–540. <https://doi.org/10.1515/bchm1.1883.7.6.523>
- French, A.D. (2014). Idealized powder diffraction patterns for cellulose polymorphs. *Cellulose*, 21 (2), 885–896. <https://doi.org/10.1007/s10570-013-0030-4>
- Freudenberg, K. & Braun, E. (1928). Methycellulose. *Justus Liebigs Annalen der Chemie*, 460 (1), 288–304. <https://doi.org/10.1002/jlac.19284600117>
- Fu, Y., Liu, Y., Shi, Z., Li, B. & Pang, W. (2002). Hydrothermal Synthesis and Characterization of Four Oxalatotitanates with Ti₄O₄(C₂O₄)₈ Tetramers as Basic Building Blocks. *Journal of Solid State*

- Chemistry*, 163 (2), 427–435.
<https://doi.org/10.1006/jssc.2001.9422>
- Gaio, S., Svensson, F.G., Breijjaert, T.C., Seisenbaeva, G.A. & Kessler, V.G. (2022). Nanoceria–nanocellulose hybrid materials for delayed release of antibiotic and anti-inflammatory medicines. *Materials Advances*, 3 (19), 7228–7234.
<https://doi.org/10.1039/D2MA00471B>
- Galkina, O.L., Ivanov, V.K., Agafonov, A.V., Seisenbaeva, G.A. & Kessler, V.G. (2015). Cellulose nanofiber–titania nanocomposites as potential drug delivery systems for dermal applications. *Journal of Materials Chemistry B*, 3 (8), 1688–1698.
<https://doi.org/10.1039/C4TB01823K>
- Gardel, M.L., Schneider, I.C., Yvonne Aratyn-Schaus & Waterman, C.M. (2010). Mechanical Integration of Actin and Adhesion Dynamics in Cell Migration. *Annual Review of Cell and Developmental Biology*, 26 (Volume 26, 2010), 315–333.
<https://doi.org/10.1146/annurev.cellbio.011209.122036>
- Greenwood, N.N. & Earnshaw, A. (1997). *Chemistry of the elements*. 2nd ed. Butterworth-Heinemann.
- Groenke, N., Seisenbaeva, G.A., Kaminsky, V., Zhivotovsky, B., Kost, B. & Kessler, V.G. (2012). Structural characterization, solution stability, and potential health and environmental effects of the Nano-TiO₂ bioencapsulation matrix and the model product of its biodegradation TiBALDH. *RSC Advances*, 2 (10), 4228–4235.
<https://doi.org/10.1039/C2RA20388J>
- Grulke, E., Reed, K., Beck, M., Huang, X., Cormack, A. & Seal, S. (2014). Nanoceria: factors affecting its pro- and anti-oxidant properties. *Environmental Science: Nano*, 1 (5), 429–444.
<https://doi.org/10.1039/C4EN00105B>
- Gu, X., Tan, Y., Tong, F. & Gu, C. (2015). Surface complexation modeling of coadsorption of antibiotic ciprofloxacin and Cu(II) and onto goethite surfaces. *Chemical Engineering Journal*, 269, 113–120.
<https://doi.org/10.1016/j.cej.2014.12.114>
- Heise, K., Delepierre, G., King, A.W.T., Kostianinen, M.A., Zoppe, J., Weder, C. & Kontturi, E. (2021). Chemical Modification of Reducing End-Groups in Cellulose Nanocrystals. *Angewandte Chemie International Edition*, 60 (1), 66–87.
<https://doi.org/10.1002/anie.202002433>
- Huang, C.-T., Chen, M.-L., Huang, L.-L. & Mao, I.-F. (2002). Uric Acid and Urea in Human Sweat. *URIC ACID*, 45 (3), 109–116

- Irvine, J.C. & Hirst, E.L. (1922). CLXXXIX.—The constitution of polysaccharides. Part V. The yield of glucose from cotton cellulose. *Journal of the Chemical Society, Transactions*, 121, 1585–1591
- Irvine, J.C. & Hirst, E.L. (1923). LXIV.—The constitution of polysaccharides. Part VI. The molecular structure of cotton cellulose. *Journal of the Chemical Society, Transactions*, 123, 518–532
- Irvine, J.C. & Soutar, C.W. (1920). CLXV.—The constitution of polysaccharides. Part II. The conversion of cellulose into glucose. *Journal of the Chemical Society, Transactions*, 117, 1489–1500
- John Rojas, Mauricio Bedoya, & Yhors Ciro (2015). Current Trends in the Production of Cellulose Nanoparticles and Nanocomposites for Biomedical Applications. In: Matheus Poletto & Heitor Luiz Ornaghi Junior (eds) *Cellulose*. IntechOpen. Ch. 8. <https://doi.org/10.5772/61334>
- Johnson, R.J.G., Schultz, J.D. & Lear, B.J. (2018). Photothermal Effectiveness of Magnetite Nanoparticles: Dependence upon Particle Size Probed by Experiment and Simulation. *Molecules*, 23 (5), 1234. <https://doi.org/10.3390/molecules23051234>
- Kanta, J. (2015). Collagen matrix as a tool in studying fibroblastic cell behavior. *Cell Adhesion & Migration*, 9 (4), 308–316. <https://doi.org/10.1080/19336918.2015.1005469>
- Karakoti, A., Singh, S., Dowding, J.M., Seal, S. & Self, W.T. (2010). Redox-active radical scavenging nanomaterials. *Chemical Society Reviews*, 39 (11), 4422–4432. <https://doi.org/10.1039/B919677N>
- Kessler, V.G., Seisenbaeva, G.A., Unell, M. & Håkansson, S. (2008). Chemically Triggered Bidelivery Using Metal–Organic Sol–Gel Synthesis. *Angewandte Chemie*, 120 (44), 8634–8637. <https://doi.org/10.1002/ange.200803307>
- Kessler, V.G., Spijksma, G.I., Seisenbaeva, G.A., Håkansson, S., Blank, D.H. & Bouwmeester, H.J. (2006). New insight in the role of modifying ligands in the sol-gel processing of metal alkoxide precursors: A possibility to approach new classes of materials. *Journal of sol-gel science and technology*, 40 (2–3), 163–179
- Khalid, A., Ullah, H., Ul-Islam, M., Khan, R., Khan, S., Ahmad, F., Khan, T. & Wahid, F. (2017). Bacterial cellulose–TiO₂ nanocomposites promote healing and tissue regeneration in burn mice model. *RSC Advances*, 7 (75), 47662–47668. <https://doi.org/10.1039/C7RA06699F>

- Kim, U.-J., Kuga, S., Wada, M., Okano, T. & Kondo, T. (2000). Periodate Oxidation of Crystalline Cellulose. *Biomacromolecules*, 1 (3), 488–492. <https://doi.org/10.1021/bm0000337>
- Klemm, D., Heublein, B., Fink, H.-P. & Bohn, A. (2005). Cellulose: Fascinating Biopolymer and Sustainable Raw Material. *Angewandte Chemie International Edition*, 44 (22), 3358–3393. <https://doi.org/10.1002/anie.200460587>
- Köhler, S. & Heinze, T. (2007). New Solvents for Cellulose: Dimethyl Sulfoxide/Ammonium Fluorides. *Macromolecular Bioscience*, 7 (3), 307–314. <https://doi.org/10.1002/mabi.200600197>
- Kokubo, T., Kushitani, H., Sakka, S., Kitsugi, T. & Yamamuro, T. (1990). Solutions able to reproduce *in vivo* surface-structure changes in bioactive glass-ceramic A-W³. *Journal of Biomedical Materials Research*, 24 (6), 721–734. <https://doi.org/10.1002/jbm.820240607>
- Kumar, N., Lin, Y.-J., Huang, Y.-C., Liao, Y.-T. & Lin, S.-P. (2023). Detection of lactate in human sweat via surface-modified, screen-printed carbon electrodes. *Talanta*, 265, 124888. <https://doi.org/10.1016/j.talanta.2023.124888>
- Labafzadeh, S.R., Vyavaharkar, K., Kavakka, J.S., King, A.W.T. & Kilpeläinen, I. (2015). Amination and thiolation of chloroacetyl cellulose through reactive dissolution in N,N-dimethylformamide. *Carbohydrate Polymers*, 116, 60–66. <https://doi.org/10.1016/j.carbpol.2014.03.077>
- Le Clainche, C. & Carlier, M.-F. (2008). Regulation of Actin Assembly Associated With Protrusion and Adhesion in Cell Migration. *Physiological Reviews*, 88 (2), 489–513. <https://doi.org/10.1152/physrev.00021.2007>
- Liang, H., Yin, D., Shi, L., Liu, Y., Hu, X., Zhu, N. & Guo, K. (2023). Surface modification of cellulose *via* photo-induced click reaction. *Carbohydrate Polymers*, 301, 120321. <https://doi.org/10.1016/j.carbpol.2022.120321>
- Lindman, B., Karlström, G. & Stigsson, L. (2010). On the mechanism of dissolution of cellulose. *Journal of Molecular Liquids*, 156 (1), 76–81. <https://doi.org/10.1016/j.molliq.2010.04.016>
- Löbmann, K. & Svagan, A.J. (2017). Cellulose nanofibers as excipient for the delivery of poorly soluble drugs. *International Journal of Pharmaceutics*, 533 (1), 285–297. <https://doi.org/10.1016/j.ijpharm.2017.09.064>
- Lombardo, S., Chen, P., Larsson, P.A., Thielemans, W., Wohler, J. & Svagan, A.J. (2018). Toward Improved Understanding of the Interactions between Poorly Soluble Drugs and Cellulose

- Nanofibers. *Langmuir*, 34 (19), 5464–5473. <https://doi.org/10.1021/acs.langmuir.8b00531>
- Marano, F., Hussain, S., Rodrigues-Lima, F., Baeza-Squiban, A. & Boland, S. (2011). Nanoparticles: molecular targets and cell signalling. *Archives of Toxicology*, 85 (7), 733–741. <https://doi.org/10.1007/s00204-010-0546-4>
- Marcial, B.L., Costa, L.A.S., De Almeida, W.B., Anconi, C.P.A. & Dos Santos, H.F. (2011). Interaction of chemically modified tetracyclines with catalytic Zn(II) ion in matrix metalloproteinase: evidence for metal coordination sites. *Theoretical Chemistry Accounts*, 128 (3), 377–388. <https://doi.org/10.1007/s00214-010-0881-9>
- Marques, M.R.C., Loebenberg, R. & Almukainzi, M. (2011). Simulated Biological Fluids with Possible Application in Dissolution Testing. *Dissolution Technologies*, 18 (3), 15–28. <https://doi.org/10.14227/DT180311P15>
- Massart, R. (1981). Preparation of aqueous magnetic liquids in alkaline and acidic media. *IEEE Transactions on Magnetics*, 17 (2), 1247–1248. <https://doi.org/10.1109/TMAG.1981.1061188>
- McCormack, W.B. & Lawes, B.C. (2000). Sulfuric and Sulfurous Esters. In: *Kirk-Othmer Encyclopedia of Chemical Technology*. John Wiley & Sons, Ltd. <https://doi.org/10.1002/0471238961.1921120613030315.a01>
- McCormick, C.L. (1981). Novel cellulose solutions.
- Monier-Williams, G.W. (1921). XC.—The hydrolysis of cotton cellulose. *Journal of the Chemical Society, Transactions*, 119, 803–805
- Montain, S.J., Cheuvront, S.N. & Lukaski, H.C. (2007). Sweat mineral-element responses during 7 h of exercise-heat stress. *International journal of sport nutrition and exercise metabolism*, 17 (6), 574–582. <https://doi.org/10.1123/ijsnem.17.6.574>
- Montini, T., Melchionna, M., Monai, M. & Fornasiero, P. (2016). Fundamentals and Catalytic Applications of CeO₂-Based Materials. *Chemical Reviews*, 116 (10), 5987–6041. <https://doi.org/10.1021/acs.chemrev.5b00603>
- Morais, D.C., Fontes, M.L., Oliveira, A.B., Gabbai-Armelin, P.R., Ferrisse, T.M., De Oliveira, L.F.C., Brighenti, F.L., Barud, H.S. & De Sousa, F.B. (2023). Combining Polymer and Cyclodextrin Strategy for Drug Release of Sulfadiazine from Electrospun Fibers. *Pharmaceutics*, 15 (7), 1890. <https://doi.org/10.3390/pharmaceutics15071890>

- Mosmann, T. (1983). Rapid colorimetric assay for cellular growth and survival: Application to proliferation and cytotoxicity assays. *Journal of Immunological Methods*, 65 (1), 55–63. [https://doi.org/10.1016/0022-1759\(83\)90303-4](https://doi.org/10.1016/0022-1759(83)90303-4)
- Nielsen, T.T. & Sørensen, N.S. (1981). Daily plasma citrate rhythms in man during feeding and fasting. *Scandinavian Journal of Clinical and Laboratory Investigation*, <https://doi.org/10.1080/00365518109092046>
- Palm, G.J., Lederer, T., Orth, P., Saenger, W., Takahashi, M., Hillen, W. & Hinrichs, W. (2008). Specific binding of divalent metal ions to tetracycline and to the Tet repressor/tetracycline complex. *JBIC Journal of Biological Inorganic Chemistry*, 13 (7), 1097–1110. <https://doi.org/10.1007/s00775-008-0395-2>
- Parisi, L., Toffoli, A., Ghezzi, B., Mozzoni, B., Lumetti, S. & Macaluso, G.M. (2020). A glance on the role of fibronectin in controlling cell response at biomaterial interface. *Japanese Dental Science Review*, 56 (1), 50–55. <https://doi.org/10.1016/j.jdsr.2019.11.002>
- Paul, T., Machesky, M.L. & Strathmann, T.J. (2012). Surface Complexation of the Zwitterionic Fluoroquinolone Antibiotic Ofloxacin to Nano-Anatase TiO₂ Photocatalyst Surfaces. *Environmental Science & Technology*, 46 (21), 11896–11904. <https://doi.org/10.1021/es302097k>
- Payen, A. (1838). Mémoire sur la composition du tissu propre des plantes et du ligneux. *Comptes rendus*, 7 (lu 17 décembre 1838), 1052–1056
- Pearson, R.G. (1963). Hard and Soft Acids and Bases. *Journal of the American Chemical Society*, 85 (22), 3533–3539. <https://doi.org/10.1021/ja00905a001>
- Popov, A.L., Zaichkina, S.I., Popova, N.R., Rozanova, O.M., Romanchenko, S.P., Ivanova, O.S., Smirnov, A.A., Mironova, E.V., Selezneva, I.I. & Ivanov, V.K. (2016). Radioprotective effects of ultra-small citrate-stabilized cerium oxide nanoparticles in vitro and in vivo. *RSC Advances*, 6 (108), 106141–106149. <https://doi.org/10.1039/C6RA18566E>
- Reid, M.S., Villalobos, M. & Cranston, E.D. (2017). Benchmarking Cellulose Nanocrystals: From the Laboratory to Industrial Production. *Langmuir*, 33 (7), 1583–1598. <https://doi.org/10.1021/acs.langmuir.6b03765>
- Roberta, P., Elena Maria, S., Carmelo, I., Fabiano, C., Maria Teresa, R., Sara, I., Antonio, S., Roberto, F., Giuliana, I. & Maria Violetta, B. (2021). Toxicological assessment of CeO₂ nanoparticles on early

- development of zebrafish. *Toxicology Research*, 10 (3), 570–578. <https://doi.org/10.1093/toxres/tfab028>
- Rueden, C.T., Schindelin, J., Hiner, M.C., DeZonia, B.E., Walter, A.E., Arena, E.T. & Eliceiri, K.W. (2017). ImageJ2: ImageJ for the next generation of scientific image data. *BMC Bioinformatics*, 18 (1), 529. <https://doi.org/10.1186/s12859-017-1934-z>
- Sadat, M.E., Kaveh Baghbador, M., Dunn, A.W., Wagner, H.P., Ewing, R.C., Zhang, J., Xu, H., Pauletti, G.M., Mast, D.B. & Shi, D. (2014). Photoluminescence and photothermal effect of Fe₃O₄ nanoparticles for medical imaging and therapy. *Applied Physics Letters*, 105 (9), 091903. <https://doi.org/10.1063/1.4895133>
- Sato, K. (1977). The physiology, pharmacology, and biochemistry of the eccrine sweat gland. *Reviews of physiology, biochemistry and pharmacology*, 79, 51–131. <https://doi.org/10.1007/BFb0037089>
- Schmid, R., Mosset, A. & Galy, J. (1991). New compounds in the chemistry of Group 4 transition-metal alkoxides. Part 4. Synthesis and molecular structures of two polymorphs of [Ti₁₆O₁₆(OEt)₃₂] and refinement of the structure of [Ti₇O₄(OEt)₂₀]. *Journal of the Chemical Society, Dalton Transactions*, (8), 1999–2005. <https://doi.org/10.1039/DT9910001999>
- Seisenbaeva, G.A., Daniel, G., Nedelec, J.-M. & Kessler, V.G. (2013). Solution equilibrium behind the room-temperature synthesis of nanocrystalline titanium dioxide. *Nanoscale*, 5 (8), 3330–3336. <https://doi.org/10.1039/C3NR34068F>
- Seisenbaeva, G.A., Fromell, K., Vinogradov, V.V., Terekhov, A.N., Pakhomov, A.V., Nilsson, B., Ekdahl, K.N., Vinogradov, V.V. & Kessler, V.G. (2017). Dispersion of TiO₂ nanoparticles improves burn wound healing and tissue regeneration through specific interaction with blood serum proteins. *Scientific Reports*, 7 (1), 15448. <https://doi.org/10.1038/s41598-017-15792-w>
- da Silva Perez, D., Montanari, S. & Vignon, M.R. (2003). TEMPO-Mediated Oxidation of Cellulose III. *Biomacromolecules*, 4 (5), 1417–1425. <https://doi.org/10.1021/bm034144s>
- Striegel, AndréM. (1997). Theory and applications of DMAC/LICL in the analysis of polysaccharides. *Carbohydrate Polymers*, 34 (4), 267–274. [https://doi.org/10.1016/S0144-8617\(97\)00101-X](https://doi.org/10.1016/S0144-8617(97)00101-X)
- Svensson, F.G., Manivel, V.A., Seisenbaeva, G.A., Kessler, V.G., Nilsson, B., Ekdahl, K.N. & Fromell, K. (2021). Hemocompatibility of Nanotitania-Nanocellulose Hybrid Materials. *Nanomaterials*, 11 (5), 1100. <https://doi.org/10.3390/nano11051100>

- Talbert, G., Stinchfield, F. & Staff, H. (1933). SIMULTANEOUS STUDY OF THE CONSTITUENTS OF THE SWEAT, URINE, AND BLOOD; ALSO GASTRIC ACIDITY AND OTHER MANIFESTATIONS RESULTING FROM SWEATING: XI. Phosphorus and Sulphur. *American Journal of Physiology-Legacy Content*, 106 (2), 488–490
- Thomas, L.C. & Chittenden, R.A. (1964a). Characteristic infrared absorption frequencies of organophosphorus compounds—I The phosphoryl (P=O) group. *Spectrochimica Acta*, 20 (3), 467–487. [https://doi.org/10.1016/0371-1951\(64\)80043-6](https://doi.org/10.1016/0371-1951(64)80043-6)
- Thomas, L.C. & Chittenden, R.A. (1964b). Characteristic infrared absorption frequencies of organophosphorus compounds—II. P-O-(X) bonds. *Spectrochimica Acta*, 20 (3), 489–502. [https://doi.org/10.1016/0371-1951\(64\)80044-8](https://doi.org/10.1016/0371-1951(64)80044-8)
- Turel, I. (2002). The interactions of metal ions with quinolone antibacterial agents. *Coordination Chemistry Reviews*, 232 (1), 27–47. [https://doi.org/10.1016/S0010-8545\(02\)00027-9](https://doi.org/10.1016/S0010-8545(02)00027-9)
- Wahid, F., Zhao, X.-J., Zhao, X.-Q., Ma, X.-F., Xue, N., Liu, X.-Z., Wang, F.-P., Jia, S.-R. & Zhong, C. (2021). Fabrication of Bacterial Cellulose-Based Dressings for Promoting Infected Wound Healing. *ACS Applied Materials & Interfaces*, 13 (28), 32716–32728. <https://doi.org/10.1021/acsami.1c06986>
- Wang, H., Shen, J., Li, Y., Wei, Z., Cao, G., Gai, Z., Hong, K., Banerjee, P. & Zhou, S. (2014). Magnetic iron oxide–fluorescent carbon dots integrated nanoparticles for dual-modal imaging, near-infrared light-responsive drug carrier and photothermal therapy. *Biomaterials Science*, 2 (6), 915–923. <https://doi.org/10.1039/C3BM60297D>
- Wright, D.A. & Williams, D.A. (1968). The crystal and molecular structure of titanium tetramethoxide. *Acta Crystallographica Section B: Structural Crystallography and Crystal Chemistry*, 24 (8), 1107–1114. <https://doi.org/10.1107/S0567740868003766>
- Zhou, J. & Zhang, L. (2000). Solubility of Cellulose in NaOH/Urea Aqueous Solution. *Polymer Journal*, 32 (10), 866–870. <https://doi.org/10.1295/polymj.32.866>
- Zhu, S., Wu, Y., Chen, Q., Yu, Z., Wang, C., Jin, S., Ding, Y. & Wu, G. (2006). Dissolution of cellulose with ionic liquids and its application: a mini-review. *Green Chemistry*, 8 (4), 325–327. <https://doi.org/10.1039/B601395C>

Popular science summary

Nanomaterials are an increasingly important technology for advanced applications, such as the removal of heavy metals in environmental applications or to for biomedical applications. The field of nanotechnology is still quite young, but its potential is great and as such methods to produce nanomaterials and hybrid nanomaterials continue to be developed and refined. Within modern society there is an increasingly stronger push towards environmentally sustainable materials and thus there is an increasing demand for bio-based materials. These bio-based materials such as the naturally occurring bio-polymer cellulose have many interesting properties, such as shape, size and affinity, which can be tuned towards different applications. Combining these bio-based nanomaterials with bio-compatible mineral nanoparticles opens new avenues for sustainable, bio-based hybrid materials. In this work cotton was turned into nano-sized particles whose surface was modified to selectively separate cobalt/nickel from lanthanides, thereby creating a bio-based material useful for recycling of rare earth-based magnets.

Additionally in this work, mineral metal oxide nanoparticles were produced and incorporated onto cellulose-based nanomaterials to produce materials suitable for wound dressing. This allows for the sustained release of pharmaceuticals into the wound environment and surroundings. The rate of which can be controlled using daylight when using the magnetic mineral oxides magnetite/maghemite. Introducing a tracer which emits light upon illumination with a blacklight/UV lamp allows for the release of pharmaceuticals to be visually inspected. Lastly, the inclusion of titanium oxide based mineral nanoparticles onto the cellulose-based materials positively influenced the expression of biomarkers involved in tissue regeneration and wound-healing process.

Populärvetenskaplig sammanfattning

Nanomaterial ger upphov till en allt viktigare teknik för avancerade tillämpningar, t.ex. för att avlägsna tungmetaller i miljötillämpningar eller för biomedicinska applikationer. Nanoteknikområdet är fortfarande ganska ungt, men dess potential är stor och därför fortsätter metoderna för att producera nanomaterial och hybrida nanomaterial att utvecklas och förfinas. I det moderna samhället finns en allt starkare strävan mot miljömässigt hållbara material och därmed en ökande efterfrågan på biobaserade material. Dessa biobaserade material, t.ex. den naturligt förekommande biopolymeren cellulosa, har många intressanta egenskaper, t.ex. form, storlek och affinitet, som kan anpassas till olika tillämpningar. Genom att kombinera dessa biobaserade nanomaterial med biokompatibla mineralnanopartiklar öppnas nya möjligheter för hållbara, biobaserade hybridmaterial. I detta arbete omvandlades bomull till partiklar i nanostorlek vars yta modifierades för att selektivt separera kobolt/nickel från sällsynta jordartsmetaller och därigenom skapa ett biobaserat material som är användbart för återvinning av magneter baserade på dessa.

I detta arbete producerades dessutom nanopartiklar av mineral metalloxid som införlivades i cellulosabaserade nanomaterial för att producera kompositer lämpade för tillverkning av sårförband. Detta möjliggjorde en långvarig frisättning av läkemedel i sårmiljön och omgivningen. Hastigheten kunde kontrolleras med hjälp av dagsljus vid användningen av de magnetiska mineraloxiderna magnetit/maghemit. Genom att införa ett spårämne som avger ljus vid belysning med en blacklight/UV-lampa kunde frisättningen av läkemedel följas visuellt. Införandet av titanoxidbaserade mineralnanopartiklar på ytan av cellulosabaserade material påverkade positivt uttrycket av biomarkörer som var involverade i vävnadsregenerering och sårläkningsprocessen.

Acknowledgements

I would like to acknowledge many people for all the help, support, advice, critique and fun they've given me over the years.

Firstly, I want to express my deepest gratitude to my principal supervisor Gulaim Seisenbaeva, who not only helped me grow as a person and young scientist but who has also been incredibly supportive when I was diagnosed with lymphoma and the many months of treatment that followed. I also want to express my gratitude for the things you've taught me and the trust you've placed in me by allowing me to play with the "toys" we have at our disposal, AFM and SEM included.

My deep gratitude to Vadim Kessler, co-professor in our group for the support during my treatment and time in the hospital. I am also thankful for all the helpful feedback, advice and knowledge you've given me over the years. You've been most informative in matters of crystallography and fundamental solution chemistry; I just hope that one day I can match a fraction of your encyclopaedic knowledge.

I would like to express special thanks to my co-supervisor Sidney JL Ribeiro for allowing me to stay with his group at the Instituto de Química in Araraquara, Brazil and of course for the churrasco, pizza and caipirinha. I hope one day I can sell a (scientific) fish as well as you can.

I would also like to thank Geoffrey Daniel, my other co-supervisor who has been most informative on matters of cellulose and TEM.

I would additionally express special thanks to Hernane Barud for the chance to collaborate and all the help you've given me in Brazil, and I hope you, Helida and your younglings are doing well!

Giovana G. Nunes, from the bottom of my heart, thank you for inviting me to visit your lab in Curitiba. The experience has brightened my mood and my life.

I would like to express my gratitude to my collaborators over the years. Thanks to Daniel Hedlund and Peter Svedlindh, who helped us with magnetic measurements and discussion. Thanks to Tatyana Budnyak, who helped with surface analysis. Fredric G. Svensson and his student Servane Gaio, thank you. Marijana Lakić, I hope you're doing well. My thanks to Inna V. Melnyk for the chance to collaborate on Janus silica particles. My thanks to Marina Fontes and her student Paulo de Abreu Fernandes for their help with biological essays. My thanks to Natalia Charczuk for the luminescence measurements shown in this work.

Olga Galkina, I've never met you but some of your work had laid a foundation for mine. Thanks to students Jelmen van Gucht, Lucia Isabel Oliver Brockmann and Marine Beyaert who did good work here and I wish them luck in their future endeavours.

Current and former group members: Filip Kozlowski, don't stress, I think you'll do fine when it's your turn. Björn Greijer, it was fun while it lasted and good luck! Rasmus Björk, I hope you're doing well. Ani Vardanyan, hopefully I didn't cause a permanent rift in your family by asking for a recipe for Lahmajoun. Sara Targonska, I hope you're surviving the heat. Jacob Whittaker, we don't see enough of you. Oksana Dudarko, we stand with Ukraine.

I want to thank the people at the Instituto de Química (UNESP) for all the help and fun times I've had. Especially Rafael Romano for showing and teaching me how to grow bacterial nanocellulose, Sergio for the luminescence measurements and Marina Abuçafy (Mariniña) for the cake, hopefully one day you'll use that magnetite for good.

My gratitude to my family and fiancé for being so supportive over the years, especially after my diagnosis. I am sorry I haven't been able to say goodbye in person to some of you.

I've met the most wonderful people over the years, so many that I could go on for quite a while longer. So, to those not mentioned, you are not forgotten and I'm grateful.



Self-assembly of ferria – nanocellulose composite fibres

T.C. Breijaert^a, G. Daniel^b, D. Hedlund^c, P. Svedlindh^c, V.G. Kessler^a, H. Granberg^d, K. Håkansson^d, G.A. Seisenbaeva^{a,*}

^a Department of Molecular Sciences, Biocentrum, Swedish University of Agricultural Sciences, Almas Allé 5, SE-756 51 Uppsala, Sweden

^b Department of Forest Biomaterials and Technology, Wood Science, Swedish University of Agricultural Sciences, Vallvägen 9C-D, 756 51 Uppsala, Sweden

^c Department of Materials Science and Engineering, Uppsala University, Box 35, 751 03 Uppsala, Sweden

^d Department of Material and Surface Design, Smart Materials, Research Institutes of Sweden (RISE), Drottning Kristinas väg 61, 114 28 Stockholm, Sweden

ARTICLE INFO

Keywords:

Nanocellulose
Magnetite
Magnetic composites
Hybrid materials
Photo-induced drug delivery

ABSTRACT

An environmentally benign synthesis of a magnetically responsive carboxymethylated cellulose nanofibril-based material is reported. Applied experimental conditions lead to the in-situ formation of magnetite nanoparticles with primary particle sizes of 2.0–4.0 nm or secondary particles of 3.6–16.4 nm depending on whether nucleation occurred between individual carboxymethylated cellulose nanofibrils, or on exposed fibril surfaces. The increase in magnetite particle size on the cellulose fibril surfaces was attributed to Ostwald ripening, while the small particles formed within the carboxymethyl cellulose aggregates were presumably due to steric interactions. The magnetite nanoparticles were capable of coordinating to carboxymethylated cellulose nanofibrils to form large “fibre-like” assemblies. The confinement of small particles within aggregates of reductive cellulose molecules was most likely responsible for excellent conservation of magnetic characteristics on storage of this material. The possibility for using the material in drug delivery applications with release rate controlled by daylight illumination is presented.

1. Introduction

The UN 2030 agenda for sustainable development, highlights key areas where the development of sustainably produced materials is expected to play a crucial role (*Transforming Our World: The 2030 Agenda for Sustainable Development* | Department of Economic and Social Affairs, n. d.). It emphasizes the need for development of innovative solid materials for key applications, such as smart packaging, advanced adsorbents, wound healing and tissue engineering scaffolds using environmentally sustainable raw materials. Major focus today is therefore set on natural bio-based polymers.

Cellulose is the most abundant renewable polymer on the planet accounting for multiple teratons of annual biomass production (Klemm et al., 2005). Cellulose is found in all plant forms where it often forms the major constituent (e.g. cotton, wood). Historically and currently, these plant derived forms of cellulose have been used for everyday applications in the form of fabrics, pulp and paper and wood constructions (Hon, 1994).

Potentially industrially important forms of cellulose can also be derived from higher order structures, which have been physically and/

or chemically treated to produce nano-sized cellulose nanofibrils (CNFs, nanocellulose) or cellulose nanocrystals (CNCs). The latter can be used in polymer matrices (Favier et al., 1995; Grunert & Winter, 2002; Oun & Rhim, 2017) as actuators (Hartings et al., 2018; Kim et al., 2006) and transistors (Lim et al., 2009), etc. (Arantes et al., 2017; Hu et al., 2009; Khalilzadeh et al., 2020; Wu et al., 2018). Due to its bio-availability, biocompatibility, and chemical functionality, cellulose is an attractive material for use in environmentally benign applications (Klemm et al., 2005).

One of the major challenges in the development and adaptation of cellulose-based materials is its relative inertness. In order to expand its usage beyond that of simple fibres or crystals, cellulose must be chemically modified to not only increase its solubility but also to diversify and increase the range of possible applications. The development of carboxymethyl cellulose (CMC) for example has led to its use in food as well as more technical applications such as protein purification (Hao et al., 2021; He et al., 2021) and coatings (Dimic-Misic et al., 2013; Souza et al., 2019). Properties of nanocellulose-derived materials are related to size, morphology and surface chemistry of the particles. The nanoparticles can be cellulose nanocrystals (CNC), cellulose nanofibres (CNF)

* Corresponding author.

E-mail address: gulaim.seisenbaeva@slu.se (G.A. Seisenbaeva).

<https://doi.org/10.1016/j.carbpol.2022.119560>

Received 18 February 2022; Received in revised form 12 April 2022; Accepted 28 April 2022

Available online 3 May 2022

0144-8617/© 2022 The Author(s). Published by Elsevier Ltd. This is an open access article under the CC BY license (<http://creativecommons.org/licenses/by/4.0/>).

or bacterial cellulose fibres (BCF) (Sacui et al., 2014).

A significant number of studies to date involving the use of natural biopolymers for advanced technical solutions have focussed on the incorporation of responsive metal oxide materials into, or onto a biopolymer matrix. By including the spinel-type iron oxides such as magnetite or iron(II)-deficient maghemite into biopolymer matrices, composite materials may be obtained with favourable magnetic and catalytic properties. These characteristics may be exploited in the development of materials suitable for applications as Magnetic Resonance Image contrasting agents (Abbasi Pour et al., 2017; Biliuta et al., 2017), antibacterial agents (Biliuta et al., 2017), in magneto-optical applications (Chen et al., 2020; Li et al., 2013), protein adsorption membranes (Wu et al., 2018), metal ion removal (Yu et al., 2012, 2014), electrochemical sensors (Khalilzadeh et al., 2020) and for medical applications (Abbasi Pour et al., 2017; Chaabane et al., 2020).

With magnetically responsive cellulose-iron oxide composite materials, work has focussed on the production of materials either by incorporating pre-synthesized iron oxide particles into a fibril-matrix or via the in-situ growth of particles onto pre-formed biopolymer fibrils/fibres surfaces. Numerous techniques have been developed for production of nano-ferria in a broad range of sizes and morphologies. They include solvothermal synthesis starting from organic precursors or iron carbonyl, resulting in small uniform well-crystallized particles that are often rendered hydrophobic by the conditions of synthesis. An alternative approach is based on co-precipitation in aqueous media. Its drawback lies, however, in relatively appreciable solubility of ferria in polar aqueous media that can result in considerable size variation because of the Ostwald ripening (Thanh, 2012). The challenge in use of pre-formed particles lies in the difficulty of their uniform distribution. With the synthesis of composites, attention has generally been towards in-situ particle growth on a matrix. For efficient distribution of the inorganic content, the matrix should be activated via surface oxidation or esterification. The reactivity of cellulose resembles in this case that of graphene oxide with oxidized surface groups, for example by carboxylation (Dimic-Misic et al., 2019). To our knowledge, no reports have so far been made on cellulose based nanocomposite materials where magnetic iron oxides and nanocellulose self-assemble into large fibre-like structures. In earlier studies, focus was on the in-situ formation of magnetite nanoparticles on relatively large, unmodified, cellulose nanofibres, resulting in the formation of magnetite particle decorated nanofibres with metal oxide particles greater than 10 nm (Galland et al., 2013).

Our hypothesis was that producing magnetic iron oxide in-situ in the presence of highly functionalized nano cellulose would result in a dense self-assembled material with:

- 1) Potentially interesting morphologies;
- 2) Stable magnetic characteristics (through protection of magnetic particles within a dense composite through encapsulation in a reductive matrix); and
- 3) Capacity for visible light controlled release of adsorbed pharmaceuticals, exploiting photo magnetic properties of the obtained composite material.

2. Materials and methods

2.1. Materials

Carboxymethylated nanocellulose fibrils (C-CNF, derived from wood, Degree of Substitution (DS) of cellulose surface hydroxyl groups 0.098) was prepared at RISE Bioeconomy and Health according to the method of Wågberg et al. (2008) as a hydrogel with solid concentration 2.26% by weight. DS is the (average) number of substituent groups attached per base unit (in the case of condensation polymers) or per monomeric unit (in the case of addition polymers). The term has been mainly used in cellulose chemistry. The DS value indicates that approximately 10% of all hydroxyl groups have been

carboxymethylated (Wågberg et al., 2008). After carboxymethylation of a softwood sulphite dissolving pulp (Domsjö Dissolving Plus), the cellulose material was passed through a homogeniser (Microfluidizer M-110EH, Microfluidics Corp., USA) at 1700 bar with two serial chambers of 200- and 100 µm, respectively. The carboxylate content of the nanocellulose was determined via conductometric titration. The C-CNF applied here differs in its characteristics from TEMPO oxidized nano cellulose in that it has a combination of both carboxyl- and carboxymethyl surface functional groups, while TEMPO-CNF has aldehyde and carboxyl groups (Aaen et al., 2019). In addition, the crystal structure is a slightly different between the two grades. Furthermore, the mechanical treatment to delaminate the pulp fibres into fibrils induces variations and commonly the C-CNF has more residual fibre fragments, unless extra cleaning and separation steps are performed.

Iron(II) sulphate heptahydrate (pro analysis), anhydrous iron(III) chloride, and ammonia (25% based on NH₃) were obtained from Sigma-Aldrich, Sweden AB. All chemicals were used without further purification. Water was purified using a Millipore system and purged with nitrogen for several hours prior to use. Ammonia solution was prepared using nitrogen purged water and stored under nitrogen.

2.2. Characterization

Samples were characterized using a Bruker Dimension FastScan Atomic Force Microscope (AFM) with a Nanoscope V controller in ScanAsyst mode using a Fastscan-B AFM probe (silicon tip, f_0 : 400 kHz, k: 4 N/m, tip radius: 5 nm nominally) and a scan rate of 1-3 Hz. Samples were prepared on freshly exfoliated mica. Data was processed using Gwyddion 2.56 with align rows-median to remove skipping lines.

Scanning Electron Microscopy (SEM) observations were conducted using a Hitachi FlexSEM 1000 at an acceleration voltage of 5 kV, spot size 20, and 5 mm working distance. Samples were prepared on Cu foil from aqueous suspensions.

For Transmission Electron Microscopy (TEM), ethanol exchanged oxides were deposited on holey carbon grids (Pelco® 50 mesh grids: Pitch 508 µm; hole width 425 µm; bar width 83 µm; transmission 70%) and observed using a Philips CM/12 microscope (Thermo Fisher Inc.) fitted with LaB6 and operated at 80 or 100 kV. Oxide treated C-CNFs were also embedded in LR White resin (London Resin Co., Basingstoke, UK) following dehydration in ethanol (20–100%, 20% steps, 5 min each). Ultrathin sections (70–100 nm thickness) were cut using a Reichert Ultracut E ultramicrotome and collected on copper grids. Negative TEM films were scanned using an Epson Perfection Pro 750 film scanner. Sections were observed unstained or after post staining with 2% w/v aq. uranyl acetate (10 min) at 80–100 kV.

Powder X-ray Diffraction (PXRD) data was obtained using lyophilized samples on a Bruker APEX-II diffractometer equipped with an AXS Smart APEX CCD Area Detector and graphite-monochromated Mo-K α (λ = 0.71073 Å) radiation source. Data was processed with the EVA-12 software package.

Fourier Transform Infrared (FTIR) analysis was done on a Perkin Elmer Spectrum 100 FT-IR Spectrometer using KBr pellets. Thermogravimetric Analysis (TGA) was done using a Perkin Elmer Pyris 1 TGA at a heating rate of 5 °C/min.

Magnetic measurements were performed using a Lake Shore Cryotronics Series 7400 vibrating sample magnetometer (VSM). Measurements were performed at 300 K (26,85 °C) in the magnetic field range ± 10 kOe with the magnetic moments normalized using the weight of iron oxide solid phase.

2.3. Synthesis

22.089 g of 2.26 wt% C-CNF (499 mg solid C-CNF) was transferred to a 250 mL round bottom flask equipped with a Teflon coated stirring bean and nitrogen inlet. C-CNF suspended in 200 mL nitrogen purged ultrapure water was added and vigorously stirred for 30 min. Then, 327

mg FeCl_3 (2.02 mmol) and 328.5 mg (1.18 mmol) $\text{FeSO}_4 \cdot 7\text{H}_2\text{O}$ was added, forming a 1.7:1 stoichiometry between $\text{Fe}^{3+}/\text{Fe}^{2+}$ and concentration of 9.10 mM $\text{Fe}^{3+}/5.33$ mM Fe^{2+} respectively. The pH was adjusted to pH 5 (according to litmus), using 0.5 mM HCl and the suspension allowed to stir for 30 min at room temperature under a constant flow of bubbling nitrogen. Then, 1.5 M NH_4OH was added dropwise using a syringe until pH 9 (according to litmus). Stirring was stopped and the particles allowed to settle for 5 min, before decanting into 50 mL falcon tubes and washing 4× with N_2 -purged ultrapure water and collection via centrifugation (10 min, 5000 RPM).

2.4. Adsorption experiments

An aliquot equating to ca. 15 mg composite material was removed and mixed with ca. 3 mg tetracycline, placed in an aluminium-wrapped falcon tube and diluted to a final volume of 40 mL. This was placed on an orbital shaker and allowed to shake for several days. Periodically, aliquots were taken and the composite collected via a strong magnet. The supernatant was measured using UV–VIS at 357 nm. Experiments were repeated in triplicate for reproducibility.

2.5. Desorption experiments

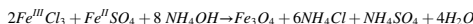
An aliquot equating to ca. 15 mg composite material was taken and mixed with ca. 3 mg tetracycline in a 50 mL pointed flask fitted with a stirring bar and diluted to 30 mL. The flask was heated overnight at 50 °C in a darkened fume hood with the setup wrapped in aluminium to avoid incident light. After stirring overnight, the product was cooled to room temperature and divided equally into two aluminium wrapped falcon tubes. The composite material was collected using a strong magnet, and the supernatant removed and diluted to 17 mL with 0.02 M citrate buffer (pH 6.0). One of the aluminium jackets was removed and

both samples placed on an orbital shaker under a daylight lamp. Aliquots were periodically removed, the composite collected, and the tetracycline content in the supernatant determined via UV–VIS at 357 nm. Experiments were repeated in triplicate for reproducibility.

3. Results and discussion

3.1. Production of iron oxide in the presence of carboxymethylated nanocellulose fibrils

Magnetite is an easily produced magnetic metal oxide with an inverse spinel structured metal oxide consisting of iron(III) and iron(II) in a 1:2 stoichiometry which may be produced by co-precipitation in the presence of ammonia in the following reaction:



Dissolution of Fe(II) and Fe(III) salts in the presence of C-CNFs followed by the slow addition of ammonia lead to the formation of a slight orange hued suspension, with the suspension darkening to a reddish-brown and then black as the pH increased. When the final pH was achieved, a black precipitate was present which slowly turned reddish-brown over time in the presence of ambient air due to the oxidation of Fe^{2+} to Fe^{3+} . Thermogravimetric analysis (SI Fig. S3) of the resulting sample showed a thermal decomposition temperature of 256–257 °C with a residual mass of 31.8 wt%.

3.2. Characterization of (bulk) composite material

3.2.1. XRD patterns of nanocomposite material

To determine which iron oxide phase is formed during the co-precipitation reaction of iron(II/III) in the presence of C-CNF, the powder X-ray pattern was measured and compared with certified

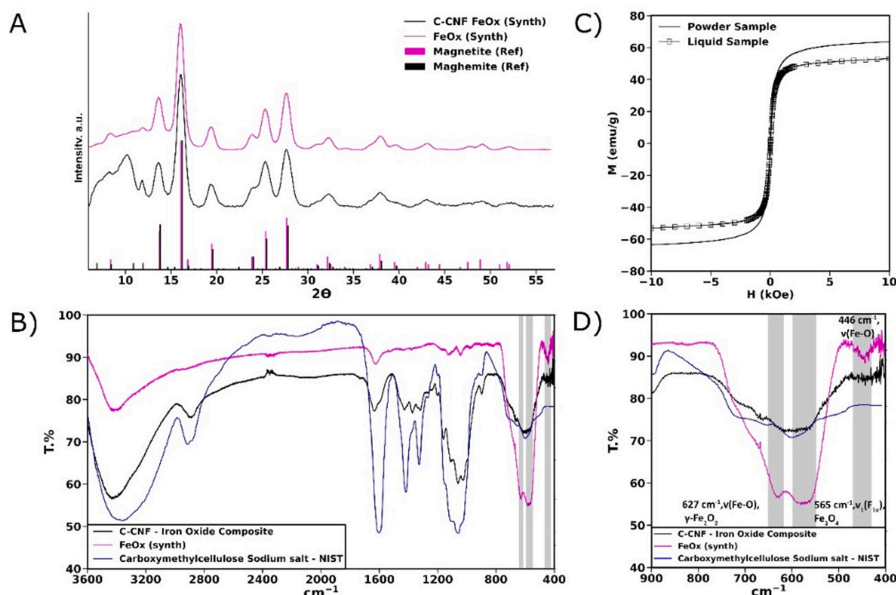


Fig. 1. A) PXRD pattern of a synthesized iron oxide – carboxymethylated cellulose nanofibril composite and iron oxide, measured using a Mo K α X-ray source. Maghemite (00-039-1346) and magnetite (00-019-0629) reference patterns overlaid. B) and D) Measured FTIR spectra of synthesized iron oxide-carboxymethylated cellulose nanofibril composite, magnetite and (sodium) carboxymethylated cellulose nanofibrils, NIST is the reference spectra. C) Magnetization vs magnetic field for powder and liquid samples.

patterns for both magnetite and the iron(II) deficient maghemite (Fig. 1A and SI Fig. S2). It was proven that the primary phase of the iron oxide formed in the presence of C-CNFs nanofibrils was magnetite, maghemite or a mixture of the two oxides. However, with the current setup it was impossible to differentiate between the two iron oxides. Scherrer analysis of the crystallite size was made applying the formula $\tau = K\lambda / (\beta \cdot \cos\theta)$ and showed that the average size of freshly produced pure ferria under the applied conditions was 3.7 nm, while for the composite it was 3.4 nm. This shows that composite formation contributed to the preservation of smaller particles.

3.2.2. Fourier Transform Infrared spectroscopy (FTIR)

In an attempt to distinguish between the magnetite and maghemite iron oxides, the product was examined using FTIR. It should be noted however, that infrared spectroscopic results of magnetite/maghemite mixtures are not absolute due to a strong overlap of the most characteristics bands of iron oxides (Ellid et al., 2003). The iron oxide produced via in-situ precipitation of iron(III) chloride and iron(II) sulphate by ammonia is shown in Fig. 1B. The product obtained exhibits strong absorption bands at 627 and 576 cm^{-1} , with a minor adsorption band in the region of 446 cm^{-1} . Ishii et al. (1972) assigned the IR band at 565 cm^{-1} to the $\nu_1(\text{F}_{1u})$ vibration mode in magnetite, while a small shift to a higher wave number may be attributed to sub-stoichiometric magnetite (Ellid et al., 2003). The peak at 627 cm^{-1} can be assigned to the Fe—O vibration in the iron(II) deficient maghemite, which has formed due to oxidation (Klotz et al., 1999). The additional peaks at 1128, 1043, 975 cm^{-1} may be attributed to the presence of bound sulphate groups present in the sample (Musić et al., 2000). Finally, the peak observed at 1624 cm^{-1} and the broad peak at 3400 cm^{-1} can be attributed to moisture.

The produced iron oxide-C-CNF composite material exhibited similar absorption bands in the range 580–620 cm^{-1} with a smaller, less well-pronounced peak at 665 cm^{-1} , which is slightly shifted, compared to the synthesized magnetite sample. This may be attributed to the magnetite formed in the sample, being coordinated to carboxylate groups present in C-CNF with some maghemite having formed due to oxidation in air. Additional absorption bands appear at 2890, 1597, 1426, 1373, 1318, 1200, 1160, 1110, 1060, 1022, 897 cm^{-1} which are primarily attributed to the various absorption bands present within C-CNF.

3.2.3. Magnetic characterization

Fig. 1C shows the magnetization versus magnetic field for the powder and liquid samples. The measured magnetizations at an applied field of 10 kOe are 63 emu/g and 53 emu/g for the powder and liquid samples, respectively. Both values are somewhat smaller than expected for magnetite and maghemite, which may be explained by spin disorder and spin canting for surface spins in iron oxide nanoparticles. Moreover, as expected, the nanoparticles exhibit superparamagnetic behaviour at 300 K (26,85 °C) and hence zero remanence and coercivity. A plausible explanation for the minor drop in magnetization of the sample dispersed in ethanol is that partial oxidation has occurred with time, but only to rather low extent. The samples were stored for 10 months before measurements and thus revealed considerable stability against oxidation. Bulk magnetic properties are demonstrated in SI Fig. S4 and in a Supplementary video. The major volume of ferria was kept in the form of non-aggregated primary particles bound within the formed self-assembly fibres. This precludes both diffusion of oxygen and release of ions from the coordination-saturated surface of the particles. As a result – no apparent oxidation occurs on storage.

3.3. Morphological investigation of iron oxide composite materials

3.3.1. Atomic force microscopy

To examine the nanoscale structures formed when iron oxide is precipitated in the presence of C-CNFs, the sample was examined using

AFM where it was apparent that the reaction is capable of producing a composite consisting of “fibre-like” structures (Fig. 2). Observations along the axis of these fibre-like structures showed random increases in surface height, likely attributed to the presence of iron oxide formed during the co-precipitation reaction.

The fibre-like structures observed had an average width of 18.55 ± 1.66 nm with lengths ranging from 70 nm to nearly a micrometer in longitudinal direction. However, the measured widths do not take tip convolution into account, which increases the observed widths compared to actual widths. By decreasing the measuring area to 200×200 nm (Fig. 2C, E), spherical to ellipsoidal particles were observed which appear surrounded by a C-CNF network.

The presence of multiple spherical to ellipsoidal particles across the longitudinal direction of the fibre-like structures (Fig. 2C, E) indicate that the iron oxide particles formed during the precipitation of iron(II) and iron(III) interact with the C-CNFs to form a composite material that self-assembled into fibre-like domains. This interesting property that should be exploited in future applications. However, it was impossible to determine from measured AFM data whether the particles were distributed on the actual surface of the network or within the C-CNF network itself without more detailed examination.

3.3.2. Electron microscopy

To supplement the AFM data, samples were prepared for SEM and TEM as described in the method section (Fig. 3). SEM confirmed that the fibre-like structures were not completely homogeneous showing aggregates along the surface of the individual fibre networks (Fig. 3A). Energy-dispersive X-ray analysis across the aggregates showed iron and oxygen, indicating the metal oxide was distributed homogeneously within the aggregate structure (Fig. 3A). Cross sections of these aggregates shown with TEM further suggest a homogeneous structure (Fig. 5).

Examination of the composite by TEM without negative staining (Fig. 4, SI Fig. S1) showed the iron-C-CNF network was composed of single fibrils having a cross section of 3–4.5 nm or double fibrils in the range of 5.5–8 nm (SI Fig. S1) and as well as strongly scattering elements in the order of 5.5–8 nm, distributed along the lateral dimensions of the network. Under normal circumstances, cellulose-based samples require staining with uranyl acetate or similar heavy metal stains to be visible. However, in the present case, the composite fibre structure was visible due to the presence of iron oxide nanoparticles bound to individual carboxymethyl cellulose fibrils.

Based on the presence of iron oxide in both the aggregates and fibril-like structures within the sample, it would seem feasible that initially the metal salts hydrolyse to form hydrated species, which then coordinate with partially deprotonated C-CNFs. The addition of base leads to further deprotonation of the C-CNFs and production of iron hydroxide species that nucleate to form magnetite at high pH (Seisenbaeva and Kessler, 2014), with the surface remaining iron coordinated to the carboxymethylated cellulose nanofibrils. However, this does not explain the formation of both the “fibre-like” assemblies and larger aggregates. Using electron microscopy and AFM, our investigation revealed three distinct composite structures. This included self-assembled fibril structures containing surface-bound iron oxide nanoparticles, larger C-CNF aggregates with iron oxide nanoparticles in the range of a few nanometers, and large iron oxide particles that formed on the surface of fibril aggregates, the latter stimulated by Ostwald ripening. The larger particles may result from both aggregation and Ostwald ripening, although the larger crystal domain size for the composite indicates domination of the Ostwald ripening phenomenon. It is assumed however, that the source of C-CNFs will play a significant role in the formation of the observed structures. In this study, the C-CNFs were derived from wood and had uniform particle sizes in the range of 3–4.5 nm for single fibrils according to TEM.

To determine whether the iron oxides are precipitated along the outer regions of the large C-CNFs network, or were incorporated within the bulk of the aggregates, samples were embedded, sectioned and

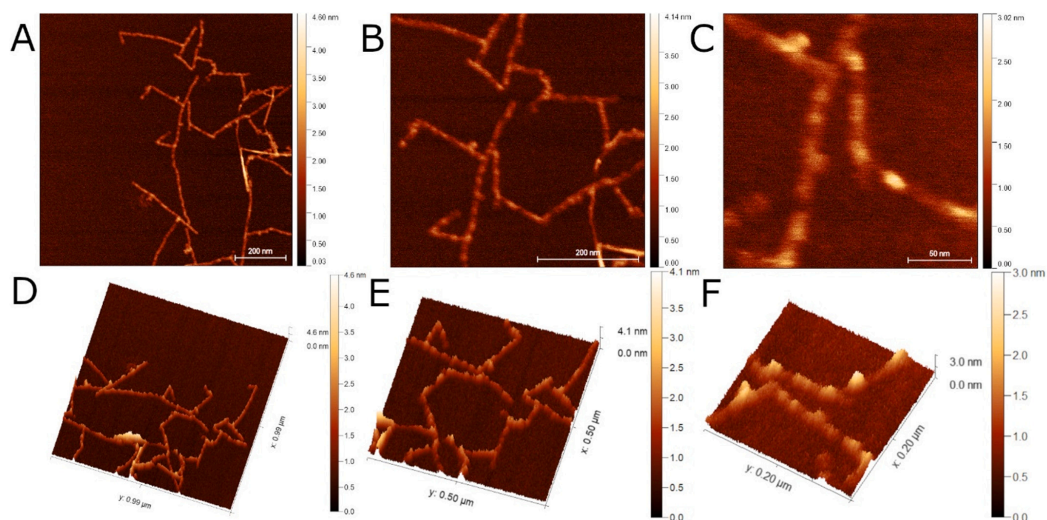


Fig. 2. Scanasyt AFM images of an iron-oxide carboxymethyl cellulose composite. Top down view at 512 px resolution and A) $1 \times 1 \mu\text{m}$, B) $500 \times 500 \text{ nm}$, C) $200 \times 200 \text{ nm}$ scan sizes. 3D view a composite at D) $1 \times 1 \mu\text{m}$, E) $500 \times 500 \text{ nm}$ and F) $200 \times 200 \text{ nm}$.

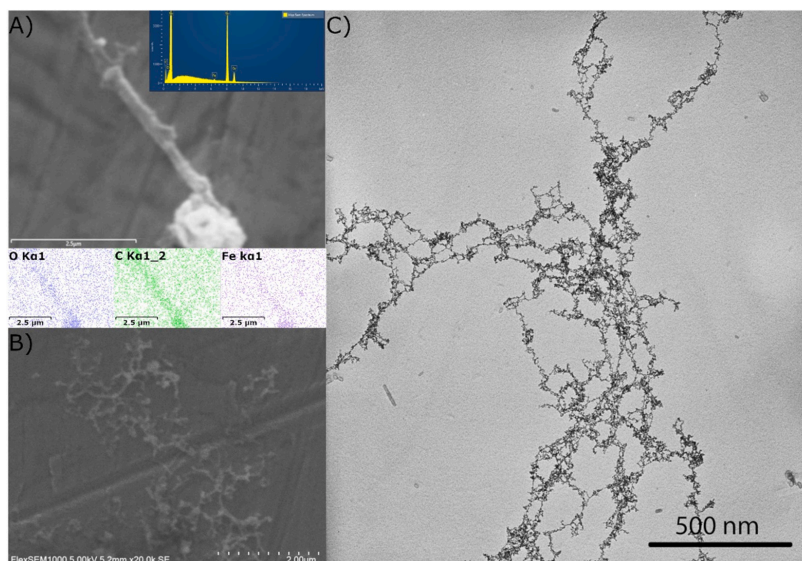


Fig. 3. A) SEM-EDS image of a large aggregate showing the presence and distribution of carbon, oxygen and iron, attributed to carboxymethylated cellulose nanofibrils and iron oxide respectively. B) SEM image of the iron oxide – C-CNF. C) TEM image without staining of iron oxide-C-CNF.

examined by TEM to provide additional information on the ultrastructural nature of the composite material.

As shown in Figs. 3–5 and S1, Fig. S1, the iron oxides were present in three major forms, including, iron oxide aggregates, inclusion of iron oxides within the C-CNF aggregate structure, and adsorption onto the C-CNF fibril surfaces. While the surface adsorbed iron oxide nanoparticles grew into large sizes due to Ostwald ripening (i.e. ca. 5.5–8 nm), the iron

oxide nanoparticles encapsulated within the C-CNF structure remained in the order of 1.5–2.5 nm. This observation is in good agreement with calculations of the average size of crystalline domain applying the Scherrer formula. It indicates that carboxymethylated cellulose nanofibrils not only allow for the formation of C-CNF-iron oxide network clusters, it is also effective in retaining the iron oxide particle size range to a few nanometers, so long as the particles are encapsulated by

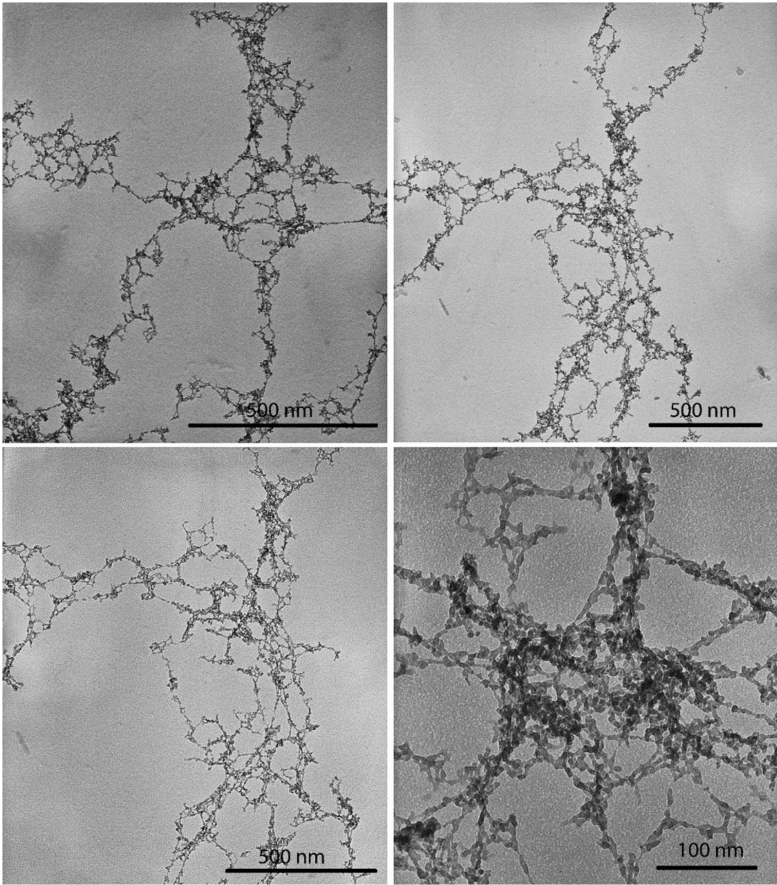


Fig. 4. TEM Images of iron-oxide carboxymethyl cellulose composites without staining and at varying magnification.

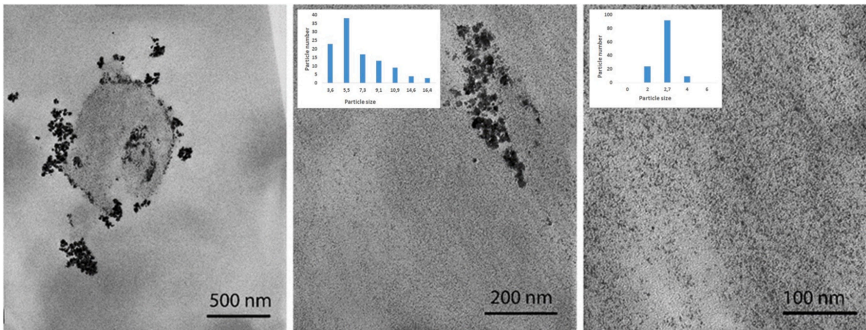


Fig. 5. TEM images of a cross-sectioned resin embedded iron oxide - C-CNFs. Large aggregates are visible on the surface (inset shows the particle size distribution in nm) and open structure of the iron-cellulose composite, while smaller particles appear aligned with individual fibrils (inset shows the particle size distribution in nm).

cellulose fibrils and not present on the surface where Ostwald ripening can occur. Ostwald ripening otherwise sometimes called isothermal distillation is a phenomenon associated with minimization of the surface energy in a precipitate, which results in dissolution of smaller particles and simultaneous growth of the larger ones in the system (Voorhees, 1985). Whether the formation of these large composite aggregates is caused by the formation of small iron oxide particles after bonding of ionic iron to C-CNF or by the intercalation of the iron oxide particles within the C-CNF after metal oxide formation remains unknown. TEM suggests the iron oxides associate with the outer regions of the nano-sized C-CNFs, following the orientation of the individual cellulose fibrils (Figs. 5, S, S1). The statistic distribution of sizes for single-domain particles according to TEM (see Fig. 5) shows that it is clearly smaller inside the fibres 2.0–4.0 nm compared to that on their surface 3.6–16.4 nm, indicating that it was in the first hand Ostwald ripening that produced the larger particles on the surface.

3.4. Drug adsorption and desorption

Fe₃O₄ NPs are of interest not only for their magnetic properties but also for their optical properties, as they are known to display photo-thermal conversion which may be exploited for therapy and drug delivery (Estelrich & Busquets, 2018; Johnson et al., 2018; Sadat et al., 2014; Wang et al., 2014). In order to examine the potential of the composite material as a drug delivery vehicle, we tested the adsorption and desorption of tetracycline, a broad-spectrum antibiotic. After 72 hour contact time, tetracycline showed a maximum drug adsorption of 62 µg/mg (79%) at room temperature with up to 27 µg/mg (35%) within the first 240 min indicating that the initial adsorption is fast and thereafter slows down (Fig. 6A).

To test the viability of the composite for drug delivery and the influence daylight plays on the release of tetracycline, samples were prepared in batches and split equally. One part was exposed to a daylight lamp during desorption, and the other kept dark by wrapping in foil. Citrate buffer was added and release of tetracycline followed by UV–VIS (Fig. 6B). Initial drug release was relatively slow with an approximate 11% release in the absence of light and 20% release in light after 3 h. This increases to 33 and 85% with- and without light respectively, after 2 days indicating that the release desorption rate of tetracycline was strongly influenced by daylight.

4. Conclusions

In this work, we demonstrated the synthesis of a magnetically responsive composite material based on carboxymethyl cellulose and in-situ synthesized magnetite, that self-assembled into fibre-like nano-structures which were characterized by AFM, SEM, TEM, FTIR, TGA and PXRD. The material displayed stable magnetic characteristics on storage, both in solid state and in solution. In addition, the novel material was studied in solution state as a potential drug vehicle for the delivery of tetracycline. Thus, the main hypothesis of this work was proved valid.

Carboxymethylated cellulose nanofibrils derived from wood were successfully decorated with iron oxide particles in an in situ process so that magnetic iron oxide particles were of relative uniform size and assembled into larger composite structures together with cellulose. These structures could be divided into three broad categories: i) Large C-CNF aggregates where the iron oxide nanoparticle size was small with growth limited by the C-CNF structure; ii) large iron oxide particles that form on the surface of the fibre aggregates, where particle growth is stimulated by Ostwald ripening, and iii) cellulose-iron oxides forming long fibre networks comprising iron oxide and cellulose with longitudinal dimensions far exceeding that of the initial components. For the fibre-like networks, it is highly likely that the morphology and pH response of both the metal oxide and C-CNF play a crucial role in its formation. Variations in cellulose source and synthetic conditions may have significant influence on the overall structures formed. The phase of iron oxide synthesized in this method is the magnetically responsive magnetite, which will oxidize to iron(III)-deficient maghemite with time in the presence of oxygen. This method is simple and cost-effective, which can lead to the development of further magnetically relevant materials. However, the synthesis of the “fibre-like” structures remains difficult with subtle changes in synthetic conditions having a profound effect on the structures obtained.

Electronic supporting information includes additional details on TEM, XRD and TGA studies, and demonstration of magnetic properties of obtained materials (as photo and video evidence). Supplementary data to this article can be found online at <https://doi.org/10.1016/j.carbpol.2022.119560>.

CRedit authorship contribution statement

TB has performed all the synthetic work and adsorption and desorption experiments and wrote the draft of the manuscript, GD has performed the TEM characterization and contributed to formulation and

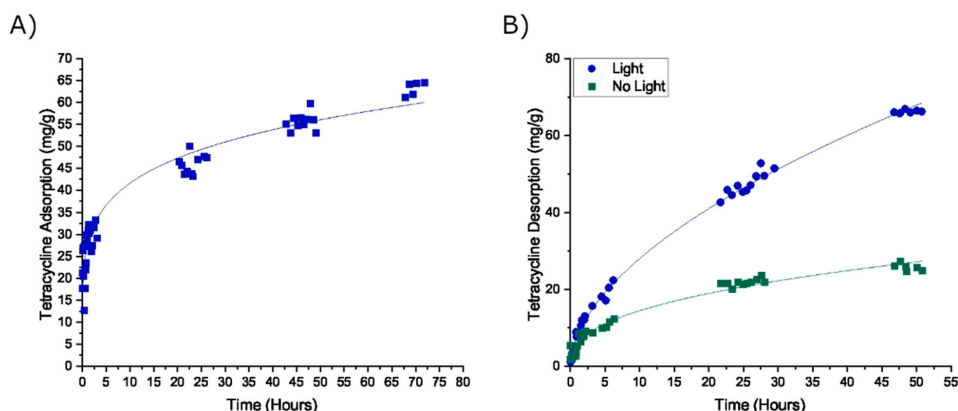


Fig. 6. Tetracycline adsorption and desorption. A) Tetracycline adsorption in mg/g and B) tetracycline desorption in mg/g as a function of time.

language editing of the manuscript, DH and PS have performed the magnetic measurements and helped with their interpretation, VK contributed with XRD measurements, HG and KH provided the C-CNF material and helped with interpretation of data, GS contributed with the project idea, TGA, FTIR, AFM and ESEM measurements and performed the final editing of the manuscript. All authors participated actively in discussion of results and contributed to editing of the manuscript.

Declaration of competing interest

The authors declare that they have no affiliations with or involvement in any organization or entity with any financial interest or non-financial interest in the subject matter or material discussed in this manuscript.

Acknowledgements

The authors are grateful to Professor Sidney Ribeiro for valuable discussions.

Funding

The authors express their gratitude to the Swedish Research Council STINT for support of the grant Nanocellulose Based Materials for Environmental and Theranostic Applications and to the Faculty of Natural Resources and Agricultural Sciences, SLU for support of TB PhD position.

References

- Aaen, R., Simon, S., Wernersson Brodin, F., & Syverud, K. (2019). The potential of TEMPO-oxidized cellulose nanofibrils as rheology modifiers in food systems. *Cellulose*, 26, 5483–5496.
- Abbasi Pour, S., Shaterian, H. R., Afradi, M., & Yazdani-Elah-Abadi, A. (2017). Carboxymethyl cellulose (CMC)-loaded co-cu doped manganese ferrite nanorods as a new dual-modal simultaneous contrast agent for magnetic resonance imaging and nanocarrier for drug delivery system. *Journal of Magnetism and Magnetic Materials*, 438, 85–94. <https://doi.org/10.1016/j.jmmm.2017.04.069>
- Arantes, A. C. C., Dauzacker, L. C. L., Bianchi, M. L., Wood, D. F., Williams, T. G., Orts, W. J., ... Almeida, C. D. G. (2017). Renewable hybrid nanocatalyst from magnetite and cellulose for treatment of textile effluents. *Carbohydrate Polymers*, 163, 101–107. <https://doi.org/10.1016/j.carbpol.2017.01.007>
- Biliuta, G., Sacarescu, L., Socoliciu, V., Iacob, M., Gheorghe, L., Negru, D., & Coseri, S. (2017). Carboxylated polysaccharides decorated with ultrasmall magnetic nanoparticles with antibacterial and MRI properties. *Macromolecular Chemistry and Physics*, 218(10), 1700662. <https://doi.org/10.1002/macp.201700662>
- Chaabane, L., Chahdoura, H., Mehdaoui, R., Snoussi, M., Beyou, E., Lahcini, M., & Baouab, M. H. V. (2020). Functionalization of developed bacterial cellulose with magnetite nanoparticles for nanobiotechnology and nanomedicine applications. *Carbohydrate Polymers*, 247, Article 116707. <https://doi.org/10.1016/j.carbpol.2020.116707>
- Chen, X., Ye, Z., Yang, F., Feng, J., Li, Z., Huang, C., Ke, Q., & Yin, Y. (2020). Magnetic cellulose microcrystals with tunable magneto-optical responses. *Applied Materials Today*, 20, Article 100749. <https://doi.org/10.1016/j.apmt.2020.100749>
- Dimic-Misic, K., Gane, P. A. C., & Paltakari, J. (2013). Micro- and nanofibrillated cellulose as a rheology modifier additive in CMC-containing pigment-coating formulations. *Industrial & Engineering Chemistry Research*, 52(45), 16066–16083. <https://doi.org/10.1021/ie4028878>
- Dimic-Misic, K., Phiri, J., Nieminen, K., Maloney, T., & Gane, P. (2019). Characterising exfoliated few-layer graphene interactions in co-processed nanofibrillated cellulose suspension via water retention and dispersion rheology. *Materials Science and Engineering: B*, 242, 37–51. <https://doi.org/10.1016/j.mseb.2019.03.001>
- Ellid, M. S., Murayid, Y. S., Zoto, M. S., Musić, S., & Popović, S. (2003). Chemical reduction of hematite with starch. *Journal of Radioanalytical and Nuclear Chemistry*, 258(2), 299–305. <https://doi.org/10.1023/A:1026285721065>
- Estelrich, J., & Busquets, M. A. (2018). Iron oxide nanoparticles in photothermal therapy. *Molecules*, 23(7), 1567. <https://doi.org/10.3390/molecules23071567>
- Favier, V., Chanzy, H., & Cavaille, J. Y. (1995). Polymer nanocomposites reinforced by cellulose whiskers. *Macromolecules*, 28(18), 6365–6367. <https://doi.org/10.1021/ma00122a053>
- Galland, S., Andersson, R. L., Salajkova, M., Ström, V., Olsson, R. T., & Berglund, L. A. (2013). Cellulose nanofibrils decorated with magnetic nanoparticles – synthesis, structure and use in magnetized high toughness membranes for a prototype loudspeaker. *Journal of Materials Chemistry C*, 1(47), 7963–7972. <https://doi.org/10.1039/C3TC31748J>
- Grunert, M., & Winter, W. T. (2002). Nanocomposites of cellulose acetate butyrate reinforced with cellulose nanocrystals. *Journal of Polymers and the Environment*, 10(1), 27–30. <https://doi.org/10.1021/0659059086>
- Hao, J., Zhang, W., Wang, H., Ziya, N., Luo, Y., Jia, P., Zhang, G., & Ng, T. (2021). Purification and properties of a lacase from the mushroom *Agaricus sinodeliciousus*. *Biotechnology and Applied Biochemistry*, 68(2), 297–306. <https://doi.org/10.1002/bab.1926>
- Hartings, M., Douglass, K. O., Neice, C., & Ahmed, Z. (2018). Humidity responsive photonic sensor based on a carboxymethyl cellulose mechanical actuator. *Sensors and Actuators B: Chemical*, 265, 335–338. <https://doi.org/10.1016/j.snb.2018.03.065>
- He, X., Lu, W., Sun, C., Khalesi, H., Mata, A., Andaleeb, R., & Fang, Y. (2021). Cellulose and cellulose derivatives: Different colloidal states and food-related applications. *Carbohydrate Polymers*, 255, Article 117334. <https://doi.org/10.1016/j.carbpol.2020.117334>
- Hon, D. N.-S. (1994). Cellulose: A random walk along its historical path. *Cellulose*, 1(1), 1–25. <https://doi.org/10.1007/BF00818796>
- Hu, L., Choi, J. W., Yang, Y., Jeong, S., Mantia, F. L., Cui, L.-F., & Cui, Y. (2009). Highly conductive paper for energy-storage devices. *Proceedings of the National Academy of Sciences*, 106(51), 21490–21494. <https://doi.org/10.1073/pnas.0908858106>
- Ishii, M., Nakahira, M., & Yamanaka, T. (1972). Infrared absorption spectra and cation distributions in (Mn, Fe)3O4. *Solid State Communications*, 11(1), 209–212. [https://doi.org/10.1016/0038-1098\(72\)91162-3](https://doi.org/10.1016/0038-1098(72)91162-3)
- Johnson, R. J. G., Schultz, J. D., & Lear, B. J. (2018). Photothermal effectiveness of magnetite nanoparticles: Dependence upon particle size probed by experiment and simulation. *Molecules*, 23(5), 1234. <https://doi.org/10.3390/molecules23051234>
- Khalilzadeh, M. A., Tajik, S., Beitollahi, H., & Venditti, R. A. (2020). Green synthesis of magnetic nanocomposite with iron oxide deposited on cellulose nanocrystals with copper (Fe3O4@CNC/Cu): Investigation of catalytic activity for the development of a venlafaxine electrochemical sensor. *Industrial & Engineering Chemistry Research*, 59(10), 4219–4228. <https://doi.org/10.1021/acs.iecr.9b06214>
- Kim, J., Yun, S., & Ounaies, Z. (2006). Discovery of cellulose as a smart material. *Macromolecules*, 39(12), 4202–4206. <https://doi.org/10.1021/ma060261e>
- Klemm, D., Heublein, B., Fink, H.-P., & Bohn, A. (2005). Cellulose: Fascinating biopolymer and sustainable raw material. *Angewandte Chemie International Edition*, 44(22), 3358–3393. <https://doi.org/10.1002/anie.200460587>
- Klotz, M., Ayral, A., Guizard, C., Ménager, C., & Cabuil, V. (1999). Silica coating on colloidal maghemite particles. *Journal of Colloid and Interface Science*, 220(2), 357–361. <https://doi.org/10.1006/jcis.1999.6517>
- Li, Y., Zhu, H., Gu, H., Dai, H., Fang, Z., Weadock, N. J., Guo, Z., & Hu, L. (2013). Strong transparent magnetic nanopaper prepared by immobilization of Fe3O4 nanoparticles in a nanofibrillated cellulose network. *Journal of Materials Chemistry A*, 1(48), 15278–15283. <https://doi.org/10.1039/C3TA12591B>
- Lim, W., Douglas, E. A., Kim, S.-H., Norton, D. P., Pearson, S. J., Ren, F., Shen, H., & Chang, W. H. (2009). High mobility InGaZnO4 thin-film transistors on paper. *Applied Physics Letters*, 94(7), Article 072103. <https://doi.org/10.1063/1.3086394>
- Musić, S., Šarić, A., Popović, S., Nomura, K., & Sawada, T. (2000). Forced hydrolysis of Fe3+ ions in NH4Fe(SO4)2 solutions containing urotropin. *Croatia Chemica Acta*, 73(2), 541–567.
- Oun, A. A., & Rhim, J.-W. (2017). Characterization of carboxymethyl cellulose-based nanocomposite films reinforced with oxidized nanocellulose isolated using ammonium persulfate method. *Carbohydrate Polymers*, 174, 484–492. <https://doi.org/10.1016/j.carbpol.2017.06.121>
- Sacui, I. A., Nieuwendael, R. C., Burnett, D. J., Jorfi, M., Weder, C., Foster, E. J., Olsson, R. T., Gilman, J. W., & Stranick, S. J. (2014). Comparison of the properties of cellulose nanocrystals and cellulose nanofibrils isolated from bacteria, tunicate, and wood processed using acid, enzymatic, mechanical, and oxidative methods. *ACS Appl. Mater. Interfaces*, 6, 6127–6138. <https://doi.org/10.1021/am500359f>
- Sadat, M. E., Kaveh Baghbador, M., Dunn, A. W., Wagner, H. P., Ewing, R. C., Zhang, J., Xu, H., Pualetti, G. M., Mast, D. B., & Shi, D. (2014). Photoluminescence and photothermal effect of Fe3O4 nanoparticles for medical imaging and therapy. *Applied Physics Letters*, 105(9), Article 091903. <https://doi.org/10.1063/1.4895133>
- Seisenbaeva, G. A., & Kessler, V. G. (2014). Precursor directed synthesis – “molecular” mechanisms in the soft chemistry approaches and their use for template-free synthesis of metal, metal oxide and metal chalcogenide nanoparticles and nanostructures. *Nanoscale*, 6, 6229–6244. <https://doi.org/10.1039/C3NR06336D>
- Souza, S. F., Mariano, M., De Farias, M. A., & Bernardes, J. S. (2019). Effect of depletion forces on the morphological structure of carboxymethyl cellulose and micro/nano cellulose fiber suspensions. *Journal of Colloid and Interface Science*, 538, 228–236. <https://doi.org/10.1016/j.jcis.2018.11.096>
- Thanh, N. T. H. (Ed.). (2012). *Magnetic Nanoparticles: From Fabrication to Clinical Applications* (1st ed.). CRC Press. ISBN-10: 1439869324.
- Transforming our world: The 2030 Agenda for Sustainable Development, n.d. Transforming our world: The 2030 agenda for sustainable development | Department of Economic and Social Affairs. (n.d.). Retrieved November 22, 2021, from <https://sdgs.un.org/2030agenda>.
- Voorthees, P. W. (1985). The theory of ostwald ripening. *Journal of Statistical Physics*, 38, 231–252.
- Wågberg, L., Decher, G., Norgren, M., Lindström, T., Ankerfors, M., & Axnäs, K. (2008). The build-up of polyelectrolyte multilayers of microfibrillated cellulose and cationic polyelectrolytes. *Langmuir*, 24(3), 784–795. <https://doi.org/10.1021/la702481v>
- Wang, H., Shen, J., Li, Y., Wei, Z., Cao, G., Gai, Z., Hong, K., Banerjee, P., & Zhou, S. (2014). Magnetic iron oxide-fluorescent carbon dots integrated nanoparticles for dual-modal imaging, near-infrared light-responsive drug carrier and photothermal therapy. *Biomaterials Science*, 2(6), 915–923. <https://doi.org/10.1039/C3BM60297D>

- Wu, H., Teng, C., Tian, H., Li, Y., & Wang, J. (2018). Fabrication of functional magnetic cellulose nanocomposite membranes for controlled adsorption of protein. *Cellulose*, 25(5), 2977–2986. <https://doi.org/10.1007/s10570-018-1750-2>
- Yu, X., Kang, D., Hu, Y., Tong, S., Ge, M., Cao, C., & Song, W. (2014). One-pot synthesis of porous magnetic cellulose beads for the removal of metal ions. *RSC Advances*, 4(59), 31362–31369. <https://doi.org/10.1039/C4RA05601A>
- Yu, X., Tong, S., Ge, M., Zuo, J., Cao, C., & Song, W. (2012). One-step synthesis of magnetic composites of cellulose@iron oxide nanoparticles for arsenic removal. *Journal of Materials Chemistry A*, 1(3), 959–965. <https://doi.org/10.1039/C2TA00315E>

Self-Assembly of Ferria – Nanocellulose Composite Fibres

Supporting information

Authors: Breijaert, T.C.^a, Daniel, G.^b, Hedlund, D.^c, Svedlindh, P.^c, Kessler, V.G.^a, Granberg, H.^d, Håkansson, K.^d, Seisenbaeva, G.A.^a.

^a*Department of Molecular Sciences, Biocentrum, Swedish University of Agricultural Sciences, Almas Allé 5, SE-756 51 Uppsala, Sweden.*

^b*Department of Forest Biomaterials and Technology, Wood Science, Swedish University of Agricultural Sciences, Vallvägen 9C-D 756 51, Uppsala, Sweden.*

^c*Department of Materials Science and Engineering, Uppsala University, Box 35, 751 03, Uppsala, Sweden.*

^d*Department of Material and Surface Design, Smart Materials, Research Institutes of Sweden (RISE), Drottning Kristinas väg 61 114 28, Stockholm, Sweden*

^{*}*Corresponding author. E-mail address:*

Transmission electron microscopy

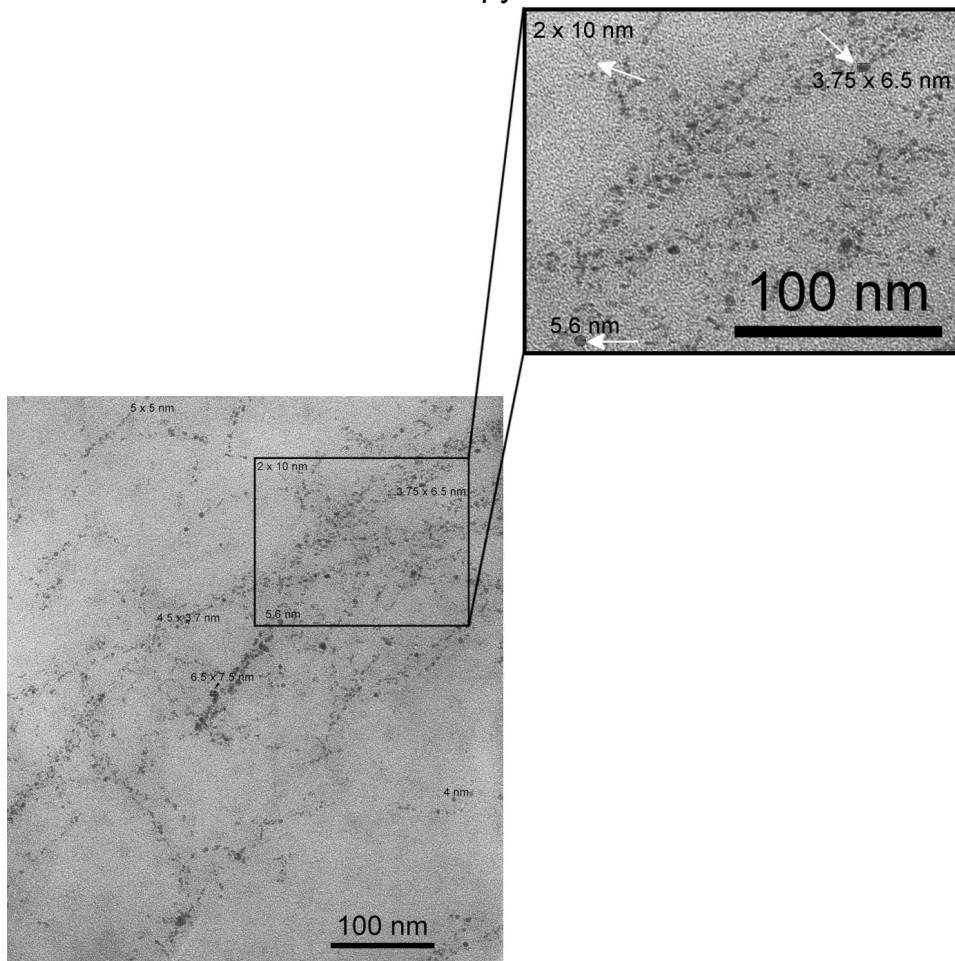


Figure S1. TEM image of carboxymethylated cellulose nanofiber - iron oxide composite. Arrows show the small iron oxide particles associated with the cellulose fibrils and their respective dimensions.

Powder X-ray Diffraction

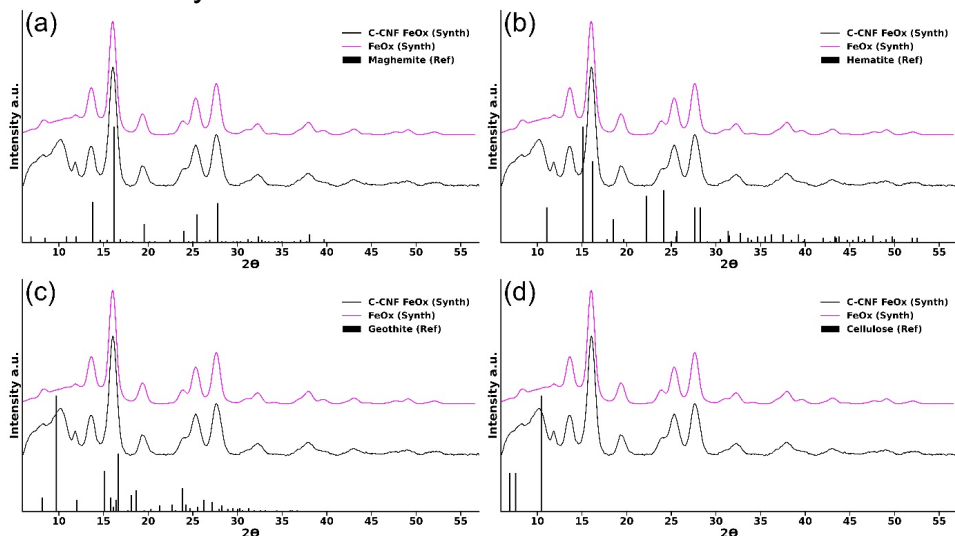


Figure S2. Reference Patterns for a) Hematite (00-033-0664), b) Maghemite (00-039-1346), c) Goethite (00-029-0713) and d) Cellulose (00-050-2241) overlaid over the synthesized iron oxide and CMC iron oxide composite.

Thermogravimetric Analysis

Thermogravimetric analysis of a freeze-dried sample of the iron-CNF composite material. Under oxygen atmosphere and at a heating rate of 5 °C/min, the composite shows a weight loss of 5.15% between 20-100 °C which is associated with adsorbed water. Between 100-200 °C the composite is quite stable losing up to 1.68% mass. Increasing the temperature leads to thermal decomposition of the material at 256.63 °C, accounting for a 65.96% total weight reduction. A further increase to 442 °C leads to a 4.25 wt% reduction, beyond which the sample remains stable until approximately 700 °C, beyond which a gradual increase of 1.57 wt% is measured. The final residual mass is 31.83 wt% which is associated with the iron oxide.

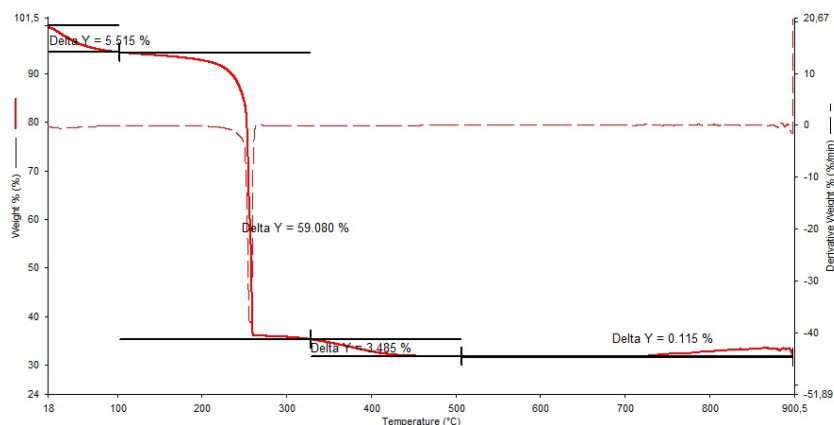


Figure S3. Thermogravimetric analysis of a FeOx-cellulose composite material.

Illustrating Magnetic Properties

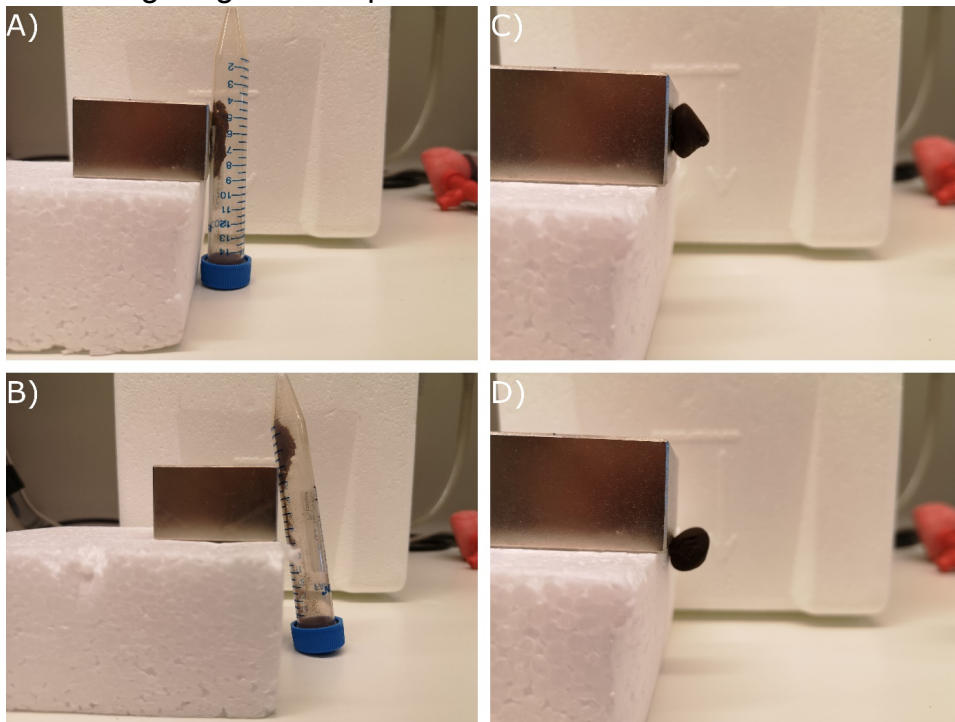
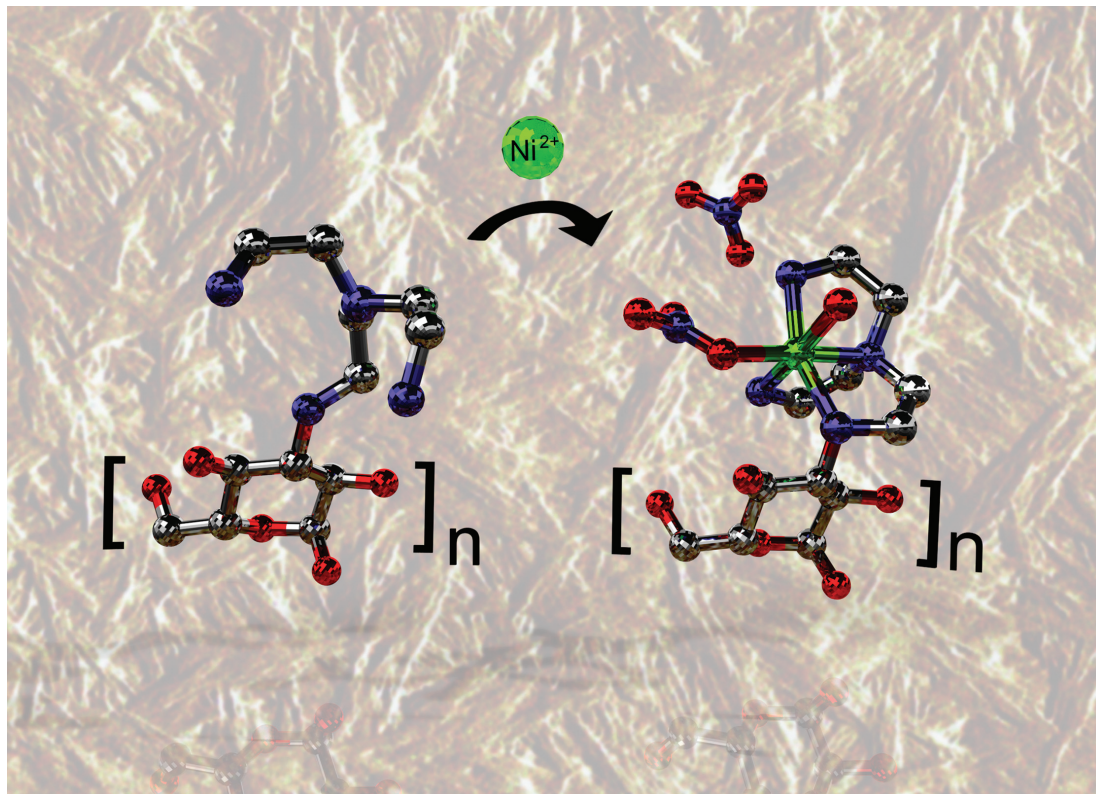


Figure S4. An illustrative composite image showcasing the retention of magnetic properties after storage for 10 months in air with A/B) showing an ethanol-exchanged, oven dried sample, ground into a coarse flakey powder and C/D) showing an ethanol-exchanged centrifuged (compressed) sample.



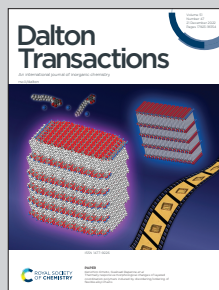
Showcasing research from Professor Gulaim A. Seisenbaeva's laboratory, Department of Molecular Sciences, Swedish University of Agricultural Sciences, Uppsala, Sweden.

Tailoring a bio-based adsorbent for sequestration of late transition and rare earth elements

Separation of Late Transition Metals (LTM) from Rare Earth Elements is principal challenge in recycling of magnetic materials from technical and electronic waste. Bio-based adsorbent material with enhanced selectivity towards LTM was produced by grafting a poly-amino ligand on a nano cellulose matrix. The material's mode of action was revealed via structural studies of relevant molecular model compounds.

Image reproduced by permission of Gulaim A. Seisenbaeva, Vadim K. Kessler and Adrian Dauphinee.

As featured in:



See Gulaim A. Seisenbaeva *et al.*, *Dalton Trans.*, 2022, 51, 17978.





Cite this: *Dalton Trans.*, 2022, **51**, 17978

Received 28th September 2022,
Accepted 14th November 2022

DOI: 10.1039/d2dt03150g

rsc.li/dalton

Tailoring a bio-based adsorbent for sequestration of late transition and rare earth elements†

Troy C. Breijaert,^a Tetyana M. Budnyak,^b Vadim K. Kessler ^a and
Gulaim A. Seisenbaeva ^{*a}

The demand for new renewable energy sources, improved energy storage and exhaust-free transportation requires the use of large quantities of rare earth (REE) and late transition (LTM, group 8–12) elements. In order to achieve sustainability in their use, an efficient green recycling technology is required. Here, an approach, a synthetic route and an evaluation of the designed bio-based material are reported. Cotton-derived nano cellulose particles were functionalized with a polyamino ligand, tris(2-aminoethyl) amine (TAEA), achieving ligand content of up to ca. 0.8 mmol g^{−1}. The morphology and structure of the produced adsorbent were revealed by PXRD, SEM-EDS, AFM and FTIR techniques. The adsorption capacity and kinetics of REE and LTM were investigated by conductometric photometric titrations, revealing quick uptake, high adsorption capacity and pronounced selectivity for LTM compared to REE. Molecular insights into the mode of action of the adsorbent were obtained via the investigation of the molecular structure of the Ni(II)–TAEA complex by an X-ray single crystal study. The bio-based adsorbent nanomaterial demonstrated in this work opens up a perspective for tailoring specific adsorbents in the sequestration of REE and LTM for their sustainable recycling.

Introduction

Rare earth elements (REE) are critical elements for the development of modern technology and industries.^{1,2} Their application in energy production and storage³ in the form of magnetic materials, permanent magnets^{4,5} and as components in NiMH batteries^{6,7} has resulted in an increased demand for these materials.² This has resulted in an increase in an acquisition by mining, which is inherently unsustainable. In that regard, recycling the existing REE-containing materials such as common REE-based magnets needs to be promoted.^{8–10} However, both mining and recycling require the use of extraction and separation techniques involving large amounts of hazardous reagents and solvents.^{5,7,11} The most common technology for REE separation is acidic leaching with various acidic leaching agents, using several precipitation steps to remove unwanted components, after which

the product can be calcined and re-dissolved.^{5,12–14} However, most established methods require repeated steps to obtain the desired metal purity as it is difficult to separate REE from late transition metals (LTM, groups 8–12), which are commonly found with REEs in REE-containing recyclable materials.^{15–17}

An alternative to the use of liquid-phase extraction and separation of REEs from late transition metals is the use of solid adsorbent materials for the extraction of metals from solution.¹⁸ Today a wide range of adsorbent materials are available that can remove metals from solution, ranging from inorganic materials such as fly ash,¹⁹ steel slag materials,²⁰ olivine and zeolites²¹ to organic materials such as tree bark,²² chitin/chitosan,^{23–25} ion exchange resins, polymers,^{26,27} protein-based adsorbents,^{28,29} lignocellulosic sources³⁰ and peat.³¹ With purely inorganic materials, it can be difficult to tune metal adsorption capacity and selectivity beyond what is inherent to the material but in some cases, at least with silicate materials^{32–36} and metal oxides,^{37,38} it is possible to graft the surface with organic ligands to improve metal uptake and selectivity. Organic adsorbents naturally contain reactive groups on the surface onto which ligands may be grafted. By choosing an appropriate type of coordinating ligand, it is possible to increase the adsorption capacity of the adsorbent materials and selectivity and therefore separate LTM from REE.^{34,37} Creating a tailored ligand monolayer on the surface of the adsorbent opens up the possibility

^aDepartment of Molecular Sciences, Biocentrum, Swedish University of Agricultural Sciences, Almas Allé 5, Box 7015, SE-750 07 Uppsala, Sweden.
E-mail: gulaim.seisenbaeva@slu.se

^bDivision of Nanotechnology and Functional Materials, Department of Materials Science and Engineering, Uppsala University, Box 35, 751 03 Uppsala, Sweden

† Electronic supplementary information (ESI) available. CCDC 2207506. For ESI and crystallographic data in CIF or other electronic format see DOI: <https://doi.org/10.1039/d2dt03150g>

to adjust it specifically for selective adsorption of target metal species, realizing the so-called molecular recognition approach.^{39–41}

Natural bio-based polymer materials are especially suitable from an environmental point of view as they are considered renewable resources.^{42–44} Cellulose, for example, is the most abundant, renewable polymer on the planet, accounting for several terra tons of annual biomass production.⁴⁵ It is found in plants as a major constituent, serving as a structural polymer, but it can also be produced by bacteria with the morphology depending on the source.^{45,46} In addition, varying the original morphology depending on the source, cellulose can be processed in order to form more advanced structures such as networks, gels and fibres. In terms of the chemical structure, it consists of polymeric β -1,4-linked D-glucose which self-assembles into higher-order structures which can be chemically modified for specific applications.^{47,48} The wide availability of cellulosic materials in nature combined with its renewable nature and low cost makes cellulose a very promising raw material for the preparation of advanced adsorbent materials.^{49–51} By grafting the surface of cellulose with ligands that have high affinity to specific metals and preferentially binding them, the recycling and separation of magnetic and battery materials can be made more environmentally sustainable.^{21,51} Amines, for example, are well known to strongly bind to late transition metals *via* the formation of coordinate covalent bonds while specific coordination geometries are known to stabilize certain metal cations. An example of such a ligand is tris(2-aminoethyl)amine, which contains four amino functions, three of which are located in freely rotating amine-containing arms and the ligand is known to form stable complexes with transition metals.^{52–55}

In this study, we present the development and characterization of a cellulose-based nano-adsorbent material containing tris(2-aminoethyl)amine as a ligand that can rapidly form stable complexes with transition metals. Additionally, the mode of surface binding and possibility of ion exchange processes have been demonstrated by the single-crystal X-ray study of the model compound. The adsorption capacity, kinetics and metal uptake selectivity of REE and LTM and the pH-dependent desorption of metals from the produced cellulosic material have been studied.

Materials and methods

Synthetic procedures

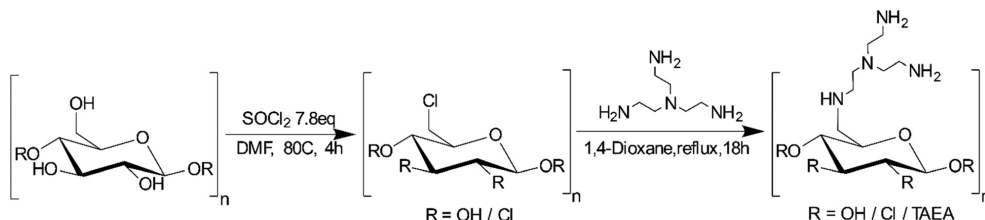
Synthesis of cellulose nanocrystals. Cellulose nanocrystals (CNCs) were synthesized according to the literature procedure.⁵⁶ In short, 16 g of raw cotton was suspended in 140 mL of 64 wt% sulphuric acid at 45 °C for 45 minutes, after which it was poured into 10-fold excess water and allowed to settle. The supernatant was decanted and CNC suspension was poured into dialysis bags (MCWO = 12 kDa) and dialyzed against miliQ until the conductivity remained unchanged.

Synthesis of chlorinated nanocellulose. A CNC suspension corresponding to 3.0 g of CNCs (18.3 mmol AGU) was lyophilized and suspended in 60 mL of sieve-dried *N,N'*-dimethylformamide (DMF, 5 wt%) in a round-bottom flask and fitted with a reflux condenser and drierite-packed drying tube. The mixture was heated to 80 °C before adding 10.5 mL of thionyl chloride (145 mmol, 7–8 eq. based on AGU) dropwise over 15–20 minutes. The reaction was allowed to stir for 4 hours and the cellulose precipitated out in water, then it was neutralized with 3% ammonia solution until the pH became neutral. The resulting suspension was homogenized using a high-shear mixer (13 500 min^{−1}, 10 minutes). The particles were collected *via* centrifugation (10 min, 10k rpm) and washed several times with miliQ, re-suspending between each washing cycle. The sample was lyophilized for further analysis.

Synthesis of tris(2-aminoethyl)amine-cellulose. An aqueous, chlorinated cellulose suspension (1.5 g) was centrifuged, water was replaced with 1,4-dioxane, and washed 4 times. Particles were allowed to stand for some time before each washing cycle. Afterwards, the Cl-CNC suspension was transferred to a round-bottom flask, followed by the addition of 1.4 mL of tris(2-aminoethyl)amine (TAEA, 9.3 mmol, 2.2 eq. based on Cl content as determined by EDS), fitted with a reflux condenser and refluxed overnight. The product was collected *via* centrifugation, washed until the conductivity was similar to that of miliQ and lyophilized. The amine content was determined *via* conductometric titration. The approach is summarized in Scheme 1.

Synthesis of single crystals of model compounds

$[Ni(\eta)(TAEA)(H_2O)(NO_3)]NO_3$ (**1**). $Ni(\eta)(NO_3)_2 \cdot 6H_2O$ (279.8 mg, 1 mmol) was dissolved in 4 mL of miliQ, followed by the addition of 1 molar equivalent (143 μ l) of the ligand and the



Scheme 1 Preparation route to the synthesis of tris(2-aminoethyl)amine modified cellulose.

solutions were allowed to slowly evaporate at room temperature, yielding violet block-shaped (prismatic) crystals.

$[N(C_2H_4NH_3)_3](NO_3)_3$ (2). 1 mmol of $REE(III)(NO_3)_2 \cdot 6H_2O$ ($REE = Sm, Dy$) was dissolved in 4 mL of miliQ, followed by the addition of 1 molar equivalent (143 μ l) of the ligand, and the solutions were allowed to slowly evaporate at room temperature, yielding colorless plate-shaped crystals in a gel-like matrix.

Characterization

Scanning electron microscopy/energy dispersive X-ray scattering. Scanning electron microscopy (SEM) observations were conducted using a Hitachi FlexSEM 1000 at an acceleration voltage of 5 kV, a spot size of 20, and a working distance of 5 mm. For energy dispersive X-ray scattering (EDS), an acceleration voltage of 20 kV, a spot size of 50, and a working distance of 10 mm were used.

Atomic force microscopy. Samples were characterized using a Bruker Dimension FastScan Atomic Force Microscope (AFM) with a Nanoscope V controller in ScanAsyst mode using a Fastscan-B AFM probe (silicon tip, f_0 : 400 kHz, k : 4 N m⁻¹, tip radius: 5 nm nominally) and a scan rate of 1–3 Hz. Data were processed using Gwyddion 2.56 with an aligned row median to remove skipping lines.

Fourier transform infrared spectroscopy. Fourier transform infrared (FTIR) analysis was performed with a Perkin-Elmer Spectrum 100 FT-IR spectrometer using KBr pellets.

Powder X-ray diffraction. Powder X-ray diffraction (PXRD) data were obtained on a Bruker D8 QUEST ECO diffractometer equipped with a proton area detector and graphite monochromated sealed-tube Mo-K α ($\lambda = 0.71073$ Å) radiation source.

Single-crystal X-ray diffraction. Data collection was carried out with a Bruker SMART Apex-II diffractometer equipped with a graphite monochromated sealed-tube Mo-K α ($\lambda = 0.71073$ Å) radiation source using omega-scans to obtain full hemisphere data down to 1.0 Å resolution ($2\theta_{\text{eta}} - 50.05^\circ$). $C_6H_{20}N_6NiO_7$, mol. wt = 346.97 Da, monoclinic, space group $P2(1)/c$, $a = 8.3129(6)$, $b = 8.3129(6)$, $c = 8.3129(6)$ Å, $\beta = 91.8660(10)^\circ$, $V = 1400.15(18)$ Å³, and $Z = 4$. The structure was solved by direct methods. The coordinates of the majority of the non-hydrogen atoms were found from the initial solution and those for the residual non-hydrogen atoms and the hydrogen atoms of the water molecule attached to the nickel atom were determined in the subsequent difference Fourier syntheses. The coordinates of other hydrogen atoms were calculated using optimized geometric approximation. All non-hydrogen atoms were refined first in isotropic and then in anisotropic approximation. Hydrogen atoms attached to carbon atoms were refined isotropically, while for the H-atoms in the hydrating water molecules, only the coordinates were refined while the thermal deviation parameters were assumed to be equal to 1.500 times the atomic deviation parameters of the corresponding oxygen atom. The refinement converged at $R_1 = 0.0836$ and $wR_2 = 0.1990$ for 2049 observed reflections ($I > 2\sigma(I)$).

Nitrogen adsorption/desorption isotherms. The specific surface area and pore volume/area were determined from nitrogen adsorption/desorption isotherms on freeze-dried samples at -196 °C (Micromeritics ASAP 2020 Surface Area and Porosity Analyser, Norcross, GA, USA). The samples were degassed at 120 °C for 3 h before the measurements.

Conductometric titration. Titrations were performed using a Metrohm Titrand 888 (2.888.0310), fitted with an 856 conductivity module (2.856.0010), 800 Dosino (2.800.0010), 5-ring conductivity measuring cell ($c = 0.7$, 6.0915.100), using TIAMO Light 2.5 as automation software. Titrers were determined using tris(hydroxymethyl)aminomethane (HCl) and potassium hydrogen phthalate (NaOH). Amine content was determined *via* conductometric titration by the back titration of protonated amine.

Photometric titrations. Metal sequestering titrations were performed by photometric titration using 5 mM ethylenediamine tetraacetic acid (EDTA). Prior to use, EDTA was standardized against calcium carbonate using eriochrome-T and ammonia buffer. Photometric titrations were performed in either acetate buffer with Xylenol Orange (Ln^{3+}) or ammonia buffer (pH 9) with murexide (Ni^{2+} and Co^{2+}).

Adsorption isotherms. For adsorption experiments, aminated samples were suspended in miliQ and the mass content was determined gravimetrically. 20 mg of cellulose was transferred to a 50 mL Falcon tube, followed by the addition of 20 mL of an appropriate metal stock (0.5, 1, 2, 3, 4, and 10 mM). Samples were left to equilibrate for 48 hours before collecting the particles *via* centrifugation and titrating the supernatant with 5 mM EDTA.

Adsorption kinetics. For adsorption kinetics experiments, 40 mg of an aminated cellulose sample was suspended in 40 mL of 10 mM of metal solution and samples were taken and titrated against 5 mM EDTA at predetermined intervals (15 min, 30 min, 1 h, 3 h, 6 h, 18 h, and 24 h).

pH-Dependent desorption. For pH-dependent desorption, 10 mg of the sample was suspended in 10 mL of 10 mM metal solution and allowed to equilibrate for 48 hours. The sample was centrifuged down and the metal solution was replaced with solutions of nitric acid with a predetermined pH and allowed to equilibrate for another 24 hours before centrifuging the particles and the supernatant was collected and titrated against 5 mM EDTA.5.

Results and discussion

Physical characterization of the adsorbent

Powder X-ray diffraction. The synthesis of tris-(2-aminoethyl) amine (TAEA) modified cellulose was performed by following a straightforward procedure. First, the substrate was made susceptible to nucleophilic substitution by chlorination with thionyl chloride in N,N -dimethylformamide. During the chlorination step, the accessible hydroxyl groups present on the AGU of cellulose were converted into chlorine ones, which then undergo nucleophilic substitution using one of

the amine groups present on TAEA to form the desired product.

One potential issue, depending on the application, with this approach, however, is that the chlorination of cellulose leads to a reduction of hydrogen-bonding along the solvent-accessible surface, which in turn allows the outer regions to dissolve in DMF. This will then precipitate out when exchanging solvent during washing or workup, leading to a change in morphology and crystallinity of the cellulose samples. The change in the cellulose structure as a result of reactive dissolution was clearly observed by pXRD (Fig. S1†). Here, we see a change in crystallinity and phase between pristine cellulose nanocrystals, composed of the Cellulose I phase, and the chlorinated product as a result of the reactive dissolution and subsequent regeneration of cellulose by precipitation in water. Further reaction of the chlorinated material with tris(2-aminoethyl)amine leads to a certain increase in crystallinity. X-ray patterns of modified products, as expected for a modified less crystalline polymer, showed essentially one broad peak with a slight shift to larger 2Theta due to the compression of hydrogen bonding as a result of the substitution of hydroxyl groups.

Textural characteristics of the cellulose–TAEA sample were investigated (Fig. S3†). Thus, the Brunauer–Emmett–Teller specific surface area (S_{BET}) was determined from the low-temperature nitrogen adsorption/desorption isotherms and found to be $11 \text{ m}^2 \text{ g}^{-1}$. The shape of the isotherm confirms the non-porous or macroporous surface of the material.⁵⁷ The pore-size distribution by volume and area was obtained using the Barret–Joyner–Halenda (BJH) method⁵⁸ by the desorption branch of the isotherms for the cellulose–TAEA sample. The BJH cumulative surface area and volume of pores between 1.7 nm and 300 nm were found to be $10.3 \text{ m}^2 \text{ g}^{-1}$ and $0.025 \text{ cm}^3 \text{ g}^{-1}$, whereas the BJH average pore width was 9.63 nm. Determination of the nano cellulose surface by nitrogen sorption is challenging because this material collapses, losing porosity even on freeze-drying that was applied. The data indicate that the surface of nano cellulose is not an active player in the adsorption process as the uptake seems to be related firsthand to the content of the functional ligand.

Fourier transform infrared spectroscopy (FTIR). In pristine cellulose nanocrystals derived from cotton by sulphuric acid hydrolysis, we can observe a strong broad peak at 3340 cm^{-1} (Fig. 1) which was attributed to OH stretch from hydroxyl present in cellulose and partly to moisture. Additionally, we observed several partly overlapping strong vibrations around 2910 cm^{-1} which were attributed to C–H stretching vibrations in the anhydroglucose backbone of the cellulose nanocrystals.

The relative position of most observed vibrations in the $3000\text{--}2800 \text{ cm}^{-1}$ window remains essentially unchanged except for their transmission intensity, which may be attributed to the regeneration of the cellulose matrix observed *via* PXRD (Fig. S1†). After chlorination, a distinctly new peak appeared around 1725 cm^{-1} , which disappeared after amination. In addition, a small shift from 1650 to 1665 cm^{-1} was observed which may be attributed to N–H bend vibrations,

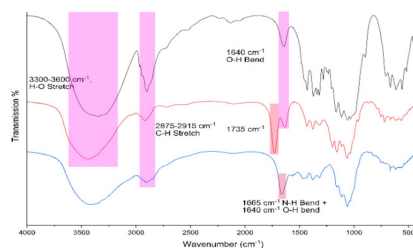


Fig. 1 FTIR spectrum of pristine cellulose nanocrystals derived from cotton by sulfuric acid hydrolysis (black), chlorinated CNCs from SOCl_2 in DMF (red) and TAEA-modified cellulose (blue).

indicating the successful grafting of tris(2-aminoethyl)amine onto the cellulose matrix.

Scanning electron microscopy (SEM)/energy dispersive X-ray scattering (EDS). This change in morphology observed by PXRD is further corroborated by AFM and SEM (Fig. 2A–F), in which we observed clear morphological changes between pristine CNCs derived from cotton and the final aminated product. In the original pristine CNCs, the rod-shaped CNCs ($\sim 40 \times 150 \text{ nm}$, AFM, Fig. 2A and B) form ordered films with the cellulose self-assembling along the longitudinal direction of the crystal (Fig. 2A). Chlorination of the pristine CNCs by thionyl chloride in N,N' -dimethylformamide leads to a change in morphology where the product undergoes a transformation from rod-shaped CNCs into global cellulose nanoparticles as a result of reactive dissolution, followed by precipitation and

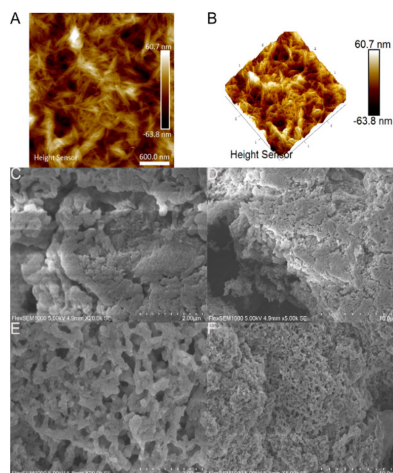


Fig. 2 AFM images of pristine CNCs derived from cotton by acid hydrolysis (A and B), and scanning electron microscopy images of chlorinated CNC derived from cotton CNCs in DMF (C and D) and TAEA-aminated cellulose (E and F).

high-shear mixing. Energy dispersive X-ray scattering (EDS) was used to analyse the surface composition of the materials. EDS analysis of the intermediate chlorinated product showed an appreciable chlorine content of approximately $2.81 \pm 0.04 \text{ mmol g}^{-1}$ for the chlorinated product. In an attempt to maintain the original CNC structure, we attempted to chlorinate lyophilized CNCs in dry toluene instead; however, this resulted in only very minor amounts of chlorine within the sample, in the range of $0.05 \pm 0.02 \text{ mmol g}^{-1}$.

The resulting chlorinated product was aminated and after lyophilisation of the sample; the final product appeared to consist of globular nanoparticles in the 150–250 nm range. EDS analysis of the resulting aminated product showed an appreciable amine content of approximately $4.67 \pm 1.55 \text{ mol g}^{-1}$ nitrogen, corresponding to $1.17 \pm 0.39 \text{ mmol g}^{-1}$ amine. The resulting material still contains $1.76 \pm 0.06 \text{ mmol g}^{-1}$ chlorine and $0.12 \pm 0.02 \text{ mmol g}^{-1}$ sulphur in addition to the newly installed amine. The remaining chlorine in the sample may be attributed in part to the reaction being incomplete and in addition, partly attributed to the internalization of chlorine-containing cellulose chains, making it inaccessible for the subsequent amination step. For metal selectivity experiments, it is important to note the presence of elements not associated with the ligand as these may in turn interact with metal cations by coordinative covalent bonds or electrostatic interactions. Conductometric titration of the final aminated product leads to an amine content of 0.84 mmol g^{-1} (Fig. S2†). The discrepancy between EDS and conductometric titrations may be explained by the surface availability of the amine in aqueous media after lyophilisation, requiring a longer equilibration time.

Metal sequestration characterization

Adsorption characteristics. In order to evaluate the suitability of the material for metal sequestering in the recycling of REE-based materials, adsorption isotherms for the materials were measured using REE neodymium, samarium and the LTMs nickel and cobalt as these are commonly found in REE-based permanent magnets. The results showed that with the increasing initial metal concentration, the adsorption from solution increases until a maximum is reached due to the saturation of available surface binding sites (Fig. 3). The maximum adsorption capacities and the corresponding ligand stoichiometries can be found in Table 1.

Based on these results, the TAEA-modified cellulose material is promising for metal sequestering, obtaining near 1 : 1 ligand to metal stoichiometry, indicating that the adsorption capacity of the material is inherently tied to the ligand grafting, *i.e.* higher ligand grafting will increase the metal adsorption capacity.

To evaluate the rate at which metals are removed from solution, the adsorption kinetics were studied (see Fig. 4), which showed that for cobalt(II), the adsorption occurs rapidly, reaching 53% within an hour and 83% within 6 hours. The next metal with the highest rate of adsorption is neodymium, showing 40% adsorption in 6 hours, followed by nickel(II) at 34% in 6 hours. Samarium in comparison is rather slow to adsorb, reaching 61% adsorption in a 24-hour window. As cobalt(II) is rapidly adsorbed by TAEA-functionalized cellulose, it may provide some kinetic selectivity between the separation of cobalt from samarium in CoSm magnets and materials with similar compositions. The separation between nickel and neo-

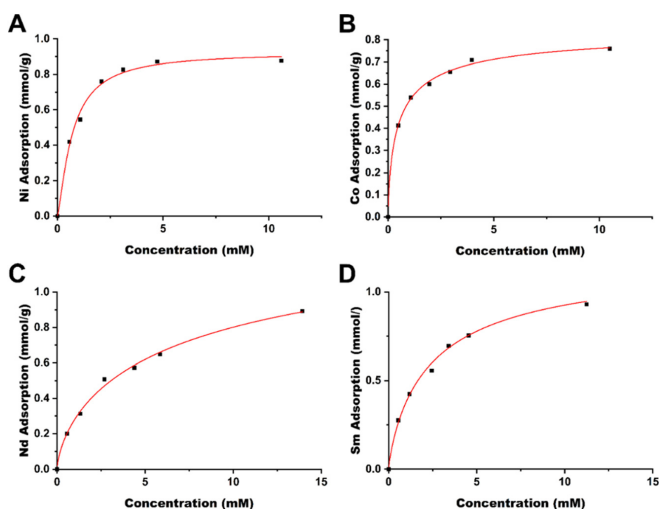


Fig. 3 Langmuir isotherms of late transition metals (A) Ni and (B) Co and rare earth elements (C) Nd and (D) Sm.

Table 1 Adsorption capacity and metal ligand stoichiometry of tris(2-aminoethyl)amine modified-cellulose

Metal	Adsorption capacity [mmol g ⁻¹]	Metal/ligand stoichiometry
Co	0.76	0.90
Ni	0.88	1.04
Nd	0.79	0.94
Sm	0.82	0.97

Table 2 Metal selectivity by tris(2-aminoethyl)amine modified-cellulose as determined by EDS analysis of the adsorbent after equilibrating in equimolar aqueous metal mixtures

Metal mixture	Ratio
Ni : Co	1 : 1.1
Nd : Ni	1 : 5.1
Sm : Co	1 : 5.7
Sm : Nd	1 : 1.2

dymium in comparison, however, does not yield any significant kinetic selectivity.

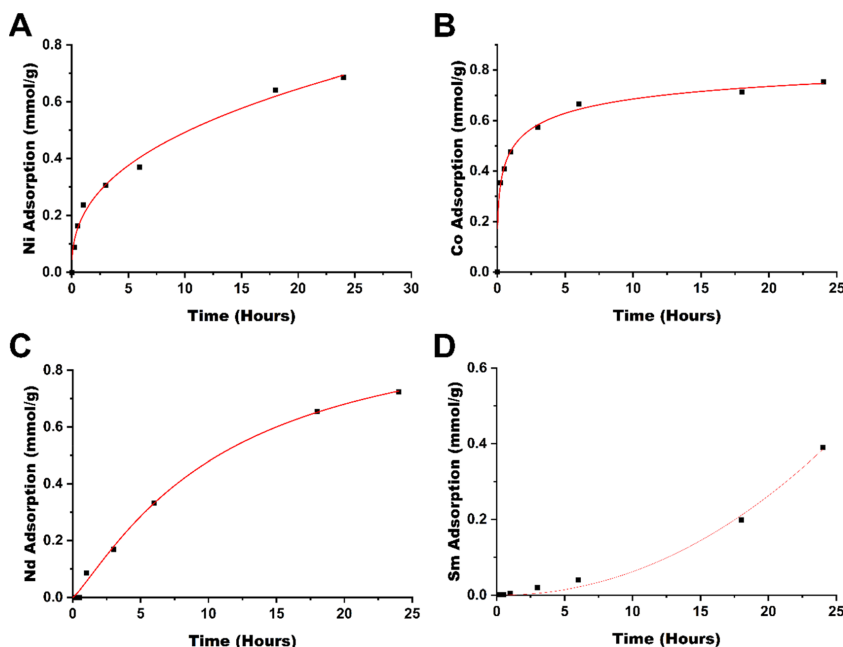
As the intended purpose of the material is to selectively remove one class of metal (LTM/REE) from solution, the adsorption selectivity between equimolar mixtures of different metal ions by the material at a solution equilibrium was studied by EDS spectroscopy. By looking at the elemental ratios between metals on different spots we can estimate the average selectivity of the material. The result of EDS analysis can be viewed in Table 2. Briefly, when presented with an equimolar mixture between a lanthanide and a late transition metal, the TAEA functionalized material has a 5 : 1 preference towards the adsorption of late transition metals (Fig. S4 and S5†). When presented with an equimolar mixture of cobalt(II) and nickel(II), the product shows negligible selectivity towards cobalt (Fig. S6†). Similarly for a samarium(III)/neodymium(III)

mixture, there is a negligible preference towards neodymium (Fig. S7†), indicating that the material is suitable for selectively adsorbing late transition metals over lanthanides from solution.

The difference between the adsorption kinetics of Sm(III) and Nd(III) is difficult to explain. It might originate from different features in the nucleation and growth of the corresponding hydroxides formed on the interaction of the ions with a local basic medium in the proximity of poly-amino ligands (please see below).

In addition, desorption tests were performed at pH values 0, 1, 2, 3, 4 and 5 using nitric acid in 50 mL Falcon tubes. After the samples were equilibrated for 48 hours, the samples were centrifuged and the pH was adjusted to predetermined values.

The samples were placed on an orbital shaker for 24 hours, after which the nanoparticles were separated by centrifugation

**Fig. 4** Adsorption kinetics of (A) Ni, (B) Co, (C) Nd, and (D) Sm by cell-TAEA in a 24 h period.

(5500 rpm, 10 min), the supernatant was collected and the pH was adjusted with a base and titrated against EDTA to determine the desorbed metal amount. The results of the desorption experiments can be seen in Fig. 5 and are summarized in Table TS1.† For most metals at least 50% recovery is possible, expect for cobalt, which appears to be more resilient to acid treatment for recycling of the material.

Single-crystal X-ray diffraction. Aiming to get insights into possible metal complexes that may form on the surface of the modified cellulose in the presence of TAEA, attempts were made to grow X-ray-quality single crystals. In order to achieve this, solutions of the corresponding metals as nitrate salts were prepared in milliQ water, followed by the addition of 1 molar equivalent of the ligand and the solutions were allowed to slowly evaporate at room temperature in *ca.* 50% humidity, produced in the case of Ni(II) violet block-shaped crystals. The crystallization residue had a very uniform appearance, indicating complete conversion into a single complex form.

The single crystal X-ray study revealed a molecular structure (see Fig. 6), where the Ni(II) cation is octahedrally coordinated with the coordination sphere composed of the four nitrogen atoms of the TAEA ligand, one oxygen atom of the coordinated water molecule and one more oxygen atom from the inner-sphere coordinated nitrate ion. The bond lengths are essentially equivalent for all the Ni–N contacts (Ni(1)–N(2) 2.085(6), Ni(1)–N(3) 2.109(6), Ni(1)–N(4) 2.072(6), and Ni(1)–N(5) 2.095(6) Å) and the coordinated nitrate oxygen atom (Ni(1)–O(1) 2.101(5) Å). The bond to hydrating the water molecule is considerably longer, Ni(1)–O(1B) 2.201(5) Å, which is a commonly observed feature. Bonding within the Ni(TAEA) fragment is comparable with that observed earlier in the structures of Ni(II) with this ligand such as Ni(TAEA)(NO₃)₂⁵⁴ and [Ni₃(TAEA)₄(H₂O)₂(TMEDA)₂]Cl₆.⁵⁹ In these latter structures, the nature of bonding was very analogous with essentially equal bonds to the five neighbours, four N-atoms of the TAEA ligands in both cases (Ni–N 2.055–2.095 and 2.080–2.117 Å respectively) and one more atom – either an O-atom in one of the nitrate ligands or a N-atom of the additional TMEDA ligand (2.075 Å in both cases). The sixth bond is much longer and stays for bonding either to an oxygen atom in an

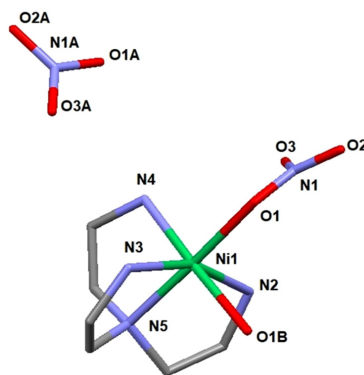


Fig. 6 Molecular structure of [Ni(TAEA)(H₂O)(NO₃)](NO₃) (1).

additional nitrate ion or to that in a water molecule. Observation of this manner of bonding actually is rather peculiar, indicating the most probable Jahn–Teller effect in the 3d⁸ configuration of the Ni(II) cation, resulting in the weakening of one bond in the octahedral coordination sphere permitting facile ligand exchange between the hydrating water and the nitrate ligand (Table 3).

Crystallization in a more humid environment in this case led to a structure with the water molecule included in the coordination sphere and “free” nitrate ion. The late transition metal cations (an analogous Co(II) structure has been reported with two nitrite ligands bound in the coordination sphere *via* N-atoms, Co(TAEA)(NO₂)₂⁵⁵ – all bonds essentially equal in length) are apparently forming stable complexes with the chelating TAEA ligand, which explains the stronger selectivity of bonding towards Ni(II) and Co(II) compared to REE of the reported adsorbent.

In the case of REE, the product of mass crystallization from an equimolar mixture of metal nitrate and TAEA ligand

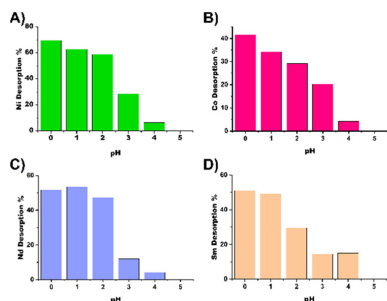


Fig. 5 pH-Dependent desorption of (A) Ni, (B) Co, (C) Nd and (D) Sm from cell TAEA.

Table 3 Details of data collection and refinement for compound 1

Compound	1
Chemical composition	C ₆ H ₂₀ N ₆ NiO ₇
Formula weight	347.09
Crystal system	Monoclinic
Space group	P2(1)/c (14)
R ₁	0.0836
wR ₂	0.1990
a [Å]	8.3129(6)
b [Å]	14.3595(11)
c [Å]	11.7358(9)
α [°]	90
β [°]	91.8660(10)
γ [°]	90
V [Å ³]	1400.15(18)
T [K]	296(2)
Z	4
No. of obs. independent refl., I ≥ 2σ(I)	2364
Residual electron density max	1.635

turned out to be solely $[\text{N}(\text{C}_2\text{H}_4\text{NH}_3)_3](\text{NO}_3)_3$ (2). The nature of the obtained product was the same for both Dy(III) and Sm(III) as indicated by unit cell parameter determination for multiple single crystals from the reaction mixture (see Table TS2 and Fig. S8†). The obtained structure is identical to that described by Bianchi *et al.*⁶⁰ This shows that the sorption mechanism of REE is supposedly principally different from that for LTM and is not involving inner sphere complexation with the grafted poly-amino ligand. The REE sorption may involve retention of either the hydrated cations or hydroxide forms. An additional argument for this option is provided by the work of Roesky *et al.*,⁶¹ where the structures of several mixed-ligand complexes of Ni(II) and REE(III) with TAEA and Schiff base carboxylate were reported. In the competition between ligands, the Ni(II) cations were binding exclusively to nitrogen atoms in TAEA and REE – to the carboxylate oxygen atoms (see Fig. S9†). Such behavior is well in line with Pearson's hard and soft acid-base theory⁶² as Ni(II) is a soft acid binding to a soft amino ligand, while REE cations are typically hard acids binding to hard oxygen donor bases.

Conclusions

The possibility of grafting a specific ligand permitting sequestration and separation of REE and LTM on a bio-based adsorbent matrix of nano cellulose has been demonstrated. Tris(2-aminoethyl)amine was attached to cellulose nanocrystals *via* a two-step route involving chlorination and amination steps. The morphology and crystallinity of the matrix were preserved, as demonstrated by PXRD and microscopy techniques. The produced adsorbent showed relatively quick adsorption kinetics at room temperature and pH = 6 for LTM, especially for Co(II), and considerably slower for REE. The adsorption capacity achieved values of *ca.* 0.8 mmol g⁻¹, corresponding to the functional ligand content and thus demonstrating the formation of surface complexes with 1 : 1 composition for all studied cations. The adsorbent revealed pronounced selectivity towards LTM compared to REE. The desorption of target cations was investigated as a function of pH, demonstrating comparably stronger retention of LTM compared to REE. The X-ray single crystal studies of molecular model compounds, $[\text{Ni}(\text{TAEA})(\text{H}_2\text{O})(\text{NO}_3)](\text{NO}_3)$ (1) and $[\text{N}(\text{C}_2\text{H}_4\text{NH}_3)_3](\text{NO}_3)_3$ (2), gave insights into the possible mode of action of the adsorbent and its cation and anion exchange processes.

Author contributions

Investigation, analysis, writing, and draft preparation – T. C. B.; Crystallography and writing – review and editing – V. G. K.; nitrogen adsorption/desorption and writing – T. M. B.; FTIR and AFM investigations, funding acquisition, and writing – review and editing – G. A. S.

Conflicts of interest

There are no conflicts to declare.

Acknowledgements

The authors would like to express their gratitude to Andreas Orthaber at Uppsala University for access to the single crystal X-ray diffractometer. In addition, the authors would like to express their gratitude to the Swedish Research Council STINT for the support of the grant Nanocellulose Based Materials for Environmental and Theranostic Applications and the Faculty of Natural Resources and Agricultural Sciences, SLU for the support of T. C. B.'s PhD position. The ÅForsk Research Foundation is gratefully acknowledged for the support of the grant Separation and Recycling of Rare Earth Elements and Nickel and Cobalt from magnets, ÅF 21-75.

References

- 1 J. B. H. Gordon, B. Haxel and G. J. Orris, *Rare Earth Elements – Critical Resources for High Technology*, <https://pubs.usgs.gov/fs/2002/fs087-02/>, (accessed 26/09/2022, 2022).
- 2 V. Balaram, *Geosci. Front.*, 2019, **10**, 1285–1303.
- 3 O. Serpell, W. Y. Chu and B. Paren, *Rare Earth Elements: A Resource Constraint of the Energy Transition*, <https://kleinmanenergy.upenn.edu/research/publications/rare-earth-elements-a-resource-constraint-of-the-energy-transition/>, (accessed 26/09/2022, 2022).
- 4 J. Cui, M. Kramer, L. Zhou, F. Liu, A. Gabay, G. Hadjipanayis, B. Balasubramanian and D. Sellmyer, *Acta Mater.*, 2018, **158**, 118–137.
- 5 Y. Yang, A. Walton, R. Sheridan, K. Güth, R. Gauß, O. Gutfleisch, M. Buchert, B.-M. Steenari, T. Van Gerven, P. T. Jones and K. Binnemans, *J. Sustainable Metall.*, 2016, **3**, 122–149.
- 6 A. Porvali, S. Ojanen, B. P. Wilson, R. Serna-Guerrero and M. Lundström, *J. Sustainable Metall.*, 2020, **6**, 78–90.
- 7 F. Holmberg, Licentiate, Chalmers University of Technology, 2017.
- 8 A. B. Patil, V. Paetzel, R. P. W. J. Struis and C. Ludwig, *Separations*, 2022, **9**, 56.
- 9 B. Deng, X. Wang, D. X. Luong, R. A. Carter, Z. Wang, M. B. Tomson and J. M. Tour, *Sci. Adv.*, 2022, **8**, eabm3132.
- 10 A. Porvali, V. Agarwal and M. Lundström, *Waste Manage.*, 2020, **107**, 66–73.
- 11 K. Korkmaz, M. Alemrajabi, Å. C. Rasmuson and K. M. Forsberg, *Sep. Purif. Technol.*, 2020, **234**, 115812.
- 12 S. Peelman, Z. H. I. Sun, J. Sietsma and Y. Yang, Presented in part at the 1st European Rare Earth Resources Conference, Milos, 07/09/2014, 2014.
- 13 R. Q. Honaker, W. Zhang and J. Werner, *Energy Fuels*, 2019, **33**, 5971–5980.

- 14 A. Yuksekdog, B. Kose-Mutlu, B. Zeytuncu-Gokoglu, M. Kumral, M. R. Wiesner and I. Koyuncu, *Environ. Sci. Pollut. Res. Int.*, 2022, **29**, 7772–7781.
- 15 M. Gergoric, C. Ekberg, M. R. S. J. Foreman, B.-M. Steenari and T. Retegan, *J. Sustainable Metall.*, 2017, **3**, 638–645.
- 16 N. Swain and S. Mishra, *J. Cleaner Prod.*, 2019, **220**, 884–898.
- 17 A. Rout and K. Binnemans, *Dalton Trans.*, 2014, **43**, 3186–3195.
- 18 Y. Hu, J. Florek, D. Lariviere, F. G. Fontaine and F. Kleitz, *Chem. Rec.*, 2018, DOI: [10.1002/tcr.201800012](https://doi.org/10.1002/tcr.201800012).
- 19 U. O. Aigbe, K. E. Ukhurebor, R. B. Onyancha, O. A. Osibote, H. Darmokoeseomo and H. S. Kusuma, *J. Mater. Res. Technol.*, 2021, **14**, 2751–2774.
- 20 H.-J. Kang, K.-G. An and D.-S. Kim, *J. Environ. Sci. Health, Part A: Toxic/Hazard. Subst. Environ. Eng.*, 2004, **39**, 3015–3028.
- 21 L. J. Westholm, E. Repo and M. Sillanpää, *Environ. Sci. Pollut. Res. Int.*, 2014, **21**, 9109–9128.
- 22 S. Martini, S. Afroze and K. Ahmad Roni, *Alexandria Eng. J.*, 2020, **59**, 1637–1648.
- 23 S. Feng, X. Du, M. Bat-Amgalan, H. Zhang, N. Miyamoto and N. Kano, *Int. J. Mol. Sci.*, 2021, **22**, 3447.
- 24 D. L. Ramasamy, A. Wojtuś, E. Repo, S. Kalliola, V. Srivastava and M. Sillanpää, *Chem. Eng. J.*, 2017, **330**, 1370–1379.
- 25 D. C. da Silva Alves, B. Healy, L. A. A. Pinto, T. R. S. Cadaval Jr. and C. B. Breslin, *Molecules*, 2021, **26**, 594.
- 26 A. Chowdhury, S. K. Das, S. Mondal, S. Ruidas, D. Chakraborty, S. Chatterjee, M. K. Bhunia, D. Chandra, M. Hara and A. Bhaumik, *Environ. Sci.: Nano*, 2021, **8**, 2641–2649.
- 27 S. Mondal, S. Chatterjee, S. Mondal and A. Bhaumik, *ACS Sustainable Chem. Eng.*, 2019, **7**, 7353–7361.
- 28 Z. Dong, J. A. Mattocks, G. J. P. Deblonde, D. Hu, Y. Jiao, J. A. Cotruvo and D. M. Park, *ACS Cent. Sci.*, 2021, **7**, 1798–1808.
- 29 X. Xie, K. Yang, Y. Lu, Y. Li, J. Yan, J. Huang, L. Xu, M. Yang and Y. Yan, *J. Hazard. Mater.*, 2022, **438**, 129561.
- 30 M. L. Pitcher, B. Huntington, J. Dominick and A. Sheikhi, *Chem. Eng. J.*, 2022, **447**, 137418.
- 31 L. Ringqvist, A. Holmgren and I. Öborn, *Water Res.*, 2002, **36**, 2394–2404.
- 32 R. M. Ashour, M. Samouhos, E. Polido Legaria, M. Svärd, J. Höglblom, K. Forsberg, M. Palmlöf, V. G. Kessler, G. A. Seisenbaeva and Å. C. Rasmuson, *ACS Sustainable Chem. Eng.*, 2018, **6**, 6889–6900.
- 33 E. Polido Legaria, I. Saldan, P. Svedlindh, E. Wetterskog, K. Gunnarsson, V. G. Kessler and G. A. Seisenbaeva, *Dalton Trans.*, 2018, **47**, 1312–1320.
- 34 A. Vardanyan, A. Guillon, T. Budnyak and G. A. Seisenbaeva, *Nanomaterials*, 2022, **12**, 974.
- 35 I. Anastopoulos, A. Bhatnagar and E. C. Lima, *J. Mol. Liq.*, 2016, **221**, 954–962.
- 36 D. Dupont, W. Brullot, M. Bloemen, T. Verbiest and K. Binnemans, *ACS Appl. Mater. Interfaces*, 2014, **6**, 4980–4988.
- 37 A. Mezy, A. Vardanyan, A. Garcia, C. Schmitt, M. Lakić, S. Krajnc, G. Daniel, A. Košak, A. Lobnik and G. A. Seisenbaeva, *Sep. Purif. Technol.*, 2021, **276**, 119340.
- 38 G. A. Seisenbaeva, I. V. Melnyk, N. Hedin, Y. Chen, P. Eriksson, E. Trzop, Y. L. Zub and V. G. Kessler, *RSC Adv.*, 2015, **5**, 24575–24585.
- 39 E. Polido Legaria, M. Samouhos, V. G. Kessler and G. A. Seisenbaeva, *Inorg. Chem.*, 2017, **56**, 13938–13948.
- 40 S. H. Gellman, *Chem. Rev.*, 1997, **97**, 1231–1232.
- 41 Y. M. Chen, C. Z. Wang, Q. Y. Wu, J. H. Lan, Z. F. Chai and W. Q. Shi, *Dalton Trans.*, 2021, **50**, 15576–15584.
- 42 N. Morin-Crini, S. Loiacono, V. Placet, G. Torri, C. Bradu, M. Kostić, C. Cosentino, G. Chanet, B. Martel, E. Lichtfouse and G. Crini, *Environ. Chem. Lett.*, 2018, **17**, 393–408.
- 43 D. Stewart, *Ind. Crops Prod.*, 2008, **27**, 202–207.
- 44 A. Boujemaoui, S. Mongkhontreerat, E. Malmstrom and A. Carlmark, *Carbohydr. Polym.*, 2015, **115**, 457–464.
- 45 D. Klemm, B. Heublein, H. P. Fink and A. Bohn, *Angew. Chem., Int. Ed.*, 2005, **44**, 3358–3393.
- 46 A. F. Jozala, L. C. de Lencastre-Novais, A. M. Lopes, V. de Carvalho Santos-Ebinuma, P. G. Mazzola, A. Pessoa Jr., D. Grotto, M. Gerenutti and M. V. Chaud, *Appl. Microbiol. Biotechnol.*, 2016, **100**, 2063–2072.
- 47 A. C. O'Sullivan, *Cellulose*, 1997, **4**, 173–207.
- 48 K. H. Gardner and J. Blackwell, *Biopolymers*, 1974, **13**, 1975–2001.
- 49 R. D. S. Bezerra, R. C. Leal, M. S. da Silva, A. I. S. Morais, T. H. C. Marques, J. A. Osajima, A. B. Meneguim, H. da Silva Barud and E. C. da Silva Filho, *Molecules*, 2017, **22**, 2039.
- 50 O. Hamed, B. A. Lail, A. Deghles, B. Qasem, K. Azzaoui, A. A. Obied, M. Algarra and S. Jodeh, *Environ. Sci. Pollut. Res. Int.*, 2019, **26**, 28080–28091.
- 51 T. Oshima, K. Kondo, K. Ohto, K. Inoue and Y. Baba, *React. Funct. Polym.*, 2008, **68**, 376–383.
- 52 X. Huang, X. Chang, Q. He, Y. Cui, Y. Zhai and N. Jiang, *J. Hazard. Mater.*, 2008, **157**, 154–160.
- 53 A. Badieli, A. Mirahsani, A. Shahbazi, H. Younesi and M. Alizadeh, *Environ. Prog. Sustainable Energy*, 2014, **33**, 1242–1250.
- 54 D. Sivanesan, K. H. Song, S. K. Jeong and H. J. Kim, *Catal. Commun.*, 2019, **120**, 66–71.
- 55 M. K. Saha and I. Bernal, *C. R. Chim.*, 2007, **10**, 1170–1179.
- 56 M. S. Reid, M. Villalobos and E. D. Cranston, *Langmuir*, 2017, **33**, 1583–1598.
- 57 K. S. W. Sing, *Pure Appl. Chem.*, 1985, **57**, 603–619.
- 58 E. P. Barrett, L. G. Joyner and P. P. Halenda, *J. Am. Chem. Soc.*, 1951, **73**, 373–380.
- 59 K. Matelková, J. Moncol, R. Herchel, L. Dlhán, R. Ivaníková, I. Svoboda, Z. Padělková and A. Mašlejová, *Polyhedron*, 2013, **56**, 1–8.
- 60 C. Bazzicalupi, A. Bencini, A. Bianchi, A. Danesi, C. Giorgi and B. Valtancoli, *Inorg. Chem.*, 2009, **48**, 2391–2398.
- 61 A. Bhunia, M. Yadav, Y. Lan, A. K. Powell, F. Menges, C. Riehn, G. Niedner-Schatteburg, P. P. Jana, R. Riedel, K. Harms, S. Dennen and P. W. Roesky, *Dalton Trans.*, 2013, **42**, 2445–2450.
- 62 R. G. Pearson, *J. Am. Chem. Soc.*, 1963, **85**, 3533–3539.

Supplementary materials

Tailoring a bio-based adsorbent for sequestration of Late Transition and Rare Earth Elements

Breijjaert, T.C.^a, Tetyana M. Budnyak^b, Kessler, V.G.^a, Seisenbaeva, G.S.^{a*}

^aDepartment of Molecular Sciences, Biocentrum, Swedish University of Agricultural Sciences, Almas Allé 5, Box 7015, SE-750 07 Uppsala, Sweden.

^bDivision of Nanotechnology and Functional Materials, Department of Materials Science and Engineering, Uppsala University, Box 35, 751 03 Uppsala, Sweden.

*Corresponding author: gulaim.seisenbaeva@slu.se

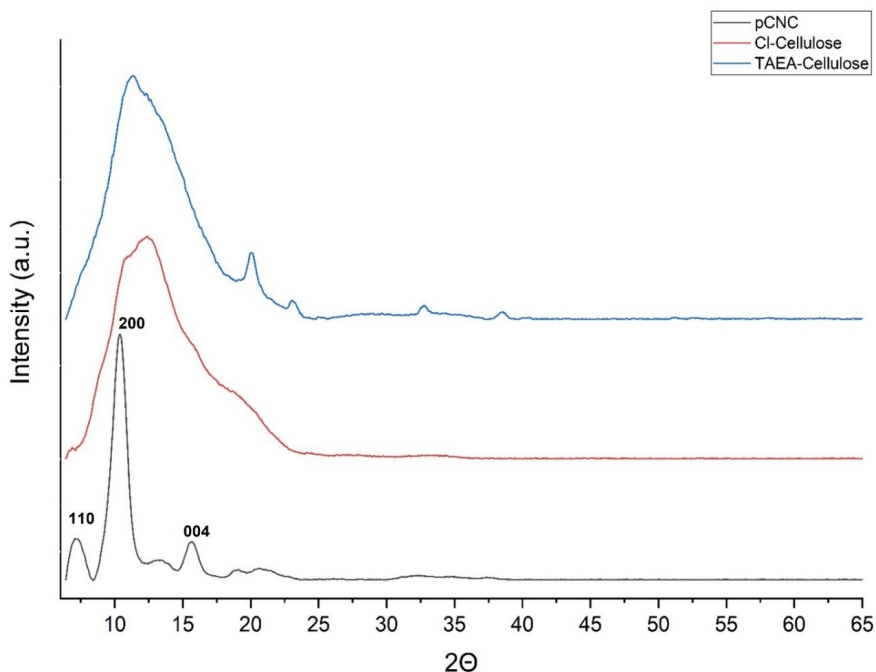


Figure S1. X-ray powder diffraction patterns of Pristine nanocellulose derived from cotton via sulfuric acid hydrolysis (black) – Cellulose I, Monoclinic, Space group $P2_1$, $a = 0.778$ nm, $b = 0.820$ nm, $c = 1.038$ nm, $\gamma = 96.51$ deg,^{S1,S2} Cellulose chlorinated in SOCl_2 in DMF (red) and tris(2-aminoethyl)amine modified cellulose.

References

- S1.** J. Gong, J. Li, Z. Xu, Z.Y. Xiang, L.H. Mo, Research on cellulose nanocrystals produced from cellulose sources with various polymorphs, *RSC Advances*, 2017, **7**, 33486-33493.
- S2.** M. Ioelovich, E. Larina, Parameters of crystalline structure and their influence on the reactivity of cellulose I, *Cellulose Chem. Technol.*, 1999, **33**, 3-12.

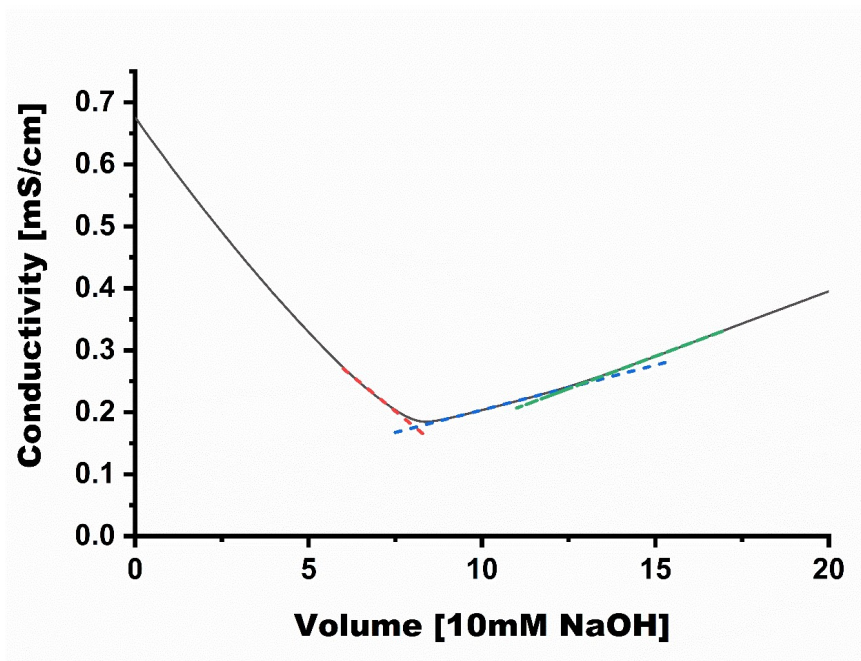


Figure S2. Conductometric titration of acidified tris(2-aminoethyl)amine modified cellulose

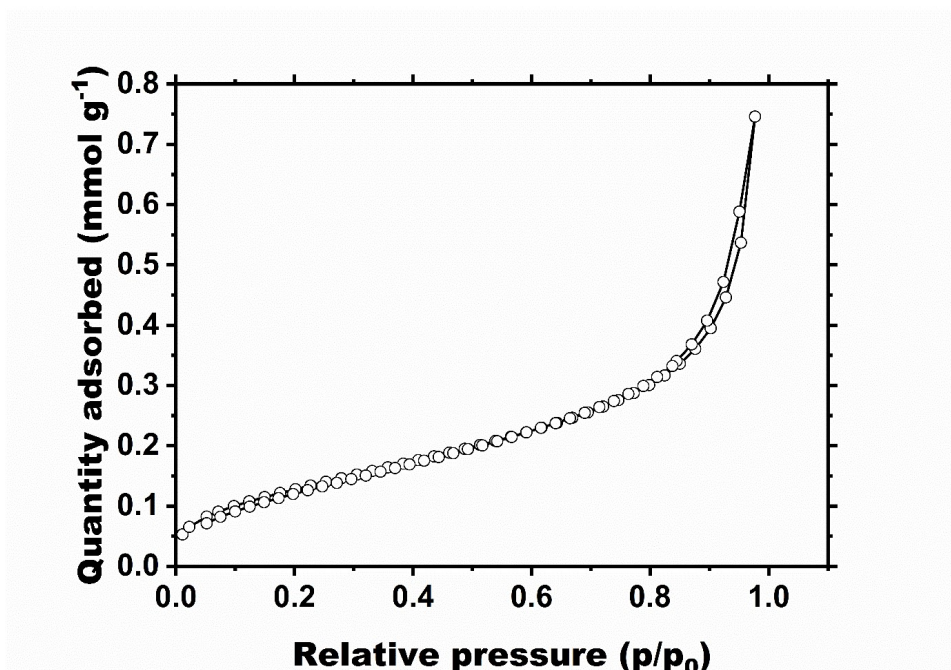


Figure S3. The nitrogen adsorption/desorption isotherm for the Cellulose-TAEA sample

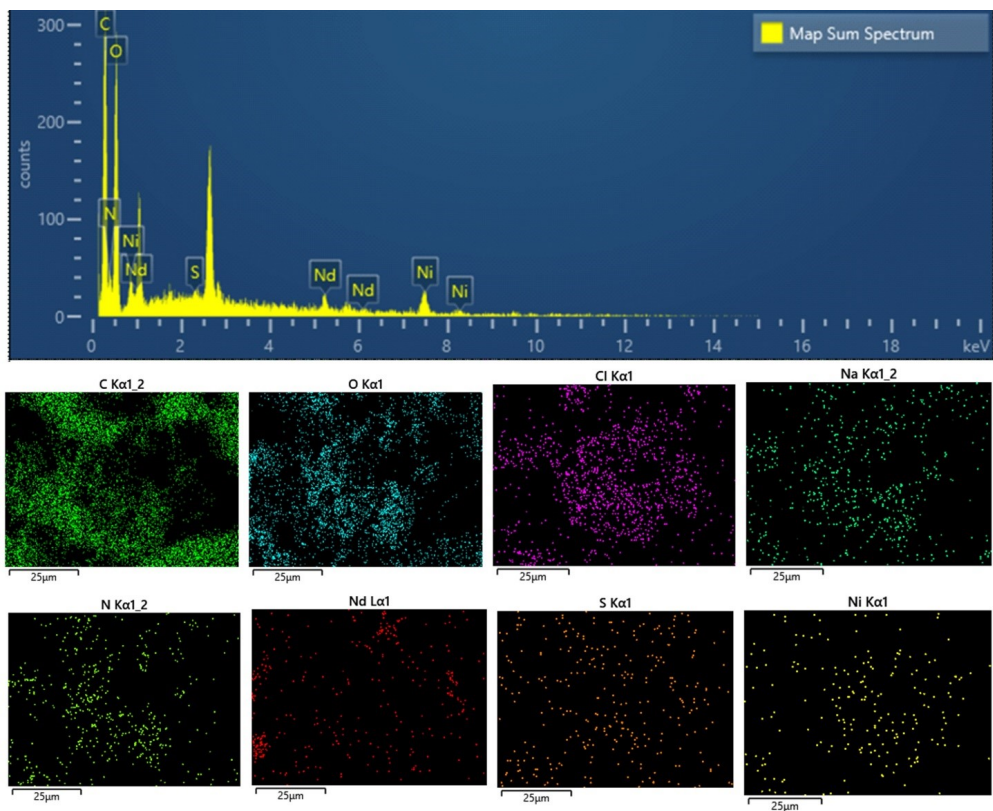


Figure S4. EDS map sum spectrum of cellulose-TAEA in the present of a equimolar mixture of Nickel(II) and Neodymium (III). (ca. 2at% Ni, 0.5at% Nd)

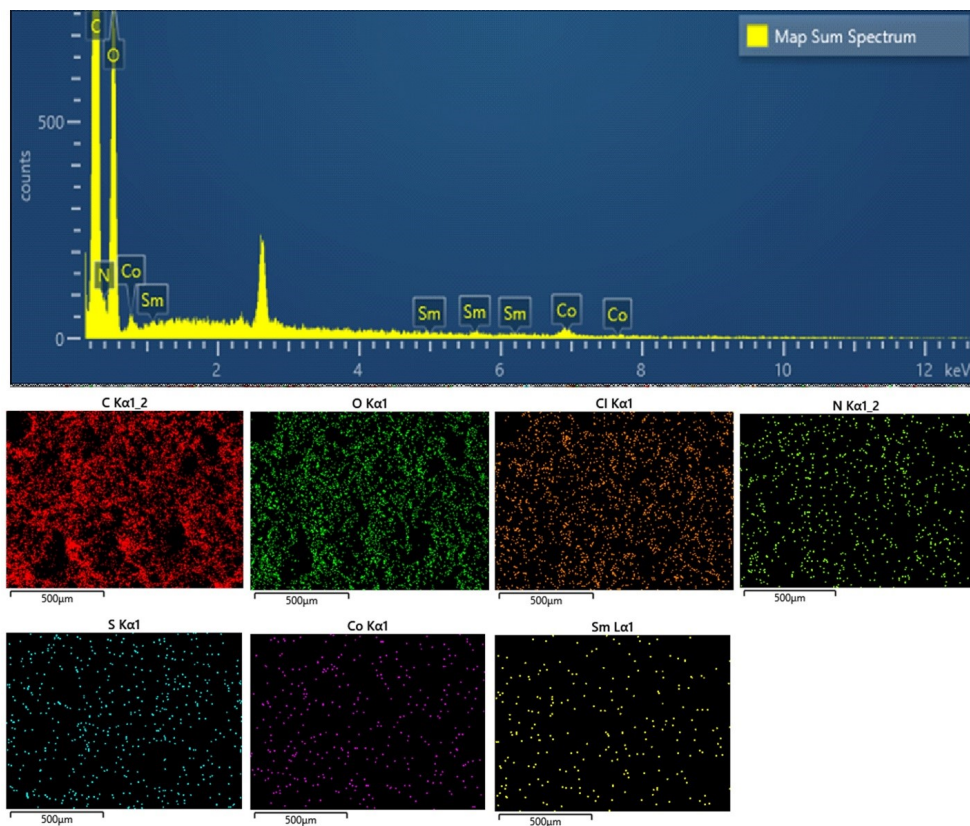


Figure S5. EDS map sum spectrum of cellulose-TAEA in the presence of an equimolar mixture of Cobalt(II) and Samarium(III). (ca. 0.3 at% Co, 0.07 at% Sm)

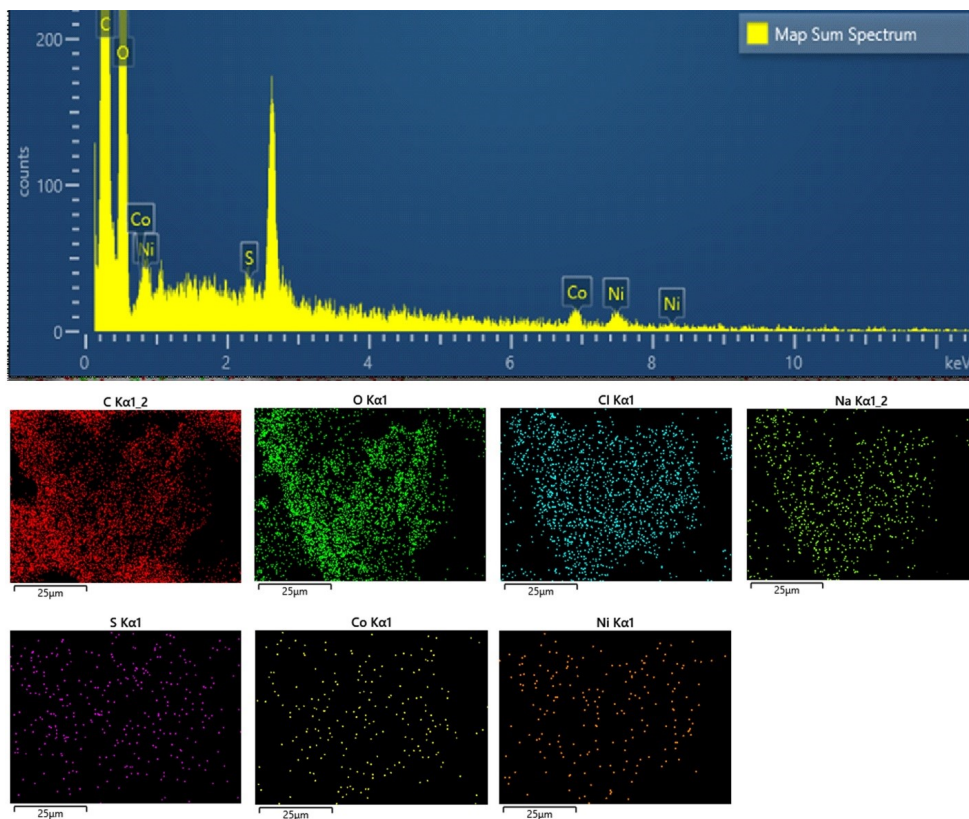


Figure S6. EDS map sum spectrum of cellulose-TAEA in the present of a equimolar mixture of Cobalt(II) and Nickel (II). (0.44 at% Co, 0.43 at% Ni).

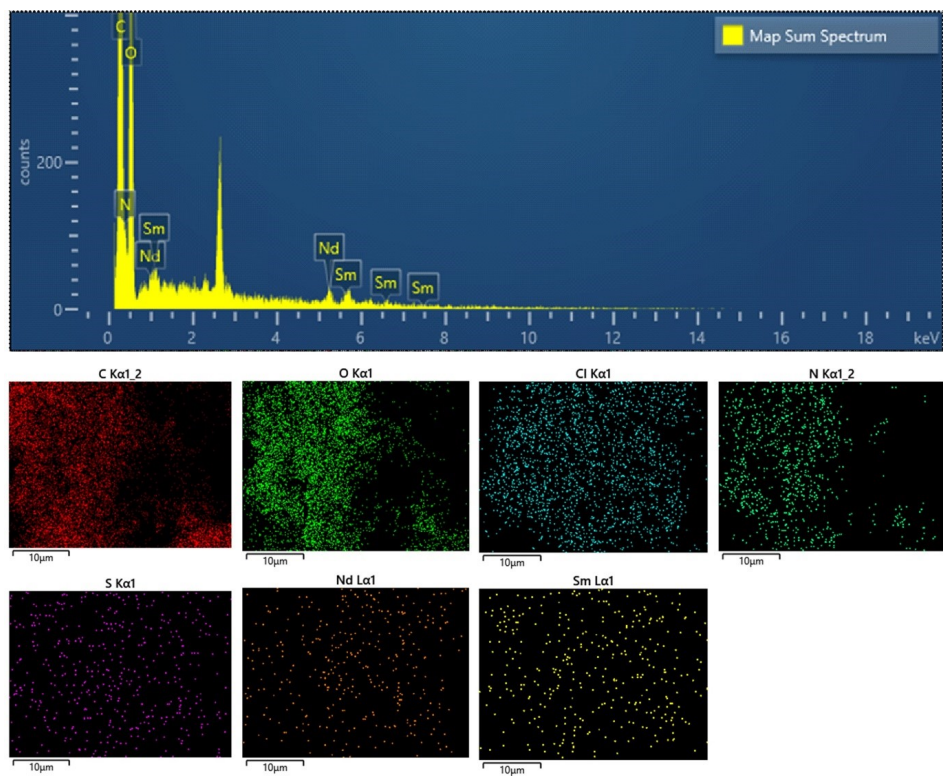


Figure S7. EDS map sum spectrum of cellulose-TAEA in the present of a equimolar mixture of Neodymium(III) and Samarium (III). (0.23 at% Nd, 0.19at% Sm).

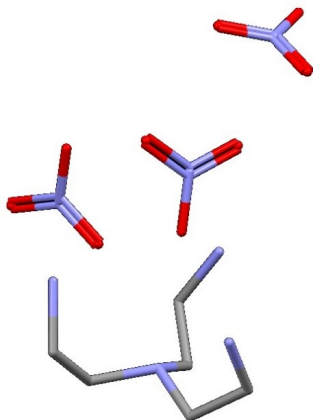


Figure S8. Molecular structure of $[N(C_2H_4NH_3)_3](NO_3)_3$, compound (2), generated by CCDC Mercury program using the data of ref. 52.

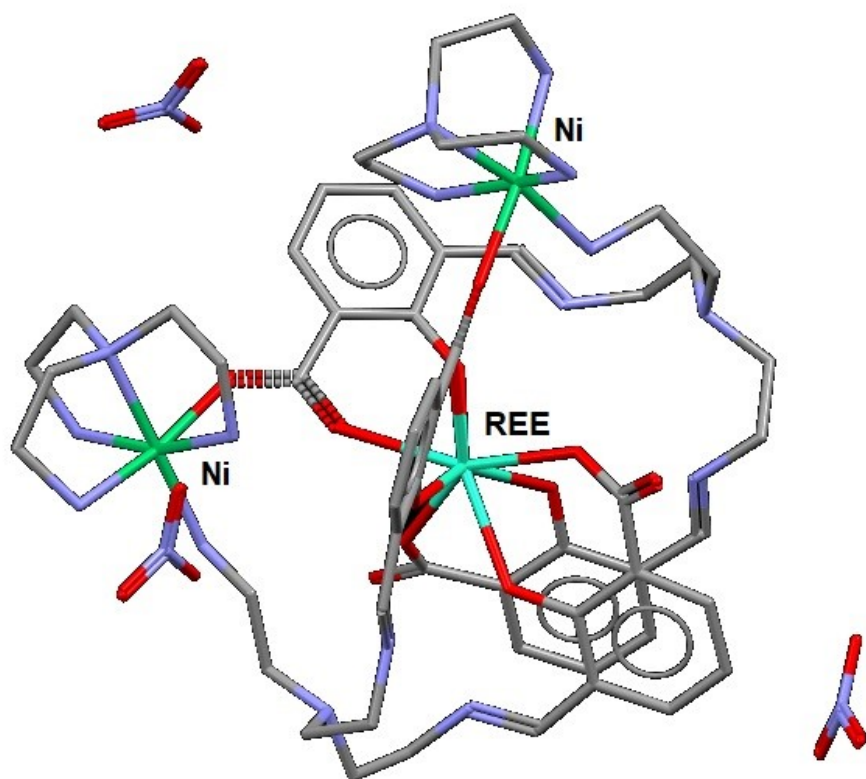


Figure S9. Molecular structure of REE{Ni(TAEA)(H₂L)}(NO₃)₃, generated by CCDC Mercury program using the data of ref. 53.

Table TS1. pH-dependent desorption of Co, Ni, Sm, Nd from Tris(2-aminoethyl)amine modified-cellulose

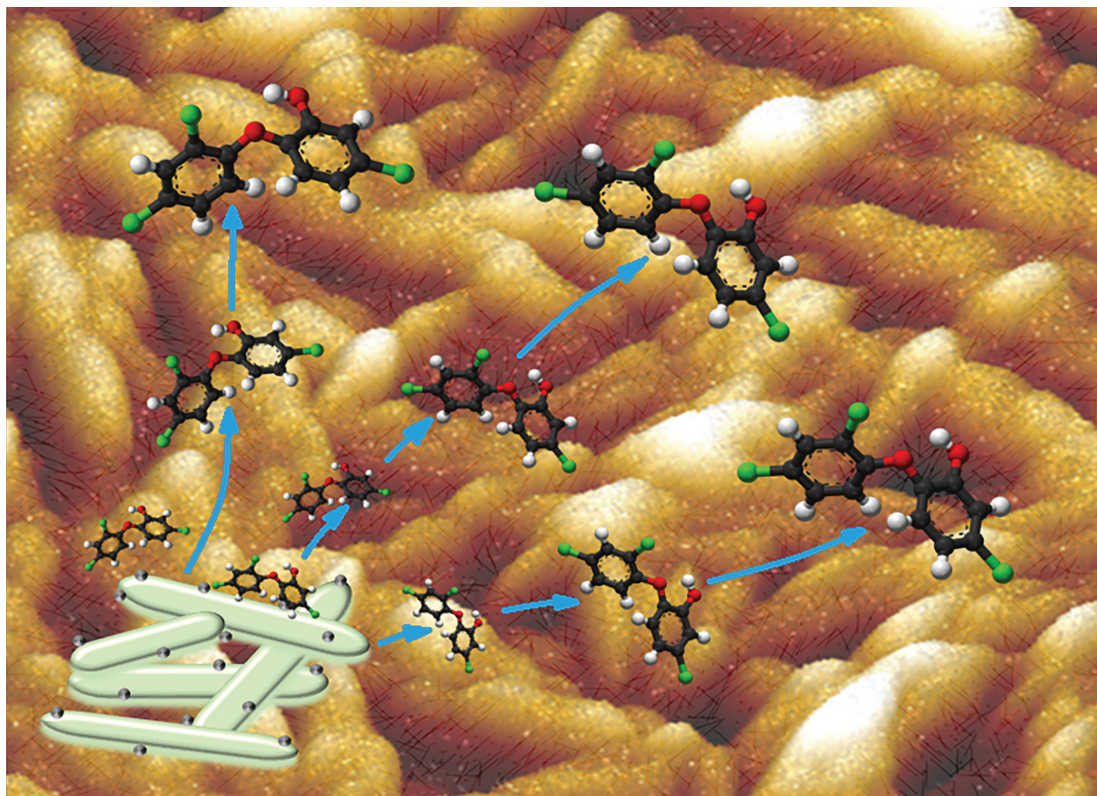
	Co	Ni	Sm	Nd
pH 0	42%	69%	51%	52%
pH 1	34%	63%	49%	54%
pH 2	29%	59%	29%	47%
pH 3	20%	29%	14%	12%
pH 4	4%	7%	15%	4%
pH 5	0%	0%	0%	0%

Table TS2. Unit cell determination of the $[N(C_2H_4NH_3)_3](NO_3)_3$ compound (2).

```

FILEID SAINT      V8.40B      4.00      09/28/22 12:28:09 SmTAEA_220928
SITEID BrukerAXS              SLU
TITLE  Integration of SmTAEA_220928
SMAP   1 0 0 0 0 0 0
CHEM   C6H12N7O9
CELL   8.7590 12.0758 14.5403 90.0000 90.7867 90.0000 1537.803
CELLSD 0.0010 0.0013 0.0017 0.0000 0.0024 0.0000 0.504
ORT1   1.8510969e-002 5.0215017e-002 -5.3385638e-002
ORT2   -4.7877077e-002 6.2643699e-002 3.4123499e-002
ORT3   1.0199036e-001 2.0292787e-002 2.6765097e-002
ZEROS  0.0000000 -0.0346542 0.0247405 -0.6903 0.5199 0.1307
SOURCE MO  0.71076 0.70930 0.71359 2.00000 50.00 20.00
LIMITS 0.00 0.00 0.00 0.00 0.00 0.00 0.00 0.00 0.00 0.00
MORPH PLATE
ADPAR   385.3068 256.2824 4.9330 512 768
ADCOR   0.0257 0.0059 0.0067 -0.2582 0.5173 0.0329
BRAVAIS Monoclinic(b-unique) P
MOSAIC 0.44 1.78
SAINTD   0 0.0000 0.0000 0 0 0.00000
SAINOV   4672 3249 25.3408 0.901206 0 0 0
SAINOV   4672 3249 25.3408 0.901206 1 0 0
SAINOV   4672 3249 25.3408 0.901206 1 1 1
SAINGL   1647 2.8732 25.4107 0 0 0
SAINGL   1647 2.8732 25.4107 1 0 0
SAINGL   1647 2.8732 25.4107 1 1 1
SAINMC   0 0 0 0.0000 0.0000 1 1 1

```

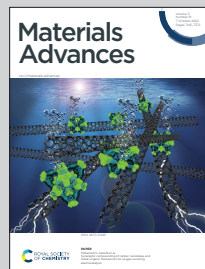



Showcasing research from Professors Seisenbaeva and Kessler laboratory, Department of Molecular Sciences, Uppsala BioCenter, Swedish University of Agricultural Sciences, Sweden.

Nanoceria-nanocellulose hybrid materials for delayed release of antibiotic and anti-inflammatory medicines

Nanoceria-nanocellulose hybrid material was developed and evaluated as a potential drug delivery system. Obtained materials possessed an open porous structure and absorbed pharmaceuticals *via* outer-sphere complexation mechanisms with ceria nanoparticles. Promising antibacterial properties and delayed release of antibiotic and anti-inflammatory medicines was observed.

As featured in:



See Vadim G. Kessler et al.,
Mater. Adv., 2022, **3**, 7228.


 Cite this: *Mater. Adv.*, 2022, 3, 7228

Nanoceria–nanocellulose hybrid materials for delayed release of antibiotic and anti-inflammatory medicines†

 Servane Gaio,‡ Fredric G. Svensson,‡§ Troy C. Breijaert,‡ Gulaim A. Seisenbaeva  and Vadim G. Kessler *

A novel nanoceria–nanocellulose hybrid material has been developed and evaluated as a potential drug delivery system. Crystalline nanoceria was synthesized *in situ* in the nanocellulose to obtain a homogenous distribution without extensive particle aggregation. The hybrid materials were loaded with two antibiotic drugs, triclosan and ampicillin, and one anti-inflammatory drug, diclofenac. The bacteriostatic effect on the gram-negative bacteria *Escherichia coli* was evaluated for the hybrid materials containing triclosan and ampicillin. The nanoceria–nanocellulose hybrid displayed a better retention of ampicillin than triclosan in the disc diffusion test, which is likely due to the presence of the carboxylic acid group in ampicillin that has better affinity for ceria compared to the phenolic group in triclosan. However, drug release studies in solution revealed rapid release of ampicillin and diclofenac, indicative of outer-sphere complexes between ceria and the drugs.

 Received 26th April 2022,
Accepted 9th August 2022

DOI: 10.1039/d2ma00471b

rsc.li/materials-advances

Introduction

Wound management is critical in preventing infections and in facilitating healing processes. Traditional wound-dressings only act as a physical barrier to provide physical protection and prevent infection by microorganisms but they neither provide antibacterial properties nor do they promote the healing processes. These are called passive wound-dressings.¹ Recently, with the emergence of nanotechnology, a new type of wound-dressing has been the focus of a lot of research, the so called active wound-dressings. These active wound-dressings facilitate healing of the wound by exhibiting antibacterial properties and/or stimulate tissue regrowth.^{2,3} For example, nanoparticles have been reported to improve wound healing by promoting immune responses.^{4,5} Nanocellulose has been under intense investigation for use as a new bandage material, owing to numerous beneficial properties such as gas permeability, exudate removal, moist environment, ease of removal, possible templating effect for tissue regrowth, and pain relief.⁶ There are three major classes of nanocellulose: crystalline nanocellulose

(CNC), cellulose nanofibrills (CNFs), and bacterial cellulose (BC). CNC has dimensions of 5–20 nm × 100–500 nm and high crystallinity. CNFs are fibrous with a high aspect ratio and lengths up to *ca.* 1 µm. BC is synthesized by some bacteria and, like CNFs, the fibres are about 1 µm long.⁷ The major drawback of all cellulose based materials, however, is the lack of antibacterial activity which means the wound could easily be infected. In efforts to overcome this, antibacterial agents have been added to the nanocellulose. For example, Volova *et al.*⁸ produced bacterial cellulose–silver nanoparticle composites which demonstrated antibacterial effect *via* the release of silver ions. In other studies, drug release from chemically unmodified nanocellulose has been investigated.^{2,9} In one study, Basu and co-workers¹⁰ cross-linked CNFs with Ca²⁺ and Cu²⁺ ions. They found that Ca²⁺ appeared to inhibit biofilm production and Cu²⁺ ions had a negative effect on bacterial proliferation. Nanocellulose has low retention for antibiotics and there is a risk that a very quick release may have toxic effects. Several articles have reported the use of nanotitania–nanocellulose hybrid materials for controlled drug delivery,^{11–13} where the good affinity of many common functional groups to the titania surface was exploited. Titania has for a long time been considered biocompatible with low toxicity. Lately, however, it has been demonstrated that titania induces very strong blood coagulation^{5,14,15} which also can promote wound-healing by initiating immune responses.⁵ For some applications, however, a strong coagulative response might be undesirable. Thus, we were interested in substituting nanotitania with nanoceria as a drug carrier in nanocellulose

Department of Molecular Sciences, Biocentrum, Swedish University of Agricultural Sciences, Almas Allé 5, SE-756 51 Uppsala, Sweden. E-mail: vadim.kessler@slu.se

† Electronic supplementary information (ESI) available. See DOI: <https://doi.org/10.1039/d2ma00471b>

‡ These authors contributed equally.

§ Present address: Department of Materials Science and Engineering, The Ångström Laboratory, Uppsala University, Lägerhyddsvägen 1, SE-75103 Uppsala, Sweden.

based wound-dressings. Cerium(IV) oxide (ceria, CeO_2) is generally considered a good biocompatible material with low toxicity and antioxidative properties owing to its non-stoichiometric composition.^{16,17} The inherent ability to produce reactive oxygen species (ROS) of many nanoparticles (e.g. TiO_2 , Ag, and Fe_3O_4) has been proposed to contribute to their cytotoxicity.¹⁸ Ceria has been subjected to numerous and diverse biomedical studies.¹⁹ For instance, Bellio and co-workers²⁰ used CeO_2 nanoparticles as adjuvants in combination with several antibiotics against multi-resistant *Klebsiella pneumoniae*. They found an increased antibacterial activity from the antibiotics which is ascribed to disruptive interactions between the cell membrane and the CeO_2 nanoparticles. In another study, ceria nanosheets were found to have a higher antibacterial activity compared to ceria nanoparticles, which was ascribed to the higher surface area of the nanosheets.²¹ Popov and co-workers¹⁶ demonstrated a radio-protective effect of citrate-coated ceria nanoparticles. This effect was explained by the effective clearance of the formed hydrogen peroxide and hydroxyl radicals. The intake of citrate-capped ceria had a positive effect on the survival of mice exposed to X-ray radiation. Furthermore, drug delivery systems including ceria have been reported, for instance CeO_2 -silicate composites.^{22,23} However, to the best of the authors' knowledge, drug delivery from nanoceria-nanocellulose hybrid materials has yet not been reported. The aim of the current work was to investigate nanoceria-nanocellulose hybrid materials as a potential drug delivery system for two different antibiotics, ampicillin and triclosan, and the anti-inflammatory drug, diclofenac. Release rates were studied *in vitro* for ampicillin and diclofenac, while the bacteriostatic effect of the hybrid material containing triclosan and ampicillin was tested against a model bacterium, the gram-negative *E. coli*.

Materials and methods

Materials synthesis

Synthesis of CNC. In a typical procedure, 4 grams of raw cotton was suspended in 100 mL of *ca.* 64 weight% sulfuric acid at 50 °C under stirring for 1 hour to produce nanocrystalline nanocellulose (CNC). Then, the CNC slurry was immediately poured into 1 L of deionized (DI) water to quench the reaction. Once sedimented, the CNC was collected and concentrated by centrifugation. The CNC was transferred to a dialysis tube and stored in a large beaker with 4 L of deionized (DI) H_2O to increase the pH to approximately neutral by acid removal. The dry weight was then determined in the final CNC product by weighing the CNC slurry and CNC dried in an oven until constant weight. The as-synthesized CNC slurry was stored in tightly sealed containers prior to use.

Synthesis of ceria nanoparticles. Ceria nanoparticles were synthesized according to a modified literature procedure.²⁴ Cerium(IV) sulfate tetrahydrate (Merck, 98%) was dissolved in DI H_2O and added to the CNC suspension. The pH was then increased to *ca.* 9 by a drop-wise addition of 2 M NaOH. Thereafter the reaction mixture (RM) was stirred at 80 °C for 1 hour.

The RM was repeatedly washed with DI H_2O and centrifuged until approximately neutral pH was reached followed by washing two times with ethanol (Solveco, 99.7%). The obtained powder was dried at 60 °C to obtain the low-temperature ceria (CeO_2 -80), similar to the *in situ* synthesis of ceria in the CNC suspension. Some of this powder was annealed at 600 °C for 2 hours to obtain high-temperature ceria (CeO_2 -600).

Modification of CNC/PEG with BTCA. The CNC was modified with 1,2,3,4-butanetetracarboxylic acid (BTCA, Aldrich, 99%) to act as an anchor for the metal oxide.²⁵ Briefly, for 1 g of CNC, 10 mmol BTCA and 10 mmol sodium hypophosphite (SHP, Aldrich, 99% (catalyst)) were dissolved in 1 mL 1 w% polyethylene glycol (PEG, Aldrich, 35 000 Da) and the RM was then stirred at 85 °C for 1 hour.

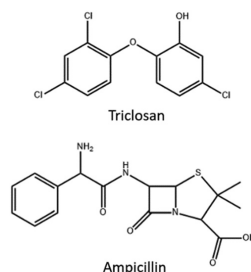
Modification of CNC/PEG/BTCA with CeO_2 . To obtain a homogenous material with small ceria particles an *in situ* synthesis of ceria in the BTCA-modified CNC was performed. First, the pH of the CNC was increased to *ca.* 9 by the addition of ammonium hydroxide. Then, an appropriate amount of cerium(IV) sulfate hydrate was added to yield a final amount of 20 w% ceria. The RM was stirred at 80 °C for 30 min and was then poured into a Petri dish and placed in an oven at 60 °C until dry.

Modification with antibiotics. To modify the hybrid materials with the drugs, ampicillin (Sigma, >96%), triclosan (Sigma, >97%), or diclofenac (Sigma, >98%) dissolved in ethanol was added to the RM of CNC/BTCA or CNC/BTCA/ CeO_2 under stirring. The suspensions were poured into Petri dishes and dried at 60 °C until dry. Pieces of hybrid material of 0.5 cm × 0.5 cm were produced (containing 0.2 mmol antibiotics per 0.25 cm² assuming homogenous distribution). For the chemical structure of the applied antibiotics, please, see Scheme 1.

Statistical tests. Significant differences between biological treatments were evaluated by Welch's two-sample *t*-test using R statistical software (version 3.4.3).²⁶ A *p*-value smaller than 0.05 was assumed to signify a statistically significant difference.

Materials characterization

Scanning electron microscopy. The morphology and homogeneity of all hybrid materials were studied by scanning electron microscopy (SEM, Hitachi TM1000 and Hitachi Flex-SEM1000II, Tokyo, Japan) coupled with energy-dispersive X-ray



Scheme 1 Chemical structures of ampicillin and triclosan.

spectroscopy (EDS, Oxford Instruments, Abingdon, UK). Dry samples were mounted on carbon tape.

Nanoparticle tracking analysis. The particle size in the solution of the unmodified CNC was investigated using a Malvern Nanosight NS300 (Malvern, UK). CNC was diluted in DI H₂O and analyzed at an infusion rate of 100 μ L in 20 s, recording four series per sample.

Zeta-potential. A Malvern Zetasizer Nano (Worcestershire, UK) was used for dynamic light scattering (DLS) and zeta-potential measurements of pure CNC. 3 series of 30 measurements per sample were performed.

Atomic force microscopy. Measurements were done on a Bruker Dimension Fastscan AFM (Billerica, USA) in the ScanAsyst mode using Fastscan-B cantilevers at a scan rate of 3 Hz and 1024 samples per line. The data were processed using Gwyddion version 2.56, with align rows-median.

Powder X-ray diffraction. The crystallinity of the *in situ* synthesized ceria and CeO₂-80 and CeO₂-600 was investigated by powder X-ray diffraction. The ceria-containing material was freeze-dried and powdered and then put into glass capillaries with a diameter of 1 mm. X-Ray data collection was performed on a Bruker D8 SMART Apex II CCD diffractometer (Billerica, USA) with $\lambda(\text{Mo-K}\alpha) = 0.71073$ Å and a graphite monochromator. The Sheldx97 program suite and EVA v12 were used for data treatment and analysis.

Fourier transform infrared spectrometry. The different materials were powdered by immersion in liquid nitrogen followed by grinding. The powders were milled in anhydrous KBr and pressed into pellets that were analysed by FTIR. The spectra were recorded using a PerkinElmer FTIR 100 spectrometer (Waltham, USA) between 4000 cm^{-1} to 400 cm^{-1} with 8 scans and 1 cm^{-1} resolution.

Photocatalytic studies. 10 mg of ceria nanoparticles, CeO₂-600 and CeO₂-80, were added to 1.5 mL of diluted methylene blue solution in plastic tubes. This was done in triplicate. These were kept in the dark for *ca.* 30 min to achieve adsorption-equilibrium. Then, the suspensions were centrifuged and absorbance was measured at 663 nm to obtain an initial absorbance using a Shimadzu UV-1800 spectrophotometer (Kyoto, Japan). After this, the solutions were subjected both to 300 W simulated sunlight (Osram) and a 15 W visible lamp (Garland) for periods of 15 min under gentle stirring. Subsequently, the solutions were centrifuged to sediment the ceria and then absorbance was measured. This was repeated three times for both treatments for a total of 45 minutes of irradiation time. The decomposition of MB was followed as the fraction of the initial absorbance.

Microbiological studies. Agar plates were prepared using Mueller Hinton broth powder (Sigma-Aldrich) at a concentration of 21 g L⁻¹ in DI H₂O containing 1.5 w% agar (Sigma-Aldrich) powder, followed by autoclaving. *Escherichia coli* (*E. coli*, strain LMG8223) was grown in liquid Mueller Hinton medium overnight at 37 °C in the dark. An aliquot of the liquid bacteria culture was diluted 100 times in isotonic NaCl and subsequently spread on the agar plates. Then, a piece of hybrid material (0.5 × 0.5 cm) was placed in the centre of the agar

plate. The agar plates were then incubated at 37 °C in the dark for 18 h to allow the bacteria to grow. The sizes of the inhibitory zones were then measured.

pH-Measurement of ampicillin addition to nanoceria-nanocellulose. For the pH-experiment was used a Metro Titando 888 system, running TIAMO 2.5 control software, equipped with an 801 stirring unit and an Ecotrode Plus combined pH electrode. The combined pH electrode was calibrated using Sigma-Aldrich certified buffers prior to use. A sample of a CeO₂ composite material was produced as previously described until the addition of ampicillin. Afterwards the composite was transferred to a suitable vessel equipped with a stirring bar, placed on the stirring unit, fitted with a thoroughly rinsed pH electrode, and allowed to equilibrate with stirring for 1 minute prior to starting the measurement. Under stirring the sample was then allowed to equilibrate for 120 seconds, measuring at 2 second intervals before the addition of ampicillin after which the change of pH was recorded for a total of 900 seconds at 2 second intervals.

Results and discussion

The aim of the current study was to investigate the nanocellulose-nanoceria hybrid as potential new materials for controlled drug delivery in wound-dressings, where nanoceria was evaluated as a substitute for nanotitania as a drug-carrier.

CNC synthesis

CNC was synthesized *via* acid hydrolysis from raw cotton. The average fiber sizes of the unmodified CNC were determined by AFM and NTA.

Atomic force microscopy

Diluted suspensions of unmodified CNC were analyzed by AFM to determine particle size and morphology (Fig. 1 and Fig. S2-S4, ESI†). As shown in Fig. 1, the CNC fibers have rod-like morphology, with a calculated average length of 112 nm (standard deviation 36 nm) and an average width of 48 nm (standard deviation 13 nm).

NTA and zeta-potential

Dilute suspensions of unmodified CNC were analysed by NTA (Fig. 2). The average particle size in solution was 113 nm, which is in good agreement with the AFM results. There are pieces of evidence for aggregation in solution. The zeta-potential of unmodified CNC was determined to be 2.44 ± 0.85 mV.

CNC modification

Polyethylene glycol (PEG) was added to CNC to increase the strength of the final material. To get better retention of the ceria nanoparticles, the CNC was modified by BTCA to introduce carboxylic functions to which the ceria nanoparticles can attach. Transmission FTIR spectra were recorded for freeze-dried powdered materials (Fig. 3). An absorption band around 1160 cm^{-1} is assigned to the C–O–C bonds in the CNC. With the introduction of BTCA a vibration from the carbonyl groups appears at 1712 cm^{-1} . When ceria is added the carbonyl band is

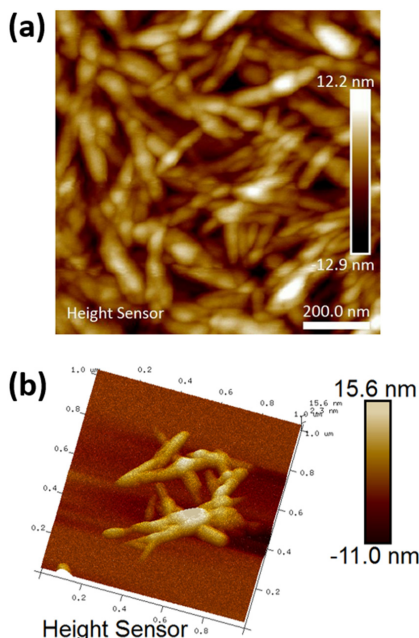


Fig. 1 (a) 2D AFM micrograph of the unmodified CNC and (b) 3D micrograph of unmodified CNC fibres.

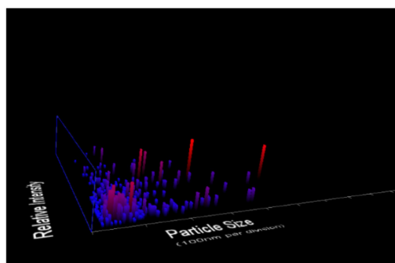


Fig. 2 NTA measurements of diluted aqueous suspension of CNC, showing size distributions. The four different trial analyses have shown a mean CNC particle size of 113 nm with a standard deviation of 97 nm.

slightly shifted to 1708 cm^{-1} , indicating interaction between CeO_2 and the carboxylic group. Additionally, two bands assigned to Ce–O vibrations emerged at 465 cm^{-1} and 617 cm^{-1} .²⁷

SEM imaging of the hybrid materials

The morphologies of the hybrid materials were visualized by SEM analysis. The hybrid materials had increased surface roughness (Fig. 4) compared to the unmodified CNC/PEG, which have a very smooth surface (Fig. S1a, ESI†).

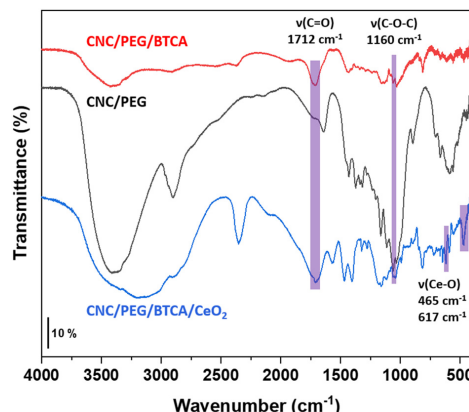


Fig. 3 FTIR spectra of powdered CNC/PEG, CNC/PEG/BTCA, and CNC/PEG/BTCA/ CeO_2 . Key absorption bands are highlighted.

in roughness is explained by the modification of BTCA and formation of ceria nanoparticles inside the materials. The addition of pre-synthesized ceria nanoparticles to the CNC/PEG suspension resulted in large aggregates of ceria unevenly distributed over the surface (Fig. S1b, ESI†). Instead, changing to an *in situ* synthesis of nanoceria in the CNC/PEG/BTCA resulted in a very good dispersion of the nanoparticles, without any visible aggregates, as clearly seen in Fig. 4.

Characterization of the nanoceria

To obtain a material of higher homogeneity and with smaller ceria particles an *in situ* low-temperature synthesis of ceria from cerium(IV) sulfate in the modified nanocellulose suspension was employed. The formation of nanocrystalline cerianite- CeO_2 in the CNC was confirmed by PXRD analysis of the hybrids. Fig. 5a shows the PXRD diffractogram of low-temperature ceria and Fig. 5b shows the diffractogram of ceria synthesized in BTCA-modified CNC. The size of low-temperature ceria was investigated by AFM, revealing a rather homogenous size distribution with particles of about 30 nm in diameter (Fig. 6 and Fig. S5 through S7, ESI†).

Photocatalytic studies

It is desirable to use in the wound dressings a metal oxide with low ROS production to avoid potential cell damage from the wound dressings. Thus, the photocatalytic activities of low-temperature ceria and ceria annealed at 600°C were investigated by following the decomposition of methylene blue (MB) under two different light sources, 300 W simulated sunlight and a 15 W lamp (Fig. 7). MB solutions without catalyst powder were used as the control. It was found that the overall degradation of MB was very small for all treatments, with more than 90% of the initial concentration remaining after 45 min of irradiation. The degradation of MB was slightly larger for the low-temperature ceria which could be explained by a larger total active surface area

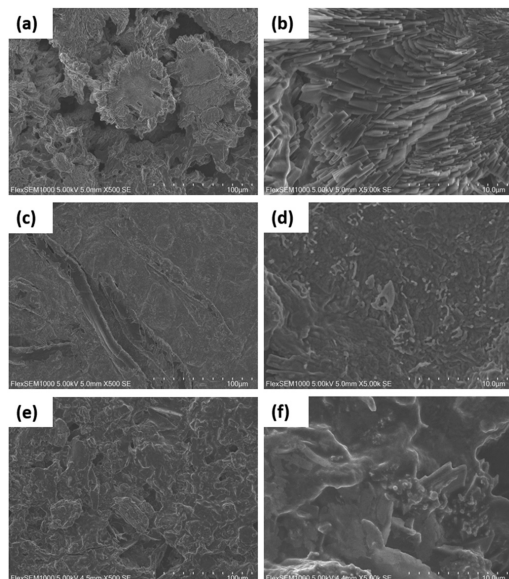


Fig. 4 SEM micrographs of CNC/PEG/BTCA/CeO₂/ampicillin at 500× (a) and 5000× (b) magnification, CNC/PEG/BTCA/CeO₂/triclosan at 500× (c) and 5000× (d) magnification, and CNC/PEG/BTCA/CeO₂/diclofenac at 500× (e) and 5000× (f) magnification.

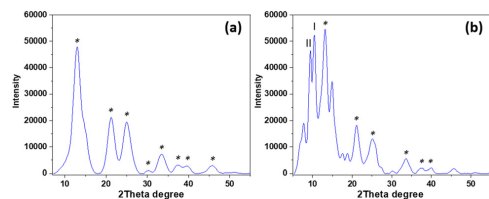


Fig. 5 PXRD diffractogram of (a) low-temperature ceria and (b) ceria synthesized *in situ* in CNC. The asterisk indicates characteristic diffraction planes of ceria (JCPDS 00-034-0394). Diffractions at 13.08°, 21.42°, 25.14°, 30.24°, 33.54°, 37.74°, 39.84°, and 45.84° represent the (1 1 1), (2 2 0), (3 1 1), (4 0 0), (3 3 1), (4 2 2), and (5 1 1) planes, respectively, of cerianite–CeO₂. Two characteristic diffractions of cellulose are present, where I represents the (2 0 0) plane of cellulose-I and II represents the (1 0 -1) plane of cellulose-II.¹²

compared to the ceria annealed at 600 °C, as extensive particle aggregation and crystallite growth occur during annealing at high temperatures. In the current study, the photocatalytic activities of both the low-temperature and the high-temperature ceria were very low and this suggests ROS production in the nanoceria–nanocellulose hybrid should be negligible.

Release studies of ampicillin and diclofenac

Release of ampicillin and diclofenac from CNC/PEG and CNC/PEG/BTCA/CeO₂ was studied. The two drugs were almost

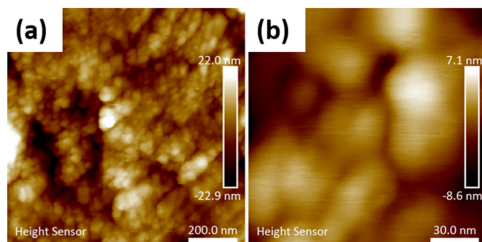


Fig. 6 (a) AFM micrograph of low-temperature nanoceria (CeO₂-80), and (b) high magnification micrograph of low-temperature nanoceria (CeO₂-80).

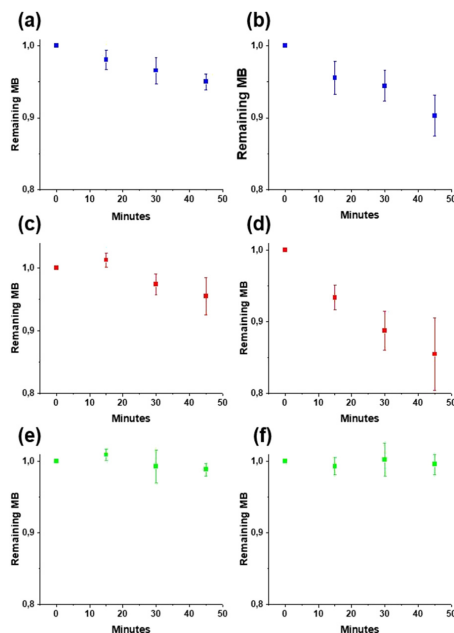


Fig. 7 Photocatalytic decomposition of methylene blue under a 15 W lamp: MB (a), CeO₂-80 (c), and CeO₂-600 (e) and 300 W simulated sunlight: MB (b), CeO₂-80 (d), and CeO₂-600 (f). The diagrams show the fraction of remaining MB after 45 min of irradiation time. Error bars represent standard deviation.

completely released within 15 minutes (Table 1) for both materials, indicating they were not strongly interacting with the ceria nanoparticles. This is in sharp contrast to diclofenac adsorbed to nanotitania–nanocellulose composites in which only 50% released after 16 hours or 28% after 15 hours, depending on the preparation method, as a result of strong complexation with the titania surface.¹²

This is further supported by the pH-measurements where upon addition of ampicillin a small, temporary downward shift

Table 1 Release data for diclofenac and ampicillin from CNC/PEG and CNC/PEG/CeO₂

	CNC/PEG	CNC/PEG/CeO ₂
Diclofenac drug loading	15.95 mg g ⁻¹	11.7 mg g ⁻¹
Diclofenac drug release	85–90% in 15 min	75–85% in 15 min
Ampicillin drug loading	15.98 mg g ⁻¹	8.9 mg g ⁻¹
Ampicillin drug release	85–100% in 15 min	85–100% in 15 min

in pH is measured after which the pH equilibrates to the previously measured value. This indicates that ampicillin is quickly transformed into the anionic form and consequently the interaction between the drug and ceria would be *via* the formation of an outer-sphere complex.

Microbiological studies

The inhibitory effect on the growth of *E. coli* was tested for the different materials *via* the disc diffusion test. The distance between the edge of the film and the end of the inhibitory zone was measured. CNC/PEG had negligible activity. The BTCA modified CNC had a certain antibacterial effect, which has been noticed previously for our CNC–TiO₂ system, originating from unbound/hydrolyzed BTCA.¹³ CNC/PEG/BTCA/CeO₂ has substantially a lower antibacterial activity compared to CNC/PEG/BTCA. This is likely due to the adsorption of BTCA on the ceria nanoparticles *via* its carboxylic groups. Thus, the influence of BTCA on the antibacterial activity in the ceria containing materials should be small. Modification with two different antibiotics, triclosan and ampicillin, was then tested. There were clear differences in the retention capacity between them, where ampicillin was released much more slowly in comparison to

triclosan in gel diffusion on a Petri dish (Fig. 8 and Fig. S9, ESI†). The inhibitory zone of CNC/PEG/CeO₂/ampicillin was significantly smaller ($p < 0.05$) compared to that of CNC/PEG/ampicillin while the difference between CNC/PEG/BTCA/triclosan and CNC/PEG/BTCA/CeO₂/triclosan was non-significant. This is likely explained by the presence of a carboxylic acid group in ampicillin which has better affinity for the ceria surface compared to the hydroxyl group in triclosan. This is also supported by the adsorption of BTCA on ceria. The release of ampicillin and diclofenac in 0.9% NaCl solution was studied by UV-spectrometry. Almost a 100% release was observed after *ca.* 15 minutes. The difference in retention of ampicillin in solution and in gel experiments can be supposedly attributed to the combination of the weakening of hydrogen bonding in the excess of aqueous medium and the mechanical washing. Complexation between ceria and the ligands appears to proceed in the form of outer-sphere complexes in contrast to complexation with titania, where inner-sphere surface complexes were easily traceable by FTIR and the release was rather apparently prolonged in time also in solution.^{12,13} It should be noted, however, that gel diffusion is more relevant as a model for drug delivery on skin and thus the developed material can be considered promising.

Conclusions

In this work we have developed a novel nanocellulose–nanoceria hybrid material and evaluated it for drug delivery for two different antibiotics, ampicillin and triclosan, against *E. coli*. It was found that ampicillin was released much slower than triclosan in the gel diffusion experiment, which was attributed to the strong interaction between its carboxylic group and nanoceria. However, rapid and almost complete release of ampicillin and diclofenac within 15 minutes in solution indicate weaker electrostatic interaction between the drugs and nanoceria, as compared to nanotitania where the drugs bond to the surfaces. No appreciable photocatalytic activity was found from the ceria nanoparticles under different visible light radiation sources, which suggests that production of harmful ROS is limited.

Author contributions

Investigation and analysis: S. G.; supervision, analysis, conceptualization, and writing – original draft preparation: F. G. S.; investigation and analysis: T. C. B.; writing – review and editing: G. A. S.; funding acquisition, conceptualization, and writing – review and editing: V. G. K.

Funding

This research was funded partly by the Swedish Research Council (Vetenskapsrådet) grant number 2014-3938 and partly by the Swedish Research Council STINT grant Nanocellulose Based Materials for Environmental and Theranostic Applications.

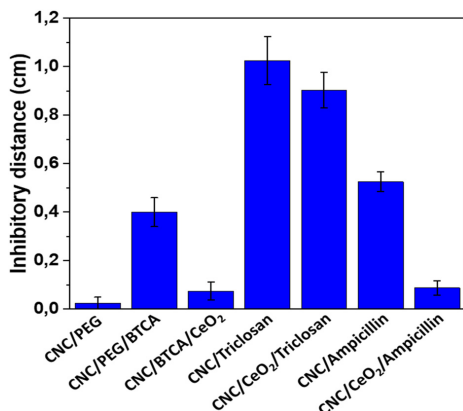


Fig. 8 Average inhibitory effect of the different materials. Error bars represent standard error of mean. At least eight replicates were made for each material. CNC/PEG/BTCA/CeO₂, CNC/PEG/BTCA/triclosan, CNC/PEG/BTCA/CeO₂/triclosan, CNC/PEG/BTCA/ampicillin, and CNC/PEG/BTCA/CeO₂/ampicillin have been abbreviated in the figure as CNC/BTCA/CeO₂, CNC/triclosan, CNC/CeO₂/triclosan, CNC/ampicillin, and CNC/CeO₂/ampicillin.

The Faculty of Natural Resources and Agricultural Sciences, SLU, is acknowledged for support of TB PhD position.

Conflicts of interest

The authors declare no conflicts of interest.

Acknowledgements

We thank Rasmus Björk for assistance with the DLS and zeta-potential measurements and Dr Jolanta Levenfors for kindly providing the *E. coli* bacteria. S. G. is grateful to the Erasmus+ Programme for financing her stay at SLU.

References

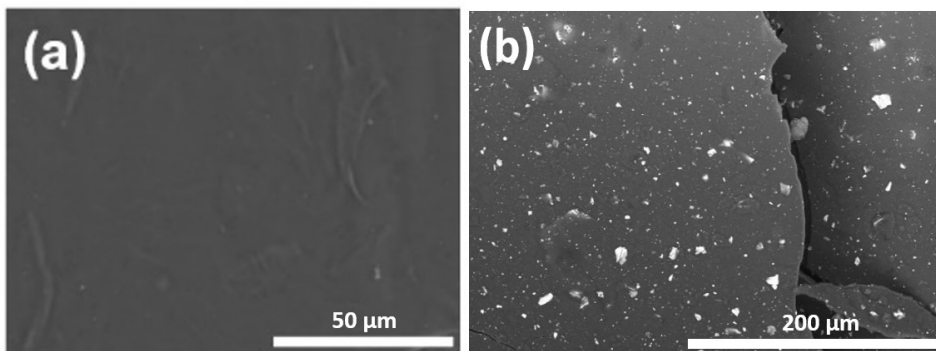
- 1 A. E. Stoica, C. Chircov and A. M. Grumezescu, *Molecules*, 2020, **25**, 2699.
- 2 S. Moritz, C. Wiegand, F. Wesarg, N. Hessler, F. A. Muller, D. Kralisch, U. C. Hipler and D. Fischer, *Int. J. Pharm.*, 2014, **471**, 45–55.
- 3 M. Li, Y. P. Liang, J. H. He, H. L. Zhang and B. L. Guo, *Chem. Mater.*, 2020, **32**, 9937–9953.
- 4 J. Tian, K. K. Y. Wong, C. M. Ho, C. N. Lok, W. Y. Yu, C. M. Che, J. F. Chiu and P. K. H. Tam, *ChemMedChem*, 2007, **2**, 129–136.
- 5 G. A. Seisenbaeva, K. Fromell, V. V. Vinogradov, A. N. Terekhov, A. V. Pakhomov, B. Nilsson, K. N. Ekdahl, V. V. Vinogradov and V. G. Kessler, *Sci. Rep.*, 2017, **7**, 15448.
- 6 M. Jorfi and E. J. Foster, *J. Appl. Polym. Sci.*, 2015, **132**, 41719.
- 7 T. Abitbol, A. Rivkin, Y. F. Cao, Y. Nevo, E. Abraham, T. Ben-Shalom, S. Lapidot and O. Shoseyov, *Curr. Opin. Biotechnol.*, 2016, **39**, 76–88.
- 8 T. G. Volova, A. A. Shumilova, I. P. Shidlovskiy, E. D. Nikolaeva, A. G. Sukovaty, A. D. Vasiliev and E. I. Shishatskaya, *Polym. Test.*, 2018, **65**, 54–68.
- 9 E. Haimer, M. Wendland, K. Schlufte, K. Frankenfeld, P. Miethe, A. Potthast, T. Rosenau and F. Liebner, *Macromol. Symp.*, 2010, **294-II**, 64–74.
- 10 A. Basu, K. Heitz, M. Stromme, K. Welch and N. Ferraz, *Carbohydr. Polym.*, 2018, **181**, 345–350.
- 11 O. L. Galkina, K. Onneby, P. Huang, V. K. Ivanov, A. V. Agafonov, G. A. Seisenbaeva and V. G. Kessler, *J. Mater. Chem. B*, 2015, **3**, 7125–7134.
- 12 O. L. Galkina, V. K. Ivanov, A. Agafonov, G. A. Seisenbaeva and V. G. Kessler, *J. Mater. Chem. B*, 2015, **3**, 1688–1698.
- 13 O. L. Evdokimova, F. G. Svensson, A. V. Agafonov, S. Hakansson, G. A. Seisenbaeva and V. G. Kessler, *Nanomaterials*, 2018, **8**, 228.
- 14 B. Ekstrand-Hammarstrom, J. Hong, P. Davoodpour, K. Sandholm, K. N. Ekdahl, A. Bucht and B. Nilsson, *Biomaterials*, 2015, **51**, 58–68.
- 15 F. G. Svensson, V. A. Manivel, G. A. Seisenbaeva, V. G. Kessler, B. Nilsson, K. N. Ekdahl and K. Fromell, *Nanomaterials*, 2021, **11**, 1100.
- 16 A. L. Popov, S. I. Zaichkina, N. R. Popova, O. M. Rozanova, S. P. Romanchenko, O. S. Ivanova, A. A. Smirnov, E. V. Mironova, I. I. Selezneva and V. K. Ivanov, *RSC Adv.*, 2016, **6**, 106141–106149.
- 17 P. Roberta, S. E. Maria, I. Carmelo, C. Fabiano, R. M. Teresa, I. Sara, S. Antonio, F. Roberto, I. Giuliana and B. M. Violetta, *Toxicol. Res.*, 2021, **10**, 570–578.
- 18 F. Marano, S. Hussain, F. Rodrigues-Lima, A. Baeza-Squiban and S. Boland, *Arch. Toxicol.*, 2011, **85**, 733–741.
- 19 A. B. Shcherbakov, V. V. Reukiv, A. V. Yakimansky, E. L. Krasnopeeva, O. S. Ivanova, A. L. Popov and V. K. Ivanov, *Polymers*, 2021, **13**, 924.
- 20 P. Bellio, C. Luzzi, A. Mancini, S. Cracchiolo, M. Passacantando, L. Di Pietro, M. Perilli, G. Amicosante, S. Santucci and G. Celenza, *Biomembranes*, 2018, **1860**, 2428–2435.
- 21 F. Abbas, J. Iqbal, T. Jan, N. Badshah, Q. Mansoor and M. Ismail, *Int. J. Miner. Metall. Mater.*, 2016, **23**, 102–108.
- 22 J. H. Zhang and Y. F. Zhu, *Microporous Mesoporous Mater.*, 2014, **197**, 244–251.
- 23 C. Xu, Y. H. Lin, J. S. Wang, L. Wu, W. L. Wei, J. S. Ren and X. G. Qu, *Adv. Healthcare Mater.*, 2013, **2**, 1591–1599.
- 24 O. Yildiz, *J. Nucl. Mater.*, 2007, **366**, 266–271.
- 25 O. L. Galkina, A. Sycheva, A. Blagodatskiy, G. Kaptay, V. L. Katanaev, G. A. Seisenbaeva, V. G. Kessler and A. V. Agafonov, *Surf. Coat. Technol.*, 2014, **253**, 171–179.
- 26 R Core Team, A Language and Environment for Statistical Computing; R Foundation for Statistical Computing, Vienna, Austria, 2016.
- 27 O. Ejeromedoghene, O. Oderinde, X. Y. Ma, M. Olusola, S. Adewuyi and G. D. Fu, *J. Mater. Sci.: Mater. Electron.*, 2021, **32**, 16324–16334.

Nanoceria-Nanocellulose Hybrid Materials for Delayed Release of Antibiotic and Anti-Inflammatory Medicines

Servane Gaio, Fredric G. Svensson, Troy C. Breijaert, Gulaim A. Seisenbaeva, and Vadim G. Kessler*

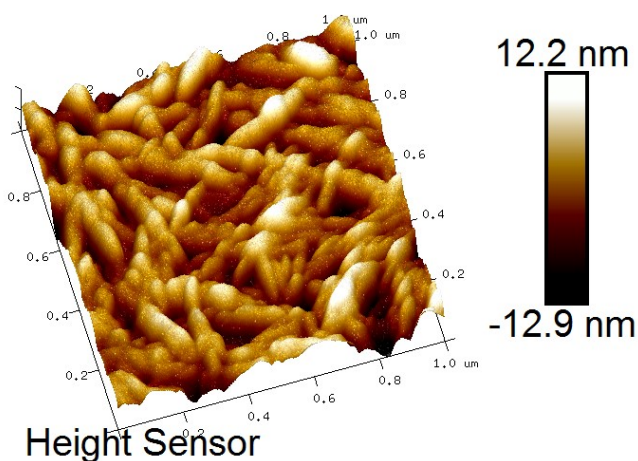
Department of Molecular Sciences, Biocentrum, Swedish University of Agricultural Sciences, Almas Allé 5, SE-756 51 Uppsala, Sweden.

1. SEM micrographs

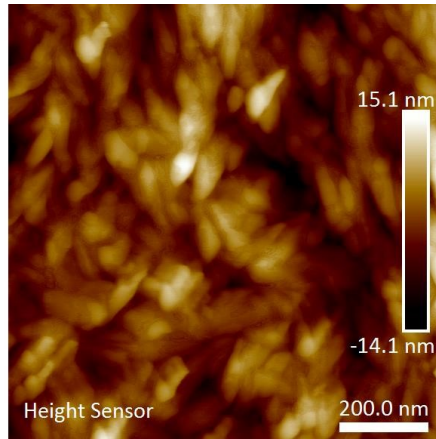


Supplementary Figure S1. SEM micrographs of (a) CNC/PEG and CNC/PEG_CeO₂ with 50 w% ceria.

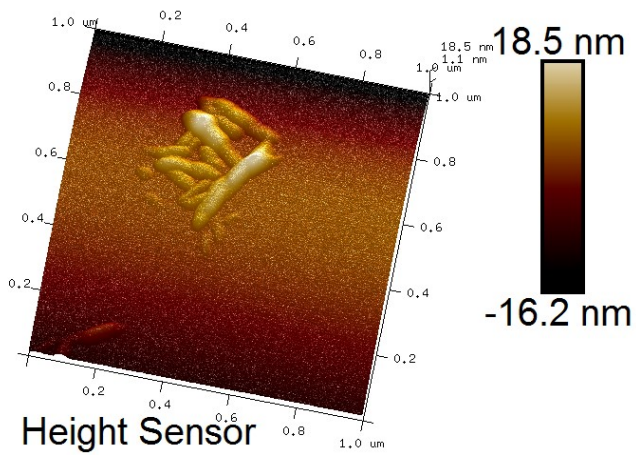
2. AFM micrographs



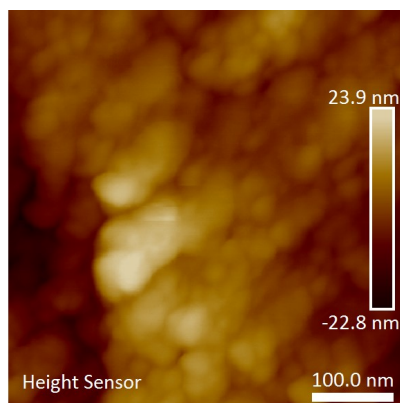
Supplementary Figure S2. 3D AFM micrograph of CNC.



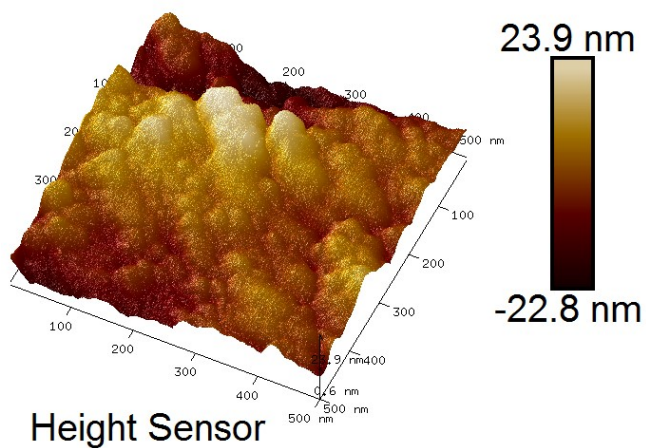
Supplementary Figure S3. AFM micrograph of CNC



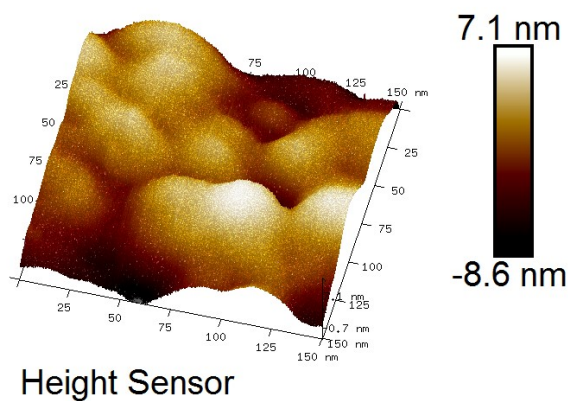
Supplementary Figure S4. AFM micrograph of CNC fibers.



Supplementary Figure S5. AFM micrograph of low-temperature ceria (CeO₂_80).

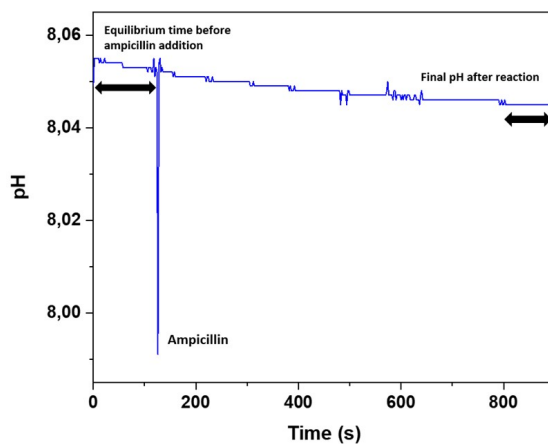


Supplementary Figure S6. 3D AFM micrograph of low-temperature ceria (CeO₂_80).



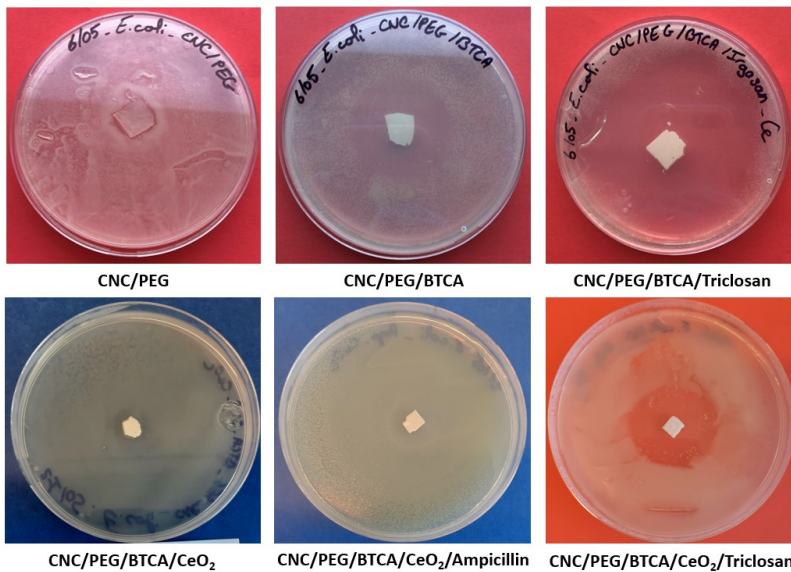
Supplementary Figure S7. 3D AFM micrograph of low-temperature ceria (CeO_2 _80), showing individual particles.

3. pH effect of Ampicillin



Supplementary Figure S8. pH-change after addition of ampicillin to the CNC reaction mixture in the final synthesis step of CNC/PEG/BTCA/ CeO_2 .

4. Optical photos



Supplementary Figure S9. The *E. coli* cultivations after growing 16 hours with the different hybrid materials.



Uptake and separation of rare earth elements and late transition metal cations by nanoadsorbent grafted with diamino ligands

Marijana Lakić^a, Troy C. Breijaert^a, Geoffrey Daniel^b, Fredric G. Svensson^c, Vadim G. Kessler^a, Gulaim A. Seisenbaeva^{a,*}

^a Department of Molecular Sciences, Biocentrum, Swedish University of Agricultural Sciences, Almas Allé 5, Box 7015, SE-750 07 Uppsala, Sweden

^b Department of Forest Biomaterials and Technology, Swedish University of Agricultural Sciences, Vallvägen 9C-D, SE-756 51 Uppsala, Sweden

^c Department of Materials Science, Solid State Physics, Box 35, Ångströmlaboratoriet, Lagerhyddsvägen 1, Uppsala University, SE-751 03 Uppsala, Sweden

ARTICLE INFO

Keywords:

Critical metals
Rare Earth Elements
Late Transition metals
Recycling
Molecular interaction model

ABSTRACT

Recycling of magnetic materials based on Rare Earth Elements (REE) is of major interest in the view of growing clean energy production and transportation. One of the major challenges in its realization is the need to separate smaller amounts of Late Transition Metals (LTM) from REE. Hybrid adsorbents are very attractive in finding such a solution. Here, novel silica-based nanoadsorbents were synthesized by grafting the surface of dense silica nanoparticles with a diamino functional ligand grafted via an arene linker to improve selectivity towards LTM. The produced adsorbent materials were characterized using SEM, TEM, AFM, XPS, FTIR, and TGA in its pure form and by DLS in suspension, and tested for the adsorption and separation of LTM (Co^{2+} and Ni^{2+}) and REE (Sm^{3+} and Nd^{3+}) in single and mixed solutions. Prepared organo-silica material showed rapid uptake of all tested cations with higher affinity towards LTM. Adsorption capacities reached values of 1.18–1.45 mmol/g for Co^{2+} and Ni^{2+} , respectively, with a 1:1 metal-to-ligand stoichiometry for Ni cations. Investigation of reusability demonstrated the potential of the prepared materials as an environmentally friendly alternative in specific separation of LTM to conventional separation techniques. Investigations of the molecular structures of the Ni^{2+} complex with the selected molecular function and of Co^{3+} with a closely related tris-aminoethyl amine ligand in combination with XPS data for corresponding surface complexes helped explaining the molecular mechanisms for adsorption and desorption of the LTM cations.

1. Introduction

Rapid population growth and accelerated advances in industrialization and urbanization and overconsumption of fossil fuels are coupled with increase emissions of climate-changing greenhouse gases [1,2]. The rise of green (low-carbon) technology with smart electrical grid programs substituting fossil-driven vehicle parks, and vehicle-to-grid technology are among the new tools for successful decarbonization and preventing further global temperature rises. Many of these fast-growing technologies, in particular, wind turbines and electric vehicles, utilize rare earth elements (REE) sourced via mining from a monopolized supply chain where there is increased demand [3–7]. Principal components in these applications are permanent magnets, i.e., FeNdB and CoSm magnets, where REE, neodymium (Nd) and samarium (Sm) are represented together with late transition metals (LTM) [8].

Scarce REE and LTM, especially copper, nickel, cobalt, platinum, and silver, are predicted to face market pressure as the production of green energy technologies intensifies [9,10]. To solve the supply issue and to meet future demands, there is a need to exploit recycling schemes for the recovery of REE from secondary resources with an emphasis on their selective separation from LTM, as a green alternative to mining and processing of solid REE [11–13]. In the recycling, the separation of REE from LTM represents thus a principal challenge. While iron can easily be separated by controlled increase in pH, separation of Co, Ni and Cu requires application of advanced approaches including fractional crystallization [14], solvent extraction [15–16] or use of solid adsorbents [17]. The drawback of the crystallization approach is the need in multi-step procedures. The solvent extraction uses large amounts of organic solvents and hazardous extractants. The solid adsorption is generally considered as a greener alternative.

* Corresponding author at: Department of Molecular Sciences, Biocentrum, Swedish University of Agricultural Sciences, Almas Allé 5, Box 7015, SE-750 07 Uppsala, Sweden.

E-mail address: gulaim.seisenbaeva@slu.se (G.A. Seisenbaeva).

<https://doi.org/10.1016/j.seppur.2023.124487>

Received 7 May 2023; Received in revised form 26 June 2023; Accepted 30 June 2023

Available online 1 July 2023

1383-5866/© 2023 The Author(s). Published by Elsevier B.V. This is an open access article under the CC BY license (<http://creativecommons.org/licenses/by/4.0/>).

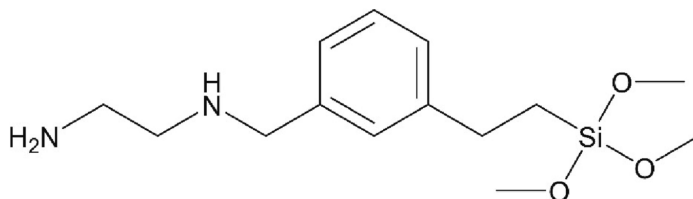


Fig. 1. Ligand N-(aminoethylaminomethyl)phenethyltrimethoxysilane.

Current hydrometallurgical recycling techniques for permanent magnets include acid leaching using inorganic acid (HCl, H₂SO₄, or HNO₃) and subsequent separation methods, such as several precipitation steps or liquid phase extraction (solvent extraction processes, ionic liquid extraction) [18]. Liquid phase extraction uses large volumes of reagents and solvents that can release volatile organic compounds (VOC), produce toxic and flammable wastes, and requires repetition of cycles to achieve appropriate metal purity due to the difficulties of REE separation from LTM. Additional disadvantages are poor contact between the extractant and desired elements and the formation of an unwanted third (heavy organic) phase due to the splitting of the organic phase into two layers, which can affect the efficiency of the extraction process, requiring additional separation steps before the extraction can be considered complete [19,20]. Solid-liquid extraction using adsorbents compensate for these disadvantages [21] and enables rapid uptake of the aqueous metals and easy separation of the treated solution from the solid sorbent [11]. In this context, adsorption represents an environmental, eco-friendly, and non-expensive alternative to the use of liquid phase extraction and meets the requirements of “Circular economy schemes” proposed by the European Union for resource recovery from solid waste or wastewater to solve scarce resource problematics, realizing the “waste to product” concept [22].

Next-generation adsorbents - nanoadsorbents with high adsorption capacity and selectivity - have gained the science community's interest [23–32]. These properties arise from the increased surface area and reactivity of nanoadsorbents compared to their bulk counterparts. A further important characteristic is their possibility for surface functionalization allowing the grafting of ligands targeting specific metal cations or contaminants. In addition to these characteristics, superior nanoadsorbents are easily dispersed in liquid media, chemically stable, uniform in size, cheap and reusable [33–37].

In our search for separation between REE and LTM, we turned to the application of polyamino ligands. It is well-known that such ligands have high affinity for LTM cations, forming stable complexes in neutral and basic medium that potentially can be destroyed at rather low pH, releasing hydrated LTM cations [38]. At the same time, it is well known that complexation between REE and polyamino ligands can be followed only in non-aqueous medium and not in water [39]. In our recent studies, we demonstrated that tris(aminoethyl)-amine, an example of polyamino ligand displayed different mechanisms in interacting with LTM and REE cations respectively. While complexation was observed with LTM in a pH-neutral medium, REE produced hydroxides as result of hydrolysis of their cations with precipitation of hydroxides and the formation of protonated ammonium salts [40]. This difference could be traced in lower adsorption of REE cations compared to LTM, on a biopolymer adsorbent grafted with tris(2-aminoethyl)-amine as well as easier desorption.

In the present work, we aimed to further increase selectivity of the interaction, and opted for introduction of an aromatic ring in direct proximity to a diamino function. This could result, either in improved control of hydrophilicity/hydrophobicity of the surface via ligand self-organization through π -stacking, or create more specific coordination surrounding for LTM with ability to distinguish between Ni²⁺ and Co²⁺

via possibility of $d\pi$ - $p\pi$ contribution. In the current study, the synthesis and characterization of hybrid silica nanoadsorbents, prepared by surface grafting of dense silica nanoparticles of an approximate size of 100 nm, with the commercially available ligand (aminoethylaminomethyl)-phenethyltrimethoxysilane (AEAM-PTMS), featuring the desired structure are presented. To the best of our knowledge, this is the first use of this ligand for selective metal uptake and adsorption. The difference in reactivity of Ni²⁺ and Co²⁺ was revealed via structural studies of molecular model compounds.

2. Experimental methods

2.1. Reagents

Tetraethyl orthosilicate (TEOS, 99 %, CAS No. 78-10-4), ethanol (99.7 %, CAS No. 64-17-5), ammonium hydroxide solution (25 %, CAS No. 1336-21-6), nickel(II) nitrate hexahydrate (94.5–105.5 % (EDTA titration), CAS No.13478-00-7), cobalt(II) nitrate hexahydrate (98 %, CAS No. 10026-22-9), neodymium(III) nitrate hexahydrate (99.9 %, CAS No. 16454-60-7), samarium(III) nitrate hexahydrate (99.9 %, CAS No. 13759-83-6), toluene (≥ 99.5 %, CAS No. 108-88-3), murexide (≥ 95 %, CAS No. 3051-09-0), Xylenol orange tetrasodium salt (≥ 95 %, CAS No. 3618-43-7), ammonium chloride (≥ 99.5 %, CAS No. 12125-02-9), acetic acid (≥ 99.7 %, CAS No. 6444-19-7), N-Benzylethylenediamine (97 %, CAS No. 4152-09-4), and Tris(2-aminoethyl) amine (96%, CAS No. 4097-89-6) were purchased from Merck. Nitric acid (65 %, CAS No. 7697-37-2) was purchased from Riedel-de Haën, sodium acetate trihydrate (≥ 99.0 %, CAS No. 6131-90-4) was purchased from VWR, ethylenediaminetetraacetic acid tetrasodium salt dihydrate (EDTA, 99 %, CAS No. 10378-23-1) was purchased from AppliChem, and aminoethylaminomethyl)phenethyltrimethoxysilane (AEAM-PTMS, 80 %, CAS No: 74113-77-2) was purchased from Gelest.

All chemicals, except toluene, were used as received without further purification. Toluene was dried via a distillation process. For the preparation of all aqueous solutions, Milli-Q water was used.

2.2. Synthesis and characterization of nanoadsorbents

2.2.1. Synthesis of dense silica particles

Dense SiO₂ nanoparticles (NPs) were synthesized using a modified Stöber method as described earlier [41]. Hydrolysis of precursor TEOS was performed in an alcoholic solution using ammonium hydroxide as a catalyst. The reaction mixture consisted of 200 mL 96% ethanol, 35 mL Milli-Q water, and 7.5 mL of 25 % ammonium hydroxide solution and was mixed in a reaction flask at 70 °C and under the nitrogen atmosphere. 11.16 mL of TEOS was added dropwise with a PET syringe supplied with a stainless steel 0.80x80mm needle, stirring the reaction mixture for 2 h. When the reaction stopped, the SiO₂ NPs were centrifuged (12000 rpm, 10 min), washed twice with ethanol (95 %) and three times with Milli-Q water. Particles were dried under nitrogen before further use.

2.2.2. Grafting of silica particles

Prior to the grafting step, dry silica particles were pre-treated with 1 M HNO_3 to enhance the surface grafting onto surface silanol groups [42,17]. 500 mg of dry and acid-pretreated silica particles were dispersed in 20 mL of dry toluene. 1 mL of ligand N-(aminoethylaminomethyl)phenethyltrimethoxysilane (AEAM-PTMS) was then added (see Fig. 1), and the components mixture was kept in a reaction flask equipped with a reflux condenser for 24 h at 80 °C and under nitrogen flow.

2.3. Synthesis of model compounds

To reveal the molecular structure of metal complexes on the surface of prepared nanoadsorbent, we attempted crystallization of the complexes between Ni(II) nitrate and N-aminoethyl aminomethyl benzene ligand in 1: 1, 1: 2 and 1: 3 M ratios and Co(II) nitrate with both N-aminoethyl-aminomethyl benzene and with tris(aminoethyl) amine ligands in 1: 1 M ratio. Light violet (lilac) coloured crystals were isolated in all cases where Ni^{2+} cation salts were used and proved as the same crystalline material of compound 1. In the case of Co^{2+} cations, the color of solution turned in all cases greenish brown with formation of a glassy product. The color indicated oxidation of Co(II) into Co(III) with formation of hydroxo complexes. Thus, to avoid hydrolysis of Co(III) species, the pH of the solution was adjusted to 3.0 by addition of nitric acid. The solutions then turned bright red. In the case of N-aminoethyl aminomethyl benzene, only a glassy solid could be isolated, while in the case of tris(aminoethyl) amine, massive crystallization of a single crystalline product compound 2 was observed.

2.4. Physical characterization of obtained adsorbent material

Scanning electron (SEM) micrographs of prepared adsorbent material were obtained using a Hitachi FlexSEM 1000II with acceleration voltage of 5 kV, a spot size 20, and a working distance of 5 mm. For Transmission Electron Microscopy (TEM) experiments, dispersions of adsorbent particles were deposited on holey carbon grids (Pelco® 50 mesh grids: Pitch 508 µm; hole width 425 µm; bar width 83 µm; transmission 70%) and observed using a Philips CM/12 microscope (Thermo Fisher Inc.) fitted with LaB_6 and operated at 100 kV.

Nanoadsorbent's selectivity to metals was characterized by elemental analysis of surfaces using energy-dispersive X-ray spectroscopy (EDS). EDS spectra were obtained using an acceleration voltage of 20 kV, a spot size of 40 and a working distance of 10 mm on the Hitachi FlexSEM 1000II microscope.

Atomic Force Microscope (AFM) images were taken with a Bruker Dimension FastScan instrument using a FastScan-B probe with a nominal tip radius of 5 nm and a scan rate of 1–3 Hz. Gwyddion 2.56 software was used for data processing.

The thermogravimetric analysis (TGA) of samples was carried out using a PerkinElmer Pyris 1 instrument in an air atmosphere at a heating rate of 5°/min in the 25–800 °C interval.

Fourier-transform infrared (FTIR) spectra were recorded as KBr pellets on a PerkinElmer Spectrum 100 instrument from 4000 to 400 cm^{-1} .

Dynamic Light Scattering (DLS) measurements for determination of the particle size and charge (zeta-potential) were carried out with a Malvern Zeta-Sizer Instrument in aqueous dispersions produced by ultrasonication.

X-ray structure determinations. Single-crystal X-Ray Diffraction analysis was performed using a Bruker D8 Quest ECO diffractometer. The data were collected at room temperature in the 2–50.05 2 θ range for a full hemisphere using MoK α radiation ($\lambda = 0.71073$ Å). **Compound 1.** $\text{C}_{18}\text{H}_{28}\text{N}_6\text{NiO}_8$, MW = 515.17 Da, Monoclinic, Space group P2(1)/c, $a = 10.206(2)$, $b = 11.324(2)$, $c = 10.377(2)$ Å, $\beta = 95.145(4)^\circ$, $V = 1194.4(4)$ Å³, $Z = 2$. The structure was solved by direct methods, obtaining coordinates of the majority of non-hydrogen atoms from the initial

solution. The coordinates of the rest of the non-hydrogen atoms were obtained from difference Fourier syntheses. All non-hydrogen atoms were refined first in isotropic and then in anisotropic approximation. The coordinates of hydrogen atoms at the carbon atoms and the terminal nitrogen atom N(1) were obtained by geometric calculation, while those on the solvating water molecule were located in difference Fourier syntheses. All hydrogen atoms were refined in riding approximation bound to corresponding non-hydrogen atoms using temperature factors of these atoms to define the isotropic temperature factors of the hydrogen atoms defined as 1.200 U_{eq} for H-atoms located at C or N atoms and 1.500 U_{eq} for those in the solvating water molecule. The final discrepancy factors were $R1 = 0.0951$, $wR2 = 0.22183$ for 1554 observed reflections [$I > 2\sigma(I)$], and $R1 = 0.1193$ and $wR2 = 0.2291$ for all 2096 data.

Compound 2. $\text{C}_6\text{H}_{14}\text{CoN}_7\text{O}_{10}$, MW = 403.17 Da, Orthorhombic, Space group Pna2(1), $a = 25.6816(11)$, $b = 7.2953(3)$, $c = 7.9417(3)$ Å, $Z = 4$. The structure was solved by direct methods, obtaining coordinates of the non-hydrogen atoms connected to the cobalt cation from the initial solution. Coordinates of nitrogen and oxygen atoms belonging to the nitrate counterions were located in subsequent difference Fourier syntheses. All non-hydrogen atoms were refined first in isotropic and then in anisotropic approximation. The coordinates of hydrogen atoms at the carbon atoms and the terminal nitrogen atoms N(2), N(3) and N(4) were obtained by geometric calculation, while those on the solvating water molecule were identified in subsequent difference Fourier syntheses. All hydrogen atoms were refined in riding approximation bound to corresponding non-hydrogen atoms using temperature factors of these atoms to define the isotropic temperature factors of the hydrogen atoms defined as 1.200 U_{eq} for H-atoms located at C or N atoms and 1.500 U_{eq} for those in the solvating water molecule. The final discrepancy factors were $R1 = 0.0683$, $wR2 = 0.1904$ for 2372 observed reflections [$I > 2\sigma(I)$], and $R1 = 0.0727$, $wR2 = 0.1972$ for all 2528 data.

Full details of data collection and structure solution and refinement are available free-of-charge from the Cambridge Crystallographic Data Centre (CCDC) at <https://www.ccdc.cam.ac.uk> citing the deposition number **2,239,325** for compound 1 and **2,260,061** for compound 2.

X-ray Photoelectron spectroscopy (XPS) was performed using a Quantera II Scanning XPS Microscope from Physical Electronics equipped with an Al K α source. For charge compensation a low-energy flood-gun, set at 1.0 V and 20.0 µA, was employed. The survey spectra were recorded using a pass energy of 224 eV and a resolution of 0.8 eV, and for the high-resolution spectra a pass energy of 55 eV and 0.1 eV resolution were employed. The samples were suspended in deionized water, dropped on glass slides, and dried under a desktop lamp. The binding energy was calibrated against the C 1 s peak of adventitious carbon at 284.8 eV from a reference sample. The data was treated in the CASA XPS software [43]. The spectra were smoothed using a Savitzky-Golay algorithm with either a 5 or 9-point window.

2.5. Functional characterization of the adsorbent material

2.5.1. Adsorption isotherms

For adsorption experiments, 20 mg of nanoadsorbent was added to a 50 mL falcon tube, followed by the addition of 20 mL of an appropriate metal stock solution with concentrations of 0.5, 1, 2, 3, 4, and 10 mM. After adding NaNO_3 solution to retain a constant ionic strength, the samples were left to equilibrate for 48 h before collecting the particles via centrifugation. The pH of initial solution was 7.5 apparently due to protonation of the ligand amino functions. The amount of metal uptake was determined by complexometric titration of the supernatant with 5 mM EDTA. Xylenol orange indicator and 1 M acetate buffer were used for REE (Sm, Nd) determination, and murexide and 1 M ammonia buffer were used for LTM (Co, Ni) determination. The titrations were repeated in triplicates for each sample, and the average value was calculated. The relation between the adsorbed metal and adsorbent mass at a fixed

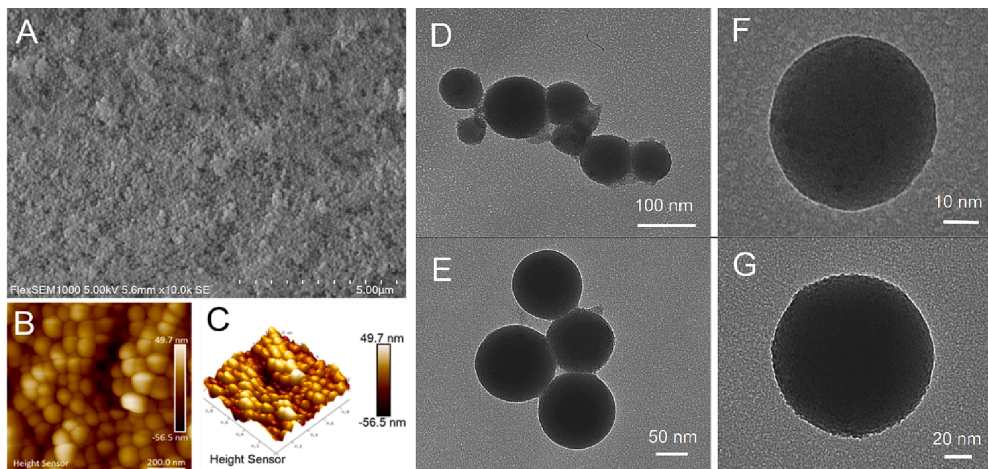


Fig. 2. SEM (A) and AFM (B & C) images of prepared pristine dense silica nanoparticles, and TEM images of D, E: SiO₂-AEAM-PTMS; F, G: SiO₂-AEAM-PTMS + Ni.

temperature are presented as adsorption isotherms. The shape of obtained isotherms provides considerable data regarding the nature of the adsorption process. Adsorption isotherms generally show a plateau at high metal concentrations, corresponding to the saturation of the adsorbent surface. To rationalize the shape of an adsorption isotherm, Langmuir and Freundlich isotherm models are used [44–46].

The Langmuir adsorption isotherm proposes that metal uptake occurs on a homogeneous adsorbent surface by monolayer sorption without interactions between adsorbed molecules. Eq. (1) presents linear and Eq. (2) nonlinear forms of Langmuir isotherm:

$$\frac{C_{ad,e}}{q_{ad,e}} = \frac{1}{q_{max} \times K_L} + \frac{C_{ad,e}}{q_{max}} \quad (1)$$

$$q_{ad,e} = \frac{K_L \times q_{max} \times C_{ad,e}}{1 + K_L \times C_{ad,e}} \quad (2)$$

Reversible and multilayer adsorption on a heterogeneous adsorbent surface is proposed by the Freundlich adsorption isotherm, where the adsorbed amount increases with the concentration in accordance with the following nonlinear (Eq. (3)) and linear equations (Eq. (4)).

$$q_{ad,e} = K_f \times C_{ad,e} \quad (3)$$

$$\ln q_{ad,e} = \ln K_f + \frac{1}{n} \times \ln C_{ad,e} \quad (4)$$

$C_{ad,e}$ denotes the equilibrium concentration of metal ions (mg/L), $q_{ad,e}$ is the amount of metal adsorbed per specific amount of adsorbent (mg/g), q_{max} is the maximum adsorption capacity of adsorbent (mg/g), and K_L is an equilibrium constant that reflects the affinity between the adsorbent and adsorbate (L/mg). The values of q_{max} and K_L were calculated by both linear (from the slope and intercept of the linear plot of $C_{ad}/q_{ad,e}$ versus C_{ad}) and non-linear (by OriginPro 9) methods.

2.5.2. Adsorption kinetics

Adsorption kinetics control the adsorption rate, determining the time required to reach equilibrium for the adsorption process. For adsorption kinetic experiments, 20 mg of grafted silica nanoparticles was suspended in 20 mL of 10 mM metal solution and shaken at RT. Samples were taken at predetermined intervals of 15 min, 30 min, 1 h, 3 h, 6 h, 18 h, and 24 h, and titrated against 5 mM EDTA.

Kinetic models can give information regarding adsorption pathways

and probable mechanism involved [47,48]. The tested kinetic models were pseudo-first order, given by Eq. (5), and pseudo-second order, given by Eq. (6):

$$q_{ad,t} = q_{ad,e} \times (1 - e^{-k_1 \times t}) \quad (5)$$

$$q_{ad,t} = \frac{k_2 \times q_{ad,e}^2 \times t}{1 + k_2 \times q_{ad,e} \times t} \quad (6)$$

$q_{ad,t}$ denotes the adsorption capacity in given time (mg/g), $q_{ad,e}$ is the equilibrium adsorption capacity (mg/g), t is the adsorption time (h), k_1 is the constant of pseudo-first-order model (1/min), and k_2 is the constant of pseudo-second-order model (g/mgmin).

2.5.3. Metal selectivity

10 mg of dry particles were equilibrated for 24 h in 10 mL of equimolar (5 mM) aqueous metal mixtures on a shaker at RT. The metal release was done using 1 M HNO₃ for 24 h at RT. The samples were dried under an N₂ atmosphere before metal mapping using EDS.

2.5.4. Desorption and reusability studies

For the desorption test, we studied two different desorption media, HNO₃ with three different concentrations and pH values (pH 0, pH 1, and pH 3) and 10 mM EDTA with pH 4.9. Desorption efficiencies were studied in an equimolar mixture of two (Co/Sm, Ni/Nd, Ni/Co, and Sm/Nd) or with all four tested metals. Reusability studies were carried out by three successive adsorption and desorption steps, using one metal solution (20 mM) in the adsorption step and 1 M HNO₃ as the desorption media. Desorption was carried out for 24 h, mixing the samples on the shaker. Afterwards, the samples were centrifuged (10000 rpm, 10 min), the supernatant collected, neutralized with ammonia to a pH value of 6.5, and titrated with 5 mM EDTA to calculate the amount of desorbed metal.

3. Results and discussion

3.1. Preparation of nanoadsorbents

The morphology of the synthesized material was analyzed by SEM, TEM and AFM techniques, proving the formation of highly uniform spherical particles with an average particle size of 100 nm preserved on

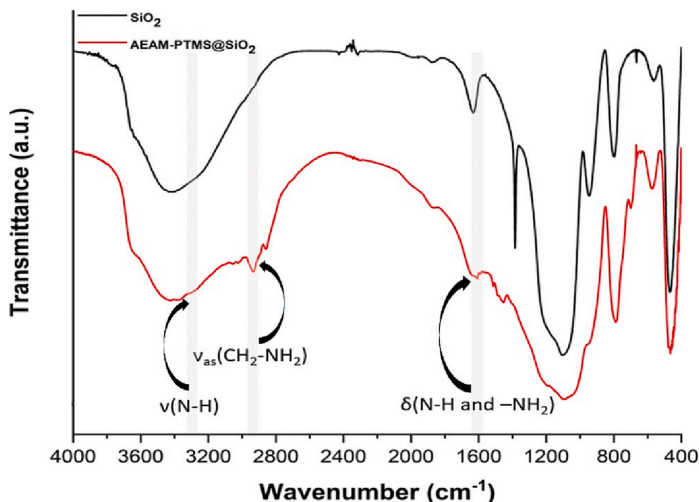


Fig. 3. FTIR spectra of synthesized control and AEAM-PTMS grafted silica particles.

all further steps of treatment, both on ligand grafting and with subsequent adsorption of metal cations (see Fig. 2).

The material produced by ligand grafting contained the required amounts of organics corresponding to monolayer formation. According to the TGA study (see Fig. S1 in Supplementary material), the first step of weight loss corresponding to approximately 3 % was observed at 25–120 °C and occurred due to dehydration of the silica surface and evaporation of the residual organic solvent (dry toluene). Above 120 °C, 16.7 % weight loss was observed until 500 °C, attributed to decomposition of the surface grafted ligand. The losses above 500 °C were related to the carbonization of organic residues on SiO₂ NPs and combustion of the residual carbon. The calculated amount of grafted ligand AEAM-PTMS was estimated from TGA data as 1.47 mmol/g.

The chemical nature of grafting of the ligand was revealed by FTIR (see Fig. 3). The spectra of surface grafted SiO₂ NPs showed characteristic peaks of SiO₂ around 1090 cm⁻¹, 800 cm⁻¹, and 460 cm⁻¹ corresponding to $\delta(\text{Si}-\text{O}-\text{Si})$, $\nu(\text{Si}-\text{O}-\text{Si})$ and $\nu_{\text{as}}(\text{Si}-\text{O}-\text{Si})$ vibrations. Bands at 1640 cm⁻¹ and 950 cm⁻¹ confirmed the presence of residual hydroxyl functions $\delta(\text{O}-\text{H})$ and $\nu_{\text{as}}(\text{Si}-\text{OH})$, respectively. Peaks at the app. 3300 cm⁻¹, 2935 cm⁻¹, and 1610 cm⁻¹ corresponded to $\nu(\text{N}-\text{H})$, $\nu_{\text{as}}(\text{CH}_2-\text{NH}_2)$, and $\delta(\text{N}-\text{H}$ and $\text{NH}_2)$ vibrations, respectively [49,50], and confirmed successful functionalization of the silica nanoparticles with the amino-containing ligand AEAM-PTMS.

The surface properties of the particles were changed strongly at each step of surface transformation as revealed by surface charge changes (zeta-potential values) obtained from DLS experiments. The pristine silica nanospheres at pH = 6.5 had a highly negative zeta-potential of -50.6 mV (± 1.18 mV), typical for a hydroxyl-terminated silica. Grafting of a ligand monolayer resulted in recharging of the surface with positive zeta-potential + 9.27 mV (± 1.15 mV), emerging apparently due to protonation of the amino functions with formation of positively charged ammonium centers on the surface. Adsorption of Ni²⁺ cations led to recharging with a final negative zeta-potential of -9.6 mV (± 0.369 mV). The positive charge was apparently removed due to complexation of the cations with chelating ligands and formation of close ion pairs as demonstrated by the investigated molecular models (please see part 3.3.1 below for details).

3.2. Adsorption equilibrium isotherms and adsorption kinetics

Fitting of the adsorption data was carried out following Langmuir, Classical Freundlich and Extended Classical Freundlich, and D-R models [44–46] (see Fig. 4A and S5). The comparison demonstrated that the adsorption isotherms followed the Langmuir model over the concentration range studied for all metals (Fig. 4A), indicating that the adsorption sites were homogeneous and that adsorption of the metal cations proceeded with formation of a monolayer of adsorbate on the uniform material surface with no interactions between adsorbed molecules [51–54]. The AEAM-PTMS ligand as expected, showed affinity towards LTM, due to the existence of two amino donor sites in its structure [55]. Nevertheless, the adsorption capacity for REE was also pronounced. The prepared nanoadsorbent had the highest affinity towards Ni (1.45 mmol/g) and Co (1.18 mmol/g), followed by Sm and Nd (0.56 and 0.47 mmol/g, respectively). Maximum adsorption capacity and metal/ligand stoichiometry results are presented in Table 1. Based on these results, it is possible to conclude that the prepared material, silica grafted with AEAM-PTMS ligand, offered a promising nano-adsorbent for LTM sequestering, obtaining near 1:1 metal to ligand stoichiometry (0.99 for Ni, and 0.80 for Co).

Adsorption kinetics were rapid for all tested metals. The kinetic curves reached equilibrium in 6 h, as seen in Fig. 4B. The adsorption kinetics showed that most of the uptake (70–90 %) occurred within the first 3 h of the interaction of metals with grafted silica nanoparticles. All the kinetics followed pseudo-second-order, which assumes that the metal uptake process is controlled by the adsorption reaction at the liquid/solid interface in the adsorbent and not by diffusion. Comparison of the fitting of pseudo-1st and pseudo-2nd order models [47,48] is presented in Fig. S6.

The mechanism behind metal adsorption onto the surface of the adsorbent is a complex phenomenon and dependent on various factors, such as physico-chemical properties of the metal cations and electrostatic attractions, ionic exchange or complexation (Lewis acid–base interaction) between positively charged metals and negatively charged surfaces of the adsorbent as well as pH of the microenvironment [56–58]. The adsorption isotherm study proved the formation of a monolayer on the surface of the nanoadsorbent and can indicate the chemisorption of targeted metals onto surface functional moieties/

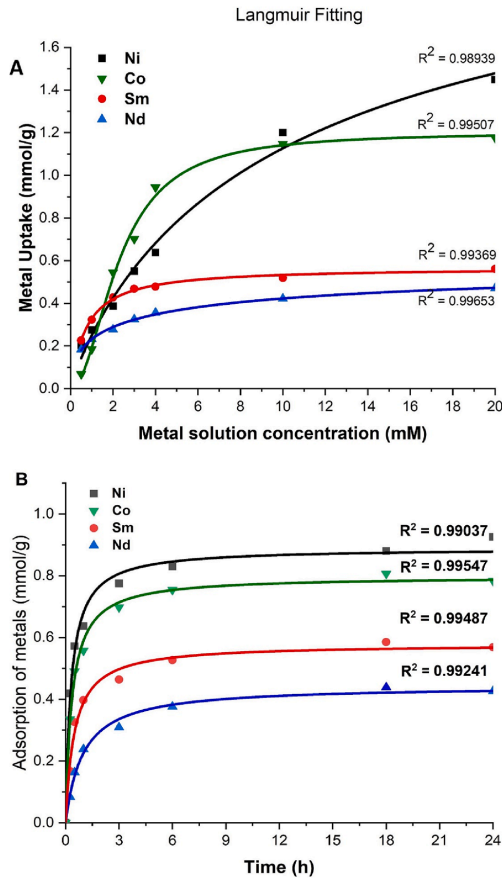


Fig. 4. Adsorption isotherms fitted with Langmuir model (A) and adsorption kinetics fitted with the pseudo-2nd order model (B) of prepared nano-adsorbent material.

Table 1

Maximum adsorption capacities of prepared nanoadsorbent and obtained metal/ligand stoichiometry.

Metal	Maximum adsorption capacities (mmol/g)	Metal/ligand stoichiometry
Co	1.18	0.80
Ni	1.45	0.99
Sm	0.56	0.38
Nd	0.47	0.32

Table 2

Selectivity of prepared nanoadsorbent material.

Metal mixture	Atomic metal ratio
Ni/Co	1/1
Ni/Nd	8.6/1
Co/Sm	3.2/1
Sm/Nd	1.4/1

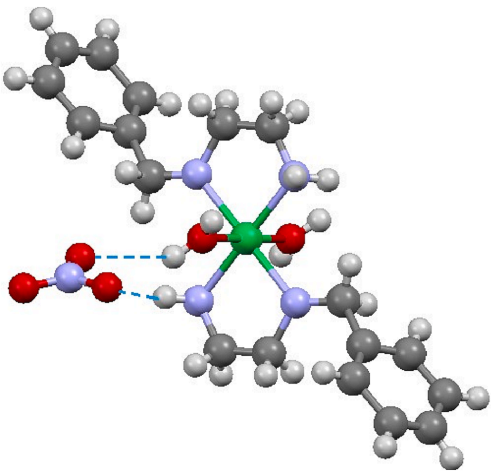


Fig. 5. Molecular structure of the complex $[\text{Ni}(\eta^2\text{-H}_2\text{NC}_2\text{H}_4\text{NHCH}_2\text{C}_6\text{H}_5)_2(\text{H}_2\text{O})_2](\text{NO}_3)_2$. Only one hydrogen bonded nitrate anion is displayed for clarity.

active sites. Prepared model molecular compounds of metals and ligand in the form of single X-ray quality crystals gave molecular insights into metal complexation (described under 3.3.1).

3.3. Nanoadsorbent selectivity

EDS analysis was used to study average nanoadsorbent selectivity after metal uptake by determining the elemental ratios between metals on different areas of the adsorbents. The results are presented in Table 2. When the adsorbent was used in the mixture of LTM and REE, Ni/Nd, and Co/Sm, the selectivity was 8.6/1 and 3.2/1, respectively. When the adsorbent was tested in an equimolar mixture of two LTMs, the adsorbent did not show selectivity towards Co or Ni. In the case of the equimolar mixture of REE, the adsorbent showed slightly higher selectivity towards Sm. The results show an adsorbent preference to preferentially bind LTM over REE.

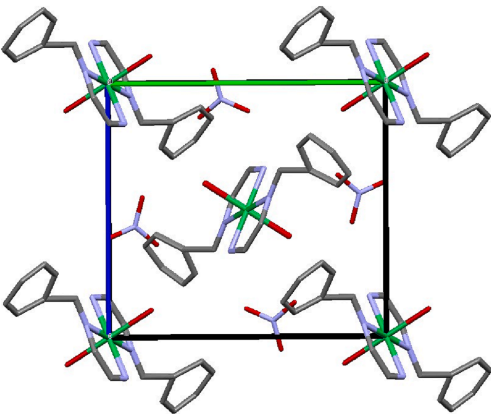


Fig. 6. The packing of $[\text{Ni}(\eta^2\text{-H}_2\text{NC}_2\text{H}_4\text{NHCH}_2\text{C}_6\text{H}_5)_2(\text{H}_2\text{O})_2](\text{NO}_3)_2$ structural units displayed along the a-axis.

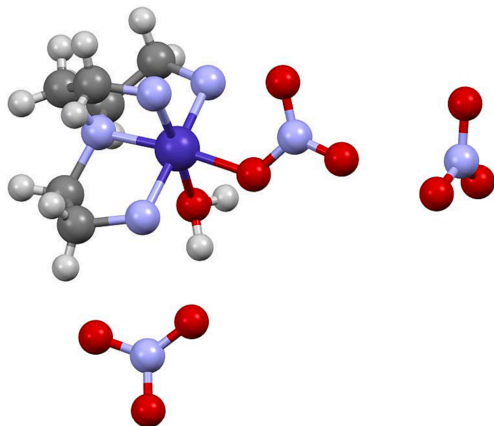


Fig. 7. Molecular structure of the complex $[\text{Co}(\text{H}_2\text{NC}_2\text{H}_4)_3\text{N}(\text{H}_2\text{O})(\text{NO}_3)](\text{NO}_3)_2$ (2).

3.4. Molecular insights into selective action – Crystallographic models

In order to gain better understanding of the observed selective action of the adsorbents, we investigated the complex formation between the ligand function, N-aminoethyl-aminomethyl benzene and metal cations. Independent of the applied ratio of reagents, the product turned to be a salt containing a centrosymmetric “propeller-like” cationic unit $[\text{Ni}(\eta^2\text{-H}_2\text{NC}_2\text{H}_4\text{NHCH}_2\text{C}_6\text{H}_5)_2(\text{H}_2\text{O})_2]^{2+}$ with two ligand molecules attached to the metal cation, along with two nitrate anions connected to the complex via short hydrogen bonding (see Fig. 5). Formation of the complexes with Ni: L = 1: 2 ratio has been reported earlier by Patel et al. [55], but no structural characterization has been provided. Coordination of the nickel cation is octahedral with four nitrogen atoms in the equatorial plane and two hydrating water molecules in the axial positions. The square planar arrangement in this case is apparently not associated with low-spin coordination of Ni(II) or any Jahn-Teller distortion, as the bond length to the nitrogen atoms 2.076(2) and 2.130(2) Å are apparently comparable with the bond length to the solvating water molecules, 2.107(2) Å.

In the crystal structure of the compound, the molecules are aligned with each other as seen from the packing motif (see Fig. 6), but are situated too far from each other for manifestation of π - π stacking – the distance between parallel benzene ring planes being equal to the length of the unit cell parameter, i.e. ca. 10 Å.

The absence of π - π stacking is also revealed via the apparent flipping movement of the benzene rings (see Fig. S2 and S3). In non-restricted refinement, the thermal ellipsoids of carbon atoms in the ring are characteristically elongated. Any attempt of splitting the ring atoms into separate positions for explanation through positional disorder were unsuccessful, making refinement unstable.

In the surface layer, the attachment of Ni^{2+} cations to the ligands should follow the same pattern of chelation, but only one ligand can be bound to the metal centre due to steric reasons. This explains the observed 1: 1 cation-to-ligand stoichiometry. The density of ligand grafting is close to maximum coverage of a smooth silica surface, implying that the separation in space between the ligand molecules should be in the range 6.3–6.8 Å [59]. It should allow better alignment of benzene rings, but is too long for orbital interactions requiring at maximum about 4.4 Å distance between the centroids [60].

No single crystals could be isolated from the Co^{2+} solutions with N-aminoethyl-aminomethyl benzene as ligand, but the color changes (see

Fig S4.) indicated rapid oxidation into Co^{3+} species. Since analogous behavior has been observed earlier with a related tris(aminoethyl) amine ligand [40], an attempt to crystallize the cobalt derivative was carried out and successful, resulting in a quantitative yield of the related complex $[\text{Co}(\text{H}_2\text{NC}_2\text{H}_4)_3\text{N}(\text{H}_2\text{O})(\text{NO}_3)](\text{NO}_3)_2$ (2) (see Fig. 7). The Chemistry of Co^{2+} cations in interaction with chelating amino-ligands is discussed in detail in N.N. Greenwood and A. Earnshaw [61], where both the analogies in reactivity and specific stability of $3d^6$ electronic configuration are described and explained. The coordination of the Co^{3+} cation is octahedral with 4 positions occupied by the nitrogen atoms of the ligand, where N(1) provides for the tertiary amino function and N(2), N(3) and N(4) – for the primary amino functions. The residual two places in the inner coordination sphere are occupied by a solvating water molecule O(1) and an oxygen atom of directly bound nitrate anion O(11). An important feature is that all the bonding distances are much shorter compared to Ni^{2+} and are very close to each other except for a considerably longer bond to the solvating water molecule: Co(1)-N(1) 1.919(6), Co(1)-O(11) 1.924(5), Co(1)-N(3) 1.930(12), Co(1)-N(2) 1.938(10), Co(1)-N(4) 1.966(9), and Co(1)-O(1) 1.970(10) Å. This indicates formation of the low-spin $3d^6$ electron configuration, characterized by strong metal-ligand bonding and high activation energy of ligand exchange – a potential hinder for Co_3 + cation desorption at low pH.

Chelating inner sphere complexation of the polyamino ligands with LTM explains the observed affinity of the functionalized adsorbent and hindered desorption of the Co-cations. REE, as demonstrated recently, do not bind to amino functional ligands, but instead can form thin layer deposits of hydroxides [40], making the adsorbent much less efficient to REE compared to LTM.

3.5. Molecular insights into selective action – XPS spectroscopy data

The hybrid adsorbents, as prepared and after uptake of Co, Ni, and Nd, were analyzed by XPS (see Fig. 8). For the Co, Ni, and Nd containing samples, two shifts for N 1s binding energies were seen, one major at about 400 eV and one minor between 406.2 and 407.3 eV. The minor shift is characteristic of NO_3^- , originating from the NaNO_3 used for maintaining the ionic strength during adsorption [62]. The major shift at 398.5 eV for the adsorbent not bearing metal cations (Fig. 8, bottom) corresponds to a protonated amino group [63]. After adsorption of the metal cations, the major N 1s signal is slightly upshifted with about 1 eV, in good agreement with previous reports of these metal ions in complexation with nitrogen containing ligands [64–66].

High resolution XPS spectra were recorded for all three metal cations. In the case of cobalt cations, as indicated by both the color change on their adsorption and seen from the molecular structure model (Fig. 7), their uptake was associated with oxidation of Co^{2+} into Co^{3+} , and the observed signal at 781 eV corresponded well to the literature data on octahedrally coordinated Co^{3+} cations [67]. In the nickel spectrum, the observed signals at 872.4 and 854.9 eV corresponded well to octahedrally coordinated Ni^{2+} cations [68], which also correlated with the investigated molecular model (Fig. 5). The spectrum of neodymium showed a split peak for Nd^{3+} , indicating potential variety in its coordination. This was expected due to a combination of the surface complexation with the growth of a hydroxide layer caused by the local pH rise via protonation of the amino functions.

3.6. Desorption and reusability study

We tested the desorption efficiency after metal uptake from equimolar metal mixtures of two or four metals. Results were obtained by EDS mapping after samples were shaken for 24 h using four different desorption solutions, HNO_3 with 3 different pH values, and 10 mM EDTA.

Results of metal release after uptake from an equimolar mixture of REE and LTM metal are presented in Fig. 9A for Co/Sm and Fig. 9B for

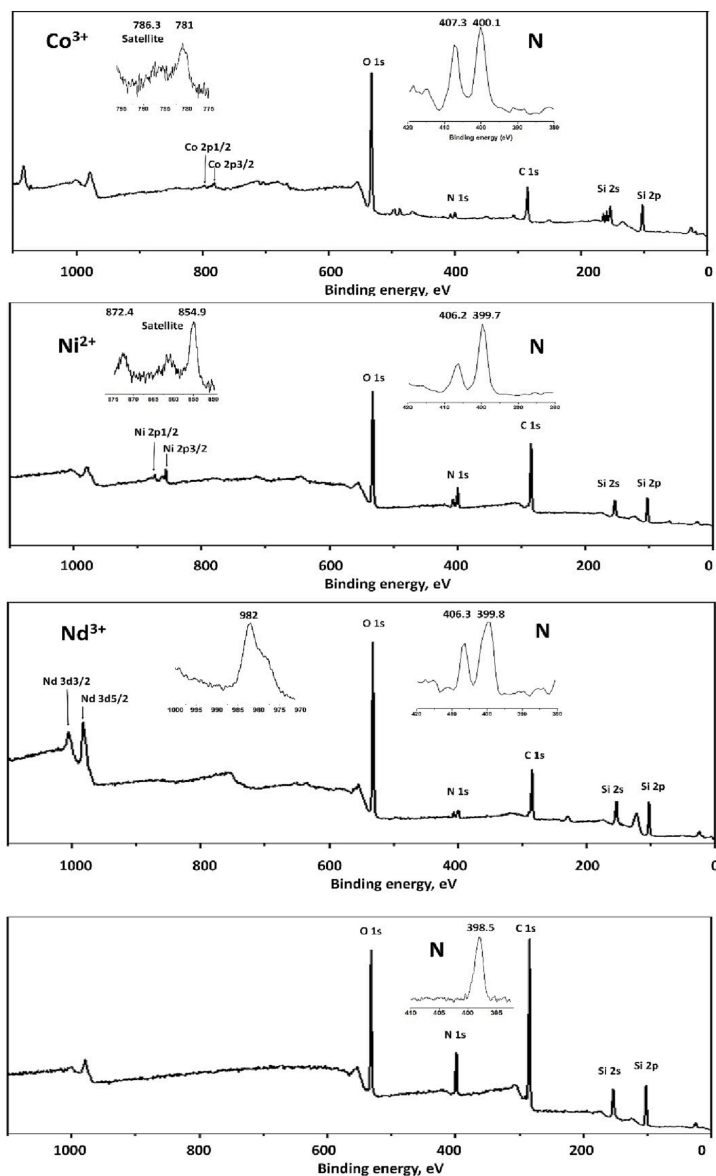


Fig. 8. XPS spectra of the hybrid adsorbent (below) and the adsorbent after uptake of Co, Ni and Nd cations respectively.

Ni/Nd mixture. HNO_3 , with the lowest pH value (pH 0), exhibited the highest removal rate of adsorbed Co, while all desorption media removed almost all adsorbed Sm (98–100 %). When the desorption step was repeated using acid with pH 1, the removal rate for Co rose from 52.5 to 75 %. In the case of the Ni/Nd equimolar mixture, the desorption efficiency was high for all metals, varying from 90.5 % (Nd at pH 1) to 100 % (Ni at pH 1). Overall, HNO_3 with pH 0 had the best desorption efficiency. Results of metal release after uptake from an equimolar

mixture of LTM cations are presented in Fig. 9C and for the release of REE cations in Fig. 9D. Typically, the Co cations appeared more resilient to acid treatment, as described earlier by our group [40]. This was apparently due to kinetic hinders caused by the crystal field activation energy for the formed Co^{3+} cations with $3d^6$ electron configuration. Characteristically, the desorption efficiency for Ni cations decreases when we try to remove them after uptake from Ni/Co mixtures compared with removal after uptake from mixtures of Ni/Nd. When we

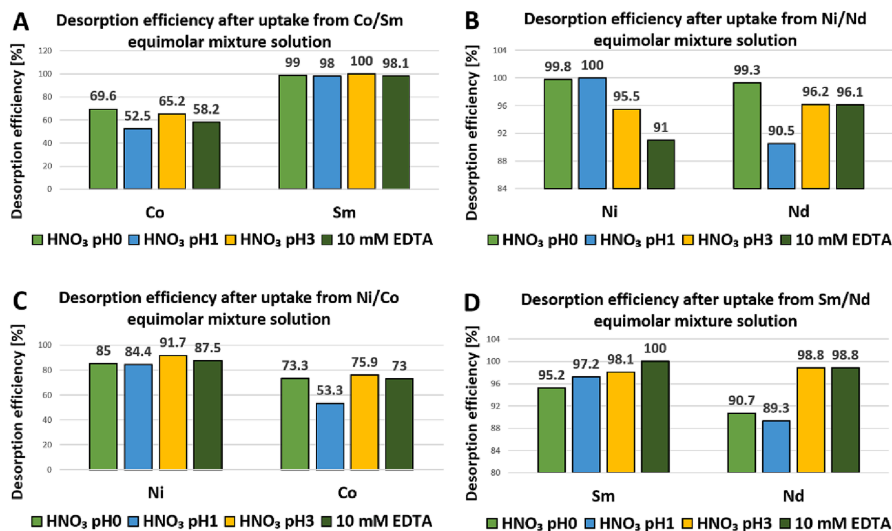


Fig. 9. Desorption efficiency after uptake from two metal equimolar solutions: (A) Co/Sm; (B) Ni/Nd, (C) Ni/Co, and (D) Sm/Nd.

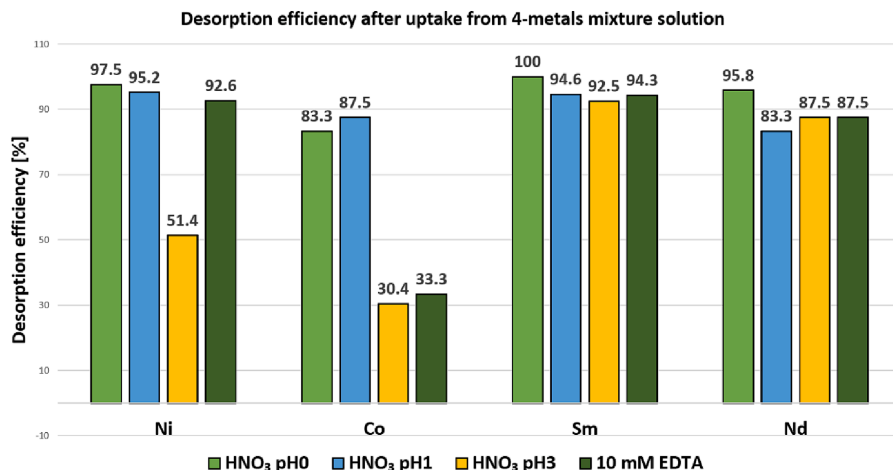


Fig. 10. Desorption efficiency after uptake from a four metal equimolar solution.

Table 3

Nanoadsorbent reusability test study, where A stands for the adsorption step and D for the desorption step.

Metal	1st cycle		2nd cycle		3rd cycle	
	A (mmol/g)	D (%)	A (mmol/g)	D (%)	A (mmol/g)	D (%)
Co	0.750	81.3	0.662	46.2	0.574	67.6
Ni	1.144	100	1.144	92.1	1.100	90
Sm	0.517	97.9	0.474	94.8	0.474	85.6
Nd	0.484	94.1	0.484	100	0.430	90

tried to release the REE cations from Sm/Nd mixtures, the desorption media with higher pH values (i.e. 10 mM EDTA and HNO₃ pH 3) exhibited slightly higher desorption efficiency.

When the desorption efficiency study was carried out after uptake using a four metal mixture, the desorption efficiency was highest using HNO₃ with pH 0 for all metals except for Co (see Fig. 10).

Table 3 shows the possibility of nanoadsorbent reusability. We can observe that samples showed good desorption rates in each cycle ranging between 70–100 %. A decrease in adsorption rates was noted after the first and second desorption cycles for Co. However, the nano-adsorbent had good adsorption/desorption rates even after three cycles for all other metals.

Table 4

Comparison of stability and selectivity between major classes of solid adsorbents with potential capacity to separate LTM from REE.

Matrix	Ligands	Uptake capacity, mmol/g (cation)	Selectivity LTM/REE	References
Silica	Ethylenediamino alkyl Pyridine thioalkyl Thiocyanate Isothiocyanate	1.83 (Co), 1.86(Ni), 1.10(Sm), 0.83(Nd)0.66(Co), 0.55(Ni), 0.56(Sm), 0.50 (Nd)0.75(Co), 0.58 (Ni)0.66(Sm), 0.67 (Nd)0.67(Co), 0.57 (Ni)0.77(Sm), 0.44 (Nd)	Ni/Nd = 5.1/1, Co/Sm = 1/1.65 Ni/Nd = 1/1.78 Co/Sm = 1/12 Ni/Nd = 1/1 Co/Sm = 1/18 Ni/Nd = 1.33/1 Co/Sm = 1/18	[17]
Chitosan&silica	EDTA	0.22(Co), 0.26(Ni)	N/A	[69]
Silica gel	Ni imprinted	0.35(Ni)	N/A	[70]
Zr phosphate	Surface hydrophosphate	0.28–0.56(Eu)	N/A	[71]
ZIF-8/U6N MOF composite	UiO66-NH ₂	1.45(Nd)	Co/Nd = 1/2	[72]
ZnBDC MOF	Graphene oxide	2.39(REE general)	N/A	[73]
ZnO	ZnBTC MOF	2.08(REE general)	N/A	[74]
COF	1,3,5-Triformylphloroglucinol (Tp) co-condensed with p-phenylenediamine (Pa)	0.59(La)	N/A	[75]
SBA-15 mesoporous silica	Triethylene pentamine	0.89(Pd) – as potential analog of Ni	N/A	[76]
SBA-15 mesoporous silica	EDTA & alkylphosphonic acid	1.1(Nd)	Ni/Nd = 261.5	[77]
Silica	Ethylenediamino benzene alkyl	1.18(Co), 1.45(Ni), 0.56(Sm), 0.47(Nd)	Ni/Nd = 8.6/1 Co/Sm = 3.2/1	This work

3.7. Comparison with earlier reported adsorbents

The task of separating REE and LTM with focus on LTM separation is of great importance for developing approaches to recycling of magnetic materials, but still remains a relatively scarcely addressed challenge. High selectivity has been proven for mesoporous silica based materials (see Table 4), but they are rather costly and suffer from hinders in desorption of adsorbed components. This emphasizes the need for understanding the principles of constructing adsorbents featuring higher selectivity towards LTM compared to REE. The material reported in the present work combines good adsorption capacity and quick desorption kinetics with pronounced selectivity towards LTM and even considerable difference in behavior between Co and Ni species, which opens new possibilities for many other potential applications.

4. Conclusions

We demonstrated a one-step grafting synthesis of hybrid SiO₂ nanoadsorbents permitting sequestration and separation of REE and LTM – a new and highly requested area of applications. The prepared material was characterized and tested for its adsorption, separation, and reusability properties in single or mixed equimolar metal solutions.

The produced adsorbent showed relatively rapid adsorption kinetics for LTM and REE at room temperature. Adsorption capacity achieved higher values for LTM, demonstrating the formation of surface complexes with 1:1 composition for studied Ni cations. The adsorbent revealed pronounced selectivity towards LTM compared to REE. Molecular insights into the origin of selective action were obtained through studies of the complex formation between the Ni(II) and the N-benzyl-ethylenediamine ligand function and Co(III) with tris(aminoethyl)amine ligand, showing chelation as a principal factor guiding LTM adsorption and desorption. Relatively dense packing of ligands on the silica surface was shown to have potential effects on their ordering permitting high adsorption capacity, resulting in 1:1 cation-to-ligand stoichiometry. The insights obtained from the model molecular structures were supported by the results of the XPS studies.

The desorption of target cations was investigated after uptake from a single metal solution and an equimolar mixture of 2 or 4 metals. The prepared nanoadsorbent exhibits high desorption rates even after three cycles of adsorption and desorption.

To summarize, this work proposes that the evaluated sorbents have potential as an environmentally friendly alternative to the conventional liquid phase separation techniques for LTM separation from REE.

CCRediT authorship contribution statement

Troy C. Breijaert: Investigation, Writing – review & editing. **Geoffrey Daniel:** Investigation, Writing – review & editing. **Fredric G. Svensson:** Investigation, Writing – review & editing. **Vadim G. Kessler:** Investigation, Writing – original draft, Writing – review & editing. **Gulaim A. Seisenbaeva:** Conceptualization, Funding acquisition, Supervision, Investigation, Writing – review & editing.

Declaration of Competing Interest

The authors declare that they have no known competing financial interests or personal relationships that could have appeared to influence the work reported in this paper.

Data availability

Data will be made available on request.

Acknowledgments

The authors would like to express gratitude to the ÅForsk foundation, grant No. 21-75, for financial support.

Appendix A. Supplementary material

Supplementary data to this article can be found online at <https://doi.org/10.1016/j.seppur.2023.124487>.

References

- [1] NASA, Global climate change The Causes of Climate Change. Human activities are driving the global warming trend observed since the mid-20th century. http://climate.nasa.gov/causes/#otp_the_role_of_humans, (accessed 15 December 2022).
- [2] J. Yu, L.H. Xie, J.R. Li, Y. Ma, J.M. Seminario, P.B. Balbuena, CO₂ Capture and Separations Using MOFs: Computational and Experimental Studies, Chem. Rev. 117 (2017) 9674–9754, <https://doi.org/10.1021/acs.chemrev.6b00626>.

- [3] M. Jowitt, G.M. Mudd, J.F.H. Thompson, Future availability of non-renewable metal resources and the influence of environmental, social, and governance conflicts on metal production, *Commun. Earth Environ.* 1 (2020) e13.
- [4] M. Le Page, The world is warming, and we know why. We also know how to stop it. To stave off the worst effects, we must wean ourselves off greenhouse gas-producing fossil fuels – and fast, hitting “net zero” carbon emissions by mid-century, *New Sci.* 251 (34–37) (2021) 41–44, [https://doi.org/10.1016/S0262-4079\(21\)01384-1](https://doi.org/10.1016/S0262-4079(21)01384-1).
- [5] T. Kobashi, Y. Choi, Y. Hirano, Y. Yamagata, K. Say, Rapid rise of decarbonization potentials of photovoltaics plus electric vehicles in residential houses over commercial districts, *Appl. Energy* 306 (2022), 118142, <https://doi.org/10.1016/j.apenergy.2021.118142>.
- [6] Z. Ye, N. Yu, R. Wei, X.C. Liu, 2022 Decarbonizing regional multi-model transportation system with shared electric charging hubs, *Transp. Res. Part C Emerg. Technol.* 144 (2022), 103881, <https://doi.org/10.1016/j.trc.2022.103881>.
- [7] B. Ballinger, D. Schmieda-Lopez, B. Kefford, B. Parkinson, M. Stringer, C. Greig, S. Smart, The vulnerability of electric-vehicle and wind-turbine supply chains to the supply of rare-earth elements in a 2-degree scenario, *Sustain. Prod. Consum.* 22 (2020) 68–76, <https://doi.org/10.1016/j.spc.2020.02.005>.
- [8] G. Bailey, M. Orefice, B. Sprecher, M.A.R. Onal, E. Herraz, W. Dewulf, K. van Acker, Life cycle inventory of samarium-cobalt permanent magnets, compared to neodymium-iron-boron as used in electric vehicles, *J. Cleaner Production* 286 (2021), 125294, <https://doi.org/10.1016/j.jclepro.2020.125294>.
- [9] C. Church, A. Crawford, Green Conflict Minerals: The Fuels of Conflict in the Transition to a Low-carbon Economy, IISD Report, International Institute for Sustainable Development, Manitoba, 2018.
- [10] T. Watari, K. Nansai, K. Nakajima, Review of critical metal dynamics to 2050 for 48 elements, *Resour. Conserv. Recycl.* 155 (2020), 104669, <https://doi.org/10.1016/j.resconrec.2019.104669>.
- [11] W.C. Wilfong, B.W. Kail, Q. Wang, F. Shi, G. Shipley, T.J. Tarka, M.L. Gray, Stable immobilized amine sorbents for heavy metal and REE removal from industrial wastewaters, *Environ. Sci.: Water Res. Technol.* 6 (2020) 1286–1299, <https://doi.org/10.1039/C9EW00915A>.
- [12] N. Swain, S. Mishra, A review on the recovery and separation of rare earths and transition metals from secondary resources, *J. Clean. Prod.* 220 (2019) 884–898, <https://doi.org/10.1016/j.jclepro.2019.02.094>.
- [13] M. Gergoric, C. Ekberg, M.R.S.J. Foreman, B.M. Steenari, T. Retegan, Characterization and Leaching of Neodymium Magnet Waste and Solvent Extraction of the Rare-Earth Elements Using TODGA, *J. Sustain. Metall.* 3 (2017) 638–645, <https://doi.org/10.1007/s40831-017-0122-8>.
- [14] J.Z. Wang, Y.H. Hsieh, Y.C. Tang, Y.H. Shen, Separation of Cobalt, Samarium, Iron, and Copper in the Leaching Solution of Scrap Magnets, *Metals* 13 (2023) 90, <https://doi.org/10.3390/met13010090>.
- [15] N. Swain, S. Pradhan, S. Mishra, Efficiency of Aliquat 336 for hydrometallurgical separation of Sm (III) and Co (II) from nitrate medium, *Miner. Eng.* 139 (2019), 105872, <https://doi.org/10.1016/j.mineng.2019.105872>.
- [16] M. Orefice, H. Audour, Z. Li, K. Binnemans, Solvometallurgical route for the recovery of Sm Co, Cu and Fe from SmCo permanent magnets, *Sep. Purif. Technol.* 219 (2019) 281–289, <https://doi.org/10.1016/j.seppur.2019.03.029>.
- [17] A. Vardanyan, A. Guillot, T. Budnyak, G.A. Seisenbaeva, Tailoring Nanoadsorbent Surfaces: Separation of Rare Earths and Late Transition Metals in Recycling of Magneto Materials, *Nanomater.* 12 (2022) 974, <https://doi.org/10.3390/nano12060974>.
- [18] Y. Zhang, F. Gu, Z. Su, S. Liu, C. Anderson, T. Jiang, Hydrometallurgical Recovery of Rare Earth Elements from NdFeB Permanent Magnet Scrap: A Review, *Metals* 10 (2020) 841, <https://www.mdpi.com/2075-4701/10/6/841>.
- [19] J. Durand, D. Bourgeois, M. Bertrand, D. Meyer, Comprehensive Studies on Third Phase Formation: Application to $U^{(VI)}$ / $Th^{(IV)}$ Mixtures Extracted by TBP in N-dodecane, *Solvent Extr. Ion Exch.* 37 (2019) 328–346, <https://doi.org/10.1080/07366299.2019.1656853>.
- [20] F. Xie, T.A. Zhang, D. Dreisinger, F. Doyle, A critical review on solvent extraction of rare earths from aqueous solutions, *Min. Eng.* 56 (2014) 10–28, <https://doi.org/10.1016/j.mineng.2013.10.021>.
- [21] Y. Hu, J. Florek, D. Larièvre, F.-G. Fontaine, F. Kleitz, Recent Advances in the Separation of Rare Earth Elements Using Mesoporous Hybrid Materials, *Chem. Rec.* 18 (2018) 1261–1276, <https://doi.org/10.1002/tcr.201800012>.
- [22] X. Vecino, M. Reig, Wastewater Treatment by Adsorption and/or Ion-Exchange Processes for Resource Recovery, *Water* 14 (2022) 911, <https://doi.org/10.3390/w14060911>.
- [23] J. Florek, A. Mushtaq, D. Larièvre, F.-G. Fontaine, F. Kleitz, Selective recovery of rare earth elements using chelating ligands grafted on mesoporous surfaces, *RSC Adv.* 5 (2015) 103782–103789, <https://doi.org/10.1039/C5RA21027E>.
- [24] J.C. Callura, K.M. Perkins, C.W. Noack, N.R. Washburn, D.A. Dzombak, A. K. Karamalidis, Selective adsorption of rare earth elements onto functionalized silica particles, *Green Chem.* 20 (2018) 1515–1526, <https://doi.org/10.1039/C8GC00051D>.
- [25] A. Hadeila, M. Lakić, M. Potocnik, A. Kosak, A. Gutmaier, A. Lobnik, Novel reusable functionalized magnetic cobalt ferrite nanoparticles as oil adsorbents, *Adsorp Sci Technol.* 38 (2020) 168–190, <https://doi.org/10.1177/0263617420922014>.
- [26] H. Zhang, Y. Pan, Z. Wang, A. Wu, Y. Zhang, Synthesis of hollow mesoporous manganese dioxide nanoadsorbents with strong negative charge and their ultra-efficient adsorption for cationic dyes, *Sep. Purif. Technol.* 295 (2022), 121241, <https://doi.org/10.1016/j.seppur.2022.121241>.
- [27] P. Moharrami, E. Motamedi, Application of cellulose nanocrystals prepared from agricultural wastes for synthesis of starch-based hydrogel nanocomposites: Efficient and selective nanoadsorbent for removal of cationic dyes from water, *Bioresour. Technol.* 313 (2020), 123661, <https://doi.org/10.1016/j.biortech.2020.123661>.
- [28] P. Pillai, S. Dharasarkar, M. Shah, R. Sultania, Determination of fluoride removal using silica nano adsorbent modified by rice husk from water, *Groundw. Sustain. Dev.* 11 (2020), 100423, <https://doi.org/10.1016/j.gsd.2020.100423>.
- [29] M.E. Peralta, D.O. Mártire, M.S. Moreno, M.E. Parolo, L. Carlos, Versatile nanoadsorbents based on magnetic mesostructured silica nanoparticles with tailored surface properties for organic pollutants removal, *J. Environ. Chem. Eng.* 9 (2021), 104841, <https://doi.org/10.1016/j.jece.2020.104841>.
- [30] S. Das, A. Samanta, K. Kole, G. Gangopadhyay, S. Jana, MnO₂ flowery nanocomposites for efficient and fast removal of mercury(II) from aqueous solution: a facile strategy and mechanistic interpretation, *Dalton Trans.* 49 (2020) 6790–6800, <https://doi.org/10.1039/D0DT01054E>.
- [31] M. Kalantari, Z. Gu, Y. Cao, C. Lei, J. Zhang, Thiolated silica nanoadsorbents enable ultrahigh and fast decontamination of mercury(II): understanding the contribution of thiol moieties' density and accessibility on adsorption performance, *Environ. Sci.: Nano.* 7 (2020) 851–860, <https://doi.org/10.1039/C9EN01123D>.
- [32] I. Ali, M. Asim, T.A. Khan, Low cost adsorbents for the removal of organic pollutants from wastewater, *J. Environ. Manage.* 113 (2012) 170–183, <https://doi.org/10.1016/j.jenvman.2012.08.028>.
- [33] S.P. Mishra, Adsorption-desorption of heavy metal ions, *Current Science*, 107 (2014) 601–612, JSTOR, <http://www.jstor.org/stable/24103532>, 2014 (Accessed 7 December 2022).
- [34] B.I. Kharisov, H.V.R. Dias, O.V. Kharisova, Nanotechnology-based remediation of petroleum impurities from water, *J. Pet. Sci. Eng.* 122 (2014) 705–718, <https://doi.org/10.1016/j.petrol.2014.09.013>.
- [35] Y. Wu, H. Pang, Y. Liu, X. Wang, S. Yu, D. Fu, X. Wang, Environmental remediation of heavy metal ions by novel-nanomaterials: A review, *Environ. Pollut.* 246 (2019) 608–620, <https://doi.org/10.1016/j.envpol.2018.12.076>.
- [36] F. Almomani, R. Bhosale, M. Khraisheh, A. Kumar, T. Almomani, Heavy metal ions removal from industrial wastewater using magnetic nanoparticles (MNP), *Appl. Surf. Sci.* 506 (2020), 144924, <https://doi.org/10.1016/j.apsusc.2019.144924>.
- [37] H. Sadegh, G.A.M. Ali, Potential Applications of Nanomaterials in Wastewater Treatment: Nanomaterials Performance, in: A. Hussain, S. Ahmed (Eds.), *Advanced Treatment Techniques for Industrial Wastewater*, IGI Global, Hershey, 2019, pp. 51–61.
- [38] H. Irving, J.M.M. Griffiths, The stabilities of complexes formed by some bivalent transition metals with N-alkyl-substituted ethylenediamines, *J. Chem. Soc.* (1954) 213–223, <https://doi.org/10.1039/JR9540000213>.
- [39] P. Paoletti, Formation of metal complexes with ethylenediamine: a critical study of equilibrium constants, enthalpy and entropy values, *Pure & Appl. Chem.* 56 (1984) 491–522, <https://doi.org/10.1351/pac198456040491>.
- [40] T.C. Breijer, T.M. Budnyak, V.G. Kessler, G.A. Seisenbaeva, Tailoring a bio-based adsorbent for sequestration of late transition and rare earth elements, *Dalton Trans.* 51 (2022) 17978–17986, <https://doi.org/10.1039/D2DT03150G>.
- [41] E. Polido Legaria, M. Samouhos, V.G. Kessler, G.A. Seisenbaeva, Toward Molecular Recognition of REEs: Comparative Analysis of Hybrid Nanoadsorbents with the Different Complexant Ligands EDTA, DTPA, and TTHA, *Inorg. Chem.* 56 (2017) 13938–13948, <https://doi.org/10.1021/acs.inorgchem.7b02056>.
- [42] M. Barczak, Functionalization of mesoporous silica surface with carboxylic groups by Meldrum's acid and its application for sorption of proteins, *J. Porous Mater.* 26 (2019) 291–300, <https://doi.org/10.1007/s10934-018-0655-7>.
- [43] N. Fairley, V. Fernandez, M. Richard-Plouet, C. Guillot-Deudon, J. Walton, E. Smith, D. Flahaut, M. Greiner, M. Biesinger, S. Tougard, D. Morgan, J. Baltrusaitis, *Appl. Surf. Sci. Adv.* 5 (2021), 100112.
- [44] K.Y. Foo, B.H. Hameed, Insight into the modeling of adsorption isotherm systems, *Chem. Eng. J.* 156 (2010) 2–10, <https://doi.org/10.1016/j.cej.2009.09.013>.
- [45] S. Kundu, A.K. Gupta, Amino adsorption onto iron oxide-coated cement (IOC): regression analysis of equilibrium data with several isotherm models and their optimization, *Chem. Eng. J.* 122 (2006) 93–106, <https://doi.org/10.1016/j.cej.2006.06.002>.
- [46] R. Flatt, I. Schöber, Superplasticizers and the rheology of concrete, in: N. Roussel (Ed.), *Understanding the Rheology of Concrete*, Woodhead Publishing Limited, Sawston, 2012, pp. 144–208.
- [47] L. Largitte, R. Pasquier, A review of the kinetics adsorption models and their application to the adsorption of lead by an activated carbon, *Chem. Eng. Res. Des.* 109 (2016) 495–504, <https://doi.org/10.1016/j.cherd.2016.02.006>.
- [48] T.R. Sahoo, B. Preot, Adsorption processes for the removal of contaminants from wastewater, in: B. Bonelli, F.S. Freyria, L. Rossetti, R. Sethi (Eds.), *Nanomaterials for the Detection and Removal of Wastewater Pollutants* (Book), Elsevier Inc., Amsterdam, 2020, pp. 161–222.
- [49] G. Socrates, *Infrared and Raman Characteristic Group Frequencies, Tables and Charts*, third ed., John Wiley and Sons, Chichester, 2004.
- [50] B. Stuart, *Infrared Spectroscopy: Fundamentals and Applications*, John Wiley & Sons, Sydney, 2004.
- [51] I. Langmuir, The Constitution and Fundamental Properties of Solids and Liquids. Part I. Solids, *J. Am. Chem. Soc.* 38 (1916) 2221–2295, <https://doi.org/10.1021/ja02268a002>.
- [52] I. Langmuir, The Adsorption of Gases on Plane Surfaces of Glass, Mica and Platinum, *J. Am. Chem. Soc.* 40 (1918) 1361–1403, <https://doi.org/10.1021/ja02242a004>.
- [53] H. Swenson, N.P. Stadie, Langmuir's Theory of Adsorption: A Centennial Review, *Langmuir* 35 (2019) 5409–5426, <https://doi.org/10.1021/acs.langmuir.9b00154>.

- [54] S. Alafnan, A. Awotunde, G. Glatz, S. Adjei, I. Alrumaih, A. Gowida, Langmuir adsorption isotherm in unconventional resources: Applicability and limitations, *J. Pet. Sci. Eng.* 207 (2021), 109172, <https://doi.org/10.1016/j.petrol.2021.109172>.
- [55] K.C. Patel, D.E. Goldberg, Aralkylpolyamine complexes—VI: Complexes of nickel (II) with N-benzylethylenediamine, *J. inorg. nucl. chem.* 36 (1974) 565–568, [https://doi.org/10.1016/0022-1902\(74\)80114-4](https://doi.org/10.1016/0022-1902(74)80114-4).
- [56] R. Garg, R. Garg, N.O. Eddy, A.I. Almohana, S.F. Almojil, M.A. Khan, S.H. Hong, Biosynthesized silica-based zinc oxide nanocomposites for the sequestration of heavy metal ions from aqueous solutions, *J. King Saud Univ. Sci.* 34 (2022), 101996, <https://doi.org/10.1016/j.jksus.2022.101996>.
- [57] X. Fan, H. Liu, E. Anang, D. Ren, Effects of electronegativity and hydration energy on the selective adsorption of heavy metal ions by synthetic NaX zeolite, *Materials* 14 (2021) 4066, <https://doi.org/10.3390/ma14154066>.
- [58] X. Xin, Q. Wei, J. Yang, L. Yan, R. Feng, G. Chen, B. Du, H. Li, Highly efficient removal of heavy metal ions by amine-functionalized mesoporous Fe₃O₄ nanoparticles, *Chem. Eng. J.* 184 (2012) 132–140, <https://doi.org/10.1016/j.cej.2012.01.016>.
- [59] E. Polido Legaria, S. Demirel Topel, V.G. Kessler, G.A. Seisenbaeva, Molecular insights into selective action of a magnetically removable complexone-grafted adsorbent, *Dalton Trans.* 44 (2015) 1273–1282, <https://doi.org/10.1039/C4DT03096F>.
- [60] S. Alvarez, A cartography of the van der Waals territories, *Dalton Trans.* 42 (2013) 8617–8636, <https://doi.org/10.1039/C3DT50599E>.
- [61] N.N. Greenwood, A. Earnshaw, *Chemistry of the Elements* ch. 26 (1986) 1116–1117.
- [62] J. Baltusaitis, P.M. Jayaweera, V.H. Grassian, XPS study of nitrogen dioxide adsorption on metal oxide particle surfaces under different environmental conditions, *Phys. Chem. Chem. Phys.* 11 (2009) 8295–8305, <https://doi.org/10.1039/B907584D>.
- [63] A. Artemenko, A. Shchukarev, P. Štenclová, T. Wågberg, J. Segervald, X. Jia, A. Kromka, Reference XPS spectra of amino acids, *IOP Conf. Series: Materials Sci. Eng.* 1050 (2021), 012001, <https://doi.org/10.1088/1757-899X/1050/1/012001>.
- [64] K.C. Dash, B. Folkesson, R. Larsson, M. Mohapatra, An Xps Investigation On A Series Of Schiff Base Dioxime Ligands And Cobalt Complexes, *J. Electron Spectrosc. Related Phenomena* 49 (1989) 343–357, [https://doi.org/10.1016/0368-2048\(89\)85022-4](https://doi.org/10.1016/0368-2048(89)85022-4).
- [65] A.R. Silva, M. Martins, M.M.A. Freitas, A. Valente, C. Freire, B. de Castro, J. L. Figueiredo, Immobilisation of amine-functionalised nickel(II) Schiff base complexes onto activated carbon treated with thionyl chloride, *Microporous Mesoporous Mater.* 55 (2002) 275–284, [https://doi.org/10.1016/S1387-1811\(02\)00429-8](https://doi.org/10.1016/S1387-1811(02)00429-8).
- [66] D. Lionetti, V.W. Day, J.D. Blakemore, Noncovalent immobilization and surface characterization of lanthanide complexes on carbon electrodes, *Dalton Trans.* 46 (2017) 11779–11789, <https://doi.org/10.1039/C7DT02577G>.
- [67] Q.L. Yang, D. Wang, C.Z. Wang, X.F. Li, K.Z. Li, Y. Peng, J.H. Li, Facile surface improvement method for LaCoO₃ for toluene oxidation, *Catal. Sci. Technol.* 8 (2018) 3166–3173, <https://doi.org/10.1039/C8CY00765A>.
- [68] A.P. Grosvenor, M.C. Biesinger, R.St.C. Smart, N.S. McIntyre, New interpretations of XPS spectra of nickel metal and oxides, *Surface Sci.* 600 (2006) 1771–1779, <https://doi.org/10.1016/j.susc.2006.01.041>.
- [69] E. Repo, J.K. Warchol, A. Bhatnagar, M. Sillanpää, Heavy metals adsorption by novel EDTA-modified chitosan–silica hybrid materials, *J. Colloid Interface Sci.* 358 (2011) 261–267, <https://doi.org/10.1016/j.jcis.2011.02.059>.
- [70] H.X. He, Q. Gan, C.G. Feng, Preparation and application of Ni(II) ion-imprinted silica gel polymer for selective separation of Ni(II) from aqueous solution, *RSC Adv.* 7 (2017) 15102–15111, <https://doi.org/10.1039/C7RA00101K>.
- [71] J. Veliscek-Carolan, T.L. Hanley, V. Luca, Zirconium organophosphonates as high capacity, selective lanthanide sorbents, *Separation Purif. Technol.* 129 (2014) 150–158, <https://doi.org/10.1016/j.seppur.2014.03.028>.
- [72] M.M. Zhang, K. Yang, J.S. Cui, H.B. Yu, Y.J. Wang, W.J. Shan, Z.N. Lou, Y. Xiong, 3D-agaric like core-shell architecture UiO-66-NH₂@ZIF-8 with robust stability for highly efficient REEs recovery, *Chem Eng J* 386 (2020) 124023, <https://doi.org/10.1016/j.cej.2020.124023>.
- [73] Z.Y. Chen, Z. Li, J. Chen, H.X. Tan, J.S. Wu, H.D. Qiu, Selective Adsorption of Rare Earth Elements by Zn-BDC MOF/Graphene Oxide Nanocomposites Synthesized via In Situ Interlayer-Confined Strategy, *Ind. Eng. Chem. Res.* 61 (2022) 1841–1849, <https://doi.org/10.1021/acs.iecr.1c04180>.
- [74] J.S. Wu, Z. Li, H.X. Tan, S.B. Du, T.Q. Liu, Y.L. Yuan, X.H. Liu, H.D. Qiu, Highly Selective Separation of Rare Earth Elements by Zn-BTC Metal–Organic Framework/Nanoporous Graphene via In Situ Green Synthesis, *Anal. Chem.* 93 (2021) 1732–1739, <https://doi.org/10.1021/acs.analchem.0c04407>.
- [75] J. Xiao, B. Li, R.B. Qiang, H.D. Qiu, J. Chen, Highly selective adsorption of rare earth elements by honeycomb-shaped covalent organic frameworks synthesized in deep eutectic solvents, *Environ. Res.* 214 (2022), 113977, <https://doi.org/10.1016/j.envres.2022.113977>.
- [76] S.Z. Xu, S.Y. Ning, Y.B. Wang, X.P. Wang, H.R. Dong, L.F. Chen, X.B. Yin, T. Fujita, Y.Z. Wei, Precise separation and efficient enrichment of palladium from wastewater by amino-functionalized silica adsorbent, *J. Cleaner Prod.* 396 (2023), 136479, <https://doi.org/10.1016/j.jclepro.2023.136479>.
- [77] O. Dudarko, N. Kobylinska, V. Kessler, G. Seisenbaeva, Recovery of rare earth elements from NdFeB magnet by mono- and bifunctional mesoporous silica: Waste recycling strategies and perspectives, *Hydrometallurgy* 210 (2022), 105855, <https://doi.org/10.1016/j.hydromet.2022.105855>.

Uptake and separation of Rare Earth Elements and Late Transition Metal cations by nanoadsorbent grafted with diamino ligands

Marijana Lakić^a, Troy C. Breijaert^a, Geoffrey Daniel^b, Fredric G. Svensson^c, Vadim G. Kessler^a, and Gulaim A. Seisenbaeva^{a,*}

^a Department of Molecular Sciences, Biocentrum, Swedish University of Agricultural Sciences, Almas Allé 5, Box 7015 SE-750 07 Uppsala, Sweden.

^b Department of Forest Biomaterials and Technology, Swedish University of Agricultural Sciences, Vallvägen 9C-D, SE-756 51 Uppsala, Sweden

^c Department of Materials Science, Solid State Physics, Box 35, Ångströmlaboratoriet, Lägerhyddsvägen 1, Uppsala University, SE-751 03 Uppsala, Sweden

* Corresponding author at: Department of Molecular Sciences, Biocentrum, Swedish University of Agricultural Sciences, Almas Allé 5, Box 7015 SE-750 07 Uppsala, Sweden.

E-mail address: gulaim.seisenbaeva@slu.se

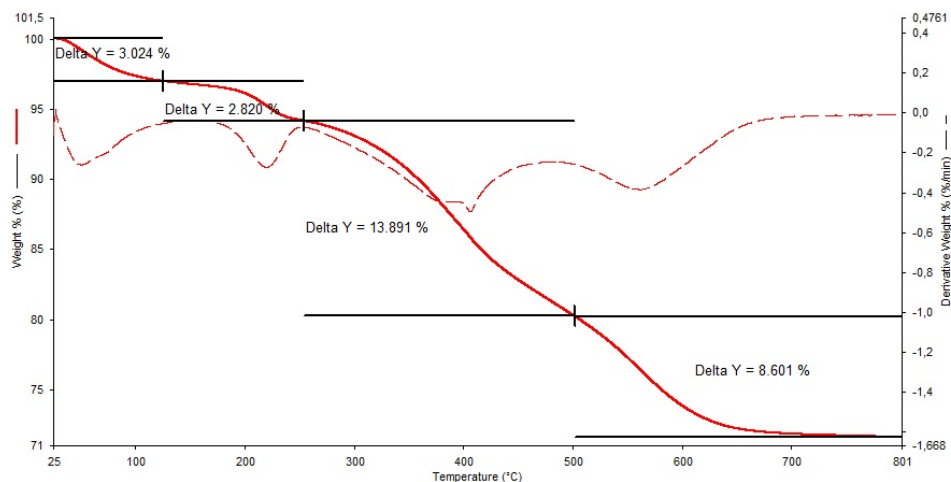


Fig. S1: TGA of prepared nanoadsorbent material.

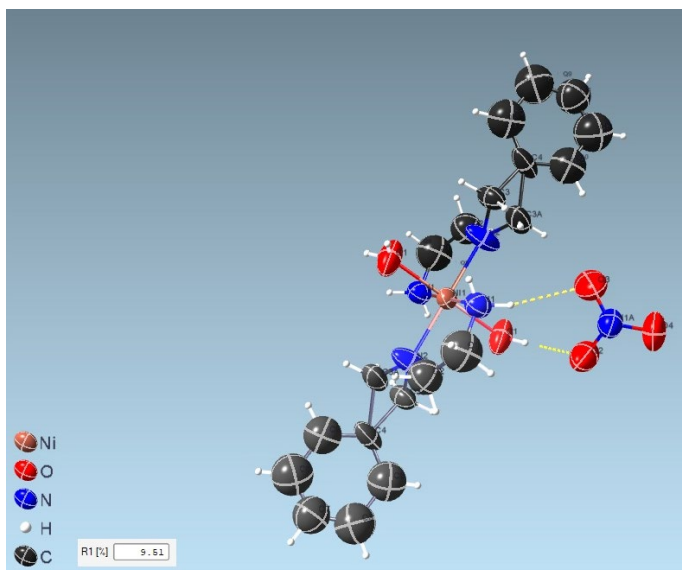


Fig. S2. Molecular structure of the $\text{Ni}(\text{H}_2\text{NC}_2\text{H}_4\text{NHCH}_2\text{C}_6\text{H}_5)_2(\text{H}_2\text{O})_2(\text{NO}_3)_2$ complex, demonstrating resolved disorder for the C(3) atom and restricted motion for C(1), C(2), C(5), C(6), C(7) and C(8) atoms.

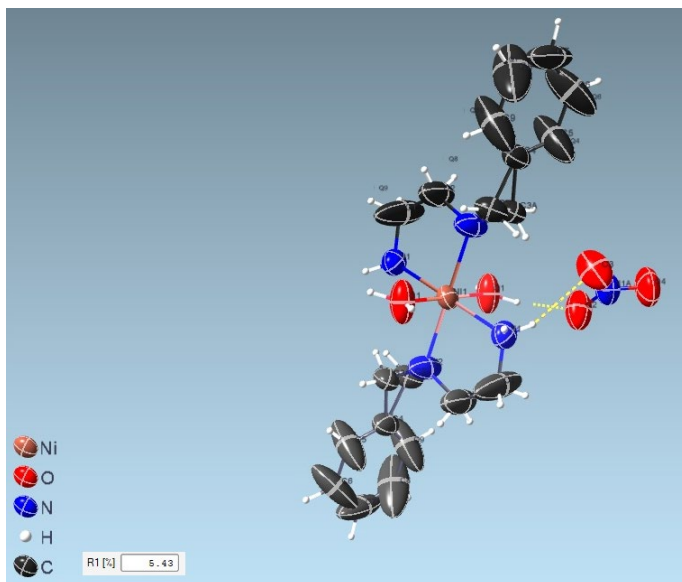


Fig. S3. Molecular structure of the $\text{Ni}(\text{H}_2\text{NC}_2\text{H}_4\text{NHCH}_2\text{C}_6\text{H}_5)_2(\text{H}_2\text{O})_2(\text{NO}_3)_2$ complex, demonstrating resolved disorder for the C(3) atom and free ligand motion, resulting in thermal disorder of especially the "flipping" benzene ring of the ligand. Please, note the drastic decrease in the discrepancy factor for such refinement.

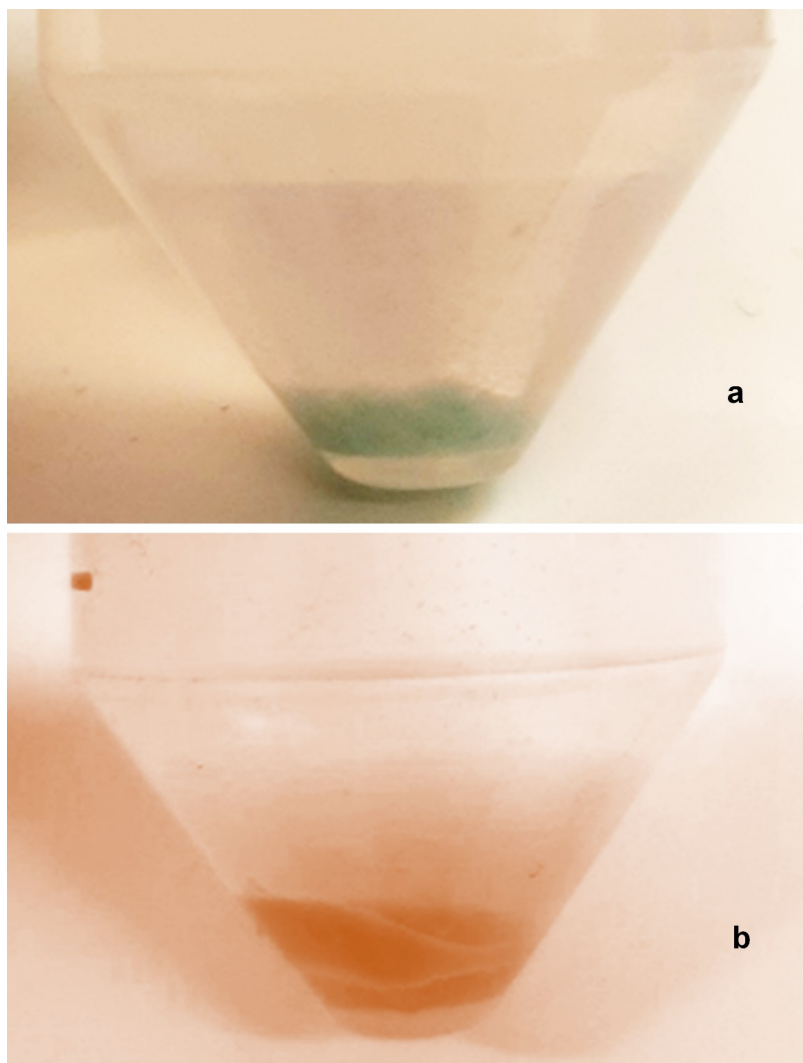


Fig. S4. Color change in the adsorbent bearing Co-ions: a) 15 min after addition of the adsorbent, b) 18 hours after addition of the adsorbent.

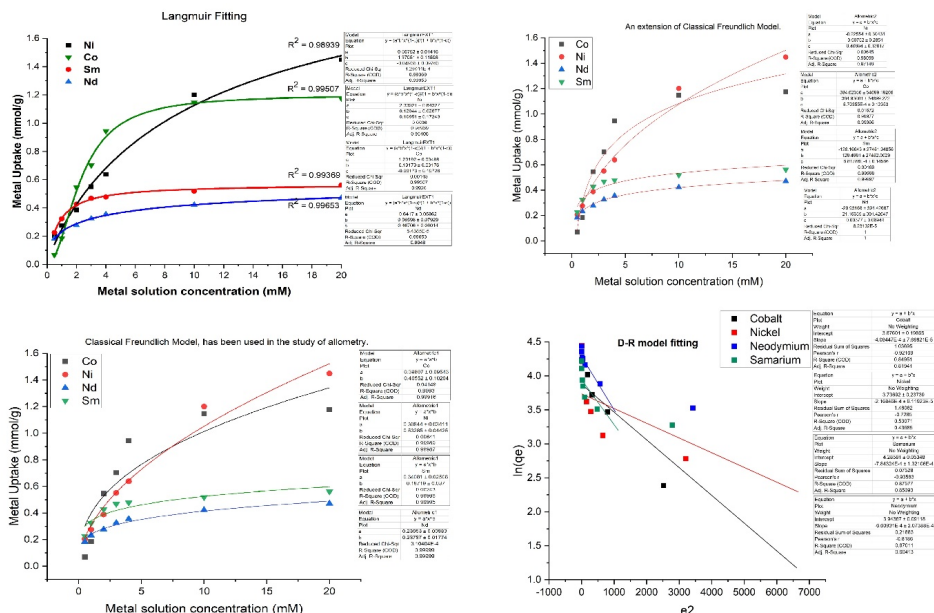


Fig. S5. Fitting of adsorption data with Langmuir, Classical Freundlich, Extended Classical Freundlich, and D-R models.

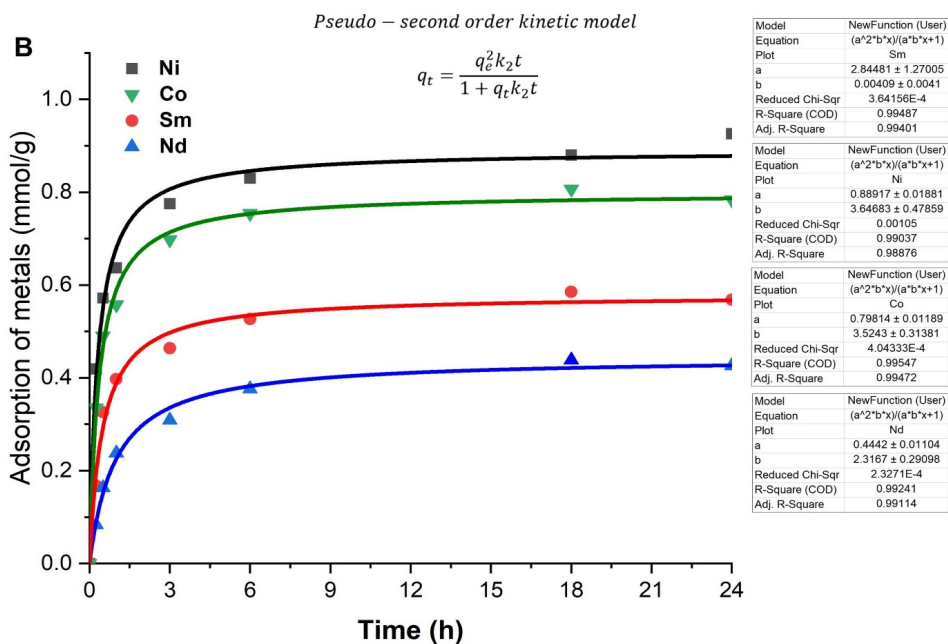
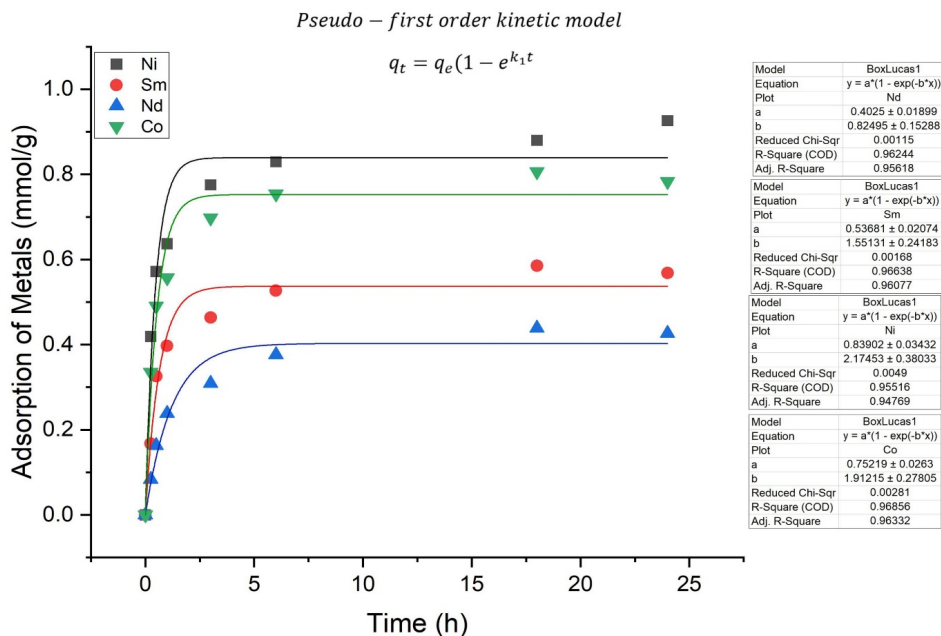


Fig. S6. Fitting of the adsorption kinetics with pseudo-1st and pseudo-2nd order models.



Contents lists available at ScienceDirect

Carbohydrate Polymer Technologies and Applications

journal homepage: www.sciencedirect.com/journal/carbohydrate-polymer-technologies-and-applications

Functionalization of bacterial nanocellulose-based wound dressing for increased drug retention

Troy C. Breijaert^a, Marina Fontes^b, Paula de Abreu Fernandes^c, Hernane da Silva Barud^{c,d}, Sidney J.L. Ribeiro^d, Gulaim A. Seisenbaeva^{a,*}^a Department of Molecular Science, Swedish University of Agricultural Science, Uppsala, 756 51 Ultuna, Sweden^b Department of Chemistry, Federal University of São Carlos (UFSCar), São Carlos, 13565-905, SP, Brazil^c Department of Biotechnology, University of Araraquara (UNIARA), 14801340, Araraquara, SP, Brazil^d Institute of Chemistry, São Paulo State University – UNESP, Araraquara, SP, 14800-900 Brazil

ARTICLE INFO

Keywords:

Bacterial nanocellulose
Wound dressing
Phosphorylation
Drug delivery
Titania

ABSTRACT

Bacterial nanocellulose is a fascinating biopolymer with immense application potential, including as a wound dressing material. It is highly biocompatible and capable of keeping humidity needed for wound healing. However, it lacks specific affinity to pharmaceuticals to be delivered in a controlled fashion in a topical application, urged by the necessity to decrease the release of medicines to the environment. Solving this problem requires tailoring of the material functionality by chemical modification. In this work, a two-step strategy applying first phosphorylation and then introduction of biocompatible mineral particles was applied. Surface modification of commercially available wound dressing material based on dried bacterial nanocellulose led to phosphate grafting of 1.5–1.8 mmol/g and then uniform coverage of individual fibers (colloidal TiO₂) or formation of aggregated platelets (TiBALDH®) on the surface (with Ti:P element ratios 0.45–0.80). To the titania functionalized dressing the broad spectrum antibiotic Tetracycline was bound (41–45 mg g⁻¹) with its release delayed over several hours / days (over 50 % in 120 h for both nanocarriers). Biological essays indicated excellent biocompatibility and improved cell adhesion, offering a path to accelerated wound closure, promising for diverse tissue engineering applications. This study demonstrated a strategy in approach to dressing materials with delayed drug release properties exploiting the affinity of pharmaceuticals to mineral nanoparticles.

1. Introduction

Materials for wound treatment are highly requested and attract continuous attention of researchers. A paramount aim in wound management is preventing bacterial infection. Commonly used wound dressing materials function by providing a physical barrier against infection caused by microorganisms, passively protecting against infection (Stoica, Chircov & Grumezescu, 2020). Therefore, antibiotics are often prescribed per-orally for systemic treatment. This results in consuming large quantities of antibiotics and their distribution into wastewater streams through excretion, leading to water streams becoming increasingly polluted by residual pharmaceuticals (Malnes et al., 2022). Exposed to increasing background concentrations of antibiotics, bacteria are becoming increasingly resistant against them, which has led to augmented interest in alternatives such as local, topical application of antibiotics for wound management.

The emergence of nanotechnology has opened up avenues for the production of active wound-dressing materials, which facilitate wound healing, exert antibacterial properties and/or stimulate tissue regrowth (Moritz et al., 2014; Li et al., 2020). Inorganic nanoparticles for example, have been reported to improve wound healing (Seisenbaeva et al., 2017; Paladini & Pollini, 2019) and they have been proven to facilitate controlled release of antibiotics (Galkina et al., 2015a; 2015b). Combining the attractive properties of inorganic nanoparticles with natural polymers, allows for the creation of hybrid materials with unique properties, which can be used for drug delivery.

Bio-based polymers such as cellulose have increasingly been addressed as matrices for active inorganic components. Cellulose is the most abundant natural polymer on the planet, accounting for 1.5 × 10¹² tons of annual biomass production (Klemm, Heublein, Fink & Bohn, 2005). It is a linear homopolymer comprised of β-1,4-linked glycopyranose (O'Sullivan, 1997; Marchessault & Sundararajan, 1983). It is

* Corresponding author.

E-mail addresses: hsbarud@uniara.edu.br (H.S. Barud), gulaim.seisenbaeva@slu.se (G.A. Seisenbaeva).<https://doi.org/10.1016/j.carpta.2025.100756>

Available online 14 March 2025

2666-8939/© 2025 The Author(s). Published by Elsevier Ltd. This is an open access article under the CC BY license (<http://creativecommons.org/licenses/by/4.0/>).

found in the cell wall of plants, in seaweed, and in fungi. In addition, it is produced by some species of bacteria, such as *Komagataibacter Xylinus* (formerly *Acetobacter* and *Gluconacetobacter*) which forms a biofilm comprised of cellulose (Brown, 1886). Cellulose and its derivatives have a long history in the pharmaceutical industry in various types of formulations as it is biodegradable, non-toxic, non-carcinogenic and biocompatible (Thoores et al., 2014). Nanocellulose for biomedical applications can be produced from many different sources such as wood, cotton or even fruit peel waste (Datta et al., 2024).

Bacterial nanocellulose (BNC) is a type of cellulose with major advantages over vegetal (plant) cellulose, owing to its unique native purity (Klemm, Schumann, Udhardt & Marsch, 2001). It is produced by fermentation and only contains microbial cells, nutrients and secondary metabolites, which can easily be removed to produce highly pure cellulose. By comparison, vegetal cellulose contains by-products such as lignin, pectin and hemicellulose (Klemm, Heublein, Fink & Bohn, 2005). BNC has outstanding physical and mechanical properties, which emerge from its unique 3D structure. BNC aggregates to form long aggregated microfibrils with a width of 70–150 nm in a reticular network which provides the material with high surface area, elasticity and flexibility (Klemm, Heublein, Fink & Bohn, 2005; Fink, Purz, Bohn & Kunze, 1997). BNC has many intrinsic characteristics that make it an ideal wound dressing material, especially for burn wounds, temporary skin substitutes or tissue regeneration as it has the capacity to absorb exudates from injured tissue and accelerate granulation (Khalid et al., 2017; Li et al., 2015). A major drawback in using BNC and other celluloses for wound dressing applications however, is a lack of antibacterial activity intrinsic to the material, meaning that wounds can easily become infected if not properly managed.

In order to overcome this challenge, antibacterial agents such as silver nanoparticles have been added to cellulose materials in order to grant it antibacterial properties (Barud et al., 2011; Volova et al., 2018). Silver nanoparticles though have been shown to be cytotoxic due to the generation of ROS by the particles itself or through the release of silver ions (Liao, Li & Tjong, 2019; Tripathi & Goshisht, 2022). An alternative approach is loading cellulose materials with antibiotics. However, cellulose itself has a low retention for many drugs and there is a risk that rapid release of drugs may have toxic effects (Horue et al., 2023).

BNC benefits from having a highly porous structure in its native state, which has been used to imbue the material with antibacterial properties by loading metal/metal-oxide nanoparticles with antibacterial properties (Khalid et al., 2017; Volova et al., 2018; Li et al., 2017) or loading pharmaceuticals for delayed drug release (Moritz et al., 2014). Nanosized TiO₂ in particular has been garnering attention as it is considered biocompatible with low toxicity. It has been demonstrated that depending on the surface chemistry involved, titania induces blood coagulation (Seisenbaeva et al., 2017; Svensson et al., 2021; Ekstrand-Hammarström et al., 2015), which promotes wound-healing by initiating an immune response (Seisenbaeva et al., 2017). Titania derived from ammonium oxo-lactato titanate by comparison has been shown to cause minimal coagulation activation, which makes it suitable for applications where coagulation is undersired (Svensson et al., 2021). Frequently reported methodology for imbuing BNC with antibacterial properties often relies on impregnating the material with nanoparticles and/or pharmaceuticals within the porous substrate, without the formation of a chemical bond, followed by lyophilizing or supercritical drying of the material, potentially leading to the release of nanoparticles into the wound environment with all consequences that entails.

Another specific limitation of using BNC is its limited swelling capacity post-drying (Klemm, Heublein, Fink & Bohn, 2005), requiring the material to be impregnated before drying. Thus, this strategy would find limited use for materials like dry BNC sheets that currently are available as wound dressing material. In the past several articles have reported the use of chemically bonded metal oxide-cellulose hybrid materials for controlled drug delivery (Galkina et al., 2015a; Galkina et al., 2015b; Gaio et al., 2022; Breijaert et al., 2022). To the best our knowledge,

nanocomposites of dry BNC wound dressing with chemically grafted metal oxides onto the surface for enhanced uptake and controlled release of pharmaceuticals have not been reported. The aim of the current work was to produce a bacterial nanocellulose based material loaded with antibiotics for controlled release. Improved retention of antibiotic drug was achieved through surface grafting of inorganic functional components such as nano titania. Two types of very uniform TiO₂ nanoparticles about 3.5 nm developed in our previous studies – the triethanol ammonium terminated titania (TATT) (Seisenbaeva et al., 2017; Kessler, Seisenbaeva, Håkansson & Unell, 2008), easily desorbing the capping ligands and highly active in blood coagulation, and the particles generated by an equilibrium described for “Dihydroxybis (ammonium lactato)titanium(IV)” (TiBALDH®), which are strongly surface capped by lactate ligands and not producing blood coagulation effects (Seisenbaeva et al., 2017; Seisenbaeva, Daniel, Nedelec & Kessler, 2013). Insights were gained into how this material would behave in tissue regeneration applications testing biocompatibility, cell adhesion and pseudo wound closure effects.

2. Materials and methods

2.1. Materials

“Dihydroxybis(ammonium lactato)titanium(IV)” (TiBALDH®) 50wt % aqueous solutions (~2.08 M Ti) were obtained from Fischer Scientific. It contains highly crystalline anatase nanoparticles terminated by lactate ligand, 3.5 nm in diameter. Triethanol ammonium terminated titania (TATT) was obtained according to literature, i.e., titanium ethoxide was first modified with triethanolamine and then the product was hydrolysed by diluted nitric acid solution in water-ethanol medium (Kessler, Seisenbaeva, Håkansson & Unell, 2008). The product has been characterized by multitude of techniques as anatase nanoparticles with an amorphous shell, 3.5 nm in diameter. Ammonium hydrogenphosphate was obtained from Kebo Lab AB, Urea was obtained from Sigma-Aldrich. Dry Bacterial nanocellulose sheets were obtained from BioSmart Nanotechnology LTDA, Araraquara, Brazil. Phalloidin-iFluor 488 (ab176753) was obtained from Abcam Ltda. Rabbit Recombinant Monoclonal anti-Collagen I conjugated to Alexa Fluor® 594 and Rabbit Recombinant Monoclonal anti-Fibronectin conjugated to Alexa Fluor® 555 also were obtained from Abcam Ltda. All chemicals were used without further purification. Water was purified using a Millipore system.

2.2. Synthesis

2.2.1. Bacterial nanocellulose

Bacteria cultures were manipulated inside a laminar flow hood, using sterilized lab ware. Bacterial nanocellulose sheets were grown by culturing *Komagataibacter Rhaeticus* (AF-1) (Machado et al., 2016) bacteria onto Hestrin-Schramm agar, containing D-glucose, yeast extract, peptone, disodium hydrogen phosphate, citric acid, agar and deionized water. The resulting inoculated HS agar plates were incubated in an air circulating oven for 72 h at 28 °C. The *K. rhaeticus* colonies were transferred to liquid Hestrin-Schramm medium and incubated for a further 72 h at 28 °C. After this period, a BNC pellicle had formed at the air-liquid interface, indicating the culture medium showed the appropriate conditions to produce a large bacterial nanocellulose sheet. The liquid culture media was transferred to trays together with fresh HS liquid media and cultured for 96 h at 28 °C. The produced hydrated bacterial nanocellulose pellicles were washed with distilled water to get rid of excess growth media, placed in 0.1 % aqueous NaOH and heated to 70 °C to remove bacteria. The wet BNC membranes were compressed and dried.

2.2.2. Phosphorylated bacterial nanocellulose

The general procedure by Ait Benhamou et al. (Ait Benhamou et al.,

2021) was modified for use with large aspect ratio bacterial nanocellulose sheets. In order to phosphorylated bacterial nanocellulose sheets a solution of 450 mg (3.91 mmol) $\text{NH}_4\text{H}_2\text{PO}_4$, 1.2 g (19.98 mmol) urea, 10 ml ultrapure water was prepared. In a petridish was placed 10×10 cm of a dry bacterial nanocellulose sheet material and allowed to soak overnight at room temperature under continuous agitation. After soaking overnight, the sheet was transferred to a wide ceramic plate and placed in a 160°C oven for variable amounts of time (0–60 min). For the preparation of a phosphorylated bacterial sheet used for functionalization with drug and nano titania, the soaked bacterial nanocellulose sheet was placed at 160°C for 20 min.

2.2.2.1. TiO_2 functionalized phosphorylated bacterial nanocellulose. For functionalization of a bacterial nanocellulose sheet, an approximately 5×5 cm sheet of bacterial nanocellulose was suspended in 5 ml ultrapure water, followed by the addition of 10 mmol of TIBALDH 50wt% solution per gram of bacterial nanocellulose. The sheets were allowed to soak overnight under continuous agitation and thoroughly washed with ultrapure water prior to analysis. For the preparation of TATT-coated cellulose sheets the same molar ratio of TATT to phosphate was used, however the sheets were allowed to soak over several days.

2.3. Characterization

Samples were characterized using a Bruker Dimension FastScan Bio Atomic Force Microscope (AFM) with a Nanoscope V controller in ScanAsyst mode using a Fastscan-B AFM probe (Silicon tip, f_0 :400 kHz, k:4 N/m, Tip radius: 5 nm nominally) and a scan rate of 1–3 Hz. Data was processed using Gwyddion 2.56 with align rows-median to remove skipping lines.

Scanning Electron Microscopy (SEM) observations of bacterial nanocellulose were conducted using a Hitachi FlexSEM 1000 at an acceleration voltage of 3–7 kV, spot size 20, and 5 mm working distance. For Energy Dispersive X-ray Spectroscopy (EDS) an acceleration voltage of 15 kv, spot size 50 and 10 mm working distance were used.

The Thermogravimetric analyzes (TGA) were performed to determine the thermal degradation, mass loss, thermal stability, degradation temperature (Tonset) and maximum degradation temperature (Tmax) of membranes. TG curves were obtained in an equipment TGA-SDT Q600/TA Instruments. The samples were heated at 25 to 600°C at $10^\circ\text{C min}^{-1}$ under a nitrogen atmosphere. The experimental parameters' adjustments were made in OriginPro 9.0 software.

Solid-state ^{13}C NMR spectra were recorded on a Bruker Avance III HD 300 spectrometer (Germany) operating at a magnetic field strength of 7.04 T and a Larmor frequency of 75.00 MHz. The analyses were conducted using a 4 mm MAS probe with ZrO_2 rotors (and Kel-F covers) at a spinning rate of 9000 Hz. A relaxation time of 1 s and a 90° pulse of 2.6 μs were applied, utilizing magic-angle spinning and cross-polarization techniques. The chemical shifts were indirectly standardized through a sample of glycine, with carbonyl sign at 176.00 ppm in relation to the TMS which is the primary standard.

The degree of polymerization (DP) of bacterial nanocellulose (BNC) was determined by viscometry using an Ostwald viscometer according to Brazilian technical standard NBR7730.

For Cell Adhesion Assays a JEOL JSM-IT500HR SEM was used, using a working distance of 8 mm and an acceleration voltage of 5 kV (Paschoalin et al., 2017). Samples were prepared on carbon tape without any special treatment.

Fourier Transform Infrared (FTIR) analysis was done on a Perkin Elmer Spectrum 100 FT-IR Spectrometer using an ATR module or a window.

Titration was performed using a Metrohm Titrand 888 (2.888.0310), fitted with a 856 conductivity module (2.856.0010), 800 Dosino (2.800.0010), 5-ring conductivity measuring cell ($c = 0.7$, 6.0915.100), using TIAMO Light 2.5 as automation software. Titres were

determined using tris(hydroxymethyl)aminomethane (HCl) and potassium hydrogen phthalate (NaOH). Phosphate content was determined via conductometric titration by titration of protonated phosphate.

Immunofluorescence images were acquired using the Zeiss LSM800 Confocal Fluorescence Microscope.

Powder X-ray Diffraction (PXRD) data was obtained on a Bruker D8 QUEST ECO diffractometer equipped with a Proton III Area Detector and graphite-monochromated $\text{Mo-K}\alpha$ ($\lambda = 0.71073 \text{ \AA}$) radiation source. Data was processed with the EVA-12 software package. As a Mo -source ($K\alpha = 0.7093 \text{ \AA}$) is used instead of the standard Cu -source ($K\alpha = 1.5406 \text{ \AA}$) there is a loss in angular resolution as short wavelengths contract the diffraction pattern towards low Bragg angles. In order to compare cellulose samples, idealized cellulose structures (French, 2014) were used to simulate a powder diffraction patterns for cellulose Ia, Ib and cellulose II. Powder diffraction patterns were simulated between 5 and 50 2θ using Mercury software with Molybdenum as a source ($K\alpha = 0.7093 \text{ \AA}$) and FWHM: 1.5 as this closely resembles the angular resolution of the x-ray machine available and can be found in the supporting information (Sup. Fig. S10). Scherrer equation is exploiting full width of an intense X-ray peak at its half height to determine the size of a diffracting domain. Crystallite sizes were calculated using the Scherrer equation.

2.4. Tetracycline adsorption and desorption

In order to prepare a tetracycline loaded TiO_2 -Bacterial nanocellulose composite, a sheet containing TiO_2 was placed in a 100 mL Duran bottle together with a 70 mg/L tetracycline solution and sealed. The drug was allowed to adsorb at 55°C overnight, drug loading was calculated by measuring the concentration before and after adsorption. For desorption experiments the sheet was placed in a 100 mL Duran bottle, followed by the addition of 50 ml citrate buffer (0.02 M, pH 6) and continuously stirred for the entire duration. Periodically 1 mL aliquots were taken for UV–Vis measurement and returned. Desorption was measured over a period of 130 h / 5–6 days.

2.5. Indirect cytotoxicity assay

To assess the cytocompatibility of the functionalized BNC composites, cytotoxicity test was performed according to the International Organization for Standardization (ISO 10,993–5/10,993–12) norms, using the extract dilution method MTT assay. L929 murine fibroblasts cells and human osteoblast-like SaOS-2 cells were obtained from the American Type Culture Collection (ATCC, VA, USA). For detailed protocol see supplementary materials.

2.6. Evaluation of pseudo-wound closure

Fibroblast (L929) and osteoblasts (SaOS-2) cells were cultured at a density of 1×10^5 cells/well in a 24-well plate, respecting the same conditions of temperature and percentage of CO_2 . The extraction media (treatments) were prepared following the same procedure described in Section 2.5. Subsequently, the confluent monolayer was confirmed 24 hours later, and then the wells were washed twice with PBS and the scratching of the cell layer was performed using a 200 μL pipette tip. To achieve straight scratches a ruler was used as a guiding device, as elucidated in Supplementary materials Fig. S1.

The cell free gaps were imaged in an inverted optical microscope (Nikon®) with a 10x objective. To ensure that pictures were always taken at the same position, a black line on the lower outside of the wells was made using a pen. The micrographs were taken above the black line at 0, 6, 24 and 48 hours until full closure of pseudo-wounds. The size of the pseudo-wounds was measured at all time points using ImageJ2 (Rueden et al., 2017). All samples were performed in triplicate. The closure (%) of the pseudo-wounds was calculated according to Equation 1 (Moraes et al., 2023; Cappiello, Casciaro & Mangoni, 2018):

$$\% \text{ pseudo - wound closure} = \frac{\text{Area } t(0) - \text{Area } t(x)}{\text{Area } t(0)} \times 100$$

Where (x) corresponds to the time each micrograph was recorded.

2.7. Cell adhesion assay

For the cell adhesion studies, the same cell lines (SaOS-2 and L929) previously described were used. First, cells (5×10^4 cells/well) were seeded on functionalized BNC films (1 cm^3) inserted into the 24-well plate and grown for 72 h at 37°C with 5 % CO_2 . At the end of incubation, the media was removed, and cells were washed with sterile filtered 0.01 M PBS at pH 7.4. Next, the cells were fixed with 3 % glutaraldehyde in 0.01 M PBS for 0.5 h at room temperature. After washing with 0.01 M PBS, samples were dehydrated through an ascending ethanol series (30 %, 50 %, 70 % and 95 %, 3 min each) with a final incubation in 100 % ethanol for 3 min (repeated 2 times). Dry samples were sputter coating to generate a 10-nm carbon layer and observed via SEM.

2.8. Immunofluorescence cell culturing

Murine L929 fibroblasts and SAOS-2 osteoblasts were cultured in DMEM, Gibco® with 10 % FBS, Gibco® and 1 % ciprofloxacin (Sigma, St. Louis, MO, USA) at 37°C in a humidified condition with 5 % CO_2 and 95 % air. The cells were used after two consecutive passages.

2.9. Fluorescence staining

Cells were seeded onto the 24-well polystyrene cell culture plate, at a density of 5×10^3 cells/well in a humidified condition with 5 % CO_2 and 95 % air for 48 h. Simultaneously, the eluates from different samples were prepared using $1 \text{ cm}^2/\text{mL}$ and maintained in agitation for 24 h in DMEM with 5 % FBS and 1 % ciprofloxacin, respectively. Then, the conventional media was replaced with 500 $\mu\text{L}/\text{well}$ of each eluate from phosphorylated BC, phosphorylated BC + TATT, phosphorylated BC + TiBALDH and control (cells maintained only with conventional media) for 48 h at the same temperature and CO_2 described above. Afterward, the eluates were removed and the wells were washed with 0.01 M PBS (300 $\mu\text{L}/\text{well}$) and then cells were fixed with 3 % glutaraldehyde (300 $\mu\text{L}/\text{well}$) for 30 min at 4°C . The cells were washed again with 0.01 M PBS (three times) and treated with 0.1 % Triton X-100 (300 $\mu\text{L}/\text{well}$) for 5 min at room temperature. After incubation, the wells were washed again, and the cells were incubated with phalloidin-iFluor 488 (1 $\mu\text{g}/\text{mL}$) in 0.01 M PBS and 1 % of Bovine Serum Albumin (BSA) for 1 h at 37°C . Simultaneously the wells were incubated overnight with Rabbit Recombinant Monoclonal anti-Collagen I conjugated to Alexa Fluor® 594 (1:200) and Rabbit Recombinant Monoclonal anti-Fibronectin conjugated to Alexa Fluor® 555 (1:200) at 4°C using the same diluent solution (0.01 M PBS/1 % BSA). Finally, the wells were washed again (three times) and maintained in a solution of 0.01 M PBS and 1 % BSA. Immunofluorescence images were acquired using the Zeiss LSM800 Confocal Fluorescence Microscope. Objective lens: 40x/1.4 NA. Excitation wavelengths: 488 nm for phalloidin-iFluor 488, 594 nm for Alexa Fluor® 594 (Collagen I), and 555 nm for Alexa Fluor® 555 (Fibronectin). Emission wavelengths: 505–550 nm for phalloidin-iFluor 488, 610–650 nm for Alexa Fluor® 594, and 570–620 nm for Alexa Fluor® 555. Image resolution: 1024×1024 pixels with 8-bit depth to ensure high image quality.

2.10. Quantitative measurement of fluorescence intensity

Fibroblast and osteoblast cells were initially seeded in 96-well plates at a density of 5×10^3 cells. The cells were cultured in DMEM with 5 % FBS and 1 % ciprofloxacin and incubated at 37°C in a humidified atmosphere with 5 % CO_2 . After 24 h, the conventional medium was replaced with eluates from phosphorylated BC, phosphorylated BC +

TATT, and phosphorylated BC + TiBALDH. The culture medium was replaced with the corresponding eluates every two days for a total culture duration of 7 days. After 7 days, the eluates were carefully removed, and the cells were washed three times with 0.01 M PBS/1 % BSA) to remove any residual media or eluates. The cells were then fixed by incubating with 3 % glutaraldehyde for 30 min at 4°C . Following fixation, the cells were washed again and permeabilized using 0.1 % Triton X-100 in PBS/1 % BSA for 5 min. Subsequently, the cells were incubated with the fluorescence markers, phalloidin-iFluor 488 (1 $\mu\text{g}/\text{mL}$) for 1 h at 37°C , and Rabbit Recombinant Monoclonal anti-Collagen I conjugated to Alexa Fluor® 594 (1:200) and Rabbit Recombinant Monoclonal anti-Fibronectin conjugated to Alexa Fluor® 555 (1:200) overnight at 4°C , following the protocol described above. The fluorescence intensity was quantified using the FLUOstar Omega Microplate Reader. Each well was scanned for fluorescence at the specific excitation and emission wavelengths corresponding to the fluorophores used. This assay was performed in two independent experiments.

3. Results

3.1. Bacterial nanocellulose

The original BNC was proved to be a chemically and thermally robust material. For its morphological characterization of BNC by AFM and surface roughness, please see Fig. S2-S5. The degradation profile of the BNC membranes by TGA showed three mass-loss steps (see Fig. S16). The first thermal stage that constituted a mass loss of 10.8 % was associated with water release between 30 and 100°C . The second step was more pronounced and occurred in Tonset = 240°C with 12 % mass loss and $T_{\text{max}} = 328^\circ\text{C}$, could be attributed to cellulose degradation, including depolymerization and decomposition of glucose units. The third step represented the degradation of carbonaceous residues that extends from 400 to 600°C with a percentage of residual at 600°C determined was 8.6 %. These results are in good agreement with generally observed thermal behavior of nanocellulose (Gan, Sam, Abdullah & Omar, 2020).

The solid state ^{13}C NMR spectra showed in Fig. S17 reveal distinct signals corresponding to the carbon atoms within the carbohydrate segment of the cellulose structure. Specifically, the signal at δ 104.91 ppm is attributed to carbon C1, while the signal at δ 88.86 ppm corresponds to carbon C4. The region between δ 84–71 ppm (83.50, 74.31 and 71.38) encompasses signals from carbons C2, C3, and C5, and the signal at δ 65.08 ppm represents carbon C6 (for details, please, see Supplementary materials). The degree of polymerization (DP) of BNC determined through viscometry was found to be 2800 (Supplementary materials Table S4), corresponding to an average molecular weight of $453.600 \text{ g mol}^{-1}$.

3.2. Phosphorylation

We confirmed the surface of dried BNC was successfully phosphorylated using a combination of Energy Dispersive X-ray scattering (EDS), conductometric titration and attenuated total reflection fourier transform infrared spectroscopy (ATR-FTIR). In EDS an increase in At% P could be measured as the reaction progresses, to around 3.3 At% P after 40 min. Using ATR-FTIR we could observe the evolution of several peaks with time (Fig. 1, right, Fig. S12), most notably around 825 cm^{-1} , 930 cm^{-1} and 1230 cm^{-1} . Additional peaks that may be related to the introduction of phosphorus appeared around 500 cm^{-1} and very diffused around $2700\text{--}2750 \text{ cm}^{-1}$ (Thomas & Chittenden, 1964a; Thomas & Chittenden, 1964b). To quantify the phosphate content conductometric titrations were performed under the assumption that only the monophosphate-cellulose ester ($\text{Cell-O-PO}_3\text{H}_2$) had formed. Under this assumption the reaction order appears to be pseudo-first order with a rate of 0.057 min^{-1} with a final phosphorylated degree of 2.7 mmol/g (Fig. 1, left). Due to the brittle nature of the BNC membranes after

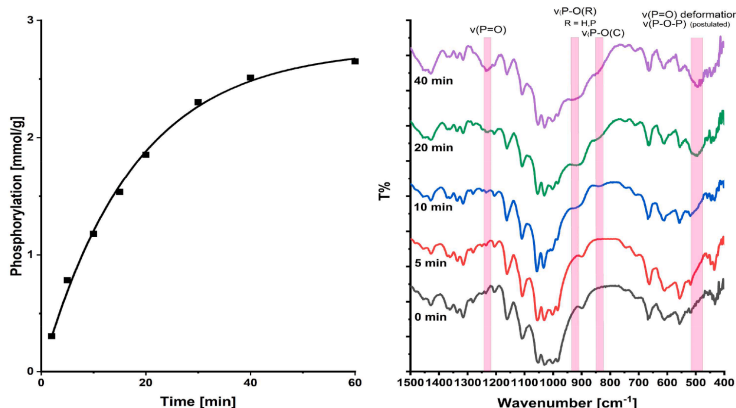


Fig. 1. Phosphorylation degree in mmol/g as a function of time for Dry Bacterial nanocellulose (■) (Left) ATR-FTIR spectra of the evolution of phosphorus related IR-peaks as a function of time. Pristine BNC (black), 5 min (red), 10 min (blue), 20 min (green) and 40 min (purple).

prolonged heating, subsequent samples were prepared using 20 min as a time point, yielding 1.5–1.8 mmol/g of phosphate.

3.3. Fiber morphology

3.3.1. Pristine dried bacterial nanocellulose

The provided dried BNC exhibits a surface morphology (Fig. 2A) consisting of long ($>1\mu\text{m}$), thin (64.9 ± 13.0 nm) twisted fibres of several micrometres in length with a large aspect ratio, which in many places are interwoven to form a fibrous mat. Allowing the sheet to swell in ultrapure water for seven days (Fig. S3 C,D) the fibres swell to 70.9 ± 12.4 nm, a 9 % increase. Treating the dried BNC with 0.1 M HCl over seven days changes the morphology, smaller crystallites appear on the surface with the overall fibre outline being maintained (Fig. S3 A,B). The fibre outline itself reduces in size to an approximate 50.9 ± 13.9 nm, with the smaller crystallites present on the surface having an approximate width of 22.3 ± 5.3 nm. When treated with 0.1 M NaOH, much of the original fibre structure is retained, with a decrease in fibre size to 60

± 12.4 nm (Fig. S3 E,F).

3.2.2. Phosphorylation of dried bacterial nanocellulose

After phosphorylation of dried BNC the surface becomes more porous on the microscale compared to pristine bacterial nanocellulose (Fig. 2B). Treatment with urea had a limited effect on surface morphology (Fig. S9). After phosphorylation the fibres retain much of their original shape and size, consisting of fibres twisted together with a minor increase in fibre diameter to 65.7 ± 12.8 nm. When stored for seven days in ultrapure water (Fig. S7, C,D), the distance between fibres increases, opening up the surface of the material. A closer examination show that the fibre morphology itself has changed, appearing notably more ribbon-like than freshly prepared phosphorylated BNC, with an average width of 68.9 ± 14.2 nm on the thinner edge of the fibres (Fig. S4, A,B). Storing the phosphorylated sheets under very acidic conditions in 0.1 M HCl resulted in the distance between fibres increasing compared to ultrapure water (Fig. S6, A,B). Opening up the

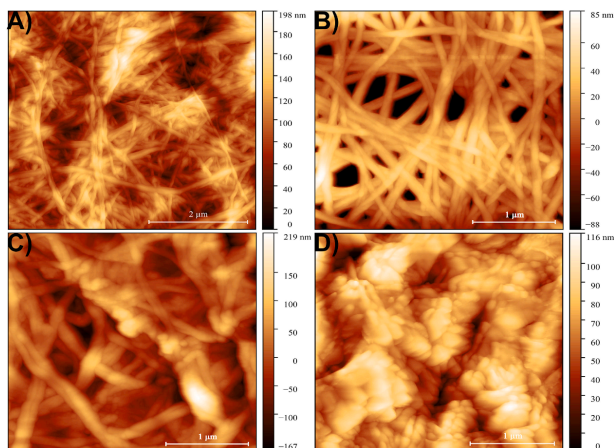


Fig. 2. AFM images of Bacterial nanocellulose Sheet as is (A $5 \times 5 \mu\text{m}$), phosphorylated BNC (B, $3 \times 3 \mu\text{m}$), phosphorylated BNC coated with pre-formed colloidal TAIT (C, $3 \times 3 \mu\text{m}$), phosphorylated BNC- modified by TiO_2 derived from TIBALDH® (D $3 \times 3 \mu\text{m}$).

structure to such an extent as to be reminded of supercritically dried BNC (Fig. S8). The phosphorous content decreased from 2.2 At% P in ultrapure water to 1.0 At% when stored under very acidic conditions. The HCl treated phosphorylated sample (Fig. S4, A,B) exhibits a ribbon-like structure with the fibre width decreasing to 63.5 ± 17.8 nm. Storing under basic conditions in 0.1 M NaOH, resulted in the formation of large several micrometer gaps between well resolved fibres while more commonly fibre clusts appear so dense as to be poorly resolved (Fig. S7, E,F). Making it difficult to differentiate between individual fibres by SEM. Using AFM the general outline of the original fibres can be seen, with the actual fibre surface containing many globular structures with an approximate dimension of 44.8 ± 9.1 nm (Fig. S4, E,F). Similar to the samples stored under acidic condition, basic conditions also lead to a decrease in phosphorous content. According to EDS the phosphorous content decreased to 1.3 At%.

3.4. Introduction of nano-TiO₂

Treating phosphorylated bacterial nanocellulose with stoichiometric excess of TiBALDH at room temperature results in a loss of the previously observed open surface structure of phosphorylated BNC, in favour of the formation of titania crystallites across the surface. The TiBALDH derived product contains relatively large, aggregated and angular structures of titania across the surface (Fig. 2D, Fig. S5, E,F). The surface titania structures formed by TiBALDH are ca. 5–10 nm in height in the smaller range and up to 25 nm in the larger range. Length wise the particles are variable with some as small as 30 nm, while others are up to 160 nm depending on surface orientation, averaging around 75.4 ± 40.7 nm. EDS data (Fig. S7) confirms the successful introduction of Titania with 1.1 At% Ti and a P:Ti ratio of 1: 0.45. Treating the phosphorylated bacterial nanocellulose with stoichiometric excess of colloidal TATT lead to uniform coverage of BCN fibres, increasing the fibre thickness from 65.7 ± 12.8 nm in phosphorylated BNC to 71.6 ± 6.6 nm in TATT-covered phosphorylated BNC (Fig. 2C, Fig. S4, G, H). This is to be expected, as the colloid consists of pre-formed hydrated TiO₂ particles, which in principle coordinate to the surface via the introduced phosphate group but may also aggregate or gelate. EDS data (Fig. S8) confirms the successful introduction of Titanium with 1.1 At% Ti and a P:Ti ratio of 1:0.8. Both phosphorylation and introduction of oxide nanoparticles are well reproducible under identified conditions facilitating potential up-scaling and therapeutic use of the material.

3.5. X-ray diffraction

The provided source of cellulose starting material (Fig. S11) was crystalline, presumably largely consisting of cellulose Ia (Wada, Okano & Sugiyama, 2001) based on peak shape between 6.5–8 2 θ . The calculated crystallinity was 49.6 % based on peak height and crystallite size of 6.3 nm based on the Scherrer equation. Hydrating pristine dry bacterial nanocellulose in ultrapure water increased the Scherrer crystallite size to 12.6 nm and decreased measured crystallinity to 34.3 %. Hydration of BNC in 0.1 M NaOH resulted in a loss of crystallinity to 26.9 % and an increase in diffraction intensity around 5–6 2 θ . Which corresponds to the calculated 1–10 miller index in cellulose II. Hydrating pristine BNC in 0.1 M HCl increased the crystallinity to 34.8 %. The diffraction pattern of as-synthesized phosphorylated BNC (Fig. S11) is similar to pristine BNC, with a higher calculated crystallinity of 58.9 % and a Scherrer crystallite size of 12 nm. In ultrapure water phosphorylated BNC behaves similarly to pristine BNC, losing some crystallinity (to 33.5 %) and increasing the Scherrer crystallite size to 17 nm. Maintained degree of crystallinity is in favor of unchanged mechanical properties such as brittleness, crucial for up-scaling and further practical use of the material. When placed in either 0.1 NaOH or HCl, there is a large change in peak ratio between 6.5–8 and 10.4 2 θ . Due to the overlap between the most intense diffraction peaks of cellulose and anatase titania samples were sintered to confirm the presence of TiO₂

(Fig. S12). After sintering at 600 °C only 7.5 wt% white residue remains of the TiBALDH modified material and 14.5 wt% white residue remains for the TATT modified material. Sintering the material at 500 °C indicates the presence of anatase titania (Fig. S12) together with some residue (turning the material brown). The remaining residue had Scherrer crystallite sizes of 19.8 nm for TiBALDH and 32.2 nm for TATT.

3.6. Tetracycline desorption

The nanocomposite derived from TiBALDH displayed adsorption of 41.4 ± 4.8 mg of tetracycline per g of cellulose dressing. The appearance of two additional shoulder peaks at 1600 cm⁻¹ and 1580 cm⁻¹ in transmission FTIR (Fig. S13) can be attributed to the inclusion of chemically bound tetracycline (Myers, Tochon-Danguy & Baud, 1983). The nanocomposite material released 30.8 ± 2.9 % tetracycline after 5 h, reaching 53.3 ± 2.9 % tetracycline release after 120 h. The TATT derived composite had 46.5 ± 2.2 mg g⁻¹ tetracycline absorbed per g of cellulose dressing. The TATT nanocomposite released 39.4 ± 0.2 % tetracycline after 5 h in desorption medium, reaching up to 61.4 ± 1.7 % after 120 h (Fig. 3).

3.7. Cell assays

As the surface modification of the BCN is intended for use in wound dressing materials, it is of paramount importance to test the cytotoxicity. In addition, pseudo-wound healing and cell adhesion assays provide additional insight into the suitability of the material and subsequent modifications for wound healing. The samples in Table 1 were evaluated.

3.7.1. Cytotoxicity assay

Given the worldwide concerns regarding nanotoxicity in biomaterials, the potential cytotoxic effects of TiO₂ nanoparticles covered BNC was investigated. Most functionalized BNC films showed cytotoxicity for both cell lines, maintaining cell viability above 85 % (Fig. 4, Table 1). Both high (1) and low (2) phosphate content BNC samples showed no decrease in cell viability for L929 Murine Fibroblasts. High phosphate content BNC did slightly decrease in cell viability for SaOS-2 osteoblastic cells. After covering phosphorylated BNC with TiO₂, both “bare” (11) and lactate covered (10) TiO₂ maintained cell viability close to 100 % for both fibroblasts and osteoblastic cells. Covering the TiO₂ with antibiotic tetracycline induced a decrease in cell viability for TATT covered (31) BNC, but not TiBALDH (30). After desorption of tetracycline in citrate buffer, cell viability for TiBALDH covered (33) BNC decreased slightly. Cell viability for TATT covered BNC (32) remained the same after desorption. In contrast to the previous samples, BNC/TiBALDH/AgNO₃ (34) showed cytotoxicity effect with a significant decrease in fibroblast (below 65 %), while the viability of osteoblastic cells reduced drastically, reaching 100 % cell death against samples 34 and 35 (cotton nanocrystals/TiBALDH/AgNO₃).

3.7.2. Evaluation of pseudo-wound closure

Previous studies have demonstrated that BC exhibits remarkable wound healing properties due to its unique physicochemical and biological characteristics. The 3D-dimensional network structure of BC effectively allows normal gas and liquids exchange, which is essential for proper wound treatment. BC also serves as an ideal carrier for the slow release of drugs, further enhancing wound healing and promoting skin tissue regeneration. Its high water absorption and retention capabilities enable efficient management of wound exudates, while its mechanical strength provides skin protection. Additionally, makes it suitable for dressing irregularly shaped wounds, as well as allows easy wound inspection due to its translucency property (Wahid et al., 2021). Khalid et al. (Khalid et al., 2017) reported that BNC/TiO₂ biocomposites notably accelerated wound closure by *in vivo* model, with wound area reduction observed from 289 mm² on day 0 to 86 mm² on day 15 in the treated

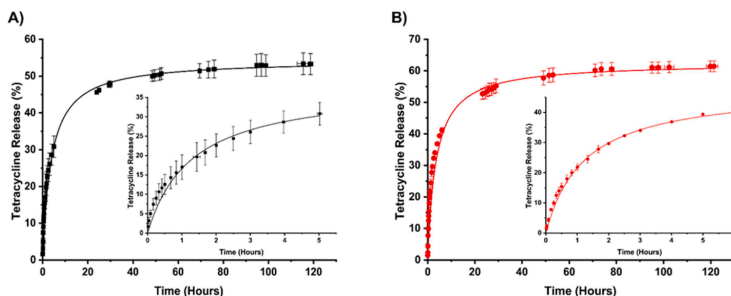


Fig. 3. Desorption of the broad-spectrum antibiotic Tetracycline from phosphorylated bacterial nanocellulose sheets covered by TiO₂ derived from TiBALDH (left, black) and colloidal triethanolamine terminated TiO₂ (right, red). Fitted with non-linear 2nd order fitting in origin.

Table 1

Samples tested for cytotoxicity, pseudo-wound healing and cell adhesion assays.

Sample number	Nomenclature
1	BNC-PO ₄ ~2.7–4 wt%
2	BNC-PO ₄ ~0.5–1.5 wt%
10	BNC-PO ₄ - TiBALDH
11	BNC-PO ₄ - TATT
30	BNC-PO ₄ - TiBALDH + tetracycline
31	BNC-PO ₄ - TATT + tetracycline
32	dry BNC-PO ₄ - TATT + tetracycline after desorption in citrate buffer
33	dry BNC-PO ₄ - TiBALDH + tetracycline after desorption in citrate buffer
34	BNC wet membrane + 10 mol % 2:1 TiBALDH: AgNO ₃
35	Cotton cellulose nanocrystals + 10 mol% 2:1 TiBALDH:AgNO ₃

group. In comparison, wounds treated with pure BC or a negative control showed significantly slower closure rates. These findings suggest that the incorporation of TiO₂ nanoparticles in BC significantly enhances its healing potential, likely by supporting fibroblast function and tissue remodeling in the wound area. Similarly, phosphate-crosslinked BC-based hydrogels also play a vital role in osteogenic as shown by Suneetha and collaborators (Suneetha, Kim & Han, 2024).

In this work (Fig. 5) the samples 2, 10, 11 and 30 had a positive effect on L929 cell migration, enabling 100 % pseudo-wound closure within 24 h as well as the positive control (only culture media) Samples 31, 33 and 34 demonstrated a negative effect on cell migration for L929 cells. For SaOS-2 cells, samples 10 and 33 promoted pseudo-wound closure within 24 h as well as the positive control. Sample 34 had a negative effect, preventing pseudo-wound closure within the analysis

timeframe. The micrographs showing the closure of the pseudo-wounds over 48 h can be observed in Fig. S2.

3.7.3. Cell adhesion assay

Data indicate that all tested samples of BNC-PO₄ (samples 1,2) and BNC-PO₄-TiO₂ composites (samples 10, 11) analyzed supported the attachment, cell adhesion, and proliferation of both cell lines (Figs. 6 and 7). Moreover, high cell spreading and a fully developed cytoskeleton were visible. Similar results were reported by Khan et al. (Khan et al., 2015), who demonstrated that regenerated BC (RBC)-TiO₂ nanocomposites exhibited excellent cell adhesion and proliferation capabilities with animal fibroblast cells, without showing any toxic effects.

3.7.4. Fluorescence staining

During cell migration, the cell initially extends protrusions, such as lamellipodia and filopodia, establishes adhesion points, and ultimately retracts its tail. The actin cytoskeleton plays a central role in this process (Le Clainche & Carlier, 2008; Gardel, Schneider, Aratyn-Schaus & Waterman, 2010). Moreover, type-I collagen and fibronectin are two critical extracellular matrix (ECM) components that significantly contribute to healing and tissue regeneration (Kanta, 2015). Type-I collagen, the most abundant ECM component provides a scaffold that binds other proteins and proteoglycans, facilitating cell interaction. Additionally, fibronectin plays a pivotal role in controlling cell adhesion, spreading, migration, proliferation, and differentiation, further highlighting its importance in tissue repair and regeneration (Parisi et al., 2020).

In the present study, confocal immunofluorescence analysis was used to visualize the F-actin, type I collagen and fibronectin biomarkers in fibroblast and osteoblast cells of different treatment group. Our findings indicated that biomarkers expression was observed in both cell lines

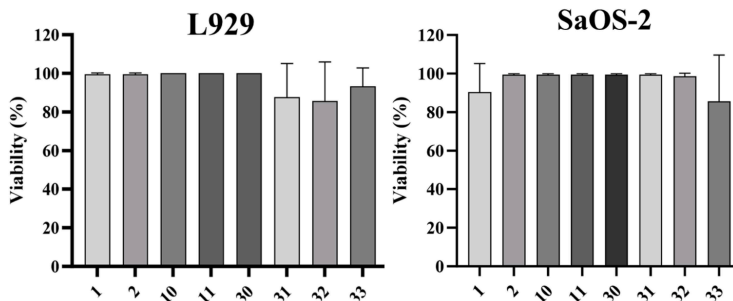


Fig. 4. Viability of L929 and SaOS-2 cells upon contact with eluates from the functionalized BNC samples.

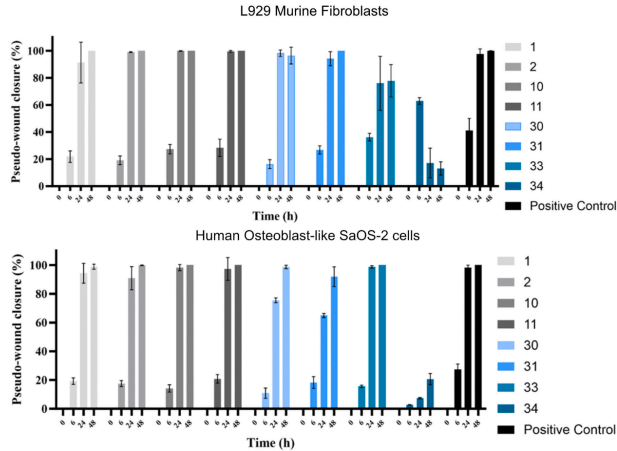


Fig. 5. Effect of different functionalized BNC composites on migration of L929 and SaOS-2 cell lines by evaluation the pseudo-wound closure at times of 0, 6, 24 and 48 h.

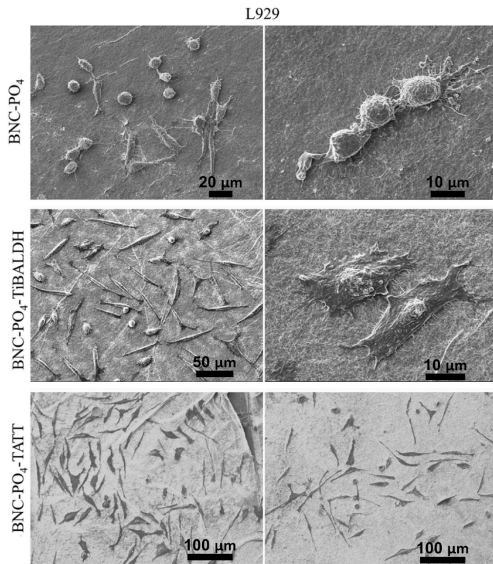


Fig. 6. L929 cells adhered on different functionalized BNC composites after 72 h of incubation.

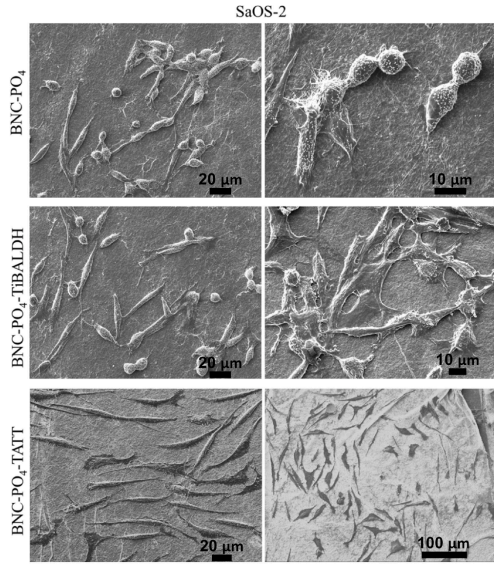


Fig. 7. SaOS-2 cells adhered on different functionalized BNC composites after 72 h of incubation.

following exposure to BNC-PO₄ composites for 7 days as shown in Figs. 8-10.

3.7.5. Quantitative measurement of fluorescence intensity

Our results involving fluorescence intensity quantification showed a significant increase in F-actin expression in L929 fibroblasts and SaOS-2 osteoblasts treated with the BNC-PO₄ group compared to BNC-PO₄-TATT, BNC-PO₄-TiBALDH and control (Fig. S15). The expression of fibronectin was significantly higher than type-I collagen, although no

significant difference in their expression were observed between the different experimental groups. It is important to mention that both cell lines treated with eluates from BNC-PO₄ composites were exposed to a culture medium containing only 5 % FBS, while the control cells received 10 % FBS. This suggests that TiO₂ nanoparticles (TiBALDH and TATT) positively influenced the expression of biomarkers investigated. Nevertheless, further molecular quantification assays and *in vivo* model studies would be beneficial to confirm the relevance of these inorganic particles in enhancing the expression of protein and cytoskeletal markers and their contribution to tissue regeneration.

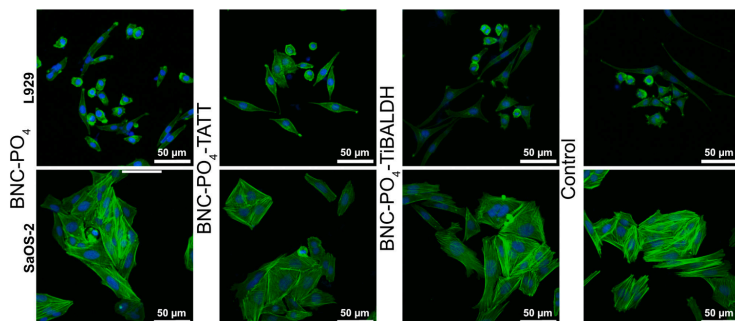


Fig. 8. Confocal imaging of murine L929 fibroblasts and SaOS-2 osteoblasts: F-actin (green) was labeled with phalloidin-iFluor 488 (green), and the nuclei (blue) counterstaining with DAPI. Fluorescence staining of the actin cytoskeleton was registered on fibroblasts and osteoblasts cultured for 7 days with different eluates from BNC-PO₄, BNC-PO₄-TATT and BNC-PO₄-TIBALDH. Control cells was maintained with only conventional media.

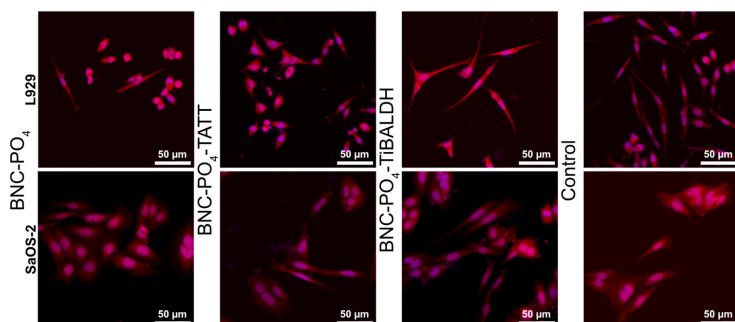


Fig. 9. Confocal imaging of murine L929 fibroblasts and SaOS-2 osteoblasts: Type I-Collagen (red) was labeled with Rabbit Recombinant Monoclonal anti-Collagen I conjugated to Alexa Fluor® 594 and nuclei counterstaining with DAPI (blue). Fluorescence staining of collagen Type I was registered on fibroblasts and osteoblasts cultured for 7 days with different eluates from BNC-PO₄, BNC-PO₄-TATT and BNC-PO₄-TIBALDH. Control cells was maintained with only conventional media.

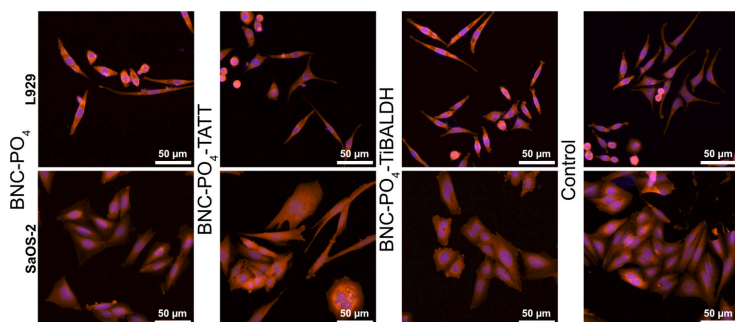


Fig. 10. Confocal imaging of murine L929 fibroblasts and SaOS-2 osteoblasts: fibronectin (red) was labeled with Rabbit Recombinant Monoclonal anti-Fibronectin conjugated to Alexa Fluor® 555 and nuclei counterstaining, with DAPI (blue). Fluorescence staining of fibronectin was registered on fibroblasts and osteoblasts cultured for 7 days with different eluates from BNC-PO₄, BNC-PO₄-TATT and BNC-PO₄-TIBALDH. Control cells was maintained with only conventional media.

4. Discussion

4.1. Phosphorylation

Phosphorylation of cellulose is an ester-forming reaction, which the surface cellulose molecules easily undergo in acidic medium (Inagaki, Nakamura, Asai & Katsuura, 1976). It forms a C–O–P bond on the surface polymer molecule, leaving 3 oxygen atoms bound to phosphorus for potential surface complexation to metal oxide nanoparticles. Titania nanoparticles should be strongly bound to such modified matrix, otherwise titania is washable due to the poor affinity between titania and cellulose, leading to the release of nanoparticles in the wound environment. As titania has excellent affinity for phosphate, forming a hydrolytically stable M–O–P bond, we decided to introduce phosphate onto the surface. As described in Section 3.1, phosphorylation was confirmed a variety of techniques, however the aforementioned EDS (on carbon tape) and FTIR analysis were difficult to quantify reliably and so the BNC surface phosphorylation degree was determined conductometrically by measuring the equivalent base consumption of the material after converting to the acid form. A large increase in hydroxide consumption was observed with increase in reaction time, corroborating EDS and FTIR results regarding successful phosphorylation. The reaction itself proceeded smoothly, though the amount of phosphate present has been noted to vary between experiments depending on the remaining surface-adsorbed liquid and shape of crucible used, with wider crucibles being favoured. Presumably because the increase surface area promotes evaporation of water, allowing adequate reaction temperatures to be reached more readily. It should be noted that the bacterial nanocellulose films became increasingly brittle with increase of reaction duration. Due to the increased brittleness, an intermediate time point of 20 min was chosen for subsequent samples as a compromise between material flexibility and phosphorylation degree.

4.2. Fiber morphology

4.2.1. Pristine dried bacterial nanocellulose

Bacterial nanocellulose (BNC) differs considerably from other types on nanocellulose. It is set apart from other cellulose sources such as vegetal cellulose by the long, interwoven microfibrils, which can be produced without the need for extensive mechanical or chemical treatment in order to obtain high-purity cellulose. It is naturally produced as a biofilm by bacteria with minimal side products, and as such, it retains most of the original morphology after purification. When freshly produced it exists as a hydrogel which can be treated further or like the commercial wound dressing used here, it can be compressed and dried as a film. Presented in its dried state, this particular cellulose source appeared to consist of long twisted fibres of several micrometres in length, forming a fibrous mat of cellulose. The constituent BNC fibres swell up after several days in water. Storage under very acidic conditions made small crystallites appear on the surface together with a reduction in fibre thickness. This is expected as cellulose, in particular the amorphous regions of cellulose present on the surface, is known to hydrolyse in acidic environment. The fibres maintained much of their original structure when treated with lye, though a small decrease in fibre width was noted. This may be due to partial base hydrolysis of cellulose, minor surface regeneration or due to selection bias as only fibres with clearly demarcated borders are chosen. It is noted that some regions on base-treated dried bacterial nanocellulose appear more globular compared to the original bacterial nanocellulose, supporting the notion that the cellulose surface packing has changed to some extent.

4.2.2. Phosphorylation of dried bacterial nanocellulose

Surface charge, charge repulsion / hydrogen bonding between fibres plays an important role in the overarching morphology of materials and it was observed that the morphological changes may be attributed to the introduction of the phosphate group. As seen in Section 3.2.2, the

observed surface structure of phosphorylated BNC strongly depended on pH storage conditions. Hydrating the materials for a prolonged period of time in ultrapure water changed the appearance of the fibres to become noticeably more ribbon-like. These ribbon-like fibres appeared at least partly folded, which made it difficult to measure an accurate width. When comparing the HCl treated phosphorylated BNC and HCl treated pristine BNC there is a noticeable difference in surface structure. In pristine BNC there are clearly observable small nanocrystalline domains distributed across the fibre surface, which are not present on phosphorylated BNC. Storage under basic conditions led to the formation of globular structures on the surface of the previously observed smooth ribbons. This could be due to cellulose regeneration, the negative surface charge of the phosphate group under strongly high alkaline conditions or another mechanism. The observed decrease in phosphorus content upon treatment with acid or base indicate that the cellulose-O-phosphate bond is liable to (partial) hydrolysis, being more sensitive to acidic conditions. The morphological changes of the material upon phosphorylation and pH treatment are notable; comparing the pristine BNC sheets with phosphorylated BNC, the surface becomes more porous upon phosphorylation and strongly influenced by pH with different morphologies present depending on storage conditions (Patoary, Farooq, Zaarour & Liu, 2021). Dried phosphorylated cellulose is a brittle material, which may pose difficulties in up-scaling of the phosphorylation process. However, if then the ready composite is kept in humid conditions this challenge can be avoided in therapeutic applications.

4.3. Introduction of nano-TiO₂

Nanosized titanium dioxide is an easily produced and up-scaled material. It is generally considered to be biocompatible and antibacterial. Depending on the surface chemistry of the TiO₂ nanoparticles involved, it may induce blood coagulation however, which may be undesirable for some applications (Svensson et al., 2021). To test the viability of the material, two versions of BNC-PO₄ – Titania composites were prepared using TiBALDH and TATT respectively. TiBALDH is a water-soluble precursor to nano-sized titania. It exists in solution equilibrium with ammonium tris-lactato-titanate (NH₄)₂[Ti(Lactate)₃] and uniform, crystalline, anatase titania which is stabilized by surface-capping with lactate (Groenke et al., 2012). This equilibrium can be shifted by change in solvent polarity, addition of salts or as used here, a strongly competing ligand, which shifts the equilibrium towards lactate-capped nano-Titania. TATT by comparison is a colloidal suspension of anatase titania, with an amorphous hydrated surface and crystalline anatase core. TATT is made via the controlled hydrolysis of a titanium alkoxide precursor in the presence of a surface capping agent (Kessler, Seisenbaeva, Håkansson & Unell, 2008). The introduction of a chelating ligand to the metal alkoxide sol leads to the formation of self-assembled micellar aggregates during hydrolysis/polycondensation. These micelles templated by self-assembly of ligands (MTSALS) are covered by residual ligands (Kessler et al., 2006), which in the case of TATT has been charged under acidic conditions to provide a charge stabilized colloid with particles in the range of 3–4 nm (Kessler, Seisenbaeva, Håkansson & Unell, 2008). In aqueous media the capping agent is hydrolysed to form a basic suspension of negatively charged colloidal, bare TiO₂ which binds to the surface via coordination with the introduced phosphate group. With TATT, there is a noticeable difference in surface morphology compared to TiBALDH. This can readily be observed as the original fibre morphology appeared to be largely preserved. The increase in observed fibre thickness corresponds to the size of two particles, indicating full coverage of the phosphorylated BNC fibres by TATT. The difference in P:Ti ratio observed here is most likely due to the alkaline hydrolysis of phosphate which was previously observed with phosphorylated BNC.

4.4. X-ray diffraction

It should be clearly noted the instrument used a Mo-source ($K\alpha = 0.7093 \text{ \AA}$) instead of a Cu-source ($K\alpha = 1.5406 \text{ \AA}$). Leading to a loss in angular resolution due to contraction of the diffraction pattern towards lower Bragg angles. Due to the lower angular resolution, idealized powder pattern only have a 69.5Cl% based on peak height. Thus, Cl% in Section 3.4 would be underreported. The observed decrease in crystallinity and increase in Scherrer crystallite size for pristine BNC was presumably due to the swelling and hydration of the cellulose fibres. In ultrapure water BNC-PO₄ behaves similar to the pristine material, with a loss in crystallinity and increase in Scherrer crystallite size. Placing the material in either acidic or basic environment causes a change in peak ratio between the diffraction at 6.5–8 and 10.4 2 θ , indicating that the packing of the material has changed. This implies that the pH not only affects the overall morphology of BNC-PO₄ as mentioned in 4.2.2 but the crystal packing of the cellulose fibres itself is also influenced by pH after phosphorylation.

4.5. Tetracycline desorption

Environmental effects of presently used paradigm of systemic antibiotic drug treatment are associated with release of residual medicines not consumed by the body into the wastewater. This leads to dangerous increase in antibiotic pollution in ground waters and water bodies, resulting in emerging multi-resistant pathogens (Larsson & Flach, 2022). An alternative to the systemic treatment is the topical one is permitting to safely dispose the residual pharmaceutical bound to an applied carrier material. The release of many pharmaceuticals from nanocrystalline cellulose and derived composites is, however, quite rapid. Thus, to delay drug release, cellulose has been modified as described in Section 4.1–4.2.3 and nano-sized titania (TiBALDH / TATT) introduced onto the surface. The surface chemistry between titania sources is notably different, TiBALDH-derived titania is presumed to have a surface capping of lactate, which coordinates quite strongly to titania via chelation with both lactate hydroxide and carboxylate groups (Groenke et al., 2012). Thus, any pharmaceutical that is to be chemisorbed onto the surface will be competing against surface bound lactate. TATT by comparison contains a surface capping which in theory hydrolyses in water to provide a bare titania surface. Thus, pharmaceuticals should be able to be chemisorbed onto the surface without any direct competition with other ligands. For drug ad-/desorption studies the drug tetracycline was chosen as it is a broad-spectrum antibiotic with oral and topical applications. In addition, it is a drug, which can be readily measured by UV–VIS due to its characteristic absorption in the range of 300–400 nm. For both sources of titania, when measuring tetracycline desorption, the nanocomposite materials appeared to release tetracycline quite slowly, which is beneficial for sustained drug release. The TATT derived composite had a slightly greater amount of tetracycline adsorbed. This is presumably due to the greater TiO₂ content in the TATT derived composite (7.5 wt% vs 14.5 wt%). The kinetics behind tetracycline desorption from both composites appeared to follow 2nd order kinetics. Indicating that the release of tetracycline is most likely dependent on the concentration of two reactants. Assuming TiO₂ in the solid state doesn't play a significant role one can assume the desorption in part relies on the concentration of desorption media itself, which in this case citrate buffer. The other component would naturally be the concentration of tetracycline in solution.

4.6. Cell assays

4.6.1. Cytotoxicity assay

A preliminary cytotoxicity assay is one of the most important evaluations of the biological properties of the biomaterials prior to *in vivo* assessment. According to the ISO 10,993–5, if the cell viability is greater than 70 %, then the material is considered as non-cytotoxic. Cell

viability of L929 and SaOS-2 was assessed in section 3.6.3 by MTT assay. It was found that of the examined pristine, phosphorylated and TiO₂ covered materials, none of the functionalized BC films showed cytotoxicity for both cell lines.

However, while the cytotoxicity assay indicated no significant toxicity for the materials *in vitro* (See Table S5) it is important to highlight the potential risks TiO₂ nanoparticles, particularly regarding their cytotoxicity and effects *in vivo* (Ayorinde & Sayes, 2023; Skocaj, Filipic, Petkovic & Novak, 2011; Zhangjian Chen et al., 2020). While some studies highlight their antimicrobial and anti-inflammatory properties in scaffolds and wound dressings, their potential to induce oxidative stress cannot be overlooked, as this biological effect can lead to DNA damage and mitochondrial dysfunction. Toxicological studies on nano-TiO₂, encompassing acute, subacute, subchronic, and chronic oral exposure, provide critical insights into their safety profile. Although acute toxicity studies generally indicate low toxicity, prolonged exposure can elicit significant biological effects, influenced not only by nanoparticle size but also by surface charge and aggregation state. Subacute and subchronic studies have reported potential bio-accumulation, oxidative stress, and inflammatory responses, particularly in the liver, kidneys, and gastrointestinal tract. Chronic exposure raises concerns regarding long-term systemic effects, including metabolic disturbances and potential carcinogenicity (Zhangjian Chen et al., 2020).

Nevertheless, several studies, including the present one, have focused on functionalization and doping strategies to mitigate these adverse effects while maintaining well-established biological properties. A deeper understanding of the mechanisms underlying nano-TiO₂ cytotoxicity, incorporating advanced molecular and omics-based approaches, is crucial for defining safe exposure limits in medical and industrial applications (Zhangjian Chen et al., 2020).

4.6.2. Evaluation of pseudo-wound closure and cell adhesion assay

Cell migration is a rate-limiting event during the wound-healing process to re-establish the integrity and normal function of tissue layers after injury. The principle of the method used is based on the creation of a 500 μm gap (pseudo-wound) on a confluent cell monolayer. The cells at the edge of the artificial "wounded" field will start migrating into the cell-free area, forming new cell-cell contacts. For both cell lines (murine fibroblasts and osteoblasts), high phosphate content on BNC (3.6, sample 1) didn't promote migration, however decreasing the phosphate content (3.6, sample 2) had a positive effect on murine fibroblasts. Covering BNC-PO₄ with either TiBALDH (3.6, sample 10) or TATT (3.6, sample 11) had a positive effect on L929 cell migration, enabling full pseudo-wound closure within 24 h, indicating that the material is quite beneficial for wound healing. In contrast, BNC-TATT with tetracycline (3.6, sample 31) appeared to negatively influence wound healing, presumably due to the decrease in fibroblast cell viability observed in section 3.6.1. For osteoblastic SaOS-2 cells, only the TiBALDH-covered BNC (sample 10) provided a positive effect on cell migration, while the other materials, including those containing TATT (sample 11) or BNC-TiBALDH with tetracycline (3.6, sample 31), lost their positive wound-healing effect on osteoblastic cells. Curiously, after tetracycline desorption in citrate buffer, BNC-TiBALDH (3.6, sample 33) displayed a negative effect on wound healing for fibroblasts but a positive effect on osteoblastic cells. Full statistical analysis is provided in Supplementary materials Tables S6–S9.

Adhesion is the first response of the cell when it comes into contact with a biomaterial, and plays an essential role in regulation of the subsequent biological behavior of cells. In the course of the cell adhesion process, cells initially "sediment" to the surface with their spherical bodies. Then, cells "flatten" mostly by nonspecific interactions. If the surface is suitable, cells "fully spread" with focal adhesion maturation and create stable contacts via actin skeleton reorganization to reach their maximum spreading area. Data in section 3.6.3 indicated that all samples analyzed (Section 3.6, samples 1, 2, 10, 11) supported the

attachment, cell adhesion, and proliferation for both cell lines. Moreover, high cell spreading and a fully developed cytoskeleton were visible. On the whole, the positive biological outcomes observed for phosphorylated and TiO₂ functionalized-samples indicate promising prospects for diverse applications in tissue engineering.

Similar to established BNC-based dressings such as Membracel®, Nexfill®, Bionext®, and Suprasorb® X + PHMB, which facilitate wound closure by promoting cell migration, tissue regeneration, as well as antimicrobial activity due to the presence of polyhexanide in its composition (Rasouli, Soleimani, Hosseinzadeh & Ranjbari, 2023; Choi et al., 2022; Zahel et al., 2022), the phosphorylated and TiO₂ functionalized BNC also exhibited remarkable potential in promoting murine fibroblast migration, as well as enhancing the spreading, adhesion, and proliferation of both osteoblastic and fibroblastic cells, as indicated by its performance *in vitro* studies. Although further experiments are necessary to confirm these findings *in vivo* models, such as the rat calvaria and skin excision wound models, its inherent antimicrobial, antioxidant, and anti-inflammatory properties, attributed to the incorporation of TiO₂ nanoparticles, emphasize its potential for advanced wound dressings that meet the evolving demands of modern wound care technologies.

4.6.3. Fluorescence staining and quantitative measurement of fluorescence intensity

Functionalized biomaterials incorporating inorganic compounds, such as phosphate groups and titanium oxide nanoparticles, have shown promising effects on the expression of extracellular matrix (ECM) and cytoskeletal biomarkers. These strategies may enhance cellular adhesion, migration, proliferation, and differentiation due to the unique properties of the inorganic particles. Given their range of sizes and high surface area, TiO₂ nanoparticles have been shown to modify the topography and roughness of biomaterials (Calabrese et al., 2021; Kubo et al., 2009). Furthermore, BNC has gained attention as a vehicle/scaffold for such inorganic particles in tissue engineering field. Its high mechanical strength, large surface area, and capacity for surface modifications make BNC an ideal candidate for development robust and biocompatible scaffolds (He et al., 2021). By combining BNC with inorganic components, novel researchers aim to develop advanced biomaterials that can support ECM synthesis and promote the structural and biochemical signals needed for effective skin and bone tissue regeneration.

In this study, we investigated the expression of three key biomarkers involved in cellular events related to tissue regeneration. We found that BNC-PO₄ significantly influenced F-actin expression in both fibroblast and osteoblast cells. Although type I collagen and fibronectin expression were also observed, no group showed increased expression compared to the control.

4.6.4. Clinical implications of the biological assays

The findings of this study suggest that phosphorylated BNC combined with TiO₂ nanoparticles could offer significant clinical benefits for advanced wound healing and tissue regeneration. The materials demonstrated enhanced cell migration, adhesion, and proliferation in both fibroblasts and osteoblasts, indicating their potential for promoting dermal and bone tissue regeneration. These properties are particularly relevant for treating chronic wounds, such as diabetic ulcers, and post-surgical wounds.

In vitro cytotoxicity testing revealed no significant toxicity, supporting the safety of these materials for clinical use. However, given the oxidative stress potential of TiO₂ nanoparticles, further *in vivo* studies are needed to assess their long-term safety and performance in animal models.

Additionally, the antimicrobial and anti-inflammatory properties of TiO₂ functionalized BNC films further support their potential as advanced wound dressings. These multifunctional materials could provide effective, safe, and accelerated wound healing, addressing both

tissue regeneration and infection control in clinical settings. Further research will be critical to confirm these promising results *in vivo*.

5. Conclusion

Dry bacterial nanocellulose is a versatile material. Depending on storage conditions it retains most of its original surface morphology, although prolonged storage under acidic conditions does lead to some hydrolysis of the surface regions and thus exposing crystalline domains. Phosphorylation of the surface occurs readily with simple reagents allowing for cost effective surface modification, though bacterial nanocellulose appears to lose some of its mechanical properties becoming more brittle in the process. The overall surface morphology of phosphorylated bacterial nanocellulose strongly depends on the storage conditions, ranging from globular surface structures patterned in the overall shape of the starting fibres when stored under basic conditions to ribbon-like cellulose fibres when stored under acidic or neutral conditions for a prolonged period of time. Thus combined phosphorylation, hydration and pH-treatment of surface-dense bacterial nanocellulose may serve as a way to alter the surface of dry bacterial nanocellulose for subsequent use. The introduction of phosphate onto the fibre surface allows for the introduction of nanosized titania with both lactate covered titania and triethanolamine terminated colloidal titania being successfully introduced. Titania in this system has been utilized to adsorb and desorb the broad-spectrum antibiotic tetracycline, with desorption taking place in a delayed manner over the course of several hours to several days. Providing a way to functionally introduce antibiotics onto commercial dry bacteria cellulose sheets. Biological assays indicated that phosphorylation and introduction of nano-sized TiO₂ via TiBALDH or TATT has promising prospects in tissue engineering via improved cell adhesion and wound closure, confirming our initial hypothesis. The steps in the proposed process in creation of functional composite are highly reproducible permitting successful up-scaling. This study provides a foundation for the future development of a broad range of BNC nanocomposites for therapeutic applications specifically in wound healing and tissue regeneration.

Hypothesis statement

Phosphorylation of bacterial nanocellulose dressing material improves its performance in wound closure due to strong interaction of epithelium cells to phosphate functions. It offers an opportunity to incorporate biocompatible mineral particles binding both phosphate ligands and pharmaceuticals, which permits slow release of the latter.

CRedit authorship contribution statement

Troy C. Breijaert: Writing – review & editing, Writing – original draft, Visualization, Investigation, Data curation. **Marina Fontes:** Writing – review & editing, Validation, Investigation, Formal analysis. **Paula de Abreu Fernandes:** Investigation, Formal analysis. **Hernane da Silva Barud:** Writing – review & editing, Supervision, Resources, Investigation. **Sidney J.L. Ribeiro:** Writing – review & editing, Supervision, Funding acquisition. **Gulaim A. Seisenbaeva:** Writing – review & editing, Supervision, Resources, Project administration, Investigation, Funding acquisition, Conceptualization.

Declaration of competing interest

The authors declare that they have no known competing financial interests or personal relationships that could have appeared to influence the work reported in this paper.

Acknowledgements

The authors would like to acknowledge the Swedish Foundation for

International Cooperation in Research and Higher Education (STINT) for financial support of the project BR2019–8506. Dr. H.S: Barud thanks São Paulo Research Foundation (grant number: 2023/17580–1); (CEMASU, FAPESP), Funding process: 2021/11965–3 and Funding Process: 2017/50334–3; National Council of Scientific and Technological Development/CNPq (Grant: 309614/2021–0), National Institutes of Science and Technology (INCTs), INCT Polysaccharides (Grant: 406973/2022–9), INCT Circularity in Polymer Materials (grant no 406925/2022–4), INCT-INFO (National Institute of Photonics). This study was financed by the Coordination of Superior Level Staff Improvement-Brazil(CAPES) - Finance Code 001. Dr. Marina Fontes thanks São Paulo Research Foundation (FAPESP, grant number: 2023/10811–8).

Supplementary materials

Supplementary material associated with this article can be found, in the online version, at [doi:10.1016/j.carpta.2025.100756](https://doi.org/10.1016/j.carpta.2025.100756).

Data availability

Data will be made available on request.

References

- Ait Benhamou, A., Kassab, Z., Nadifyfine, M., Salim, M. H., Sehaqui, H., Moubarik, A., et al. (2021). Extraction, characterization and chemical functionalization of phosphorylated cellulose derivatives from giant reed plant. *Cellulose*, 28, 4625–4642. <https://doi.org/10.1007/s10570-021-03842-6>
- Ayorinde, T., & Sayes, C. M. (2023). An updated review of industrially relevant titanium dioxide and its environmental health effects. *Journal of Hazardous Materials Letters*, 4, Article 100085. <https://www.sciencedirect.com/science/article/pii/S2666911023000114>
- Barud, H. S., Regiani, T., Marques, R. F. C., Lustri, W. R., Messaddeq, Y., & Ribeiro, S. J. L. (2011). Antimicrobial bacterial cellulose-silver nanoparticles composite membranes. *Journal of Nanomaterials*, 2011, 1–8. <https://doi.org/10.1155/2011/721631>
- Breijaert, T. C., Daniel, G., Hedlund, D., Svedlindh, P., Kessler, V. G., Granberg, H., et al. (2022). Self-assembly of ferria – nanocellulose composite fibres. *Carbohydrate Polymers*, 291, Article 119560. <https://doi.org/10.1016/j.carbpol.2022.119560>
- Brown, A. J. (1886). XIX—The chemical action of pure cultivations of bacterium acetii. *Journal of the Chemical Society, Transactions*, 49, 172–187. <https://doi.org/10.1039/CT8864900172>
- Calabrese, G., Franco, D., Petralia, S., Monforte, F., Condorelli, G. G., Squarzone, S., et al. (2021). Dual-functional nano-functionalized titanium scaffolds to inhibit bacterial growth and enhance osteointegration. *Nanomaterials*, 11, 2634. <https://doi.org/10.3390/nano11102634>
- GVAI-89-97- Capiello, F., Casciaro, B., Mangoni, M.L. (2018). A novel in vitro wound healing assay to evaluate cell migration. *JoVE*, 17:56825. <https://doi.org/10.3791/56825>
- Choi, S. M., Rao, K. M., Zo, S. M., Shin, E. J., & Han, S. S. (2022). Bacterial cellulose and its applications. *Polymers*, 14(6), 1080. <https://doi.org/10.3390/polym14061080>
- Datta, D., Prajapati, B., Jethva, H., Agrawal, K., Singh, S., & Prajapati, B. G. (2024). Value-added nanocellulose valorized from fruit peel waste for potential dermal wound healing and tissue regenerative applications. *Regenerative Engineering and Translational Medicine*. <https://doi.org/10.1007/s40883-024-00348-y> (in press).
- Ekstrand-Hammarström, B., Hong, J., Davoodpour, P., Sandholm, K., Ekdahl, K. N., Bucht, A., et al. (2015). TiO2 nanoparticles tested in a novel screening whole human blood model of toxicity trigger adverse activation of the kallikrein system at low concentrations. *Biomaterials*, 51, 58–68. <https://doi.org/10.1016/j.biomaterials.2015.01.031>
- Fink, H.-P., Purz, H. J., Bohn, A., & Kunze, J. (1997). Investigation of the supramolecular structure of never dried bacterial cellulose. In *Macromolecular Symposia*, 120 pp. 207–217. <https://doi.org/10.1002/masy.19971200121>
- French, A. D. (2014). Idealized powder diffraction patterns for cellulose polymorphs. *Cellulose*, 21, 885–896. <https://doi.org/10.1007/s10570-013-0030-4>
- Gaio, S., Svensson, F. G., Breijaert, T. C., Seisenbaeva, G. A., & Kessler, V. G. (2022). Nanoceria-nanocellulose hybrid materials for delayed release of antibiotic and anti-inflammatory medicines. *Materials Advances*, 3, 7228–7234. <https://doi.org/10.1039/D2MA00471B>
- Galkina, O. L., Ivanov, V. K., Agafonov, A. V., Seisenbaeva, G. A., & Kessler, V. G. (2015a). Cellulose nanofiber-titanium nanocomposites as potential drug delivery systems for dermal applications. *Journal of Materials Chemistry B*, 3, 1688–1698. <https://doi.org/10.1039/C4TB01823K>
- Galkina, O. L., Önnely, K., Huang, P., Ivanov, V. K., Agafonov, A. V., Seisenbaeva, G. A., et al. (2015b). Antibacterial and photochemical properties of cellulose nanofiber-titanium nanocomposites loaded with two different types of antibiotic medicines. *Journal of Materials Chemistry B*, 3, 7125–7134. <https://doi.org/10.1039/C5TB01382H>
- Gan, P., G. Sam, S. T., Abdullah, M. F., bin, & Omar, M. F. (2020). Thermal properties of nanocellulose-reinforced composites: A review. *Journal of Applied Polymer Science*, 137, 48544. <https://doi.org/10.1002/app.48544>
- Gardel, M. L., Schneider, I. C., Aratyn-Schaus, Y., & Waterman, C. M. (2010). Mechanical integration of actin and adhesion dynamics in cell migration. *Annual Review of Cell and Developmental Biology*, 26, 315–333. <https://doi.org/10.1146/annurev.cellbio.011209.122036>
- Groenke, N., Seisenbaeva, G. A., Kaminskyy, V., Zhivotovskiy, B., Kost, B., & Kessler, V. G. (2012). Structural characterization, solution stability, and potential health and environmental effects of the Nano-TiO₂ bioencapsulation matrix and the model product of its biodegradation TIBALDH. *RSC Advances*, 2, 4228–4235. <https://doi.org/10.1039/C2RA20388J>
- He, W., Wu, J., Xu, J., Mosselhy, D. A., Zheng, Y., & Yang, S. (2021). Bacterial cellulose: functional modification and wound healing applications. *Advances in Wound Care*, 10, 623–640. <https://doi.org/10.1089/wound.2020.1219>
- Horue, M., Silva, J. M., Berti, I. R., Brandão, L. R., Barud, H. D. S., & Castro, G. R. (2023). Bacterial cellulose-based materials as dressings for wound healing. *Pharmaceutics*, 15, 424. <https://doi.org/10.3390/pharmaceutics15020424>
- Inagaki, N., Nakamura, S., Asai, H., & Katsura, K. (1976). Phosphorylation of cellulose with phosphorous acid and thermal degradation of the product. *Journal of Applied Polymer Science*, 20, 2829–2836. <https://doi.org/10.1002/app.1976.070201017>
- Kanta, J. (2015). Collagen matrix as a tool in studying fibroblastic cell behavior. *Cell Adhesion & Migration*, 9, 308–316. <https://doi.org/10.1080/19336918.2015.1005469>
- Kessler, V. G., Seisenbaeva, G. A., Håkansson, S., & Unell, M. (2008). Chemically triggered biodelivery using metal-organic sol-gel synthesis. *Angewandte Chemie International Edition*, 47, 8506–8509. <https://onlinelibrary.wiley.com/doi/abs/10.1002/anie.200803307>
- Kessler, V. G., Spijksma, G. L., Seisenbaeva, G. A., Hakansson, S., Blank, D. H., & Bouwmeester, H. J. (2006). New insight in the role of modifying ligands in the sol-gel processing of metal alkoxide precursors: a possibility to approach new classes of materials. *Journal of Sol-Gel Science and Technology*, 40, 163–179.
- Khalid, A., Ullah, H., Ul-Islam, M., Khan, R., Khan, S., Ahmad, F., et al. (2017). Bacterial cellulose-TiO₂ nanocomposites promote healing and tissue regeneration in burn mice model. *RSC Advances*, 7, 47662–47668. <https://doi.org/10.1039/C7RA06699F>
- Khan, S., Ul-Islam, M., Khattak, W. A., Ullah, M. W., & Park, J. K. (2015). Bacterial cellulose-titanium dioxide nanocomposites: nanostructural characteristics, antibacterial mechanism, and biocompatibility. *Cellulose*, 22, 565–579. <https://doi.org/10.1007/s10570-014-0528-4>
- Klemm, D., Heublein, B., Fink, H.-P., & Bohn, A. (2005). Cellulose: fascinating biopolymer and sustainable raw material. *Angewandte Chemie International Edition*, 44, 3358–3393. <https://doi.org/10.1002/anie.200460587>
- Klemm, D., Schumann, D., Udhardt, U., & Marsch, S. (2001). Bacterial synthesized cellulose — Artificial blood vessels for microsurgery. *Progress in Polymer Science*, 26, 1561–1603. [https://doi.org/10.1016/S0079-6700\(01\)00021-1](https://doi.org/10.1016/S0079-6700(01)00021-1)
- Kubo, K., Tsukimura, N., Iwasa, F., Ueno, T., Saruwatari, L., Aita, H., et al. (2009). Cellular behavior on TiO2 nanonodular structures in a micro-to-nanoscale hierarchy model. *Biomaterials*, 30, 5319–5329. <https://doi.org/10.1016/j.biomaterials.2009.06.021>
- Larsson, D. G. J., & Flach, C. F. (2022). Antibiotic resistance in the environment. *Nature Reviews Microbiology*, 20, 257–269. <https://www.nature.com/articles/s41579-021-00649-x>
- Le Clinche, C., & Carlier, M.-F. (2008). Regulation of actin assembly associated with protrusion and adhesion in cell migration. *Physiological Reviews*, 88, 489–513. <https://doi.org/10.1151/physrev.00021.2007>
- Li, M., Liang, Y., He, J., Zhang, H., & Guo, B. (2020). Two-pronged strategy of biomechanically active and biochemically multifunctional hydrogel wound dressing to accelerate wound closure and wound healing. *Chemistry of Materials*, 32, 9937–9953. <https://doi.org/10.1021/acs.chemmater.0c02823>
- Li, Y., Jiang, H., Zheng, W., Gong, N., Chen, L., Jiang, X., et al. (2015). Bacterial cellulose-hyaluronan nanocomposite biomaterials as wound dressings for severe skin injury repair. *Journal of Materials Chemistry B*, 3, 3498–3507. <https://doi.org/10.1039/C4TB01819B>
- Li, Y., Tian, Y., Zheng, W., Feng, Y., Huang, R., Shao, J., et al. (2017). Composites of bacterial cellulose and small molecule-decorated gold nanoparticles for treating gram-negative bacteria-infected wounds. *Small*, 13, Article 1700130. <https://doi.org/10.1002/smll.201700130>
- Liao, C., Li, Y., & Tjong, S. C. (2019). Bactericidal and cytotoxic properties of silver nanoparticles. *International Journal of Molecular Sciences*, 20, 449. <https://doi.org/10.3390/ijms20020449>
- Machado, R. T. A., Gutierrez, J., Tercjak, A., Trovati, E., Uahib, F. G. M., de, P., et al. (2016). Komagataeibacter rhaeticus as an alternative bacteria for cellulose production. *Carbohydrate Polymers*, 152, 841–849. <https://doi.org/10.1016/j.carbpol.2016.06.049>
- Malmes, D., Ahrens, L., Köhler, S., Forsberg, M., & Golovko, O. (2022). Occurrence and mass flows of contaminants of emerging concern (CECs) in Sweden's three largest lakes and associated rivers. *Chemosphere*, 294, Article 133825. <https://doi.org/10.1016/j.chemosphere.2022.133825>
- Marchessault, R. H., & Sundararajan, P. R. (1983). Cellulose. *The polysaccharides* (pp. 11–95). Elsevier. <https://doi.org/10.1016/B978-0-12-065602-8.50007-8>
- Morais, D. C., Fontes, M. L., Oliveira, A. B., Gabbai-Armelin, P. R., Ferrisse, T. M., De Oliveira, L. F., et al. (2023). Combining polymer and cyclodextrin strategy for drug release of sulfadiazine from electrospon fibers. *Pharmaceutics*, 15, 1890. <https://doi.org/10.3390/pharmaceutics15071890>

- Moritz, S., Wiegand, C., Wesarg, F., Hessler, N., Müller, F. A., Kralisch, D., et al. (2014). Active wound dressings based on bacterial nanocellulose as drug delivery system for otenidine. *International Journal of Pharmaceutics*, 471, 45–55. <https://doi.org/10.1016/j.ijpharm.2014.04.062>
- Myers, H. M., Tochon-Danguy, H. J., & Baud, C. A. (1983). IR absorption spectrophotometric analysis of the complex formed by tetracycline and synthetic hydroxyapatite. *Calcified Tissue International*, 35, 745–749. <https://doi.org/10.1007/BF02405117>
- O'Sullivan, A. C. (1997). Cellulose: the structure slowly unravels. *Cellulose*, 4, 173–207. <https://doi.org/10.1023/A:1018431705579>
- Paladini, F., & Pollini, M. (2019). Antimicrobial silver nanoparticles for wound healing application: progress and future trends. *Materials (Basel)*, 12, 2540. <https://doi.org/10.3390/ma12162540>
- Parisi, L., Toffoli, A., Ghezzi, B., Mozzoni, B., Lumetti, S., & Macaluso, G. M. (2020). A glance on the role of fibronectin in controlling cell response at biomaterial interface. *Japanese Dental Science Review*, 56, 50–55. <https://doi.org/10.1016/j.jdsr.2019.11.002>
- Paschoalin, R. T., Traldi, B., Aydin, G., Oliveira, J. E., Rütten, S., Mattoso, L. H. C., et al. (2017). Solution blow spinning fibres: new immunologically inert substrates for the analysis of cell adhesion and motility. *Acta Biomaterialia*, 51, 161–174. <https://doi.org/10.1016/j.actbio.2017.01.020>
- Patoary, M. K., Farooq, A., Zaarour, B., & Liu, L. (2021). Phosphorylated cellulose nanofibrils: structure-morphology-rheology relationships. *Cellulose*, 28, 4105–4117. <https://doi.org/10.1007/s10570-021-03786-x>
- Rasouli, M., Soleimani, M., Hosseinzadeh, S., & Ranjbari, J. (2023). Bacterial cellulose as potential dressing and scaffold material: toward improving the antibacterial and cell adhesion properties. *Journal of Polymers and the Environment*, 31, 4621–4640. <https://doi.org/10.1007/s10924-023-02779-0>
- Rueden, C. T., Schindelin, J., Hiner, M. C., DeZonia, B. E., Walter, A. E., Arena, E. T., et al. (2017). ImageJ2: ImageJ for the next generation of scientific image data. *BMC Bioinformatics*, 18, 529. <https://doi.org/10.1186/s12859-017-1934-z>
- Seisenbaeva, G. A., Daniel, G., Nedelec, J. M., & Kessler, V. G. (2013). Solution equilibrium behind the room-temperature synthesis of nanocrystalline titanium dioxide. *Nanoscale*, 5, 3330–3336. <https://pubs.rsc.org/en/content/articlelanding/2013/nr/c3nr34068f>
- Seisenbaeva, G. A., Fromell, K., Vinogradov, V. V., Terekhov, A. N., Pakhomov, A. V., Nilsson, B., et al. (2017). Dispersion of TiO₂ nanoparticles improves burn wound healing and tissue regeneration through specific interaction with blood serum proteins. *Scientific Reports*, 7, 15448. <https://doi.org/10.1038/s41598-017-15792-w>
- Skocaj, M., Filipic, M., Petkovic, J., & Novak, S. (2011). Titanium dioxide in our everyday life; is it safe? *Radiology and Oncology*, 45(4), 227–247. <https://pubmed.ncbi.nlm.nih.gov/22933961/>
- Stoica, A. E., Chircov, C., & Grumezescu, A. M. (2020). Nanomaterials for wound dressings: an up-to-date overview. *Molecules*, 25, 2699. <https://doi.org/10.3390/molecules25112699>
- Suneetha, M., Kim, H., & Han, S. S. (2024). Bone-like apatite formation in biocompatible phosphate-crosslinked bacterial cellulose-based hydrogels for bone tissue engineering applications. *International Journal of Biological Macromolecules*, 256, Article 128364. <https://doi.org/10.1016/j.ijbiomac.2023.128364>
- Svensson, F. G., Manivel, V. A., Seisenbaeva, G. A., Kessler, V. G., Nilsson, B., Ekdahl, K. N., et al. (2021). Hemocompatibility of nanotitania-nanocellulose hybrid materials. *Nanomaterials*, 11, 1100. <https://doi.org/10.3390/nano11051100>
- Thomas, L. C., & Chittenden, R. A. (1964b). Characteristic infrared absorption frequencies of organophosphorus compounds—I The phosphoryl (P=O) group. *Spectrochimica Acta*, 20, 467–487. [https://doi.org/10.1016/0371-1951\(64\)80043-6](https://doi.org/10.1016/0371-1951(64)80043-6)
- Thomas, L. C., & Chittenden, R. A. (1964a). Characteristic infrared absorption frequencies of organophosphorus compounds—II. P-O-(X) bonds. *Spectrochimica Acta*, 20, 489–502. [https://doi.org/10.1016/0371-1951\(64\)80044-8](https://doi.org/10.1016/0371-1951(64)80044-8)
- Thoorens, G., Krier, F., Leclercq, B., Carlin, B., & Evrard, B. (2014). Microcrystalline cellulose, a direct compression binder in a quality by design environment—A review. *International Journal of Pharmaceutics*, 473, 64–72. <https://doi.org/10.1016/j.ijpharm.2014.06.055>
- Tripathi, N., & Goshisht, M. K. (2022). Recent advances and mechanistic insights into antibacterial activity, antibiofilm activity, and cytotoxicity of silver nanoparticles. *ACS Applied Bio Materials*, 5, 1391–1463. <https://doi.org/10.1021/acsabm.2c00014>
- Volova, T. G., Shumilova, A. A., Shidlovskiy, I. P., Nikolaeva, E. D., Sukovaty, A. G., Vasiliev, A. D., et al. (2018). Antibacterial properties of films of cellulose composites with silver nanoparticles and antibiotics. *Polymer Testing*, 65, 54–68. <https://doi.org/10.1016/j.polymeresting.2017.10.023>
- Wada, M., Okano, T., & Sugiyama, J. (2001). Allomorphs of native crystalline cellulose I evaluated by two equatorial spacings. *Journal of Wood Science*, 47, 124–128. <https://doi.org/10.1007/BF00780560>
- Wahid, F., Zhao, X.-J., Zhao, X.-Q., Ma, X.-F., Xue, N., Liu, X.-Z., et al. (2021). Fabrication of bacterial cellulose-based dressings for promoting infected wound healing. *ACS Applied Materials & Interfaces*, 13, 32716–32728. <https://doi.org/10.1021/acsami.1c06986>
- Zahel, P., Beekmann, U., Eberlein, T., Schmitz, M., Werz, O., & Kralisch, D. (2022). Bacterial cellulose—adaptation of a nature-identical material to the needs of advanced chronic wound care. *Pharmaceutics (Basel)*, 15(6), 683. <https://doi.org/10.3390/ph15060683>
- Zhangjian Chen, Z., Han, S., Zhou, S., Feng, H., Liu, Y., & Jia, G. (2020). Review of health safety aspects of titanium dioxide nanoparticles in food application. *Nano Impact*, 18, Article 100224. <https://www.sciencedirect.com/science/article/pii/S2452074820300185>

Functionalization of Bacterial Cellulose-based Wound Dressing for Increased Drug Retention

Troy C. Breijaert^a, Marina Fontes^b, Paula de Abreu Fernandes^c, Hernane da Silva Barud ^{†c,d}, Sidney J.L. Ribeiro^d and Gulaim A. Seisenbaeva^{†a}

^aDepartment of Molecular Science, Swedish University of Agricultural Science, 756 51 Ultuna, Sweden.

^bDepartment of Chemistry, Federal University of São Carlos (UFSCar), 13565-905, São Carlos, SP, Brazil

^cDepartment of Biotechnology, University of Araraquara (UNLARA), 14801340, Araraquara, SP, Brazil.

^dInstitute of Chemistry, São Paulo State University – UNESP, 14800-900, Araraquara, SP, Brazil.

[†] Corresponding author, email: Gulaim.Seisenbaeva@slu.se, tel: (Sweden), hernane.barud@gmail.com, tel: +55 16 98123-3935 (Brazil)

Keywords: Bacterial nanocellulose, Wound Dressing, Phosphorylation, Drug Delivery, Titania

Indirect Cytotoxicity Assay

L929 murine fibroblasts cells and human osteoblast-like SaOS-2 cells were obtained from the American Type Culture Collection (ATCC, VA, USA). Cells were seeded in 96-well plates at 10^4 cells per well in 100 μ L of DMEM (Dulbecco's Modified eagle Medium, Gibco®) supplemented with 10% FBS (Fetal Bovine Serum, Gibco®) and 1% of ciprofloxacin (Sigma, St. Louis, MO, USA), and incubated at 37 °C in 5% CO₂ atmosphere for 24 h. Simultaneously, the extract media from functionalized BNC composites were prepared using 3 cm² of each sample into 3 mL of DMEM culture that was stirred at 37 °C for 24 h. Then 100 μ L of each extract medium was added to each well. Two different controls were included: culture media only, i.e., no cells; (2) cells incubated in culture medium alone (survival control). After 24 h of incubation, the extract media were removed and the wells were washed with 0.01 M phosphate-buffered saline (PBS). Thereafter, 100 μ L of MTT (1 mg/mL) was added into each well, and the cells were further incubated for 4 h. Finally, the supernatant was removed and 50 μ L isopropanol was added into each well. The absorbances were measured at a wavelength of 570 nm and then converted into percentages of cell viability.[1] All samples were performed in triplicate.

Pseudo-Wound Healing

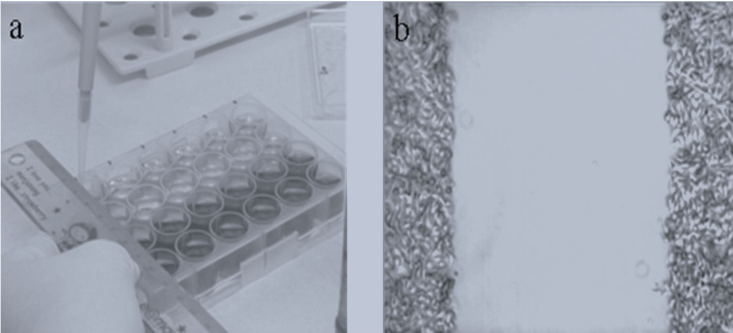
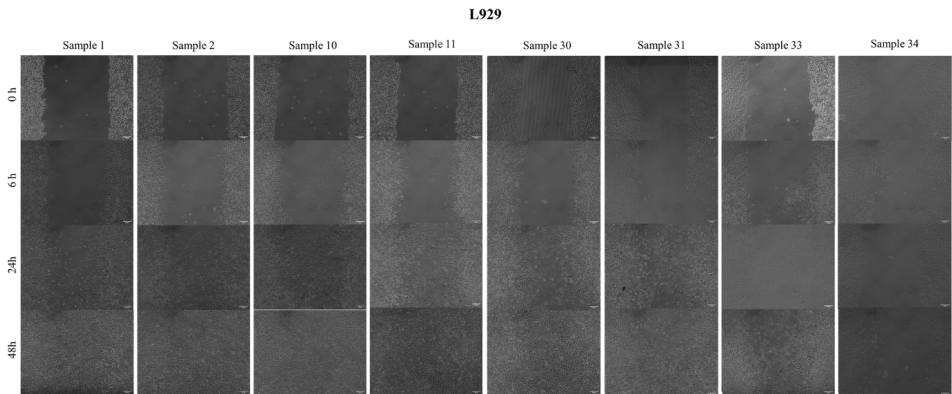


Figure S1. Preparation of Pseudo-wound closure samples



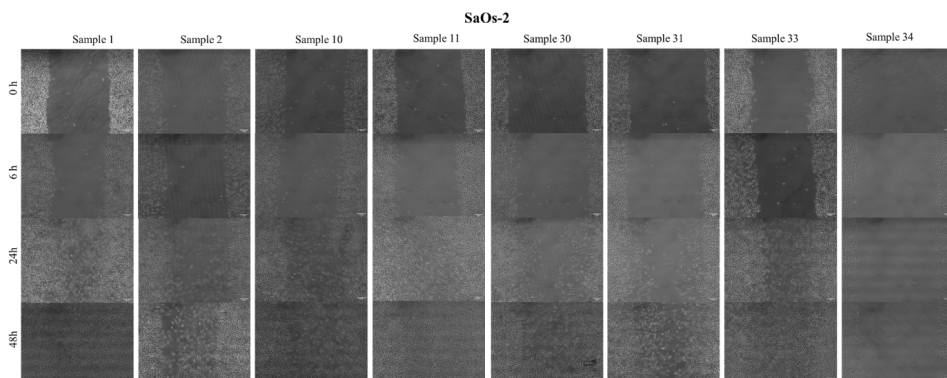


Figure S2. Micrographs of the pseudo-wound healing assay using murine fibroblast and osteoblast cell lines over 48 hours of testing, with eluates derived from different BNC samples.

Atomic Force Microscopy

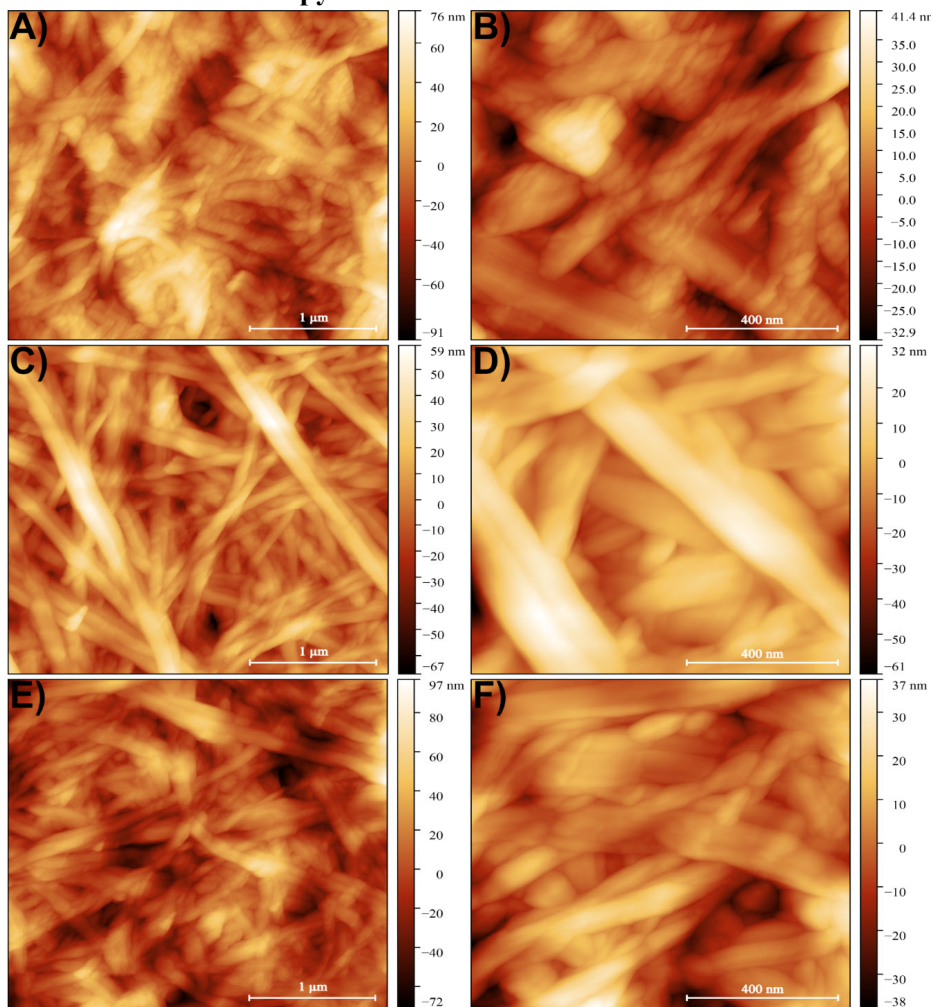


Figure S3. Atomic Force Microscope images showcasing the effect pH has on the surface structure of a dried bacterial cellulose sheet after 7 days in 0.1M HCl (A,B), ultrapure water (C, D) and 0.1M NaOH (E, F)

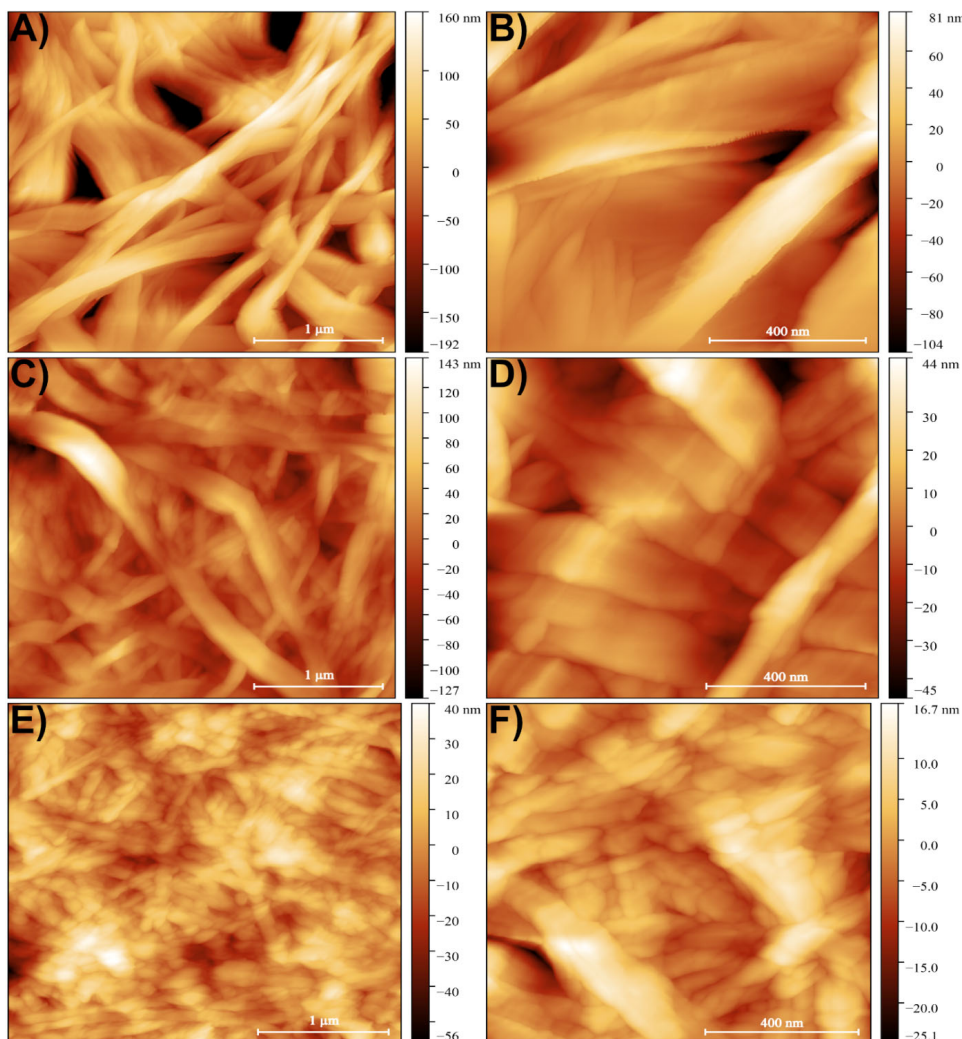


Figure S4. Atomic Force Microscope images showcasing the effect pH has on the surface structure of a phosphorylated dried bacterial cellulose sheet after 7 days in 0.1M HCl (A,B), ultrapure water (C, D) and 0.1M NaOH (E, F)

Table S1. Fiber dimensions and RMS surface roughness of pH treated bacterial cellulose materials

	Fiber Dimensions (n=20)	Surface Roughness (RMS, 3x3μm, n=1)
BC-HCl treated 7 days	50.9±13.9 nm / (22.3±5.3nm crystals)	23.12 nm
BC-Ultrapure water 7 days	70.9±12.4	16.44 nm
BC-NaOH treated 7 days	60.0±12.5	21.04 nm
BC-PO4-HCl treated 7 days	63.5±17.8	58.54 nm
BC-PO4-Ultrapure water 7 days	68.9±14.2	28.95 nm
BC-PO4-NaOH treated 7 days	44.8±9.1	10.58 nm

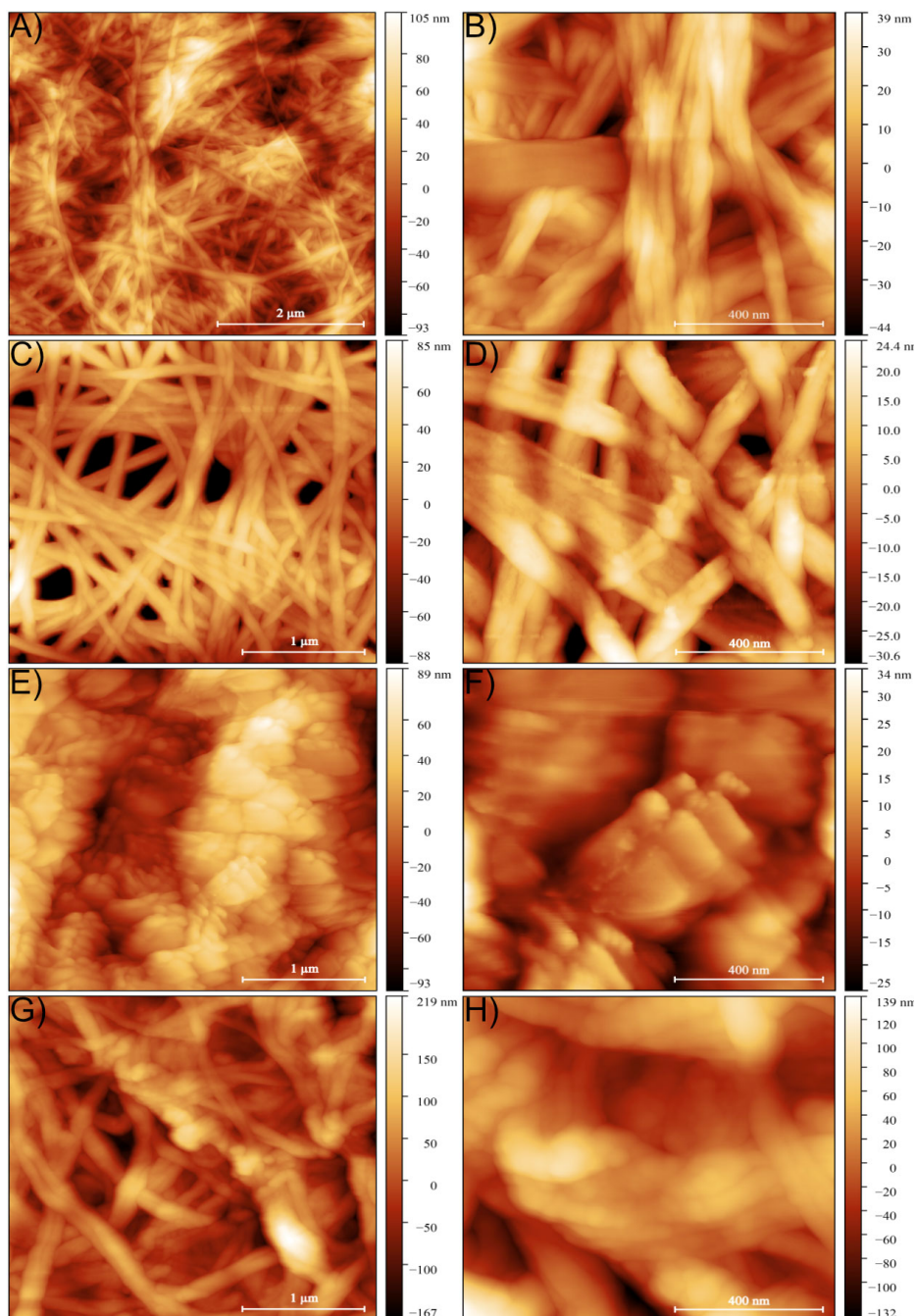


Figure S5. Atomic Force Microscope images showcasing the physical surface structure of (A,B) Dry Bacterial Cellulose, (C,D) Phosphorylated Bacterial Cellulose after synthesis, (E,F) Phosphorylated Bacterial Cellulose treated with 10 eq TiBALDH and (G,H) Phosphorylated Bacterial Cellulose treated with TATT.

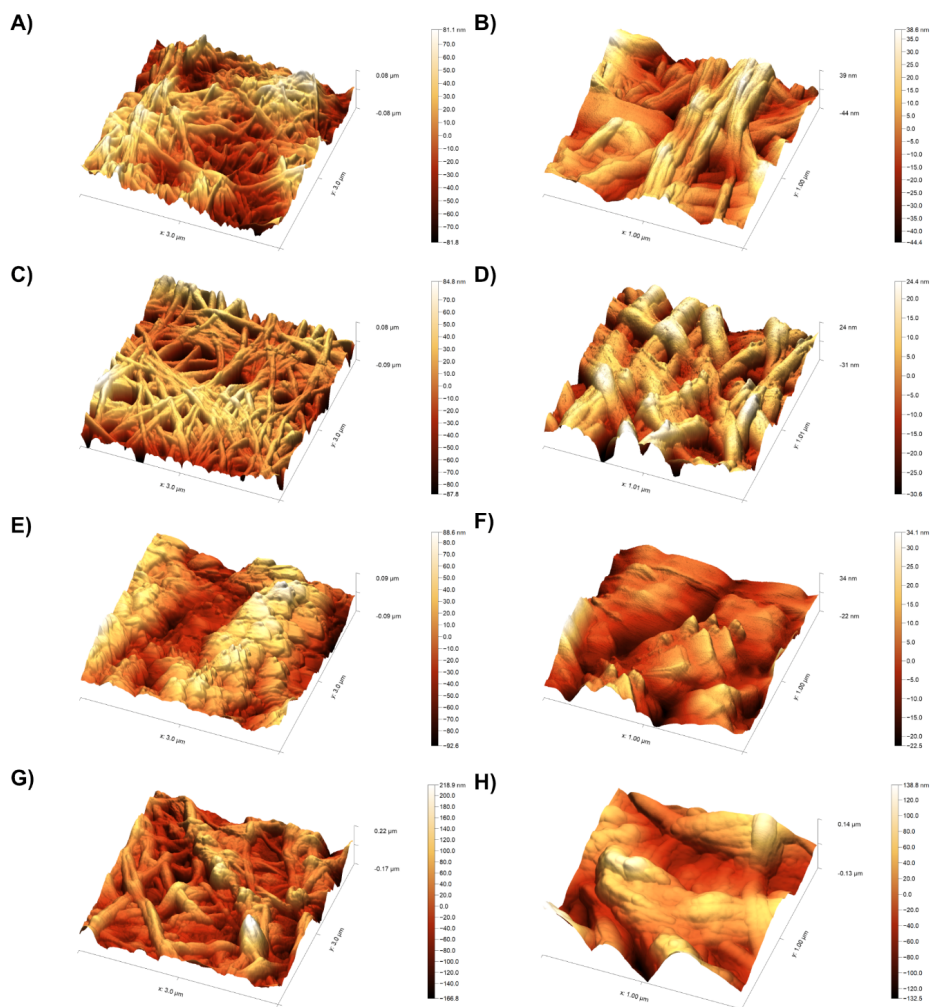


Figure S6. Atomic Force Microscope images (3D projection) showcasing the physical surface structure of (A) Dry Bacterial Cellulose, (B) Phosphorylated Bacterial Cellulose after synthesis, (C) Phosphorylated Bacterial Cellulose treated with 10 eq TiBALDH and (D) Phosphorylated Bacterial Cellulose treated with TATT.

Table S2. Fiber dimensions and RMS surface roughness determined by AFM of (un-)functionalized bacterial cellulose materials

	Fiber Dimensions	Surface Roughness (RMS)
BC-Dry sheet	64.9 ± 13.0 nm	29.3 nm
BC-PO4 (as-synth)	65.7 ± 12.8 nm	28.4 nm
BC-PO4-TiBALDH	-	27.5 nm
BC-PO4-TATT	71.6 ± 6.6 nm	50.3 nm

Scanning Electron Microscopy

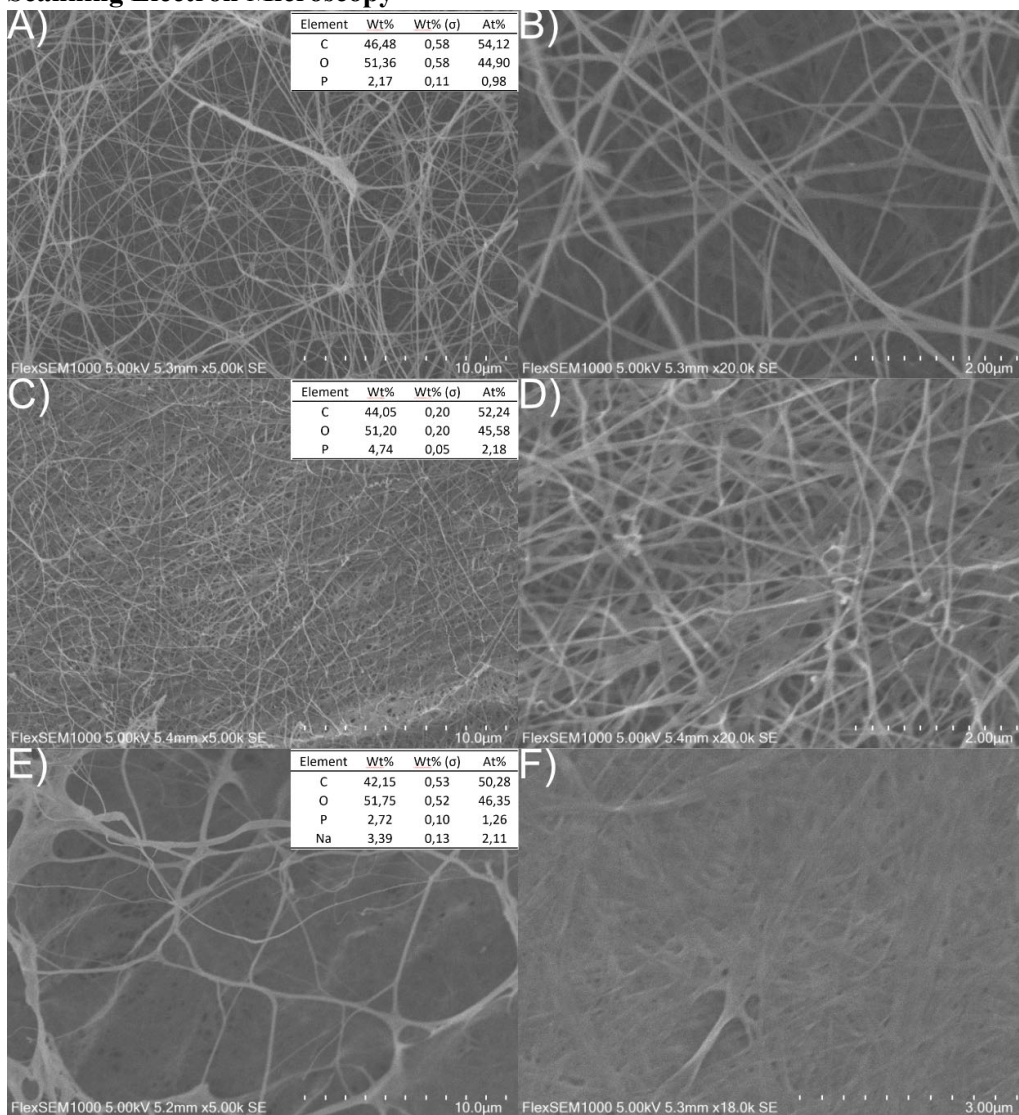


Figure S7. SEM images showcasing the different surface morphology of phosphorylated bacterial cellulose after 7 days in 0.1M HCl (A,B), ultrapure water (C,D) and 0.1M NaOH (E, F)

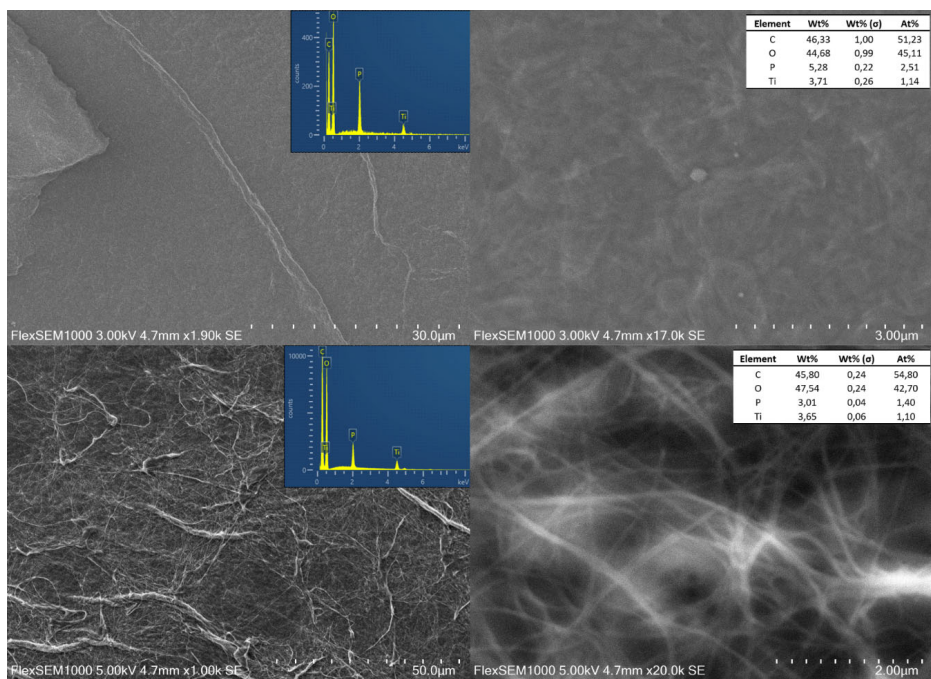


Figure S8. SEM images showcasing the microscale surface morphological differences between TiBALDH modified and TATT modified bacterial cellulose.

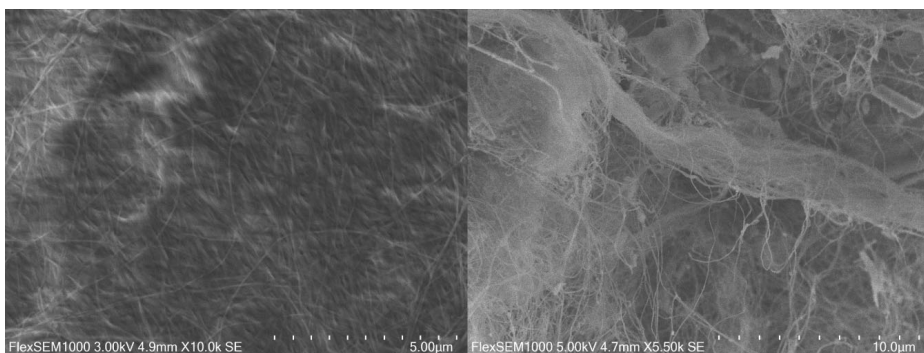


Figure S9. Urea-treated dried sheet bacterial cellulose after treatment at 160°C (left) and supercritically dried native bacterial cellulose (right)

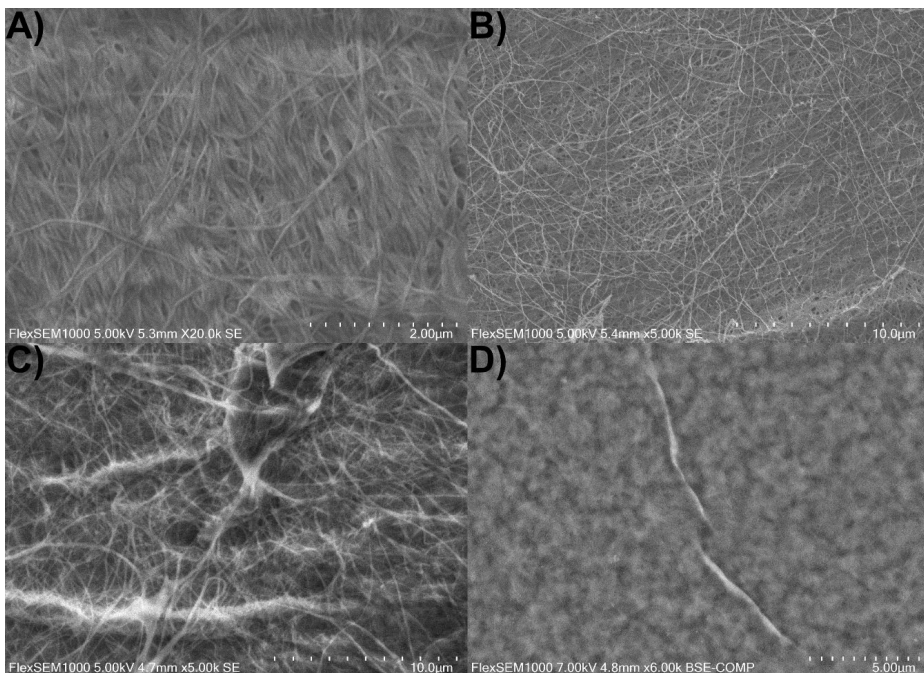


Figure S10. SEM (without coating images of Bacterial nanocellulose Sheet as is (A, SE, 20K, B 5x5µm), phosphorylated BNC (C, SE, 5K, D, 3x3µm), phosphorylated BNC- modified by TiO_2 derived from TiBALDH® (E, 6K, BSE, F, 3x3µm), phosphorylated bacterial nanocellulose coated with pre-formed colloidal TATT (G, SE, 5K, H, 3x3µm

X-ray Diffraction of cellulose films

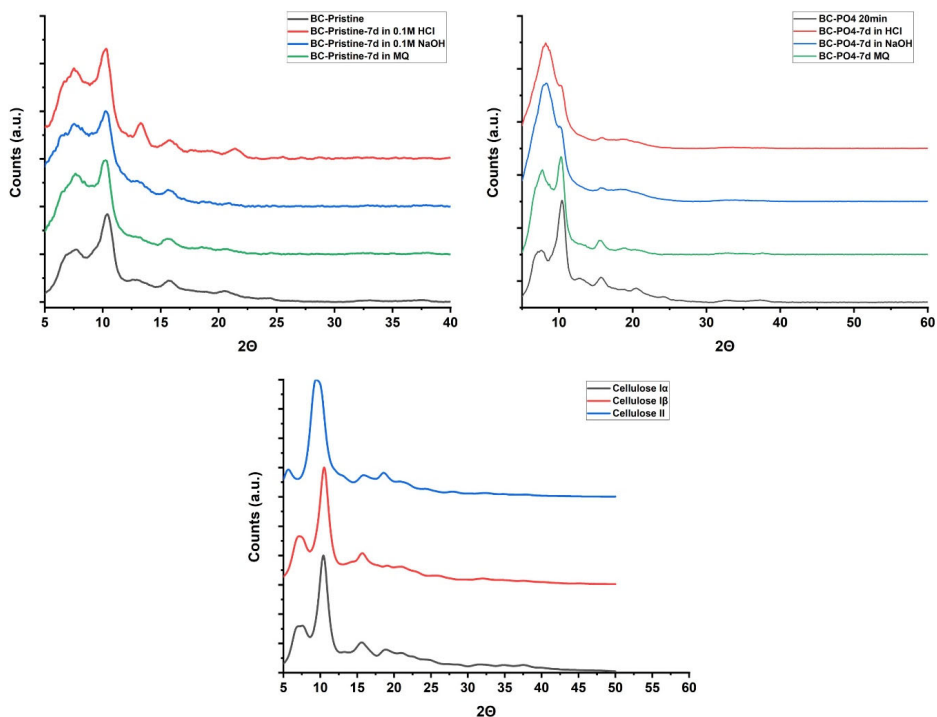


Figure S11. XRD patterns of (**top left**) aqueous treated BNC films as delivered (black), 7 days in ultrapure water (green), 7 days in 0.1M NaOH (blue) and 7 days in 0.1M HCl (red). (**top right**) XRD patterns of aqueous treated phosphorylated BNC films as synthesized (black), 7 days in ultrapure water (green), 7 days in 0.1M NaOH (blue) and 7 days in 0.1M HCl (red). (**bottom**) simulated patterns (using idealized diffraction patterns[2] and Mercury, $\lambda=0.7093$ Å, FWHM=1.5)) of cellulose I α , I β and cellulose II.

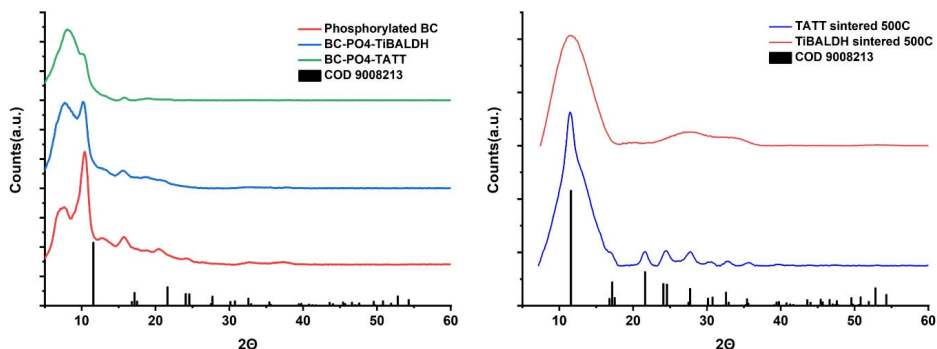


Figure S12. XRD patterns for (**Left**): Phosphorylated BNC (Red) TiBALDH covered BNC (blue), TATT covered BNC (green), reference pattern for anatase TiO₂. (**Right**) sintered BNC with TATT (blue), TiBALDH (red) and COD 9008213 anatase TiO₂ reference

ATR-FTIR

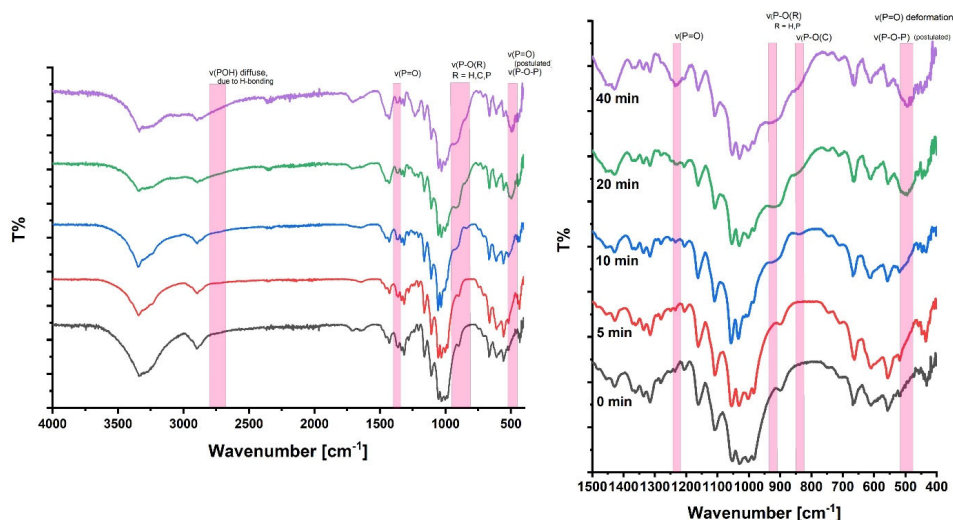


Figure S13. Attenuated Total Reflectance-FTIR spectra of the evolution of phosphorus related IR-peaks as a function of time. Pristine BC (black), 5 minutes (red), 10 minutes (blue), 20 minutes (green) and 40 minutes (purple)

Transmission FTIR

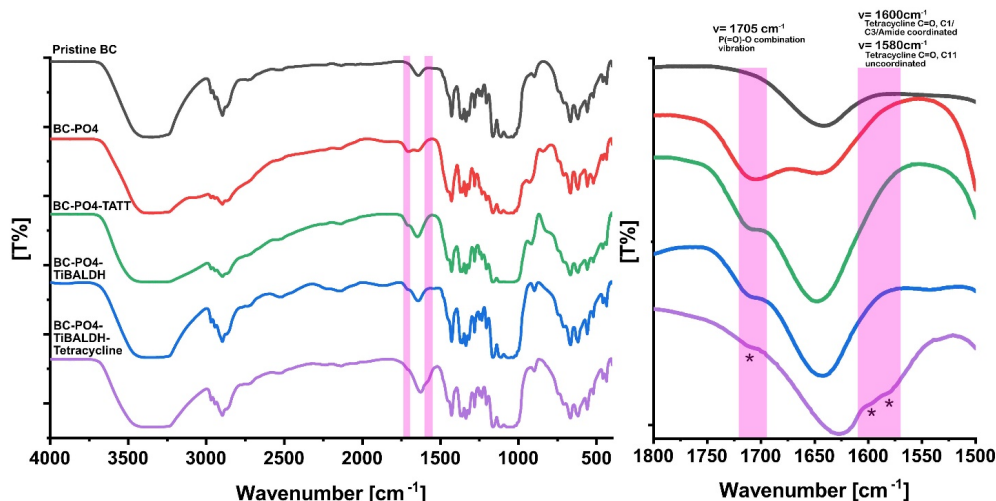


Figure S14. (left) Overlay of transmission FTIR spectra of pristine bacterial cellulose (black), phosphorylated bacterial cellulose (red), TiBALDH modified phosphorylated bacterial cellulose (blue), Tetracycline adsorbed TiBALDH-PO4-cellulose (purple) and TATT modified phosphorylated bacterial cellulose (green). **(right)** transmission spectra between 1500-1800 cm^{-1} , marking the appearance of the P(=O)-O combination vibration (1705 cm^{-1}) after phosphorylation[3] and the appearance of two shoulder peaks at 1580 cm^{-1} and 1600 cm^{-1} after the introduction of tetracycline attributed to C=O vibrations in tetracycline.[4]

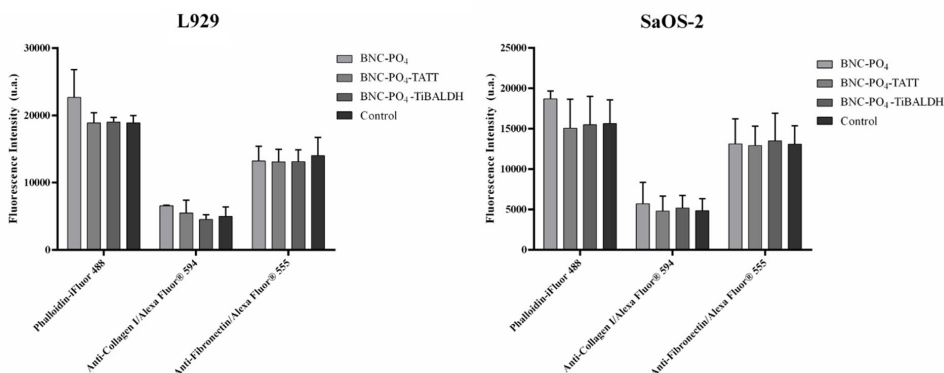


Figure S15. Measurement of fluorescence intensity of F-actin, type-I collagen and fibronectin on L929 fibroblasts and SaOS-2 osteoblasts cultured for 7 days with different eluates from BC-PO₄, BC-PO₄-TATT and BC-PO₄-TiBALDH. Control cells were maintained with only conventional media.

Table S3. Maximum thermal degradation temperature (T_{peak}) and mass loss data for BNC membrane obtained from thermogram (for interpretation, please, see [5-6]).

Sample	Mass loss 1 (%)	T_{peak1} (°C)	Mass loss 2 (%)	T_{peak2} (°C)	Mass loss 3 (%)	T_{peak3} (°C)
BNC	10.8	100	12.0	240	45.1	328

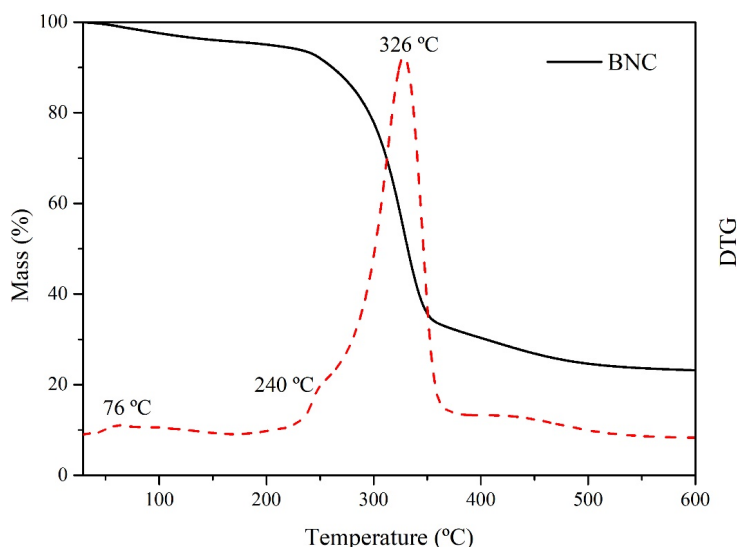


Figure S16. TG/DTG thermogram of the BNC.

The solid state ¹³C NMR spectra showed in Figure S16 reveal distinct signals corresponding to the carbon atoms within the carbohydrate segment of the cellulose structure. Specifically, the signal at δ 105 ppm is attributed to carbon C1, while the signal at δ 89 ppm corresponds to carbon C4. The region

between δ 74–71 ppm encompasses signals from carbons C2, C3, and C5, and the signal at δ 65 ppm represents carbon C6 [7, 8].

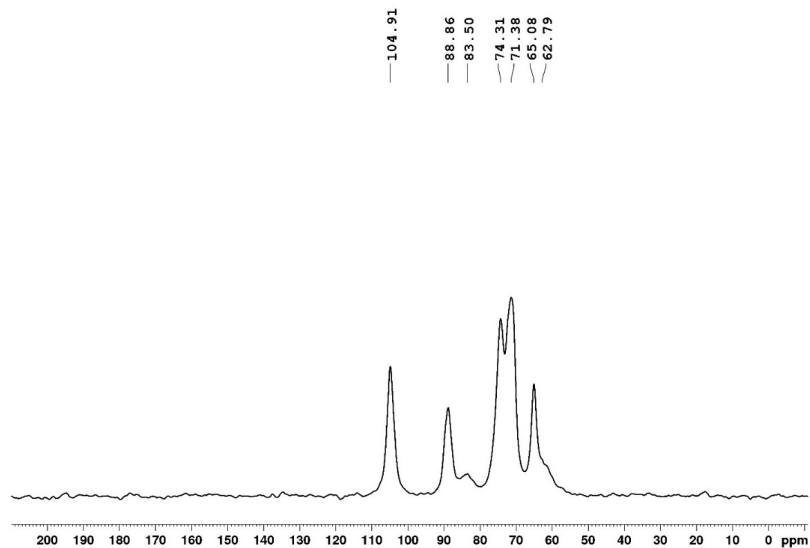


Figure S17. ^{13}C NMR spectra of pristine BNC.

The degree of polymerization (DP) of BNC determined through viscometry was found to be 2800 (Table S4), corresponding to an average molecular weight of 453.600 g/mol [9, 10].

Table S4. Degree of polymerization obtained from viscosity measurement.

Sample	DP
BNC	2800

Table S5. The statistical analysis of cell viability percentage among different groups against to the SaOS-2 cell line was performed using a Two-way ANOVA followed by Tukey's multiple comparisons test. Statistically significant values are presented as (****) $p < 0.0001$.

Samples	p value
1 vs. 34	****
1 vs. 35	****
2 vs. 34	****
2 vs. 35	****
10 vs. 34	****
10 vs. 35	****
11 vs. 34	****
11 vs.35	****
30 vs. 34	****
30 vs. 35	****
31 vs. 34	****
31 vs. 35	****
32 vs. 34	****
32 vs. 35	****
33 vs. 34	****
33 vs.35	****

Pseudo-Wound Healing – Statistical Analysis

Table S6. The statistical analysis of the pseudo-wound healing assay in the SaOS-2 cell line was performed using a Two-way ANOVA followed by Tukey's multiple comparisons test. The analysis was conducted between different time points within the same group. Statistically significant values are presented as (*) $p < 0.05$; (**) $p < 0.01$; (***) $p < 0.001$; (****) $p < 0.0001$.

Sample	Time					
	0 h vs. 6 h	0 h vs. 24 h	0 h vs. 48 h	6 h vs. 24h	6 h vs. 48 h	24 h vs. 48 h
1	****	****	****	****	****	ns
2	****	****	****	****	****	**
		****	****	****	****	ns
10	****					
11	****	****	****	****	****	ns
30	***	****	****	****	****	****
31	****	****	****	****	****	****
33	****	****	****	****	****	ns
Positive control	****	****	****	****	****	ns

Table S7. The statistical analysis of the pseudo-wound healing assay in the SaOS-2 cell line was performed using a Two-way ANOVA followed by Tukey's multiple comparisons test. The analysis was conducted between different time points among different groups. Statistically significant values are presented as (*) $p < 0.05$; (**) $p < 0.01$; (***) $p < 0.001$; (****) $p < 0.0001$.

Time	1 vs. 30	1 vs. Positive control	2 vs. Positive control	10 vs. Positive Control	11 vs. 30	30 vs. Positive control	31 vs. Positive control	33 vs. Positive control
6 h	*	*	**	****	**	****	*	***

Time	1 vs. 30	1 vs. 31	2 vs. 30	2 vs. 31	10 vs. 30	10 vs. 31	11 vs. 30	11 vs. 31	30 vs. 31	30 vs. 33	30 vs. Positive control	31 vs. 33	31 vs. Positive control
24 h	****	****	****	****	****	****	****	****	**	****	****	****	****

Time	10 vs. 31		11 vs. 31		31 vs. 33		31 vs. Positive control	
48 h	*		*		*		*	

Table S8. The statistical analysis of the pseudo-wound healing assay in the L929 cell line was performed using a Two-way ANOVA followed by Tukey's multiple comparisons test. The analysis was conducted between different time points within the same group. Statistically significant values are presented as (*) $p < 0.05$; (**) $p < 0.01$; (***) $p < 0.001$; (****) $p < 0.0001$.

Sample	Time					
	0 h vs. 6 h	0 h vs. 24 h	0 h vs. 48 h	6h vs. 24h	6 h vs. 48 h	24 h vs. 48 h
1	****	****	****	****	****	ns
2	***	****	****	****	****	ns
10	****	****	****	****	****	ns
11	****	****	****	****	****	ns
30	**	****	****	****	****	ns
31	****	****	****	****	****	ns
33	****	****	****	****	****	ns
Positive control	****	****	****	****	****	ns

Table S9. The statistical analysis of the pseudo-wound healing assay in the L929 cell line was performed using a Two-way ANOVA followed by Tukey's multiple comparisons test. The analysis was conducted between different time points among different groups. Statistically significant values are presented as (*) $p < 0.05$; (**) $p < 0.01$; (***) $p < 0.001$; (****) $p < 0.0001$.

Time	1 vs. Positive control	2 vs. 33	2 vs. Positive control	30 vs. 33	30 vs. Positive control
6 h	**	*	**	**	****

Time	1 vs. 33	2 vs. 33	10 vs. 33	11 vs. 33	30 vs. 33	31 vs. 33	33 vs.Positive Control
24 h	*	***	****	***	***	**	***

Time	1 vs. 33	2 vs. 33	10 vs. 33	11 vs. 33	30 vs. 33	31 vs. 33	33 vs.Positive Control
48 h	***	***	***	***	**	***	***

References

[1] Mosmann, T., (1983). Rapid colorimetric assay for cellular growth and survival: Application to proliferation and cytotoxicity assays. *Journal of Immunological Methods*, 65, 55–63. [https://doi.org/10.1016/0022-1759\(83\)90303-4](https://doi.org/10.1016/0022-1759(83)90303-4).

[2] French, A.D., (2014). Idealized powder diffraction patterns for cellulose polymorphs. *Cellulose*, 21, 885–896. <https://doi.org/10.1007/s10570-013-0030-4>.

[3] Thomas, L.C., Chittenden, R.A., (1964). Characteristic infrared absorption frequencies of organophosphorus compounds—II. P-O-(X) bonds. *Spectrochimica Acta*, 20, 489–502. [https://doi.org/10.1016/0371-1951\(64\)80044-8](https://doi.org/10.1016/0371-1951(64)80044-8).

[4] Myers, H.M., Tochon-Danguy, H.J., Baud, C.A. (1983). IR absorption spectrophotometric analysis of the complex formed by tetracycline and synthetic hydroxyapatite, *Calcif Tissue Int*, 35, 745–749. <https://doi.org/10.1007/BF02405117>.

[5] Claro, A.M., Do Amaral, N.C., Colturato, V.M.M. *et al.* (2022). Siloxane-modified bacterial cellulose as a promising platform for cell culture. *Cellulose*, 29, 9597–9608 [DOI: 10.1007/s10570-022-04872-4](https://doi.org/10.1007/s10570-022-04872-4)

[6] Daicho, K., Fujisawa, S., Kobayashi, K. et al. (2020) Cross-polarization dynamics and conformational study of variously sized cellulose crystallites using solid-state ¹³C NMR. *Journal of Wood Science*, 66, 62. [DOI: 10.1186/s10086-020-01909-9](https://doi.org/10.1186/s10086-020-01909-9)

[7] De Oliveira Barud, H.G., Barud, H.S., Cavicchioli, M. et al (2015). Preparation and characterization of a bacterial cellulose/silk fibroin sponge scaffold for tissue regeneration. *Carbohydrate Polymers*, 128, 41–51. [DOI: 10.1016/j.carbpol.2015.04.007](https://doi.org/10.1016/j.carbpol.2015.04.007)

[8] Kono, H., Yunoki, S., Shikano, T. et al (2002). CP/MAS ¹³C NMR study of cellulose and cellulose derivatives. 1. Complete assignment of The CP/MAS ¹³C NMR spectrum of the native cellulose. *Journal of American Chemical Society*, 124, 7506–7511

[9] NBR7730.Pulp—determination of viscosity in cupriethylenediamine solution (CUEN) using capillary viscometer.1998

- [10] Oliveira, R.L., Barud, H.S., Assunção, R. M. N., Meireles, C. S., Carvalho, G. O., Filho, G. R., Messaddeq, Y., Ribeiro, S. J. L. (2011) Synthesis and characterization of microcrystalline cellulose produced from bacterial cellulose. *J Therm Anal Calorim*, 106, 703–709 DOI 10.1007/s10973-011-1449-1.

ACTA UNIVERSITATIS AGRICULTURAE SUECIAE

DOCTORAL THESIS NO. 2025:53

This thesis focuses on the synthesis and characterization of cellulose-based hybrid materials. These materials can be used for environmental applications such as selective separation of metals for the recycling of rare earth-based magnets. Other applications include delayed drug delivery and wound-dressing materials. By combining cellulose nanomaterials with metal oxides, unique composites can be formed that improve wound-healing or allow for the light-controlled release of pharmaceuticals.

Troy C. Breijaert received his graduate education at the Department of Molecular Sciences, SLU, Uppsala. He received his B.Sc. degree in Chemistry from the University of Applied Science in Leiden, and his M.Sc. degree in Chemistry from Leiden University.

Acta Universitatis Agriculturae Sueciae presents doctoral theses from the Swedish University of Agricultural Sciences (SLU).

SLU generates knowledge for the sustainable use of biological natural resources. Research, education, extension, as well as environmental monitoring and assessment are used to achieve this goal.

ISSN 1652-6880

ISBN (print version) 978-91-8046-562-5

ISBN (electronic version) 978-91-8046-567-0